SEISMIC PERFORMANCE ANALYSIS OF MID-RISE CONCRETE SHEAR WALLS REINFORCED WITH SUPERELASTIC SHAPE MEMORY ALLOYS

MARINA MACIEL

A THESIS SUBMITTED TO THE FACULTY OF GRADUATE STUDIES
IN PARTIAL FULFILLMENT OF THE REQUIREMENTS
FOR THE DEGREE OF MASTER OF APPLIED SCIENCE

GRADUATE PROGRAM IN CIVIL ENGINEERING
YORK UNIVERSITY
TORONTO, ONTARIO

July 2019

ABSTRACT

This thesis investigates the seismic performance of hybrid Shape Memory Alloy (SMA)-steel reinforced concrete shear walls containing Nickel-Titanium (Ni-Ti) superelastic SMA as alternative reinforcement in the plastic hinge region. This wall system permits self-centering with high levels of energy dissipation and significant reduction of permanent deformations. Conventional steel-reinforced concrete shear walls were designed for a prototype 10-storey office building, assuming seismic design scenarios in eastern and western Canada. Equivalent hybrid SMA-steel reinforced concrete shear walls were defined following the designed cross-sections of the conventional walls. Full-scale, 2-D finite element models of the walls were developed and subjected to nonlinear, static and time-history analyses, employing historical and simulated ground motion records for the latter. The numerical results confirmed the superior self-centering capacity of the hybrid SMA-steel reinforced walls, showing potential to optimize the seismic performance of reinforced concrete buildings, particularly in high seismic zones, by controlling residual deformations and reducing damage.

ACKNOWLEDGEMENTS

First and most importantly, the author would like to express her genuine gratitude to Professor Dan Palermo for all the support and encouragement in the two years of this research project. The confidence demonstrated in the author's ability and the assuring guidance in the face of uncertainty were highly appreciated. The author's gratitude is extended to Dr. Leonardo Cortés-Puentes for accepting the task to co-supervise this research project, for all the valuable insights regarding the numerical analysis, and for the reviews that helped with the structure of this thesis and additional research papers.

The author gratefully acknowledges the financial support provided by York University and by Mitacs Inc., the latter being what permitted the first contact of the author with the topic of this research, through the Mitacs Globalink Summer Internship program in 2015, and what incentivized the continuation of the research in the MASc program through the Globalink Graduate Fellowship.

Special thanks are due to the technical and administrative staff of the Civil Engineering Department at York University. Thanks to Sindy Mahal for being the reliable source of accurate information and dependable problem-solver, as well as for the emotional support; and to Robert for promptly providing the technical assistance that allowed the conclusion of the numerical analyses of this thesis. Thanks are extended to all the colleagues and friends for the patience and support provided during these years, including Pedro, Diana, and Rita. Special thanks are due to the professors the author had the honor to learn from.

To my parents, Eliseu and Isamar, there are not enough words in any language to thank you enough. Thank you for supporting all my choices in life, for prioritizing my education, for the emotional support that crossed all distances and gave me the motivation to face any challenge. Thank you for teaching me that I could go as far as my dedication would take me. Thanks to my sister Gabriela, to my grandmother Helena, and in special to Everton, for all the love. To all of them, I dedicate this work.

TABLE OF CONTENTS

LIST OF TABLES

APPENDIX B:

APPENDIX C:

LIST OF FIGURES

CHAPTER 3: DESIGN OF SHEAR WALLS

CHAPTER 4: NUMERICAL ANALYSIS

LIST OF SYMBOLS

A_f	austenite finish temperature (°C)
A_s	austenite start temperature (°C)
A_g	area of the gross section of a structural element (mm^2)
A_{s1}	area of concentrated reinforcement in a cross-section (mm^2)
B	maximum of all values of B_x in both orthogonal directions
b_w	minimum shear wall thickness (m)
B_x	ratio of maximum storey displacement to average displacement at level x used to determine torsional sensitivity
c	depth of the compression zone (mm)
D	dead loads (kN)
E_c	elastic modulus of concrete (MPa)
E_i	initial elastic modulus (MPa)
El_r	residual elongation
El_u	ultimate elongation
E_s	elastic modulus of steel (MPa)
E_{SMA}	elastic modulus of SMA (MPa)
f'_c	compressive concrete strength (MPa)
f'_t	tensile concrete strength (MPa)
F_{max}	peak lateral load sustained by the wall (kN)
f_u	ultimate strength of reinforcement (MPa)
f_y	yield strength of steel (MPa)
F_y	yield strength of the wall (kN)
h_n	total height of the building (m)
h_s	storey height (m)
I_E	importance factor of the building
k_{eff}	effective stiffness of the wall (kN m)
L_p	length of plastic hinge region (m)
l_u	unsupported length of shear wall (m)
l_w	length of shear wall (m)
M_v	higher mode factor
M_f	factored bending moment (kN m)
M_f	martensite finish temperature (°C)

M_s	Martensite start temperature (°C)
P	axial loads (kN)
R_0	over-strength factor of seismic-force-resisting-systems
R_d	force modification factor of seismic-force-resisting-systems
S_a	pseudo-acceleration (g)
S	snow loads (kN)
$S(T)$	uniform hazard spectrum, as defined by the NBC 2015 (NRC, 2015)
$S_g(T)$	acceleration response spectrum of selected ground motion record
$S_t(T)$	target acceleration response spectrum
T	period (s)
T_1	period of the fundamental mode of vibration (s)
$T_{90\%}$	period of the highest mode of vibration necessary to accumulate 90% of the structure mass (s)
T_a	empirical fundamental period (s), as defined by the NBC 2015 (NRC, 2015)
T_{lim}	upper limit for the fundamental period of the structure (s), as specified by the NBC 2015 (NRC, 2015)
T_R	period range of interest for selection of ground motion records for dynamic analysis (s)
T_{RS}	scenario-specific period range for selection of ground motion records for dynamic analysis (s)
T_{RSA}	fundamental period of the structure computed by response spectrum analysis (s)
V	base shear (kN)
V_d	design base shear (kN)
$V_{d\text{-}i}$	design shear force at the level i of shear wall (kN)
V_{el}	elastic base shear (kN)
V_i	shear force in the level i (kN)
V_{max}	maximum base shear suggested by the NBC 2015 (NRC, 2015) (kN)
V_{min}	minimum required base shear according to the NBC 2015 (NRC, 2015) (kN)
V_{RSA}	elastic base shear resulting from response spectrum analysis (kN)
V_{st}	static base shear (kN)
W	seismic weight of the building (kN)
γ_w	wall overstrength factor
α_1	ratio of average stress in rectangular compression block to the specified concrete strength
α_w	factor to account for degraded stiffness in dynamic analysis
β	factor that accounts for shear resistance of cracked concrete

β_1	ratio of depth of rectangular compression block to depth to the neutral axis
γ_c	concrete specific weight (kN/m^3)
Δ	lateral displacement (mm)
δ	drift (%)
Δ_{avg}	average lateral displacement at storey level between Δ_{min} and Δ_{max} (mm)
Δ_f	displacement at the top of the wall under factored loads (mm)
Δ_i	inelastic interstorey displacement
δ_i	interstorey drift (%)
Δ_{max}	maximum lateral displacement registered at storey level (mm)
Δ_{min}	minimum lateral displacement registered at storey level (mm)
Δ_u	ultimate displacement (mm)
Δ_y	yield displacement (mm)
ε_{cu}	ultimate concrete strain
ε_o	strain in concrete membrane element (mm/mm)
ε_{sh}	strain hardening strain of reinforcement (mm/mm)
ε_{su}	ultimate strain of reinforcement (mm/mm)
θ	angle of the compression strut in the plastic hinge region of shear wall in shear design (degrees)
$\theta + 1$	factor to account for P-Δ effects in amplifying the seismic lateral forces
θ	stability coefficient in seismic design
θ_{ic}	rotational capacity
θ_{id}	inelastic rotational demand
λ	factor to account for low-density concrete
μ	displacement ductility
ν	concrete Poisson's ratio
ξ_{eq}	equivalent viscous damping (%)
ρ	reinforcement ratio
ρ_1	ratio of vertical distributed reinforcement
ρ_t	ratio of horizontal distributed reinforcement
σ	normal stress in concrete membrane element (MPa)
τ_{xy}	shear stress in concrete membrane element (MPa)

1. GENERAL INTRODUCTION

1.1 Background

Seismic design standards around the world are primarily developed to ensure life safety of the occupants of buildings during the design-level seismic event. For reinforced concrete structures, design provisions are developed based on yielding of the longitudinal reinforcement as the primary mechanism to dissipate the energy of large earthquakes. Due to the post-yield plastic properties of steel reinforcing bars, the use of the inelastic capacity of the steel results in permanent deformations, as is observed in the characteristic stress-strain relationship of the material illustrated in Figure 1-1 (a). Figure 1-1 (b) illustrates the stress-strain relationship of superelastic shape memory alloys. The consequence of strong ground motions on reinforced concrete structures is the substantial damage to non-structural and structural components, leading to significant economic losses due to repair costs and inactivity of the structures for a significant period of time. The extent of damage can even render repair prohibitive and, very often, demolition is the only solution.

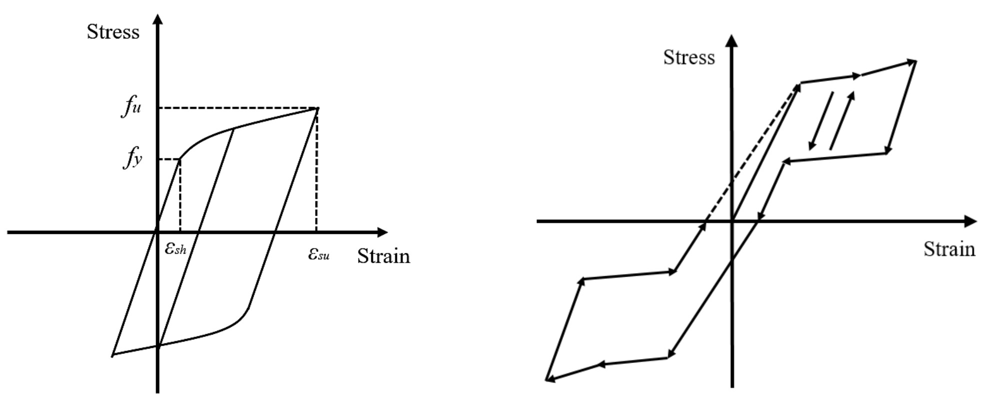

(a) (b)

Figure 1-1 - Schematic stress-strain relationship of reinforcing bars: (a) steel bars (modified from Abraik and Youssef, 2018) and (b) superelastic SMA bars (modified from Abdulridha and Palermo, 2017)

The current reliance on yielding of steel reinforcement in reinforced concrete structures can lead to adverse post-earthquake scenarios even when life safety is ensured, as widespread severely damaged structures within a city or region could drastically disrupt the economy. For instance, the level of damage to building structures inflicted by the 2010-2011 Canterbury Earthquake, in the city of Christchurch, New Zealand, rendered repair unfeasible and led to demolition of approximately 60% of the multi-storey reinforced concrete buildings in the Central Business District of the city, forcing its closure for over two years (Marquis et al., 2017). The building depicted in Figure 1-2 (a), an 11-storey RC frame and shear wall building located in the Central Business District of Christchurch, is part of the list of structures that were abandoned/demolished after the earthquake (EERI, n.d.). The RC buildings in the region were designed according to modern seismic codes, which satisfactorily guaranteed life safety and collapse prevention during the seismic event. The damage sustained by structural elements of the building after the event can be observed in Figure 1-2 (b) and (c). The post-earthquake responses were dictated by the level of damage and repairability of the buildings, followed by insurance issues, business strategies, perception of risks, building regulations, and government decisions. The Christchurch experience has been recognized to have instigated a change in building owners' and tenants' preferences towards damage-resisting technologies that minimize disruption, economic impacts, and dependency on insurance (Marquis et al., 2017).

(a) (b) (c)

Figure 1-2 - 11-storey RC frame with shear walls building in Central Business District of Christchurch (EERI, n.d.): (a) building prior to 2010-2011 earthquake series, (b) damage to column in the first floor and (c) shear and axial failure of column in the basement

In order to mitigate such consequences, there has been a growing trend among the engineering community towards performance-based design and the development of smart structures. Smart structures are capable of detecting their own damage and adopting changes to repair their condition. In other words, they can adapt to the surrounding environment, provide optimal operating conditions, improve overall life cycle performance, and substantially decrease maintenance costs (Alam et al., 2007). This recent trend has given rise to the development of high-performance structural systems that aim to provide enhanced deformation capacity and ductility, higher damage tolerance, and recovered permanent deformations (Alam, Nehdi and Youssef, 2008).

Contrary to the substantial permanent deformations sustained by conventional structural systems, novel systems with inherent self-centering capacity can mitigate damage by undergoing severe earthquakes with little or even negligible damage to non-replaceable elements. In shear-wall-type elements, the conventional energy dissipation mechanisms are yielding of longitudinal reinforcement and crushing of the concrete at the base, as illustrated in Figure 1-3. Due to their relatively high stiffness, reinforced concrete shear walls are commonly employed in the lateral force-resisting system of buildings. In contrast, self-centering systems are a new class of Seismic Force-Resisting Systems (SFRS) that possess the ability to return to their original position when loading has ceased, enabling the possibility of immediate occupancy and reducing the socio-economic costs associated with severe seismic hazards. In these systems, damage is localized in energy dissipation devices that can be readily replaced after strong ground shaking, representing a significant advancement when compared to conventional concrete structures that require inelasticity to be developed in the primary structural members in order to dissipate energy. One way of achieving such desirable behaviour is to incorporate smart materials such as Shape Memory Alloys (SMAs) to conventional structural systems.

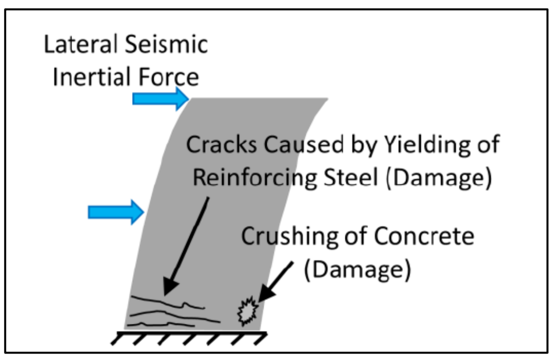

Figure 1-3 - Inelastic mechanisms in reinforced concrete shear walls (Chancellor et al., 2014)

SMAs are metallic alloys with the ability to sustain large deformation and to recover to a predetermined shape when heated (shape memory effect) or when loading is removed (superelastic feature). SMAs can absorb and dissipate energy by undergoing a reversible hysteretic shape change when subjected to cyclic loading. Due to these unique features, SMAs have become popular in engineering for sensing and actuation, impact absorption, and vibration damping applications (Lagoudas, 2008). Prior to their implementation in civil engineering, SMAs have been widely utilized in a broad range of fields and industries, including aviation and aerospace, automotive, biomedical, and oil exploration. One of the most prevalent SMAs is the Nickel-Titanium alloy. This alloy was discovered by Buehler and coworkers at the Naval Ordnance Laboratory in 1963 (Buehler et al., 1963) and represented the breakthrough of SMA for engineering applications (Lagoudas, 2008). This alloy, commonly referred to as NiTiNOL (Nickel Titanium Naval Ordnance Laboratory), is of particular interest for seismic engineering applications due to characteristics such as large superelastic strain recovery, high energy dissipation, and excellent low-cycle and high-cycle fatigue properties (Tarzav and Saiidi, 2015). The reverse transformation that occurs during unloading of superelastic SMA initiates the recovery of displacements in SMA-reinforced structural elements, as illustrated in the hysteretic constitutive model of SMA in Figure 1-1 (b). Meanwhile, the linear unloading path characteristic of steel, shown in Figure 1-1 (a), induces large permanent displacements in conventional steel-reinforced structural elements (Abdulridha and Palermo, 2017). The self-centering capacity of SMA also has the potential of facilitating post-earthquake repairing, as the need to re-align structural elements prior to repair can be substantially reduced (Cortés-Puentes et al., 2018). Moreover, the resistance to corrosion is much greater in SMA compared to steel (Alam et al., 2007).

The opportunities for implementing superelastic SMA-based systems in structures for seismic applications are various, including their use in new concrete structures and in retrofitting of existing structures. In new structures, SMAs have been investigated as internal reinforcement, bracing, bolted connections, restrainers, and prestressing strands (Alam et al., 2007). For retrofitting of existing structures, the beneficial features of SMAs can be exploited in the form of braces, dampers, isolators, and post-tensioning tendons. The specific application of SMA as alternative reinforcement is still in its infancy. The world's first SMA-reinforced Engineered Cementitious Composite (ECC) bridge column was recently constructed in Seattle, WA, in 2017 (Baker et al., 2018). Figure 1-4 (a) depicts the South Dearborn Street off-ramp bridge under construction, and Figure 1-4 (b) illustrates the superelastic Ni-Ti bars coupled to steel bars at the critical region of a bridge column. The use of superelastic SMA as reinforcement is an important asset in the development of smart and resilient structures, and which its potential has room for further exploitation.

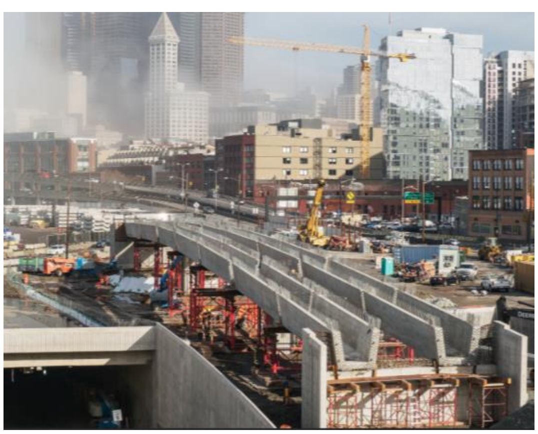

(a)

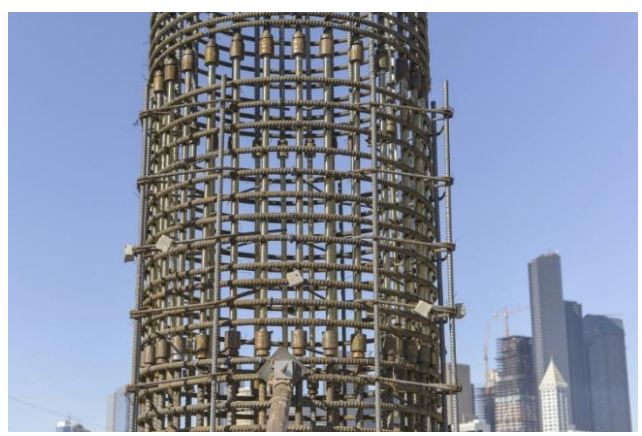

(b)

Figure 1-4 - South Dearborn Street off-ramp bridge in Seattle, WA: (a) during construction (Schlosser, 2016) and (b) reinforcement of bridge column containing SMA (Doughton, 2017)

1.2 Proposed study

This thesis investigates the seismic response of self-centering Reinforced Concrete (RC) shear walls containing Ni-Ti superelastic SMA as alternative reinforcement. A prototype, 10-storey office building with four rectangular slender RC shear walls in each principal direction serving as the lateral force resisting system is considered for two distinct design locations: one in a high seismic zone in western Canada (Vancouver, BC); and the other in a moderate seismic zone in eastern Canada (Montreal, QC). A conventional-reinforced RC ductile shear wall is designed for the Vancouver location, whereas a moderately ductile type of wall is adopted for Montreal, to represent standard practice. The lower seismic demand in Montreal does not justify the use of a ductile wall, which requires more complex detailing. To determine the seismic forces and resulting displacements experienced by the shear walls, 3-D models of the building were developed and subjected to dynamic modal response spectrum analysis. Design of the conventional RC shear walls followed the seismic detailing provisions prescribed by the 2015 National Building Code of Canada (NRC, 2015) and the Canadian Standards Association Standard A23.3-14 for Design of Concrete Structures (CSA, 2014).

A second set of companion shear walls is proposed with the implementation of Ni-Ti superelastic SMA as reinforcement in strategic regions. The design of these walls is based on the conventional steel-reinforced walls, with comparable dimensions and reinforcement details, except for the longitudinal steel-reinforcing bars in the plastic hinge zone within the boundaries, which are replaced by Ni-Ti superelastic SMA bars of similar diameter. The use of the cross-section and reinforcement layout of the steel-reinforced walls to define the design of the hybrid SMA-steel walls is due to the lack of explicit provisions for seismic design of SMA-reinforced concrete members. Full-scale Finite Element (FE) models of the designed walls were developed using the software program VecTor2 (Vecchio et al., 2013) and were subjected to static and dynamic nonlinear analyses. Detailed finite element analysis permitted an explicit evaluation of damage, including cracking and crushing of concrete, and strain and deformation of the reinforcing steel and SMA. Understanding the full performance becomes important where emerging materials are being used to better comprehend their interaction to other materials. The response of the walls was evaluated, including the following response parameters: lateral strength, and displacement capacity, residual drifts, wall rotation, energy dissipation, and recovery capacity. The developed models were also used to conduct a thorough investigation of modelling aspects and analysis parameters that influence the response of complex, large-scale finite element models subjected to nonlinear static and dynamic analyses in VecTor2, with an aim to contribute to the improvement of numerical simulation of SMA-reinforced concrete structural elements in the FE program.

Ultimately, dynamic analyses of the walls employing ground motion records representative of the seismic hazard of the two design locations were performed to investigate the improvement in seismic performance due to the implementation of SMA bars in the two types of walls. Eleven ground motions were selected among simulated and natural earthquake records to represent each seismic zone. The records were scaled according to the NBC 2015 guidelines to match the uniform hazard spectra of Vancouver and Montreal along a defined period of interest. Amplified ground motion records were also employed for the Vancouver scenario, permitting further investigation of the behaviour of hybrid SMA-steel reinforced concrete shear walls in high seismic zones. Permanent drifts and recentering capacity of the walls resulting from nonlinear time history analysis were compared to seismic performance limits prescribed by current provisions, such as the ASCE/SEI 41-17 (ASCE, 2017) and by supplementary research studies.

1.3 Research objectives

The prime objective of this research is to assess the seismic performance of mid-rise hybrid SMA-steel concrete shear walls reinforced with Ni-Ti superelastic SMA in the plastic hinge zone through numerical simulation. The potential benefits of implementing this novel material as reinforcement, including self-centering and energy dissipation capacity, were investigated by comparing the seismic response of ductile and moderately ductile conventional steel-reinforced walls to the response of equivalent SMA-reinforced walls using nonlinear finite element analysis. The use of full-blown finite element analysis was intended to permit a comprehensive understanding of the interaction of this novel material with the conventional materials in reinforced concrete, evaluating potential localized effects that could not be modelled with simpler modelling tools. The analyses in this research permitted:

1. The evaluation of the lateral capacity of the walls through monotonic and reverse cyclic loading in terms of:
    - 1.1 Lateral strength;
    - 1.2 Effective stiffness;
    - 1.3 Drift capacity;
    - 1.4 Displacement ductility;
    - 1.5 Wall rotation;
    - 1.6 Self-centering capacity;
    - 1.7 Energy dissipation capacity; and
    - 1.8 Failure mechanism.

2. The evaluation of the seismic performance of the walls through comparison of seismic performance limits from the literature to response parameters obtained from dynamic analysis of the walls, including:

   2.1 Transient and permanent roof drifts;

   2.2 Transient and permanent interstorey drifts;

   2.3 Progress of damage; and

   2.4 Recovery.

A secondary objective of this research was to contribute to the improvement of numerical simulation of SMA-reinforced concrete structural elements in the finite element analysis program employed. To achieve this objective, a sensitivity analysis was conducted. The influence on the response of the complex, large-scale finite element models was evaluated, based on various modelling aspects and analysis parameters.

In summary, this research intends to contribute to the advancement of the use of SMA as reinforcement in concrete structures by providing the response of full-scale, mid-rise shear walls, which are investigated using detailed finite element, nonlinear dynamic analyses that includes the behaviour of the hybrid structural system in moderate and high seismic zones.

1.4 Research significance

Several researchers have demonstrated the superior seismic response of concrete elements reinforced with SMA bars, including excellent self-centering and restoring capacities associated with substantial energy dissipation (Alam et al., 2007, 2012; Alam, Youssef and Nehdi, 2008; Abraik and Youssef, 2015, 2016, 2018; Cortés-Puentes et al., 2018; Cruz-Noguez and Saiidi, 2013; Ghassemieh et al., 2017; Tarzav et al., 2015, 2018; Wang and Zhu, 2018; and Youssef et al., 2008, 2010). In shear walls, experimental tests and complementary numerical studies have demonstrated that hybrid SMA-steel RC walls can recover large inelastic displacements despite the presence of steel reinforcement in the web portion of the walls (Abdulridha and Palermo, 2017). Numerical studies investigating the effects of axial loading have also demonstrated the energy dissipation capabilities of SMA-reinforced concrete shear walls (Maciel et al., 2016). Regardless of the lower energy dissipation, flag-shaped hysteretic behaviours, similar to that of RC shear walls containing SMA, have been verified by numerical studies to provide equivalent or even improve the seismic response of low-strength systems relative to elastic-plastic hysteretic behaviour (Christopoulos et al., 2002), such as that of steel-reinforced walls. Flag-shaped hysteretic behaviours combine the beneficial effect of energy dissipation with self-centering, mitigating undesirable effects of natural earthquakes in structures, such as ratcheting. Ratcheting is the progressive accumulation of inelastic deformation along one side of the hysteretic response of a structure, which can occur when the amplitude of stresses exceeds the elastic limit. Recentering delays the accumulation of plastic strains in a single direction, reducing the likelihood of ratcheting occurring in systems capable of self-centering.

The arrangement of SMA bars in the hybrid SMA-steel reinforced walls investigated in this thesis has been recognized as the most cost-effective for moderate and squat SMA-reinforced shear walls (Abraik and Youssef, 2015) and for slender 3-storey walls (Abraik and Youssef, 2016). In these studies, the arrangement of SMA bars in the boundary zones within the plastic hinge region was the most effective among the investigated layouts in reducing residual drifts and damage in the hybrid walls. Numerical results also indicated that the beneficial effects of employing SMA when bars are restricted to the plastic hinge region become noticeable for shear walls with aspect ratios greater than 0.9 (Abraik and Youssef, 2015). Due to the high initial cost of SMA, it has been suggested that the use of the material should be restricted to critical regions (Abdulridha and Palermo, 2017).

The hybrid SMA-steel reinforced concrete shear walls investigated in this study were geared to achieve optimal seismic performance with high self-centering capacity, controlled damage, reduced residual deformations, and significant energy dissipation. When applied to building structures, this behaviour potentially reduces and simplifies post-earthquake repairs, rendering buildings functional more readily and drastically minimizing economical losses after seismic hazards. Given the improvements in behavioural response, specifically considering direct and indirect costs such as repair and downtime, hybrid SMA-steel RC shear walls can be an alternative to conventional structural systems in earthquake-prone buildings.

Repair costs can have a major impact in cost-effectiveness of SMA-based systems. As an example, the repair of damaged RC beam-column joints subjected to reverse cyclic testing was estimated by Nehdi et al. (2011) to be three to five times more costly, laborious and time-consuming in steel-reinforced specimens than in equivalent SMA-reinforced specimens. Nehdi et al. state that the reduced initial cost in construction of steel-reinforced frames, about 10-20% lower, would be irrelevant when compared to the significantly higher cost of repair after a large earthquake. SMA-based systems also do not incur additional costs for maintenance or replacement over the lifespan of the structure as is required for other dampers and isolation devices (Alam et al., 2007).

In order to introduce SMA-reinforced concrete shear walls into structures, a comprehensive understanding of the seismic response of the walls when part of building structures is paramount. The majority of studies available on SMA-reinforced concrete shear walls have focused on the analysis of single-storey walls, not addressing the implications associated with the use of SMA as reinforcement in shear walls of multi-storey dimensions. In addition, the novel application of SMA bars as reinforcement in concrete requires detailed analysis of potential localized effects caused by the material, such as the bond to concrete and the consequent development of large localized cracking. To address these issues, the numerical models in this thesis were developed as full-scale, mid-rise shear walls in the finite element program VecTor2 (Vecchio et al., 2013), permitting a thorough assessment of the seismic response of reinforced concrete shear walls containing SMAs. Program VecTor2 can predict the combined effects of shear and flexure on the response of the concrete and can be used to appropriately predict the shear force distribution envelope of RC shear walls under seismic events when test results are not available (Luu et al., 2013). Furthermore, Ghorbani-Renani et al. (2009) acknowledged that VecTor2 can capture the failure mechanism associated with shear sliding behaviour observed in experimental tests, which cannot be captured by simpler frame models with lumped plastic hinges.

The numerical analyses conducted in VecTor2 as part of this thesis included nonlinear time history analysis, which provides more realistic results that properly captures the nonlinear behaviour of reinforced concrete structures. Time history analysis methods capture the various response parameters as time histories, permitting a temporal assessment of deformations of the structure. In contrast, cyclic analyses provide results limited to the static response of a structural element, failing to reproduce the effects of real earthquakes in terms of permanent deformations and of other effects that can be developed over time, such as ratcheting, which significantly affects the permanent deformation of structures and can lead to premature and catastrophic failure. The earthquake records used for the analyses permit the identification of the benefits of using SMA in RC structures within different levels of seismic activity, specifically for two seismic zones in Canada.

The use of dynamic analysis in this thesis was motivated by the fact that residual drifts in self-centering RC shear walls at the conclusion of an earthquake can be much lower than the maximum residual drifts demonstrated by cyclic hysteresis loops, as observed by Henry et al. (2016) after extensive time-history analysis of a sample self-centering concrete wall system. For that reason, more realistic evaluations of residual drifts also consider the post-peak behaviour of the structure, which is characterized by the dynamic response of the structure during the remainder of the ground motion and the free vibration response subsequent to the end of the input motion. Moreover, the complete understanding of the effects of the lower stiffness of hybrid shear walls on the seismic response, given the lower modulus of elasticity of Ni-Ti SMA compared to that of deformed steel, requires the use of nonlinear dynamic analysis (Abdulridha and Palermo, 2017). It is worthy to note that the lower stiffness of SMA-reinforced walls does not necessarily implicate in an inferior seismic performance, since a lower stiffness elongates the fundamental period of the structure which, in turn, would result in lower seismic forces.

1.5 Research limitations

1.5.1 Design provisions for SMA-reinforced concrete elements

The design of the hybrid SMA-steel reinforced walls investigated in this thesis was based on the design of conventional steel-reinforced walls. Traditional methods for the analysis and design of reinforced concrete structures have been acknowledged to be suitable for SMA-reinforced concrete elements (Abdulridha and Palermo, 2017). This equivalent design was employed herein for a proof-of-concept investigation of the behaviour of mid-rise RC shear walls reinforced with SMA, but it is important to note that it does not represent an optimal design for this innovative wall system. It has been acknowledged that the conventional relationships adopted by design codes regarding strength, period and ductility demand may not be valid for self-centering systems, as systems with flag-shaped hysteretic behaviour are susceptible to higher ductility demand than systems with bilinear elastoplastic hardening behaviour when the system has low energy dissipation (Chancellor et al., 2014). Performance can be corrected, nevertheless, if enough post-yield stiffness and energy dissipation are provided. Therefore, a resilient seismic design method addressing self-centering shear walls and specifically SMA-reinforced concrete walls needs to be established by future studies.

1.5.2 Validation against test results

Given that available research studies have only considered experimental testing on scaled or single-storey SMA-reinforced concrete walls, the cornerstone of this thesis was to extend the investigation of the behaviour of this wall system to mid-rise, multistorey walls with the use of numerical analysis. The finite element models and analysis parameters employed herein were extended from previous research (Maciel et al., 2016; Abdulridha and Palermo, 2017). However, the numerical results could not be validated against equivalent experimental testing results. To the extent of the author’s knowledge, hybrid walls with the same characteristics of the walls in this study (height in particular) have not been built and tested. This corroboration with experimental results could be addressed by more comprehensive studies in the future.

1.5.3 Self-centering of the building

To achieve the damage-free post-earthquake performance targeted by self-centering systems such as that investigated in this thesis, control of damage must be extended to secondary elements, including the gravity force-resisting system and non-structural components. If extensive damage is present in these secondary elements, the entire structure may not completely recenter once the ground excitation ceases, despite the self-centering capacity of the main structural system (Henry et al., 2016). Supplementary structural and nonstructural components of a building containing self-centering precast concrete walls have been acknowledged by analytical studies to strongly alter the hysteretic behaviour of the structure in terms of strength, energy dissipation and residual drifts (Henry et al., 2012). However, the hysteretic response of secondary elements is typically characterized by strong degradation, pinched hysteretic behaviour and consequent small residual strength after large displacement cycles; therefore, the negative effects on the overall self-centering of the structure may not be significant (Chancellor et al., 2014). In buildings containing SMA-RC walls, greater deformation can be imposed on columns, which can be permanent and consequently inhibit recentering of the building if insufficient ductility is provided to the columns, as observed by Abdulridha (2013). According to Abdulridha, the use of superelastic SMA-RC columns could be an alternative, although the low modulus of elasticity of SMA could increase top-storey drifts. Therefore, it is paramount for the self-centering of buildings that serviceability and minimal levels of damage are ensured to partitions, floor diaphragms, cladding, to name a few. In this thesis, the columns of the building were considered as leaning columns that do not participate in the lateral resistance of the building and sustain the lateral deformation within the elastic range. Ductility could be provided to the columns, allowing them to experience inelasticity; however, this option was not investigated herein. Although this discussion represents an important factor to the overall application of self-centering shear wall systems, the assessment of the self-centering capacity of the building including secondary elements is beyond the scope of this thesis. Further investigations need to be conducted to address this challenge.

1.4 Thesis outline

This thesis is organized into eight chapters, as follows.

- **Chapter one:** This chapter introduces important concepts around seismic-resisting structures, self-centering systems, and shape memory alloys. The proposed study is presented, along with the research objectives. Research contributions are highlighted, including the benefits of SMA-based self-centering systems, the pioneering use of dynamic analysis in full-scale finite element models of SMA-reinforced concrete shear walls, and the more accurate response provided by this type of analysis. In addition, research limitations are discussed, involving the constraints around the real self-centering capacity of a building, the lack of proper design guidelines for concrete elements reinforced with SMAs, and the unavailability of experimental results compatible with the hybrid wall system under study;
- **Chapter two:** This chapter presents a literature review on the state-of-the-art research, applications and limitations of the use of SMA as reinforcement in concrete structures. An overview of the seismic design procedure for concrete shear walls in Canada is also presented. This chapter addresses the characteristics of the finite element program employed in this thesis, including discussion of available modelling options and other modelling aspects, as well as the procedure for proper selection of ground motion records for dynamic analysis. Lastly, seismic performance assessment methods are presented, along with the definition of several parameters relevant to the evaluation of the seismic response of structures;
- **Chapter three:** This chapter includes the seismic design of the shear walls investigated in this thesis, following the NBC 2015 (NRC, 2015) and the CSA A23.3-14 (CSA, 2014) for the design of moderate ductile and ductile reinforced concrete shear walls as the main lateral seismic force-resisting system, including flexural and shear design. The 3-D model that was developed to conduct dynamic modal response spectrum analysis is presented, which provided the seismic force demands and resulting displacements of the building in the two design locations. The design adopted for the hybrid SMA-steel reinforced wall is also presented;
- **Chapter four:** This chapter presents important features of the finite element program Vector2 (Vecchio et al., 2013) and the characteristics of the models developed for the walls. Thereafter, the parameters adopted for each type of analysis are discussed, including nonlinear static pushover, reverse cyclic, and dynamic time history analysis. The ground motion records selected and scaled to represent the two seismic zones of interest, employed in the latter type of analysis, are presented next;
- **Chapter five:** Several analyses conducted in order to determine the best models for the walls investigated in this thesis are presented in this chapter. The hypotheses tested include numerous modelling aspects and variation of analysis parameters, as well as variation in the design of the hybrid walls. The

influence in the static and dynamic responses of each hypothesis is discussed, and the preferred options are justified;

- **Chapter six:** This chapter presents results from the static and dynamic numerical analyses, and the determination of important parameters of the monotonic, hysteretic and seismic response of the walls, including lateral strength, equivalent stiffness, displacement ductility, failure mechanisms, transient and permanent roof and interstorey drifts;
- **Chapter seven:** This chapter contains a discussion around the results obtained in this study, with a comparison between the response of the conventional steel-reinforced shear walls and the hybrid SMA-steel reinforced shear walls. Parameters such as energy dissipation capacity, recovery capacity, and wall rotation are determined from the static response of the walls and assessed against each other. The seismic response of the walls is ultimately evaluated based on seismic performance assessment methods;
- **Chapter eight:** This chapter outlines the conclusions of this thesis. The benefits of employing superelastic Ni-Ti SMA as reinforcement in concrete shear walls based on the performed analyses are outlined, along with the improvements in seismic performance provided by this hybrid system in moderate and high seismic zones of Canada. Moreover, recommendations for future studies are presented.

2. LITERATURE REVIEW

Beyond assuring life safety, the current challenge in seismic design is to mitigate the damage that earthquakes inflict on structures, consequently reducing the loss of serviceability, recovery time, and repair costs. The seismic performance of buildings can be improved by the implementation of self-centering systems, through the incorporation of advanced materials with inherent features that are beneficial for the seismic response, such as high energy dissipation and large strain recovery.

This chapter introduces theoretical concepts relevant to the subject of this thesis, such as the definition of shape memory alloys and their thermomechanical properties, as well as the benefits and constraints of their application in seismic-resistant RC structures. In addition, an overview of relevant studies involving the use of Ni-Ti SMA as reinforcement in concrete is presented.

The chapter provides a review of the seismic design procedures adopted by the Canadian seismic provisions, also addressing the inherent seismic design philosophy. Next, important concepts regarding the assessment of the structural seismic performance are discussed, and numerical simulation is introduced as a resourceful tool to investigate the seismic behaviour of structures. In this context, different analysis methods are presented, as well as advantages of finite element analysis. Further discussion is provided regarding this type of analysis, including the FE program employed in this thesis, important analysis parameters in static and dynamic analyses, and the selection of earthquake records for nonlinear time history analysis. The different characteristics of Canadian seismicity, which should be understood for an adequate selection of earthquake records, are briefly outlined. Lastly, seismic response indexes and seismic performance levels that can be used to evaluate the results of structural analysis are presented.

2.1 Shape Memory Alloys

2.1.1 Thermomechanical behaviour

SMAs are active materials capable of developing mechanical response when subjected to a non-mechanical field (thermal, magnetic, electrical, etc.) (Lagoudas, 2008). The magnitude of the mechanical response in active materials is typically much greater than the response of conventional materials. In particular, the coupling of the thermal and the mechanical fields controls the behaviour of SMAs. Either the mechanical or the non-mechanical field can serve as input while the other serves as output (Lagoudas, 2008). As a result, thermomechanical loads control the state of SMAs, and different combinations of temperature and stress induce reverse and forward transformations from the two phases that constitute these materials. One is a low temperature phase, the Martensite, and the other is a high temperature phase called Austenite. Cubic-shaped crystals define the Austenite phase, which have an internal structure that is distinct from that of the Martensite phase. Solid-solid martensitic transformations occur when the material in the Austenite phase is cooled in the absence of stress and constitutes a forward transformation. The reverse transformation happens when the martensitic phase is heated, transforming back to Austenite with no associated shape change. During phase transformation, both Austenite and Martensite phases coexist.

SMAs are polymorphic, which means they possess more than one crystal structure having the same chemical composition (Alam et al., 2007). Polycrystalline SMAs are formed by several grains exhibiting different crystallographic orientations. The martensitic crystals resulting from the transformation can each assume a different orientation, and the assembly of these crystals can exist in two forms: the twinned Martensite and the detwinned Martensite, the latter being defined by a predominant orientation. The temperatures that trigger these transformations are very sensitive to the magnitude of the applied stress. However, these temperatures are independent of the direction of the applied stresses (tension or compression). Greater loads yield in higher transformation temperatures (Lagoudas, 2008).

Aside from thermally induced phase transformation, SMAs can also present stress-induced transformation, and this phenomenon is associated with the pseudoelastic behaviour of SMAs. In temperatures above the Austenite finish temperature (A_f), increasing loads on the Austenite phase lead to accumulation of strain, which is followed by strain recovery during the unloading path (Lagoudas, 2008). The same strain recovery can be achieved by an increase in temperature, even without unloading, which causes the atoms to reassemble themselves and the material to regain its original shape. The aforementioned thermomechanical processes can be organized as transformation regions in a stress-temperature space, as illustrated in Figure

2-1, where the start and finish transformation temperatures are represented by M_s and M_f for Martensite, and by A_s and A_f for Austenite.

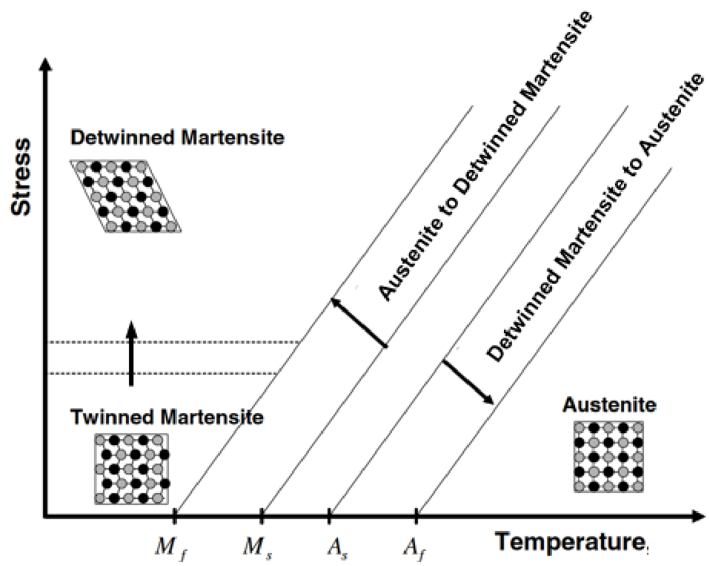

Figure 2-1 - Stress-temperature phase diagram of SMA (Lagoudas, 2008)

Within the superelastic strain range, SMAs subjected to cyclic loading dissipate energy without retaining permanent deformation. The phase transformation from Austenite to Martensite that occurs during loading and the respective reverse transformation during unloading result in a net release of energy. When this process occurs in the Martensitic phase, a full hysteresis loop is formed around the origin, ensuring the dissipation of a much higher amount of energy due to the larger loop of Martensitic compared to that of the Austenite phase. However, the Martensite phase is not self-balanced, exhibiting significant residual strain at zero stress upon unloading (Alam et al., 2007). Given the capacity to dissipate a significant amount of energy while retaining negligible residual strains, SMAs in the Austenite phase are preferable for cyclic and seismic applications.

2.1.2 Superelastic Ni-Ti SMA

The alloy of Ni-Ti, discovered by Buehler and coworkers in the early 1960s (Buehler et al., 1963), was originally an equiatomic combination of the two metals. It was discovered that the 50%-50% composition resulted in the highest A_f, reaching 120°C. While decreasing the atomic percentage of Nickel (Ni) did not alter the transformation temperatures, small increments of this material triggered large attenuation in A_f, with A_f reaching as low as -40°C if the atomic percentage of Ni was increased to 51% (Lagoudas, 2008). Therefore, controlled variations in the composition of Ni-Ti were determined to provide pseudoelasticity to this type of SMA at room temperature (23°C).

Figure 2-2 illustrates the typical stress-strain response of Ni-Ti SMA. The response is characterized by upper (UPS) and lower (LPS) plateau stresses, initial elastic modulus (E_i), residual (El_r) and ultimate (El_u) elongations, and equivalent viscous damping (ξ_{eq} – based on the area inside the hysteretic loop) (ASTM, 2014). The strain of 6% in Figure 2-2 represents the recoverable strain of Ni-Ti, and the strain of 3% corresponds to the UPS. Superelastic Ni-Ti alloys follow an elastic response with E_i until reaching the critical stress that corresponds to the start of the Martensite variant reorientation. Beyond the onset of reorientation, the modulus of elasticity drops to 10-15% of E_i (Cortés-Puentes and Palermo, 2015). For strains greater than the recoverable strain of 6%, the material stiffens and the modulus of elasticity reaches 50-60% of E_i (Elbahy et al., 2009). Permanent deformations are accumulated upon unloading at this stage and beyond, but can be recovered through heating (shape memory effect). It is important to note that yielding, as it implies permanent deformation, is not experienced by superelastic SMAs. The stress-strain response exhibits a substantial change in stiffness similar to yielding of steel. The change in stiffness, however, is due to phase transformation rather than yielding and does not incur in permanent deformation (Tarzav and Saiidi, 2015).

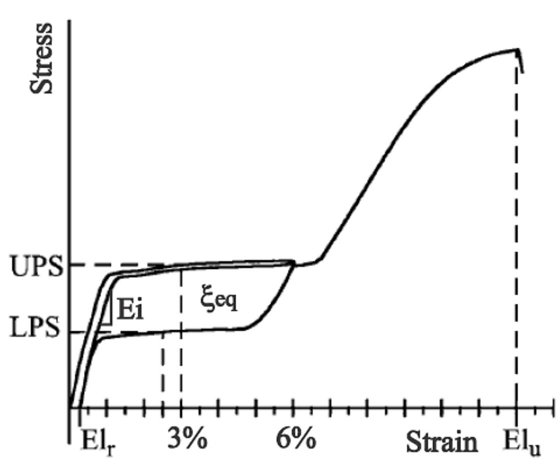

Figure 2-2 - Typical stress-strain response of Ni-Ti SMA (ASTM, 2014)

Table *2-1* provides mechanical properties of large diameter Ni-Ti bars at room temperature (Yin et al., 2015). Although SMAs develop an asymmetrical stress-strain response to tension and compression, models assuming symmetric mechanical properties based on the expected tensile properties are commonly adopted. Tarzav and Saiidi (2015) concluded that symmetric tensile-based models are sufficiently accurate to represent the behaviour of SMA for reinforcing applications, after conducting extensive analytical investigations of Ni-Ti samples produced by different manufacturers and tested by different methods.

Table 2-1 - Properties of large diameter SMA bars at room temperature (Yin et al., 2015)

Property	Value
Upper plateau stress (UPS)	400-550 MPa
Ultimate tensile stress (f_u)	1100-1400 MPa
Modulus of Elasticity (E_{SMA})	40-75 GPa
Ultimate elongation (El_u)	15-20%

2.2 Concrete elements reinforced with superelastic Ni-Ti SMA

This section presents a review of the state-of-the-art research involving the application of superelastic Ni-Ti SMA as alternative reinforcement in reinforced concrete members. The review focuses on reinforced concrete elements including shear walls, moment-resisting frames, beam-column connections, beams, columns, and bridge piers. Many of the studies addressed in this section have investigated the seismic response of SMA-reinforced members through experimental testing and numerical analyses, following static cyclic and dynamic loadings. Several studies also address the repair and restoration of the load-carrying capacity of the structural elements to mitigate the post-earthquake damage. In general, the aspects of the behavioural response of SMA-reinforced concrete members evaluated in the studies covered by this literature review involve the lateral strength, displacement ductility, progress of damage, energy dissipation and self-centering capacities.

2.2.1 Shear walls

This section will present the available studies that focus on the investigation of concrete shear walls reinforced with SMA bars. In the studies, experimental testing of the concrete walls on shake tables, or subjected to quasi-static cyclic loading, is often complemented by numerical simulations. The numerical simulations involve reverse cyclic and time history analyses and are frequently used to evaluate the effects of varying multiple parameters on the response of the walls. Evaluation of the post-earthquake condition of the walls is typically present, including the characterization of sustained damage and associated repairability.

Abdulridha and Palermo (2017) investigated the performance of shear walls reinforced with superelastic Ni-Ti SMA in the plastic hinge region, as illustrated in Figure 2-3 (a). Experimental tests and complementary numerical studies were performed. The hybrid SMA-steel wall sustained large inelastic deformation without significant loss in load carrying capacity and recovered 92% of the lateral displacements at the end of testing. The recovery in a companion steel-reinforced wall was limited to 31%, as is evident in Figure 2-3 (b). In comparison with the steel-reinforced wall, the hybrid wall exhibited lower initial stiffness but comparable yield and ultimate strengths, superior restoring capacity at drifts up to 3.0%, equal total rotation at peak lateral load capacity, similar displacement capacities and lower, but significant, energy dissipation.

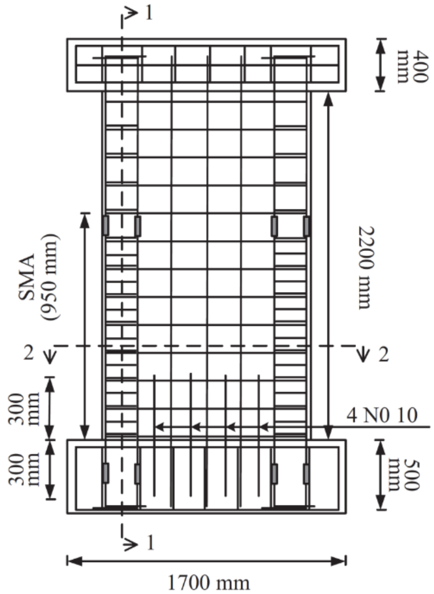

(a)

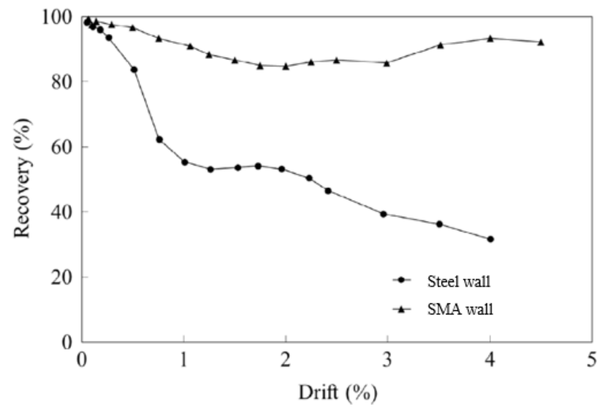

(b)

Figure 2-3 - Study by Abdulridha and Palermo (2017): (a) Elevation of SMA wall and (b) displacement recovery capacity-drift response of the walls

Maciel et al. (2016) extended the study on the hybrid SMA-steel shear wall tested by Abdulridha and Palermo (2017) by investigating the effect of axial load on the restoring capacity of the wall under simulated reverse cyclic analysis. The results suggested that the effectiveness of hybrid SMA-steel walls in controlling permanent displacements was substantially greater when axial load ratios ($P/A_g f'_c$) were limited to 10%. The hysteretic response of the hybrid wall subjected to 10% axial load ratio is provided in Figure 2-4 (b), while the wider hysteretic loops exhibited by the steel-reinforced wall is shown in Figure 2-4 (a). Beyond this level of axial load, the benefits of using SMA were not as evident. This is a direct result of the restoring effect of the higher axial loads. When compared to the companion deformed-steel-reinforced wall, the hybrid wall demonstrated superior restoring of residual displacements, and similar lateral load and displacement capacities.

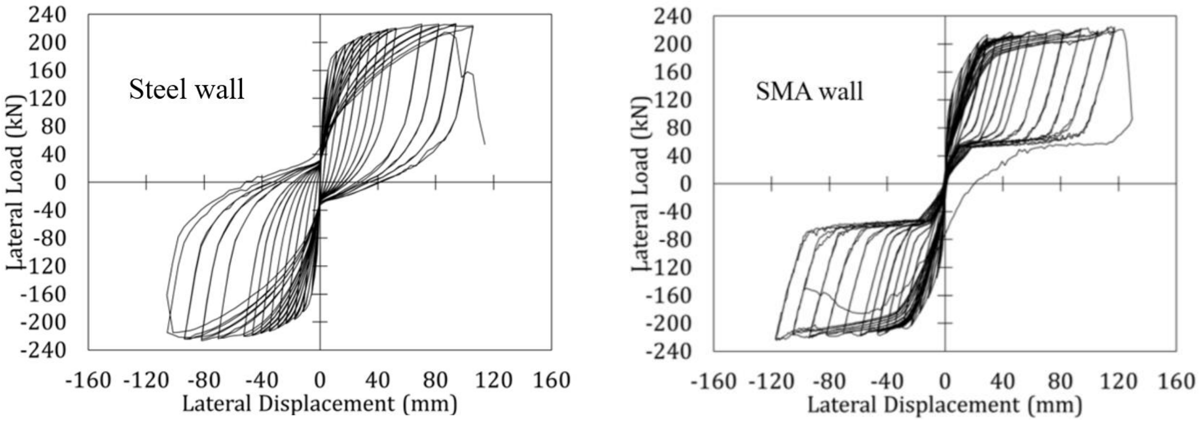

(a) (b)

Figure 2-4 - Hysteretic response of walls under 10% axial load (Maciel et al., 2016): (a) steel-reinforced wall and (b) SMA-reinforced wall

Abraik and Youssef (2015) investigated the optimal location for SMA bars targeting seismic performance in intermediate and squat RC shear walls, with aspect ratios of 0.6, 0.9 and 2.2, through the use of numerical analysis. The squat walls were modelled according to three distinct configurations: longitudinal reinforcement composed exclusively of SMA bars; longitudinal steel bars replaced by SMA bars in 1/3rd of the height of the wall; and four bars replaced by SMA bars at the edges of the wall, with steel bars elsewhere. The intermediate wall was designed with two reinforcement layouts: SMA bars in the plastic hinge region, and SMA bars limited to the edge zones of the plastic hinge region. Detailing of the walls are depicted in Figure 2-5. The numerical results indicated that the arrangement with SMA bars over the full height of the wall provided the best performance, demonstrating 70% drift recovery. The use of SMA bars restricted to the plastic hinge region only exhibited beneficial effects in the response of walls with aspect ratios greater than 0.9. Meanwhile, the intermediate walls benefited the most from the arrangement with SMA bars restricted to the plastic hinge region, which provided 50% drop in the residual drifts and 94% drift recovery.

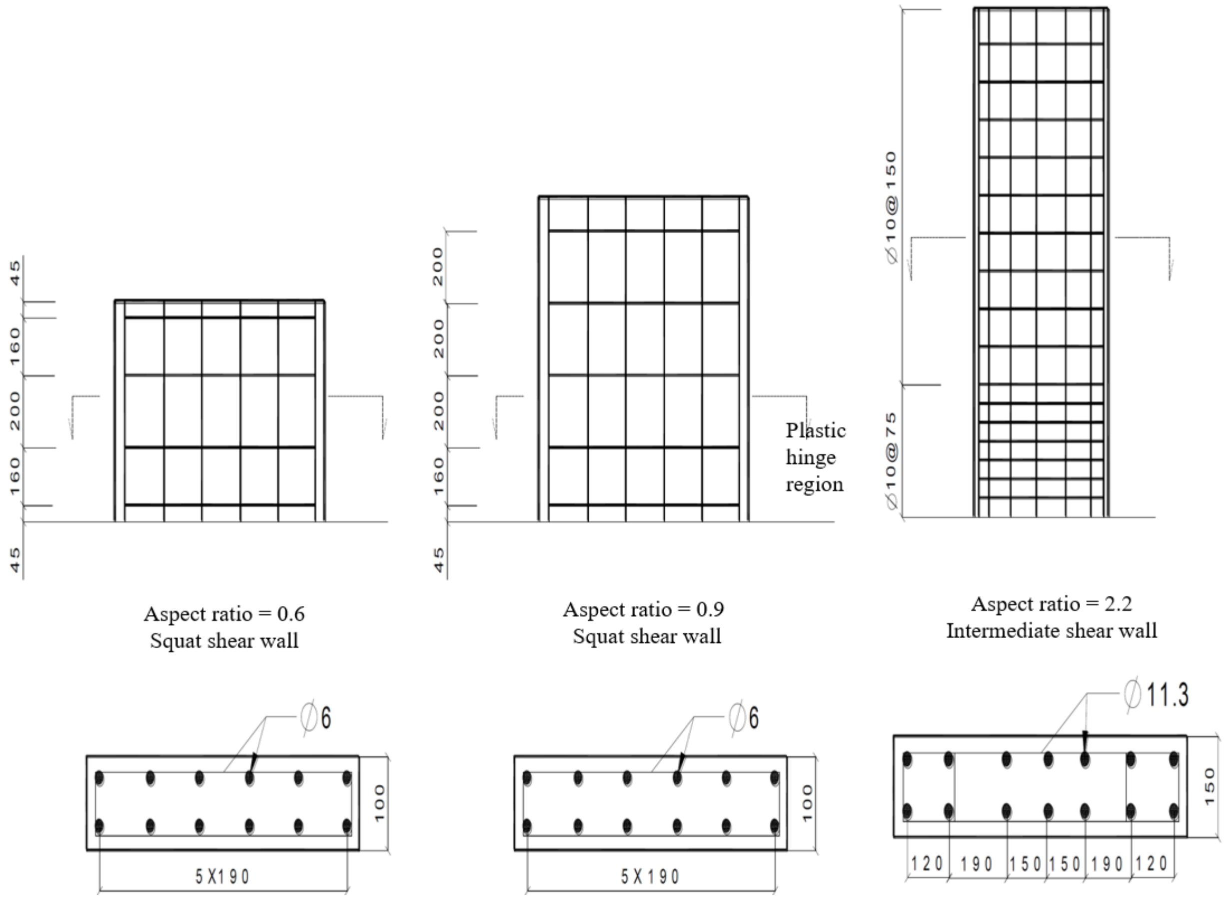

Figure 2-5 - Elevation and cross-section of walls investigated by Abraik and Youssef (2015) (dimension in mm)

In a subsequent study, Abraik and Youssef (2016) evaluated the response of 3-storey SMA RC shear walls using Incremental Dynamic Analysis. Different potential locations for SMA bars were investigated, as depicted in Figure 2-6. The results demonstrated that the most effective arrangement in reducing residual drifts and damage on the walls was that with SMA bars restricted to the plastic hinge region of the first storey. The presence of SMA in the walls permitted a more reliable seismic performance compared to that of the conventional RC walls. Furthermore, eigenvalue analyses presented an increase of 9.0%, on average, in the fundamental period of the walls caused by the introduction of SMA bars in the RC walls.

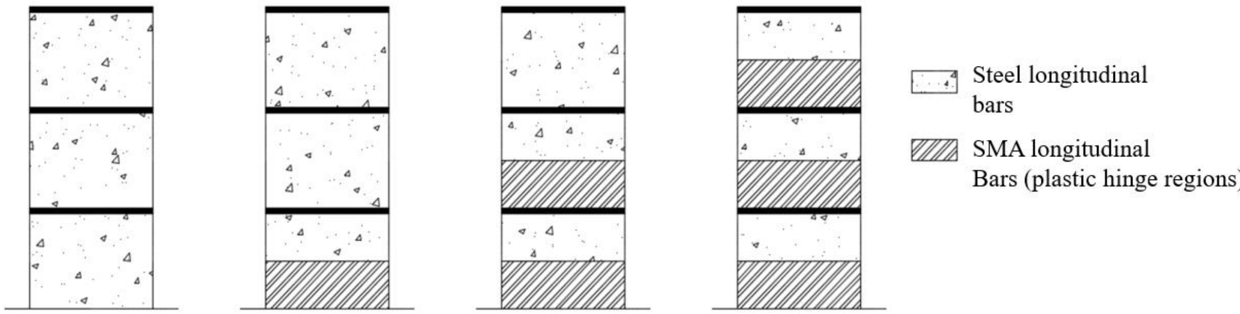

Figure 2-6 - Shear wall configurations investigated by Abraik and Youssef (2016)

In a different approach, the same authors assessed the seismic fragility of RC shear walls reinforced with Ni-Ti SE-SMA in the boundaries of the two plastic hinge regions that were considered (Abraik and Youssef, 2018). The regions had a length of approximately 20% of the wall height and were located at the base and at mid-height sections. Models of prototype 10- and 20-storey walls were developed in a fiber section analysis program and were subjected to ground motion records representative of seven different hazard levels with return periods ranging from 72 to 2475 years. Fragility curves were adopted to express the probability of damage for a given seismic intensity. Results demonstrated a significant reduction in wall fragility at low levels of seismic excitations in the walls with SMA, with reductions of 66% and 50% in the probability of collapse of the 10- and 20-storey walls, respectively. The SMA-reinforced walls provided improved seismic performance, including lower shear forces and bending moments, and reduced residual displacements. Residual drifts of the 10-storey walls when subjected to different seismic intensities are illustrated in Figure 2-7. For moderate and high seismic intensities, the reduction in residual displacements ranged from 19% to 50%. Therefore, the SMA-reinforced walls were deemed less vulnerable to seismic damage in terms of residual drifts compared to the conventional steel-reinforced walls.

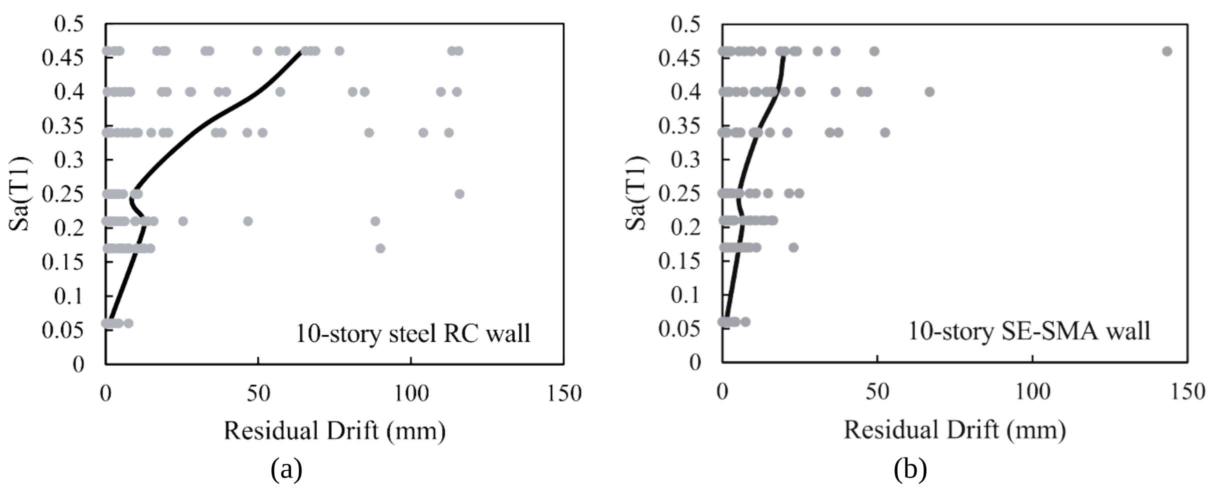

Figure 2-7 - Residual drifts of 10-storey walls for different ground motion accelerations for (Abraik and Youssef, 2018): (a) RC wall and (b) SE-SMA wall

Ghassemieh et al. (2017) investigated the benefits of replacing diagonal steel rebars with Ni-Ti SE-SMA bars in coupling beams of two-storey RC coupled shear walls. The prototype walls consisted of a steel-reinforced coupled shear wall (SW1), a coupled shear wall with diagonal steel rebars embedded in the coupling beams (SW2), and a coupled shear wall with diagonal SMA bars embedded in the coupling beams and in the opening corners (SW3). The walls were modelled as three-dimensional finite element models and subjected to static cyclic lateral loading. The analytical models were validated against the results of an existing experimental test. Results confirmed the capacity of diagonal rebars to reduce damage to the coupling beams and opening corners, particularly when SMA rebars were adopted. The lateral resistance of the shear walls at stages of large deformation was improved by the presence of SMA, which preserved the integrity of the shear walls by delaying damage in the coupling beams. The presence of SMA also minimized the permanent displacements and drifts in the shear walls, and provided similar energy dissipation capacity compared to the other walls, as illustrated in Figure 2-8 (a) and (b).

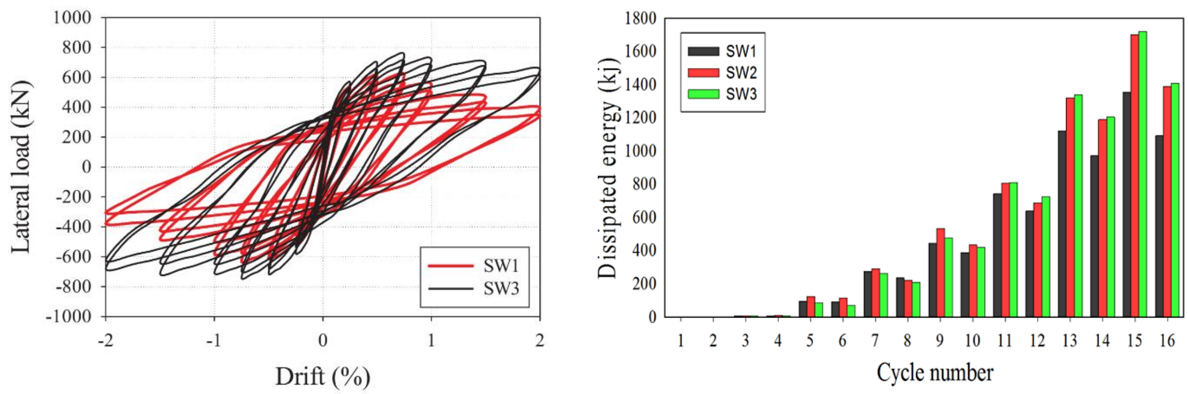

(a) (b)

Figure 2-8 - Response of walls (Ghassemieh et al., 2017): (a) load-deformation response and (b) dissipated energy per cycle

Kian and Cruz-Noguez (2018) assessed the seismic performance of three innovative types of shear walls consisting of different self-centering systems. Four slender walls, with an aspect ratio of 2.0, were built with identical geometry and boundary conditions, and tested up to failure under pseudo-elastic, cyclic loads, following the same load protocol. The first specimen was a conventional RC shear wall used as a control wall. The remaining three specimens consisted of hybrid RC shear walls reinforced with mild steel and Ni-Ti SMA bars, glass fiber reinforced polymer bars (GFRP), and high-strength steel strands (PPT), respectively. The SMA and the PPT walls were specified with steel fiber reinforced concrete, whereas the cementitious material in wall GFRP contained fibers made of poly-vinyl alcohol (PVA). Details of the investigated walls are illustrated in Figure 2-9. Residual drift ratios, ductility, damage propagation, and dissipated energy were evaluated.

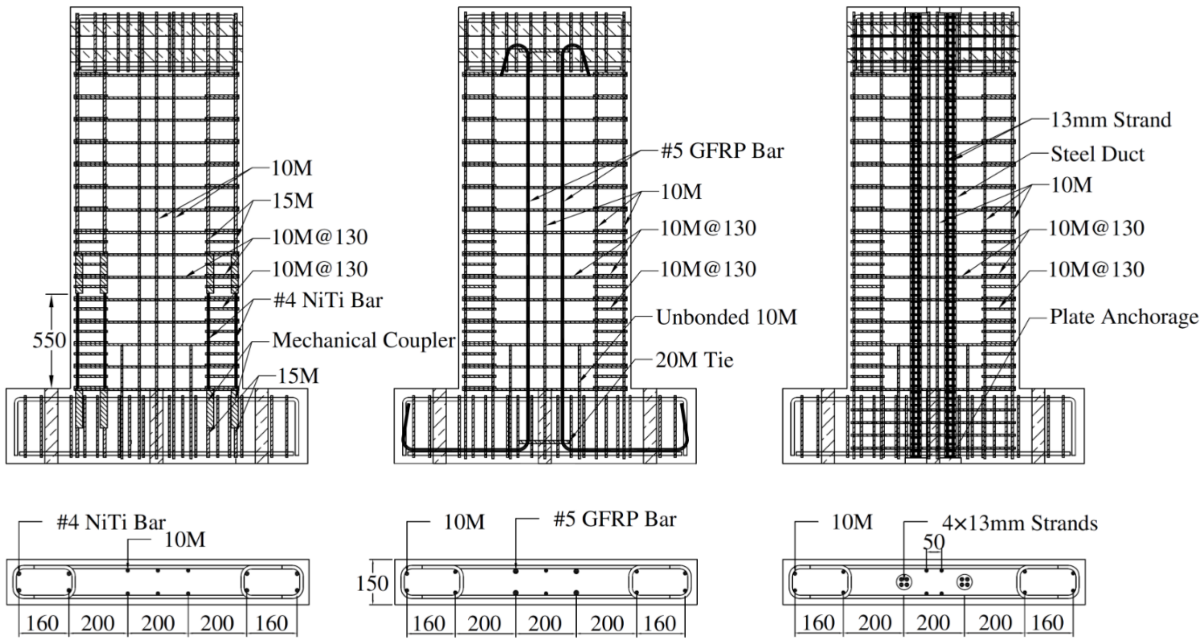

(a) (b) (c)

Figure 2-9 - Elevation and cross-section of walls (Kian and Cruz-Noguez, 2018): (a) SMA wall, (b) GFRP wall and (c) PPT wall

In general, the innovative shear walls experienced smaller residual drift ratios and higher self-centering, formed fewer but wider cracks, and exhibited some extent of crack closure upon unloading when compared to the control wall. Improvement in self-centering in the PPT wall was noticeable from the onset of the test, which indicates that this wall system is suitable to improve immediate occupancy and life safety seismic performance levels of concrete structures. The SMA and GFRP walls exhibited improved self-centering at drifts greater than 1.0%, thus being appropriate wall systems to optimize the seismic performance of structures at life-safety and collapse-prevention levels. The SMA wall exhibited the highest ductility, as well as the highest drift capacity, with failure at 5.0% drift due to fracture of the steel bars in the web. The responses are provided in Figure 2-10 (a) and (b). The SMA wall was the only wall where rupture of the bars in the boundary regions was not observed, which led to a notable increase in its ductility.

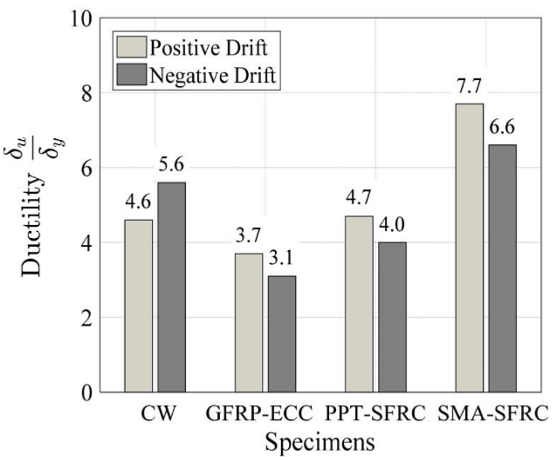

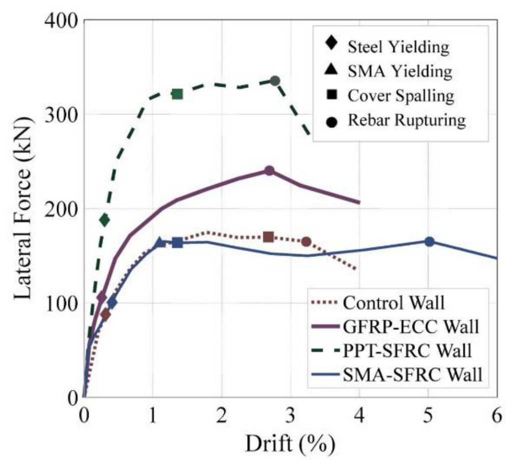

Figure 2-10 - Comparison between the response of the walls (Kian and Cruz-Noguez, 2018): (a) displacement ductility and (b) load-deformation response

Cortés-Puentes et al. (2018) investigated the seismic response of a repaired slender RC shear wall reinforced with Ni-Ti SE-SMA. The wall contained Ni-Ti SE-SMA bars as longitudinal reinforcement in the boundary regions of the plastic hinge zone (RW2-NR), and was assessed against a companion steel-reinforced wall (RW1-SR). Experimental testing of the walls in the undamaged state (W2-NR and W1-SR) was conducted in a previous study (Abdulridha and Palermo, 2017) and in the repaired state in this study. The walls were subjected to reverse cyclic testing followed by repair, which included removal of the severely damaged concrete in the plastic hinge zone and replacement with high-strength, self-consolidating concrete, replacement of ruptured and buckled steel bars, and shortening of the SMA bars. The state of the SMA wall prior to repair, and the repaired reinforcement of the same wall are shown in Figure 2-11 (a) and (b). Prior to repair, external lateral loads were applied in order to realign the companion wall (RW1-SR) from its displaced position. In contrast, the self-centering capacity demonstrated by the wall with SMA largely facilitated the repair of this specimen. Repair was effective in restoring yield and ultimate lateral load capacities of both walls, with 80% recovery capacity observed in the SMA wall (RW2-NR) up to 2.0% drift. The envelopes of drift response for both walls are provided in Figure 2-11 (c) and (d). Beyond 2.0% drift, rupturing of the SMA bars caused a significant decrease in the recovery capacity of the wall. Since 2.0% is within the current design drift range, the retrofit strategy was deemed successful and it was able to improve cracking, energy dissipation, rotation, and shear strain in the walls. The reuse of SMA bars, which where shortened but not replaced, did not affect the self-centering capacity of the SMA wall. The SMA bars maintained enough of their original properties to provide a retrofitted wall with excellent recovery and energy dissipation capacity.

(a)

(b)

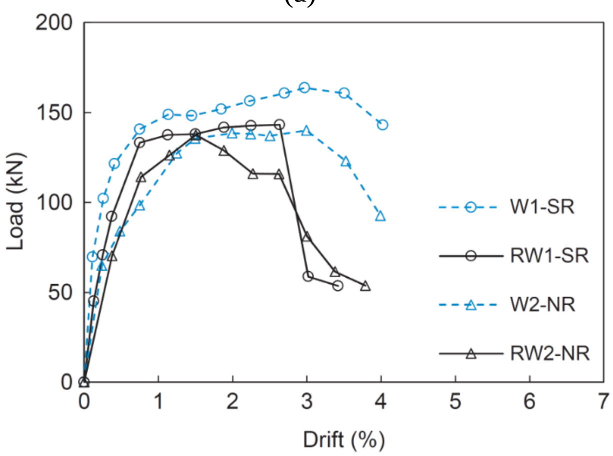

(c)

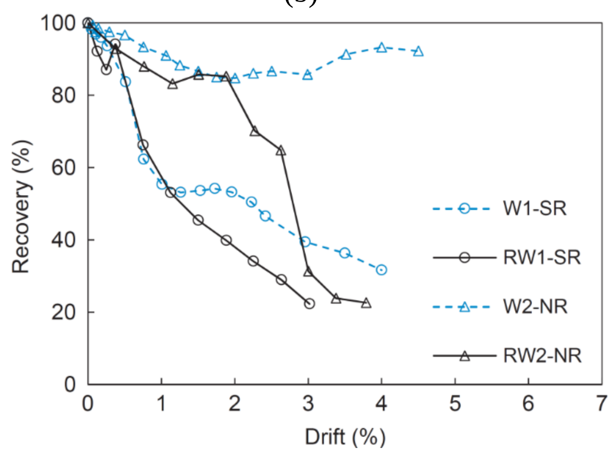

(d)

Figure 2-11 - Study by Cortés-Puentes et al.(2018): (a) SMA wall prior to repair, (b) repaired reinforcement at the base of SMA wall, (c) load-drift envelopes of walls and (d) wall recovery versus drift

Wang and Zhu (2018) proposed a self-centering RC wall system combining superelastic SMA bars in the boundary zones within the plastic hinge region (which also received external steel jacketing) with horizontal bottom slits. A parametric study investigated the effects of axial compressive load ratio, bottom slit length and lower plateau stress factor for SMA. The investigated slit lengths were equal to 29% (172 mm), 57% (343 mm) and 100% (610 mm) of the wall width, where the latter formed a through-gap that completely separated the concrete base of the wall from the foundation and converted it into a rocking wall. Numerical simulations indicated that the residual deformations were negligible (less than 0.05%) up to 2.5% peak drift in all walls. Peak strain in the outermost SMA bars was 3.3%, which is below the superelastic strain limit of 6.0% for SMA. The lateral strength of the non-rocking SMA walls was improved when the axial load ratio was increased, as the axial load delayed pseudo-yielding of SMA bars in tension. Damage in the walls was reduced with increasing slit length, which was beneficial for the self-centering capacity. The rocking wall showed no need for repair after unloading. In turn, this wall dissipated the least amount of energy, leading to the conclusion that additional energy dissipation devices are required for practical use of this system. The results indicated improved ductility of the walls taking advantage of the SMA alone, as well as remarkable self-centering ability, and repairable damage restricted to the central area of the concrete walls. Residual drifts for different combinations of parameters are presented in Figure 2-12 as a function of the peak drift, where RC wall represents a conventional steel-reinforced wall, SCW refers to self-centering wall and the parameters include slit length ("*l*" of 117, 343 or 610), axial load ratio (*"n"* of 0, 0.07 or 0.15) and lower plateau stress factor of SMA (*"β"* of 0, 0.25 and 0.5).

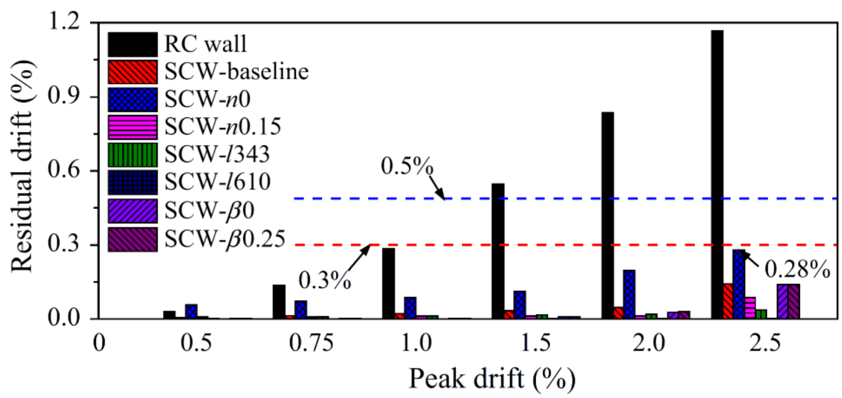

Figure 2-12 - Residual drift-peak drift response of walls with different parameters (Wang and Zhu, 2018)

2.2.2 Moment-resisting frames

In this section, studies addressing the use of SMA as reinforcement in concrete moment-resisting frames will be presented. The investigated components also comprise isolated beam-column joints and beams. It is clear that maximum residual drift is an important parameter for the assessment of the seismic response of moment-resisting frames, as the use of SMA renders frames more flexible. This section also includes several studies that focused on the suitability of existing code provisions and design methods from steel-reinforced concrete sections to hybrid SMA-steel concrete sections.

Alam et al. (2009) investigated the seismic response of an 8-storey concrete frame reinforced with superelastic SMAs in the plastic hinge regions of the beams, with regular steel elsewhere. The response of the frames was assessed against the response of a control concrete frame, reinforced with regular steel. The frames were designed for western Canada seismicity and subjected to time history analyses to determine maximum interstorey drift, roof drift, interstorey residual drift, and roof residual drift. The results demonstrated the capacity of the SMA-RC frame to recover most of the post-yield deformation, even after strong earthquakes, exhibiting significantly higher recentering capacity than the steel-reinforced frame. The authors affirmed that the advantages of using SMA were more evident when the frame was subjected to higher seismic loads. The maximum strain levels in the SMA bars remained within the superelastic strain range of the material for all levels of excitation. As a result, the SMA-RC joints recovered nearly all the experienced rotation, returning to their original position. This demonstrated that the SMA-RC joints can be effective and serviceable after earthquakes.

Youssef and Elfeki (2010) also verified the superior seismic response of SMA-RC frames through the analysis of 6-storey SMA-RC frames subjected to time history analysis with earthquake records of multiple seismic intensities. The authors evaluated the response of six different distributions of SMA reinforcement throughout the frames, to optimize the seismic performance of typical concrete frames in terms of damage distribution and residual deformations. The numerical results indicated the best configuration was that with SMA in the critical section of the fourth floor beams, as well as at the beam ends of the first floor, as illustrated in Figure 2-13. The use of SMA significantly reduced the maximum residual interstorey drifts of the concrete frame under all tested seismic intensities. The authors also designed and simulated the response of an equivalent steel moment-frame for comparison purposes. The SMA concrete frame experienced a lower number of crushed columns at the end of analysis than the steel frame. Although the SMA frame experienced slightly larger maximum interstorey drifts than the steel frame, the maximum residual interstorey drifts indicated excellent performance. As a result, the SMA frame was deemed resistant to earthquakes of higher intensities than the equivalent steel-reinforced moment-frame.

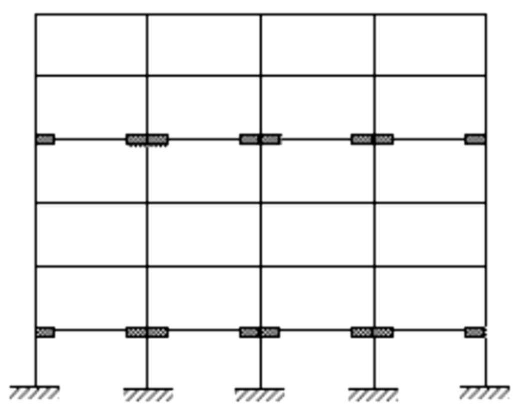

Figure 2-13 - Location of SMA bars in RC frame with optimal performance (Youssef and Elfeki, 2010)

To further investigate the suitability of SMA as reinforcement in concrete frames, Youssef et al. (2008) tested two large-scale beam-column joints under reversed cyclic loading. The first specimen was reinforced with regular steel reinforcing bars, whereas SMA bars were used in the second specimen. This study was the first reported attempt of using SMA as reinforcement in beam-column joints. The SMA-reinforced specimen experienced a higher beam rotation and dissipated reduced energy. However, it successfully relocated the plastic hinge region away from the column face to a distance of approximately half of the beam depth, while recovering most of its post-yield deformation. The observed behaviour demonstrated that the SMA-reinforced beam-column joints require minimum repair after large earthquakes (Nehdi et al., 2011).

Nehdi et al. (2011) tested an SMA-reinforced beam-column joint, along with a companion steel-reinforced specimen, with similar dimensions to that studied by Youssef et al. (2008). The SMA-reinforced beam-column joints were repaired with flowable Structural-Repair-Concrete (SRC) and re-tested under reversed cyclic loading. The reinforcement details of the specimen containing SMA bars are depicted in Figure 2-14. The use of SRC contributed to recovery of the full capacity of the SMA-reinforced beam-column joint, which performed similarly to the steel-reinforced specimen in terms of initial stiffness, energy dissipation, and strains in the reinforcing bars. In contrast, the steel-reinforced specimen underwent large strains during testing and sustained a substantial degree of damage. If repair was to be implemented to this specimen, damaged bars would have to be replaced, epoxy would have to be applied, and concrete would have to be replaced in the joint region as well, as opposed to solely in the beam. More importantly, extra support would have been required to sustain the axial load and transfer it to lower members due to the compromised column axial load capacity. The authors emphasized that the required strengthening techniques for the steel-reinforced specimen would be 3 to 5 times more costly, laborious and time-consuming than the simple and effective technique used to repair the SMA-reinforced specimen.

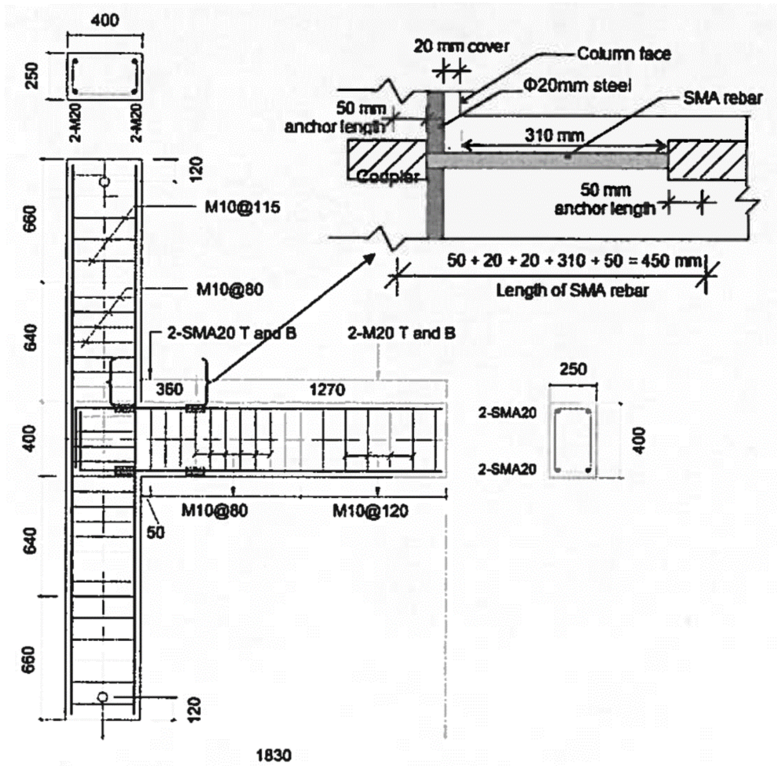

Figure 2-14 - Reinforcement details of beam-column joint reinforced with SMA bars tested by Nehdi et al. (2011)

Alam, Youssef and Nehdi (2008) examined the applicability of existing design methods based on steel-reinforced concrete to SMA-reinforced members in terms of predicting the length of the plastic hinge region, crack width, crack spacing, and bond-slip relationship. A FE program was used to analyze the behaviour of SMA-reinforced concrete columns and beam-column joints and to verify the suitability of the discussed methods. Numerical results from the FE program provided fair accuracy in predicting the moment-rotation and load-displacement curves. The methods that provided best accuracy according to the study were the Paulay and Priestley method for predicting the plastic hinge length, and the Eurocode-2 method for predicting the average crack spacing and maximum crack width.

Elbahy et al. (2009) investigated the suitability of using sectional analysis to evaluate the monotonic moment-curvature relationship of SMA-RC sections. Important indexes, such as the ultimate concrete strain ε_{cu} and the stress block parameters α_1 and β_1, were evaluated, and new equations were proposed for SMA-RC sections. Experimental tests on SMA-RC beams and a parametrical study with several steel and SMA-RC sections were conducted to estimate the effects on the moment-curvature due to cross-section height and width, tensile and compressive reinforcement ratios, concrete compressive strength, and axial load level. The results demonstrated that, despite the lower initial stiffness of SMA-RC sections compared to steel-RC sections at zero axial load, the difference in stiffness becomes negligible at higher levels of axial load, as the axial load delays cracking in the section. Higher curvature was observed in the SMA-RC sections at the critical stress of SMA compared to that observed in the steel-RC sections at yield stress, which was also attributed to the lower elastic modulus of SMA. For all the analyzed sections, rupture of SMA bars did not govern failure given the high ultimate tensile strain of SMA; failure was governed by crushing of concrete. ε_{cu} was found to be dependent on the axial load level for SMA-RC sections. As a result, Elbahy et al. proposed new values of ε_{cu} as a function of the axial load ratio.

Following the study on moment-curvature above, Elbahy et al. (2010) evaluated the suitability of existing models to estimate the deflection of superelastic SMA RC beams. A parametric study was conducted focusing on the effects of concrete compressive strength, reinforcement ratio, modulus of elasticity, and cross-section height and width. Due to the recognized smaller elastic modulus of SMA, the equation provided by the CSA A23.3-04 (2007) to calculate deflections was found to significantly overestimate the stiffness of the hybrid beams under study, resulting in severe underestimation of the deflections. In addition, variations of the concrete compressive strength and cross-section geometry were found to have negligible effect on the effective moment of inertia of the beams, whereas the reinforcement ratio and modulus of elasticity caused significant impact.

Alam and Tesfamariam (2012) investigated the ductility and overstrength factor of three different configurations of moderately ductile RC moment-resisting frames with 3, 6, and 8 storeys. The three models consisted of one steel-reinforced frame, one frame with hybrid beams reinforced with Ni-Ti SE-SMA within the plastic hinge zones and with steel elsewhere, and one frame with beams reinforced solely with Ni-Ti SE-SMA. The columns were reinforced with steel in all frames. Nonlinear pushover analyses were performed using 2-D fiber element models of a typical interior frame for each case, followed by nonlinear time history analyses with an ensemble of 10 earthquake records representative of the city of Vancouver. The SMA RC frames experienced higher capacity/demand ratios compared to the steel-reinforced frame and the steel-SMA RC frame. The ratio decreased as the number of storeys increased in the three frames. The SMA and the steel-SMA RC frames were found to have 16-24% and 8-18% less ductility than the steel RC frame, respectively. The frames containing SMA experienced larger interstorey and roof drifts compared to the steel RC frame, as is evident in Figure 2-15. The increase in interstorey and roof drifts was attributed to the lower elastic modulus characteristic of SMA. As a result, Alam and Tesfamariam suggested that the design of frames with SMA should be based on the reduced stiffness and effective moment of inertia of SMA members.

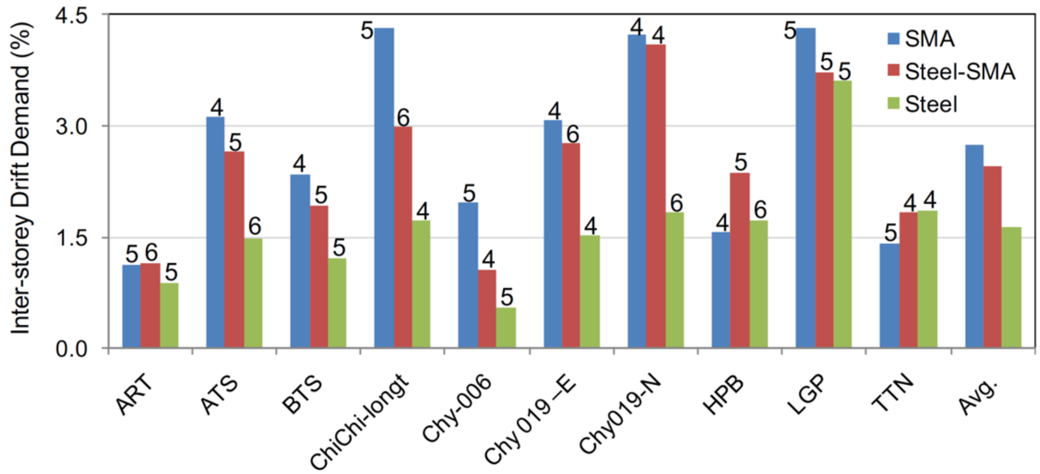

Figure 2-15 - Interstorey drift demand of the three 8-storey RC frames under different earthquake records (Alam and Tesfamariam, 2012)

Abdulridha et al. (2013) investigated the performance of concrete beams reinforced with superelastic Ni-Ti SMA in plastic hinge regions. The study involved experimental testing and numerical modelling in a FE program. In addition, a hysteretic constitutive model was proposed for superelastic SMAs, presented in Figure 1-1 (b), and applicable for nonlinear finite element analysis. The constitutive tri-linear model with plastic offset was incorporated in the finite element program VecTor2 (Vecchio et al., 2013). Finite element results confirmed the model could predict the response of the SMA-reinforced beams, as well as the response of SMA-reinforced shear walls. The SMA-reinforced beams, compared to the steel-reinforced beams, exhibited similar displacement ductility and similar energy dissipation capacity, and experienced higher yield and ultimate loads when subjected to cyclic loading. Conversely, the stiffness was approximately 40% lower and the dissipated energy was approximately 54% of that of the steel-reinforced beams under reverse cyclic loading.

2.2.3 Columns

This section presents several research studies addressing concrete columns reinforced with SMA bars, with applications in buildings and bridges. The application of SMA as reinforcement in bridge piers has been subject of research for over two decades and has already been incorporated into existing structures (Baker et al., 2018). Most applications in seismic engineering make use of superelastic SMAs to develop resilient systems. Martensite SMAs, on the other hand, have an interesting shape memory effect that can also be exploited in structural applications. As an example, an investigation of Martensite SMA employed as prestressed cables in bridge systems is briefly presented in this section.

Hosseini et al. (2017) evaluated the seismic response of short-square RC columns with longitudinal steel rebars replaced by SMA bars in various percentages (25%, 37.5%, 62.5%, and 100%). Two types of SMAs were studied, a copper-based alloy and a nickel-based alloy. Numerical simulations demonstrated that both alloys successfully provided superelastic behaviour and restoring capacity to the columns. The columns with the copper-based alloy reached the maximum superelastic strain of the material, 3.0%, whereas the columns with the nickel-based alloy remained below the maximum strain of 6.5%. For this reason, plastic strains in the first type of column were higher than that in the second type.

Alam, Nehdi and Youssef (2008) conducted a thorough investigation of the benefits of including SMA-based structural solutions in bridge piers, girders, decks, and monitoring systems. One investigation involved dynamic analyses of bridge piers represented by two quarter-scale spiral RC columns reinforced with SMA bars within the plastic hinge zone, which were previously tested on a shake table by Wang (2004). Details of the reinforcement adopted are shown in Figure 2-16. Results from the time history analyses, which employed 15% to 300% of the main base acceleration time history, provided fair accuracy in predicting the dynamic behaviour of SMA-reinforced piers. The experimental results demonstrated the superior capacity of the columns in limiting top displacements and residual displacements (Wang, 2004). The SMA-reinforced columns were also capable of withstanding larger earthquake amplitudes compared to conventional steel-reinforced columns.

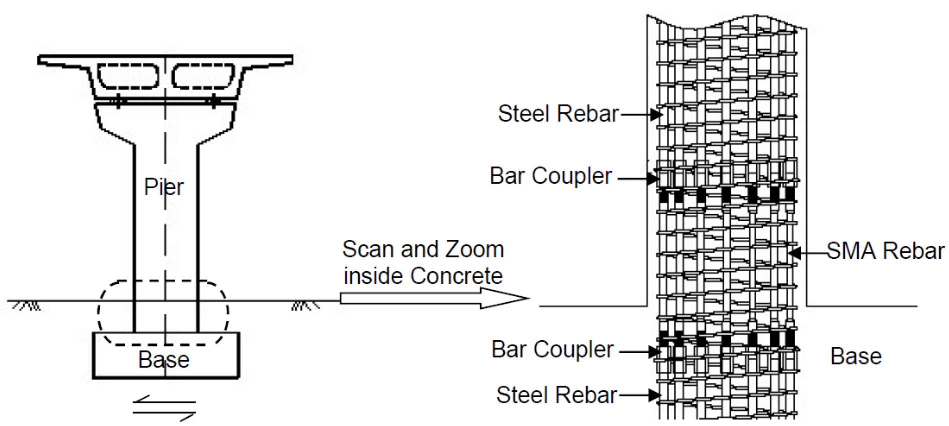

Figure 2-16 - Detailing of bridge pier with coupled SMA-steel reinforcement (Alam, Nehdi and Youssef, 2008)

A review of current applications of SMA that can be employed to develop smart bridge systems was also conducted by Alam, Nehdi and Youssef (2008), including the use in new structures (prestressing, reinforcement, smart isolators), in retrofitting strategies (external post-tensioning, bracing, dampers, isolators, and restrainers), and in sensing devices. One application involves the use of Martensite SMA as prestressed cables/wires. In structural elements, adjustment in the stiffness and strength through external applications would be possible due to the unique ability of Martensite SMA to change shape simply by heating, without any mechanical effort. Electrical heating of the SMA wires embedded in concrete induces large shrinkage strains due to phase transformation from Martensite to Austenite. The strain energy generates significant prestressing forces in the concrete. According to the authors, SMA prestressing is superior to conventional prestressing as it does not involve jacketing or strand cutting and permits an active control of the level of prestressing with increased additional load carrying capacity. Moreover, this type of prestressing is not subjected to elastic shortening, to friction or to anchorage loss over time.

Saiidi et al. (2010) evaluated the seismic response of large-scale RC bridge columns subjected to earthquake records on a multiple shake table. The experimental results were correlated with numerical results from a fiber section analysis program. Four circular columns were built with different typologies: a conventional steel-reinforced RC column; a SMA-reinforced concrete column with ECC; a post-tensioned column with built-in elastomeric pads; and a post-tensioned column with conventional reinforced concrete. Details of the columns are depicted in Figure 2-17. Test results exposed the effectiveness of post-tensioning and of the innovative materials in mitigating damage and permanent displacements in the columns. The plastic hinge regions of the SMA/ECC column and the column with elastomeric pads exhibited only minimal damage, indicating the potential to ensure serviceability for bridges after strong earthquakes due to the drastically reduced damage. Meanwhile, post-tensioning in the columns led to minimized permanent lateral displacement, but at the expense of a relatively small energy dissipation capacity. Severe damage was observed in the plastic hinge region of the post-tensioned columns, indicating that post-tensioning alone is not sufficient to provide serviceability to bridges after a strong earthquake. One observation of the study is that the superelastic characteristics of SMA bars observed in individual bar tests could also be observed in the SMA-reinforced concrete columns.

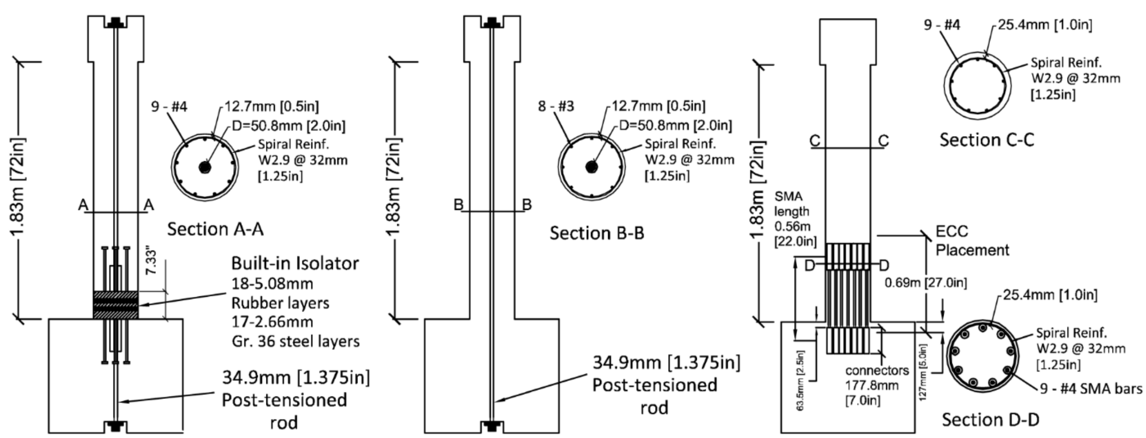

(a) (b) (c)

Figure 2-17 - Elevation of bridge piers tested by Saiidi et al. (2010): (a) post-tensioned column with elastomeric pads, (b) post-tensioned steel-reinforced column and (c) SMA/ECC column

Subsequently, Cruz-Noguez and Saiidi (2013) modified the design of the column with elastomeric pads from the work of Saiidi et al. (2010) to improve the performance of this column beyond drift levels of 3.0%. A new large-scale four-span RC bridge with the same three innovative bridge piers from the previous study was implemented. Experimental results indicated larger load capacity corresponding to the pier with elastomeric pads. The SMA/ECC pier exhibited reduced strains in the longitudinal reinforcement, being capable of minimizing the residual displacements in the bridge and ensuring serviceability after the maximum design earthquake.

Billah and Alam (2016) conducted a parametric study on the effects of different design parameters on the plastic hinge length of RC bridge piers reinforced with SMA. An expression was developed to estimate the plastic hinge length of SMA-RC circular columns, which provided reasonable accuracy when validated against test results. FE analysis of the columns indicated an increase in the plastic hinge length with increasing axial load, aspect ratio, and yield strength of SMA bars. Conversely, the increase in concrete strength and in the ratio of longitudinal and transverse reinforcement reduced the plastic hinge length. The effect of longitudinal reinforcement ratio on the plastic hinge length of the columns is presented in Figure 2-18.

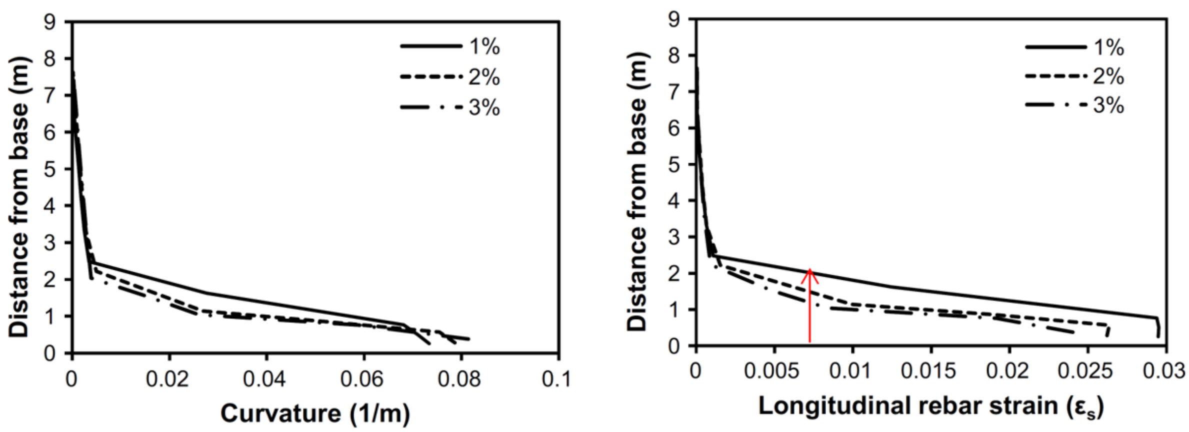

(a) (b)

Figure 2-18 - Evaluation of plastic hinge length in SMA-reinforced columns (Billah and Alam, 2016): (a) effect of longitudinal reinforcement ratio on curvature profile and (b) effect of longitudinal reinforcement ratio on longitudinal rebar strain profile

Tarzav and Alam (2018) summarized the state-of-the-art applications of SMA in bridges, including extensive parametric studies, surveys, and experimental tests. From experimental studies, the authors concluded that SMA-reinforced bridge columns, specifically when ECC is incorporated in the plastic hinge region, are low-damage, with damage limited to the concrete cover, ductile, result in minimal residual displacements, and easily repairable, even after a severe earthquake.

2.2.4 Other self-centering concrete wall systems

Prior to the use of SMA as alternative reinforcement in concrete shear walls, other solutions were proposed to implement self-centering to RC shear walls, where energy is dissipated through friction elements or through replaceable yielding energy dissipation devices. Post-tensioned rocking wall systems, for instance, combine the use of unbonded post-tensioned tendons with supplementary energy dissipation devices to create a hybrid system with characteristic flag-shaped hysteretic loops (Wang and Zhu, 2018). Self-centering is performed by restoring forces generated by the post-tensioned tendons and the vertical loads. This system can sustain reduced, or even negligible, residual deformations and damage levels during earthquakes due to rocking motions, allowing gap opening/closing at the wall base that elastically softens the structural response and limits the overturning moments (Chancellor et al., 2014). When the gap opens, the lateral stiffness of the system drops substantially. This softening effect is desirable since it elongates the period of the structure, reducing the forces that are generated in the elements. A more substantial reduction in the interstorey shear forces of the first mode of vibration occurs due to the allowed rocking of the walls. The reduction in interstorey shear forces, however, makes rocking walls sensitive to higher mode effects; greater interstorey shear forces may be produced by higher modes of the response (Chancellor et al., 2014). One application of rocking wall systems is the hybrid precast wall system proposed by Smith et al. (2011) that utilizes high-strength unbonded post-tensioning steel to provide lateral resistance across horizontal joints, as illustrated in Figure 2-19. This system uses mild steel bars to ensure energy dissipation. An issue faced by all self-centering structural systems is the actual capacity to return the entire structure to a plumb position. Elements that are not part of the SFRS, such as interior partitions, horizontal floor diaphragms, exterior cladding, etc., may undergo inelastic deformations during strong ground shaking, inducing additional forces contrary to the restoring forces provided by the self-centering system (Chancellor et al., 2014).

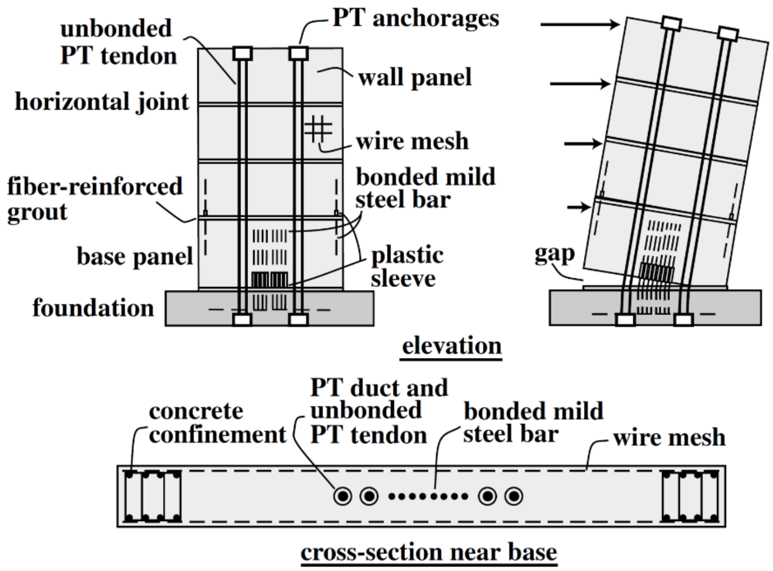

Figure 2-19 - Details of the post-tensioned rocking wall system proposed by Smith et al. (2011)

2.2.5 Limitations of SMA as a construction material

Although the benefits of employing SMAs in seismic-resisting structural systems have been consistently confirmed by researchers, this novel material has not yet completed the transition from research to practice in civil engineering. In this section, several limitations related to the implementation of SMA as a recurring construction material will be discussed.

Production of SMA:

SMAs are associated with a high production cost. Difficulties in the manufacturing process contribute to this high cost. In the case of Ni-Ti, machining large-diameter bars is complicated due to the hardness of the alloy. A stringent control in the production process is demanded when dealing with SMAs, as the mechanical properties of SMA are largely dependent on the heat-treatment temperature to which they are subjected to during manufacture (Alam et al., 2007). A slight variation in temperature can cause significant alterations in properties. The use of SMA in large-scale is also limited by the current lack of flexibility in fabricating products in various shapes and sizes (Alam et al., 2007).

Research on the manufacturing process is expected to make SMA-based systems more cost-competitive in the near future. Evidence of that is the large reduction in cost that occurred in a ten-year period, during which costs were cut back from US$1000/kg in 1997 to US$150/kg in 2007 (Alam et al., 2007). Recent construction employing Ni-Ti SMA as reinforcement in bridge piers in Seattle, WA, USA (Baker et al., 2018) reported that the SMA bars cost ninety times the price of conventional deformed-steel bars. However, the combined used of SMA reinforcement and ECC represented an increase of only 5% in the overall cost of the bridge (Doughton, 2017).

Bond to concrete:

SMA bars currently available have smooth surfaces. When used as reinforcement in concrete, the smoothness incurs in reduced bond to concrete compared to conventional deformed steel rebars. Fewer but wider cracks are expected to surface in SMA-reinforced concrete elements, as observed by Abdulridha and Palermo (2017) on SMA-reinforced concrete walls tested under reverse cyclic loading. In conventional RC, the bond between deformed steel and concrete distributes the stresses from the cracks along the bar length and into the surrounding concrete, resulting in smaller but more numerous cracks in the concrete. In contrast, the stresses are accumulated at the cracks when smooth bars are present, as the absence of bond hinders the distribution of the stress, resulting in localized, wider cracks. The smoothness of SMA bars also poses difficulties in fulfilling the design development length requirements of longitudinal reinforcement in concrete members (Youssef et al., 2008). Alternatively, alloys of other metals have been proposed to address the limitations related to SMAs consisting of superelastic Ni-Ti. Iron-based SMAs, for instance, have good mechanical properties, such as wide transformation hysteresis. These alloys are cheaper to manufacture due to their machinability and weldability and have better bond with concrete than Ni-Ti SMA (Alam et al., 2007). Their shape recovery, however, is poor, and the corresponding stress is low, making iron-based SMAs not as attractive for seismic applications as Ni-Ti SMAs.

2.2.6 Summary and conclusions from the literature review

Several studies on the seismic performance of SMA-reinforced concrete structural elements were reviewed in this section. The performance, investigated using experimental testing and numerical simulations, was often assessed against that provided by equivalent conventional steel-reinforced concrete specimens. In general, results of the studies presented in the literature review exposed the superior self-centering and restoring capacity of SMA-reinforced elements, constantly showing negligible residual deformations, minor damage localized at the plastic hinge region, stable hysteretic response with substantial energy dissipation, and acceptable serviceability performance requiring minimum repair after severe earthquakes. Although a significant number of studies that address the use of SMA as alternative reinforcement in concrete are available, research focusing on the application in shear walls was found to be limited. Moreover, most of the studies in SMA-reinforced walls were conducted in low-rise walls. As a result, the behaviour of RC shear walls containing SMA as reinforcement, particularly in the case of multi-storey walls, requires a complete understanding. Extensive research is required in order to produce a robust database that can validate analytical models and culminate in the development of design provisions customized to effectively use novel SMA materials.

2.3 Seismic design procedure

A literature review on the main aspects of the seismic design procedure of slender reinforced concrete shear walls will be presented in this section, addressing flexural and shear design according to the CSA A23.3-14 standard, Design of Concrete Structures (CSA, 2014), and the determination of seismic demand per design location according to the 2015 edition of the National Building Code of Canada (NRC, 2015). An overview on the seismic design philosophy adopted by these documents is also presented below.

2.3.1 Seismic design philosophy

Most seismic design codes around the world apply the capacity design method to proportion structural elements to withstand the demand of earthquakes. The capacity design method proposes the establishment of a strength hierarchy along the path of the seismic load on the structure, with careful selection of sacrificial structural elements to attract the deformation demand due to their designed lower strength. The design of these elements assures that yielding will be reached upon the design earthquake. These elements provide ductility through mechanisms of inelastic deformation that can be controlled so they can undergo the cyclic excitation of earthquakes with a stable response without signs of brittle failure. Other components of the seismic force-resisting systems (SFRS) are protected of damage and can be designed to behave essentially in the elastic range. These components are capacity protected, and their design is force controlled. Therefore, the seismic design of a structure is controlled by the capacity of the ductile elements, which are deformation controlled. The capacity design strategy also prevents the rest of the structure from being overloaded given the uncertainties involved in determining the design earthquake, as the seismic-induced forces are limited by the capacity of the SFRS independently of the intensity of the ground motion that hits the structure (Filiatrault et al., 2013).

The NBC 2015 classifies the types of SFRS allowed in Canada according to their probable ductility and establishes limits to their application, such as a maximum building height. In addition, force-modification factors are provided for each type of SFRS to be used to directly reduce the seismic force demand for design. The first factor, R_d, is a ductility-related factor that represents the reduction in base shear expected according to the inelastic response developed by the system, which follows the equal displacement principle. According to this principle, the lateral deformation experienced by a structural system is independent of the system's lateral strength. However, the ductility demand, defined as the ratio of the ultimate displacement to the yielding displacement, increases linearly with the decrease of the system's yielding strength. This means that, although the ultimate displacement would be similar, systems that yield at earlier stages will experience greater ductility demand and, consequently, will be subjected to a longer inelastic range. The second force-modification factor, R_0, is overstrength-related. Lateral overstrength is defined as the additional strength provided by a structure above that required by the design seismic load, which can be measured as the ratio of the maximum capacity upon full development of the plastic mechanism to the minimum specified seismic resistance. In general, overstrength is beneficial for the seismic response of structures. It increases the level of lateral load necessary to initiate the inelastic response, thus reducing the inelastic demand on the ductile elements. In addition, it contributes to the increase in energy dissipation capacity, reducing the deformation demand. Overstrength can result from the use of resistance factors in design, increased size of elements resulting from rounding-off, actual strength of materials being higher than specified, and other design criteria that prevail during design, such as drift limits, load combinations, etc. In highly ductile SFRS, strain hardening response of yielding components and progressive yielding during the development of the full inelastic mechanism are also potential sources of overstrength (Filiatrault et al., 2013).

In conjunction with the NBC 2015, design codes such as the CSA A23.3-14 provide specific and extensive design requirements, which aim to ensure the development of the probable ductility of the system in the final structure. The more ductile a system is, the more complex the detailing requirements are so premature failure can be avoided and stable inelastic response can be expected. Detailing requirements for reinforced concrete shear walls encompass distributed and concentrated reinforcement, as well as concrete section, and confinement reinforcement.

In slender RC shear walls, the desired ductile mechanism is the formation of a single flexural plastic hinge at the base of the wall, and design is conducted so that the wall reaches flexural yielding prior to any other type of premature failure. When the plastic hinge is formed, the amplitude of the force demand in any other component of the structure is bounded by the capacity of the ductile element. The cross-section at the base of the wall must be then designed to yield at the flexural demand arising from the seismic loading. Design of the wall above the plastic hinge should resist the scaled flexural and shear demands according to the relationship between flexural demand and capacity of the as-designed cross-section within the plastic hinge. This relationship is defined by the wall overstrength factor (γ_w) as the ratio of the flexural resistance to the flexural demand of the plastic hinge and is used to amplify the bending moments above the plastic hinge region and the shear forces along the wall height. Probable flexural resistance should be considered for ductile walls, whereas nominal resistance should be used for moderately ductile shear walls.

2.3.2 Seismic demand

To determine the seismic demand at a given site, the NBC 2015 provides Uniform Hazard Spectra (UHS) for a probability of exceedance of 2% in 50 years, which corresponds to the 5% damped spectral response of equivalent single degree of freedom oscillators with fundamental period ranging from 0 to 10 s, considering the site's seismicity and soil type. The equivalent single degree of freedom system is defined as schematized in Figure 2-20. To account for possible soil amplification of the ground motion, the NBC 2015 provides amplification factors that are applied to the response spectrum. Using the developed response spectrum, a reduction in the design base shear (*V*) is permitted, proportionally to the expected ductility of the selected SFRS.

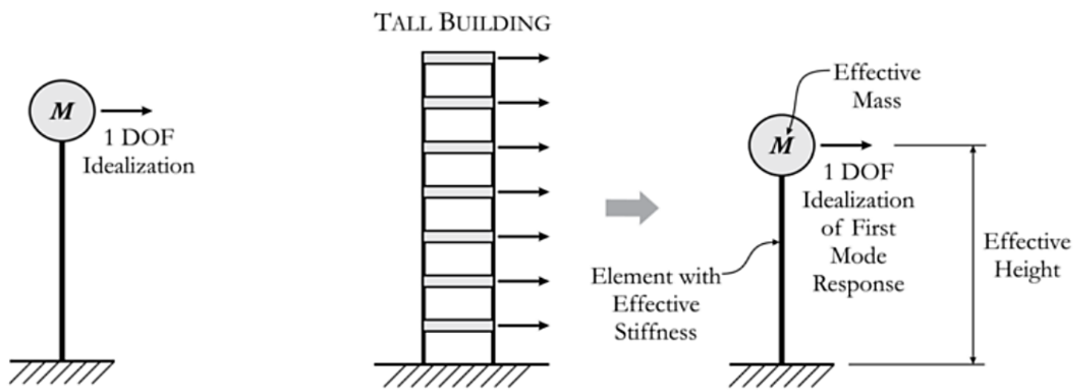

Figure 2-20 - Equivalent single degree of freedom systems of buildings (Filiatrault et al., 2013)

The value of *V* is calculated as shown in Equation 2-1. There are limits above which no further reduction of the base shear is permitted by the NBC 2015, due to current uncertainties around the behaviour of structures with very long periods. To estimate the fundamental period (T_1) of the structure, the code provides empirical equations for each type of structural system based on the total height of the building (h_n). For RC shear walls, the empirical period (T_a) is determined as shown in Equation 2-2. The upper limit of T_1 is two times T_a for strength requirements. When checking displacements, however, the code allows the use of a more relaxed period, with an upper limit of 4.0 s for RC shear walls. A maximum base shear is also suggested for structures with $R_d \geq 1.5$; therefore, *V* does not need to be taken as greater than the base shear calculated according to Equation 2-3.

$$V = (S(T_a) M_v \, I_E W)/(R_d \, R_0) \qquad \text{2-1}$$

$$T_a = 0.05 \times (h_n)^{3/4} \qquad \text{2-2}$$

$$2/3\ V\ (T = 0.2\ \text{s}) \quad \text{2-3}$$

In Equation 2-2, $\underline{M_v}$ is the higher mode factor, I_E is the importance factor of the building (equal to 1.0 for normal importance buildings) and W is the seismic weight of the building. W is calculated based on the dead (D) and snow (S) loads as expressed in Equation 2-4, except when live loads are likely to engage in the cyclic response of the building.

$$W = 1.0D + 0.25S \quad \text{2-4}$$

To determine the distribution of the seismic forces along the height of the building, an equivalent static force procedure can be applied provided that certain criteria are met. Buildings deemed as regular according to the eight types of irregularities defined by the NBC 2015, which do not exceed 60 m in height and that have T shorter than 2.0 s can be designed according to the equivalent static force procedure. In this method, the base shear is distributed as lateral forces acting at each storey level, following the shape of an inverted triangle. An additional load is placed at the roof level in order to reproduce higher mode effects. Subsequently, an accidental eccentricity of the centre of rigidity equal to 10% is considered, creating a torsional effect that amplifies the previously calculated lateral forces. The resulting lateral loads, including the torsional effect, can then be combined with the gravity loads to provide the design forces for the capacity-designed elements of the SFRS. The possible increase in the lateral displacement demand due to gravity loads acting on a structure subjected to lateral loads (P-Δ effects) must be considered in order to anticipate P-Δ effects and avoid dynamic seismic instability. The stability coefficient θ (Equation 2-5) is calculated at every storey level and should not exceed 0.4, in which case redesign of the structure would be required.

$$\theta = (P \times \Delta_i)/(R_0 \times V_i \times h_s\ ) \quad \text{2-5}$$

In Equation 2-5, P is the gravity load, Δ_i is the inelastic interstorey displacement and V_i is the shear force, all associated to the storey level i under consideration, and h_s is the storey height. If θ is smaller than 0.4 but greater than 0.1 in any storey level, the resulting lateral force at that storey level must be amplified by the factor $(\theta + 1)$. Only force response parameters require the amplification by $(\theta + 1)$. The SFRS can then be designed for the calculated seismic forces, and, at the end of the design procedure, lateral deflections along the height of the building must be checked against code limits. The interstorey deflection at any level must be lower than 2.5% for normal importance buildings.

If any irregularity is present in the structure, the NBC 2015 requires that more comprehensive analysis be conducted. Past seismic engineering experience has shown that structural irregularities can lead to concentration and amplification of damage during seismic events, which hinders the predictability of the structural response (Filiatrault et al, 2013). One example of irregularity is the torsional sensitivity, which is evaluated based on the B ratio. B relates the maximum storey displacement recorded at the in-plan edges of the structure to the average of the edge displacements, developed when the equivalent static forces are applied to the centre of rigidity shifted by 10%. If B is greater than 1.7, a dynamic analysis procedure must be conducted. The dynamic analysis can be linear (Modal Response Spectrum Method or Numerical Integration Linear Time History Method) or nonlinear (Nonlinear Time History Analysis). Other irregularities listed in the NBC 2015 involve discontinuities in vertical stiffness, geometry of the SFRS, mass distribution of the structure, in-plan asymmetry, and geometric discontinuity of the SFRS. If the SFRS' components are oriented along axes orthogonal to each other, the interaction between the seismic loading in each direction can be ignored, and the dynamic analysis can be run along the two principal directions of the structure independently.

Dynamic analyses require modelling of the structure. As a minimum, any structural model must include all structural members that constitute the SFRS, as well as any component that may contribute to the lateral response of the building, as elements that increase the lateral stiffness could shorten the structural period and thus increase the seismic loads. The structural model can be developed as 3-D or reduced into 2-D views of the principal directions. Three-dimensional models can lead to a better representation of the structure's distribution of stiffness, strength, and mass. Moreover, they permit an explicit consideration of the torsional effects caused by any eccentricity present on the structure.

When a dynamic analysis is selected, the equivalent static procedure can serve as a preliminary design for the structural elements, which will be used as the initial starting point for the model. The code permits the eccentricity for accidental torsion to be reduced from 10% to 5% when dynamic analysis is employed, provided $B < 1.7$. According to the CSA A23.3-14, for the analysis of buildings with lateral load resistance provided only by structural walls or by a combination of walls and frame members, all shear walls shall be considered cracked. Thus, a degraded stiffness should be adopted in the model through the calculation of a reducing factor α_w, determined according to Equation 2-6.

$$\alpha_w = 1.0 - 0.35((R_d\, R_0)/\gamma_w - 1.0) \geq 0.5\ and\ \leq 1.0 \qquad \text{2-6}$$

When dynamic analysis is performed in regular structures, the NBC 2015 states that, for strength requirements, the design base shear (V_d) must be taken as a minimum of 80% of the static base shear (V_{st}) calculated using Equation 2-1 with T_a equal to the upper limit from the code. Therefore, the elastic base shear resulting from Response Spectrum Analysis (V_{RSA}) must be divided by R_dR_0 (to provide inelastic results) and compared with V_{st}. For drift requirements, V_{RSA} can be used if it is greater than 80% of V_{st} calculated with T equal to 4.0 s, in the case of shear walls. If $V_{RSA} < 0.8V_{st}$, the forces and displacements resulting from the analysis must be multiplied by the scaling factor expressed by Equation 2-7. In the case where $V_{RSA} \geq 0.8V_{st}$, V_d can be taken as equal to $V_{RSA} / R_d R_0$, without considering the scaling.

$$\frac{(0.8V_{st})}{V_{RSA}} \tag{2-7}$$

2.3.3 Flexural design of reinforced concrete shear walls

Reinforced concrete shear walls are planar vertical elements that work as lateral load-resisting elements in a concrete structure. Shear walls with an aspect ratio (height over length) greater than 2.0 are considered slender walls, thus generally controlled by flexural behaviour, tending to form a plastic flexural hinge near the base of the wall when subjected to severe lateral loading. The ductility capacity of shear walls is a function of: the amount of longitudinal reinforcement concentrated near the boundaries and distributed along the web of the wall, the web thickness and, ultimately, the required level of lateral shear to initiate flexural yielding. Reduced ductility capacity can be expected for walls subjected to higher axial and shear stresses.

Shear walls, when part of a structurally regular SFRS, are intended to form a single plastic hinge at a well-defined section at the base. The location of the plastic hinge is a design decision, which is, however, frequently constrained by the geometry of the building. The CSA A23.3-14 (CSA, 2014) prescribes especial detailing for the reinforcement and concrete section within the plastic hinge region of shear walls. The plastic hinge region must be extended upwards from the point where the vertical reinforcement will first yield by a minimum distance L_p, calculated through Equation 2-8, where h_n and l_w are the height and length of the wall, respectively, in the direction under consideration.

$$L_p = 0.5\, l_w + 0.1\, h_n \tag{2-8}$$

To prevent out-of-plane buckling of the damaged wall due to inelastic cyclic demand, the CSA A23.3-14 specifies a minimum wall thickness that must be maintained, specifically within the potential plastic hinge region. An option to providing this minimum wall thickness is to include flanges or cross walls, which will serve as a continuous lateral support to the wall. The minimum wall thickness (b_w) depends on the clear span or unsupported length (l_u) of the wall, which typically corresponds to the interstorey height. Minimum wall thickness within the plastic hinge region is expressed by Equation 2-9.

$$b_w \geq l_u/10 \qquad \text{for ductile shear walls}$$
2-9
$$b_w \geq l_u/14 \qquad \text{for moderately ductile shear walls}$$

Bonding between concrete and steel is addressed by the definition of longer development and lap lengths. The ratio of distributed reinforcement, both vertical (ρ_1) and horizontal (ρ_t), should be specified respecting the minimum ratio indicated by Equation 2-10. The distributed reinforcement should be spaced at no more than 300 mm and 400 mm within the plastic hinge region of ductile and moderately ductile walls, respectively, and no more than 450 mm above the plastic hinge region in both types of walls. Vertical and horizontal reinforcement shall be arranged in two curtains when the wall thickness exceeds 210 mm. Even when this limit is not surpassed, it is good practice to use two curtains of reinforcement, as this provides some confinement to the concrete, increasing the load-carrying capacity of the wall. The bar diameter selected for the distributed reinforcement should be smaller or equal to 10% of the wall thickness in order to aid construction of shear walls. The distributed vertical reinforcement should be tied if the final area of steel surpasses a specified limit.

$$\rho_1 = \rho_t \geq 0.0025 \tag{2-10}$$

For lap splices, the seismic design clause of the Canadian concrete code requires lap splice development length to be increased by 50% to accommodate the overstrength stress induced by yielding of the flexural reinforcement. For ductile shear walls, the ratio of concentrated vertical reinforcement is limited to 0.06 in any region, including lap splices. Following the capacity design philosophy, the intent of this limit is to prevent a significant overstrength to surface, triggered by a moment capacity increase due to well-constructed lap splices, which would incur in greater design forces for the other components of the SFRS.

Resistance to the overturning moments is the role of the longitudinal reinforcement, distributed throughout the web zone and concentrated at the edges. The area of concentrated reinforcement (A_{s1}) should meet the minimum calculated by Equation 2-11, for ductile shear walls, and by Equation 2-12, for moderately ductile shear walls. Moreover, the CSA A23.3-14 requires all ductile walls to have tied cages at their ends, which should contain at least four bars placed in two layers, and to be designed to resist the stresses not resisted by the vertical distributed reinforcement. The bars at the edges must be tied against bucking, including crossties when needed. The ties should also provide the required confinement for the concrete.

$$\begin{cases} A_{s1} = 0.0015 b_w l_w & \text{within the plastic hinge region} \\ A_{s1} = 0.0010 b_w l_w & \text{above the plastic hinge region} \end{cases} \quad \text{2-11}$$

$$\begin{cases} A_{s1} = 0.00075 b_w l_w & \text{within the plastic hinge region} \\ A_{s1} = 0.0005 b_w l_w & \text{above the plastic hinge region} \end{cases} \quad \text{2-12}$$

Ultimately, the Canadian concrete code requires that the inelastic rotational demand (θ_{id}) in the plastic hinge be assessed against the rotational capacity (θ_{ic}) of the wall, which are demonstrated by Equations 2-13 and 2-14, respectively. This check can be understood as an explicit verification of the wall's ability to undergo lateral deformation.

$$\theta_{id} = \frac{\left(\Delta_f R_d R_0 - \Delta_f \gamma_w\right)}{h_n - l_w/2} \qquad \begin{matrix} \geq 0.004 \text{ for } \mathrm{R_d} \geq 3.5 \\ \geq 0.0035 \text{ for } \mathrm{R_d} \geq 2.0 \end{matrix} \quad \text{2-13}$$

$$\theta_{ic} = \left(\frac{\varepsilon_{cu} l_w}{2c} - 0.002\right) \leq 0.025 \quad \text{2-14}$$

In Equations 2-13 and 2-14, c is the depth of the compression zone in the cross-section; Δ_f is the displacement at the top of the wall under factored loads; 0.004 and 0.003 represent the minimum rotational demand for ductile and moderately ductile shear walls, respectively; 0.025 is the maximum θ_{ic} (based on the steel-tension strain limit), and ε_{cu} is the ultimate concrete strain, generally taken as 0.0035. It is possible to assign values to ε_{cu} up to 0.010. In order to do so, confinement reinforcement must be provided, respecting provisions from the code, over a distance from the compression face determined by Equation 2-15.

$$\frac{c(\varepsilon_{cu} - 0.0035)}{\varepsilon_{cu}} \quad \text{2-15}$$

2.3.4 Shear design of reinforced concrete shear walls

Following the capacity design fundamentals, bending moments and shear forces resulting from dynamic analysis must be amplified by the flexural overstrength factor γ_w, which compares moment capacity to moment demand at the base of the plastic hinge region. This magnification is based on the fact that the as-designed flexural strength of the wall will induce shear at the base of the wall (Filiatrault et al., 2013). The amplified factored shear forces must be further scaled to account for inelastic effects in higher modes, which is handled by employing a factor determined through the comparison of the fundamental period of vibration of the building to limits provided by the code. The final shear forces do not need, however, to be taken as greater than the output shear forces from the design load combination including earthquake effects when $R_dR_0 = 1.3$ is considered.

To calculate the concrete and steel contributions to the shear resistance, the CSA A23.3-14 (CSA, 2014) acknowledges that inelastic rotational demand affects the concrete capacity to resist shear forces. Thus, the values assumed by the factor that accounts for shear resistance of cracked concrete (β) vary with θ_{id} from zero to 0.18. Another parameter that influences the calculation of shear resistance is the axial compression ratio on the wall. The angle of the compression strut in the plastic hinge region (θ) will range from 35° to 45°, depending on the magnitude of the axial load acting as part of the critical load combination.

2.4 Investigation of the seismic performance of structures

The seismic performance assessment of structures is discussed in this section, where numerical analysis is presented as one method of investigation. An introduction is given on the types of structural analysis, focusing on the advantages of finite element over other methods that justify the selection of this type of analysis for this thesis. Next, relevant seismic response indexes and seismic performance levels are outlined, some of which will be used in this thesis to evaluate the seismic performance of the shear walls obtained with dynamic analysis. An overview of the seismic hazard in Canada is also presented, focusing on the aspects that distinguish eastern and western Canada's seismicity and that are critical for the selection of earthquake records to perform dynamic analysis.

2.4.1 Seismic performance of structures

The level of serviceability or reparability of a structure after an earthquake will depend on several factors, including the extent of damage, the feasibility of reverting the sustained damage, the capacity of the structure to resist probable future ground motions, and the effect of repair on successfully restoring structural safety. Various methods to assess the performance of structures subjected to earthquakes have been proposed by a number of researchers. Some of these methods have been incorporated into seismic provisions. In existing structures, assessment methods can be based on quick inspections of visible damage or can require more detailed evaluations of the structural condition. Quick inspection methods use evidence such as crack size, spalled concrete cover, and ruptured/buckled reinforcing bars as indicators of the probable capacity of the structure to resist future loads or deformations. When inspection methods are applied, judgement of the safety level of a structure is somewhat subjective and intuitive. Therefore, uniformity is likely to be jeopardized when a great number of structures is evaluated, as the final assessment is strongly dependent on the inspector's judgement.

In contrast, detailed evaluation methods propose the development of numerical models of the structure to estimate parameters such as residual energy dissipation capacity and probable deformation with respect to various seismic hazard levels. To assess the seismic performance of structures according to detailed methods, it is necessary to evaluate the extent of stiffness and strength degradation suffered by the structural components. Beyond that, the correlation between the degradation and the capacity of the structure to sustain static and dynamic loads must be understood. The degradation of stiffness and strength is strongly associated with the maximum deformations sustained (Yazgan, 2010). Detailed assessment methods, however, rely on the availability of additional information about the building to provide representative models and meaningful results.

2.4.2 Structural response using numerical analysis

Numerical analysis can be a resourceful tool to investigate and predict the behaviour of structures under seismic excitation. Different types of analyses, with different levels of complexity, can provide relevant information and contribute to the seismic performance assessment of structures. The monotonic response of a structure, which can be obtained through the application of incremental lateral displacements up to failure, permits evaluation of the maximum lateral capacity, effective stiffness, and the yield displacement of the structure if nonlinearity is considered in the analysis. Using nonlinear reversed cyclic analysis, the hysteretic behaviour of the structure can also be investigated, which provides further information about residual deformations, energy dissipation and recentering capacities, and stiffness/strength degradation under cyclic excitation. Ultimately, the use of dynamic analysis can incorporate the effects of natural earthquake records and can permit the assessment of the post-earthquake condition of the structure, including permanent deformations.

When nonlinear time history analysis is performed, the nonlinear response of the structural elements that are expected to undergo significant inelastic deformations must be modelled. Modelling approaches include concentrated plasticity models using predefined plastic hinges, fiber section modelling with nonlinear material properties specified at discrete locations, and distributed plasticity based on 2-D or 3-D finite element modelling. The different modelling approaches are illustrated in Figure 2-21. The accuracy of the selected model is of crucial importance as the analysis results are often used as the basis for decisions regarding safety and retrofitting strategies. Thus, an inaccurate analysis can lead to an underestimation of the risks offered by the structure when subjected to ground motions, or to the selection of an ineffective retrofitting system. Although finite element modelling is the most complex and time-consuming modelling approach, it is considered to be the most accurate, as it yields a better prediction of the response at local levels and allows for the shear-flexure-axial force interaction to be incorporated in the analysis (Filiatrault et al., 2013).

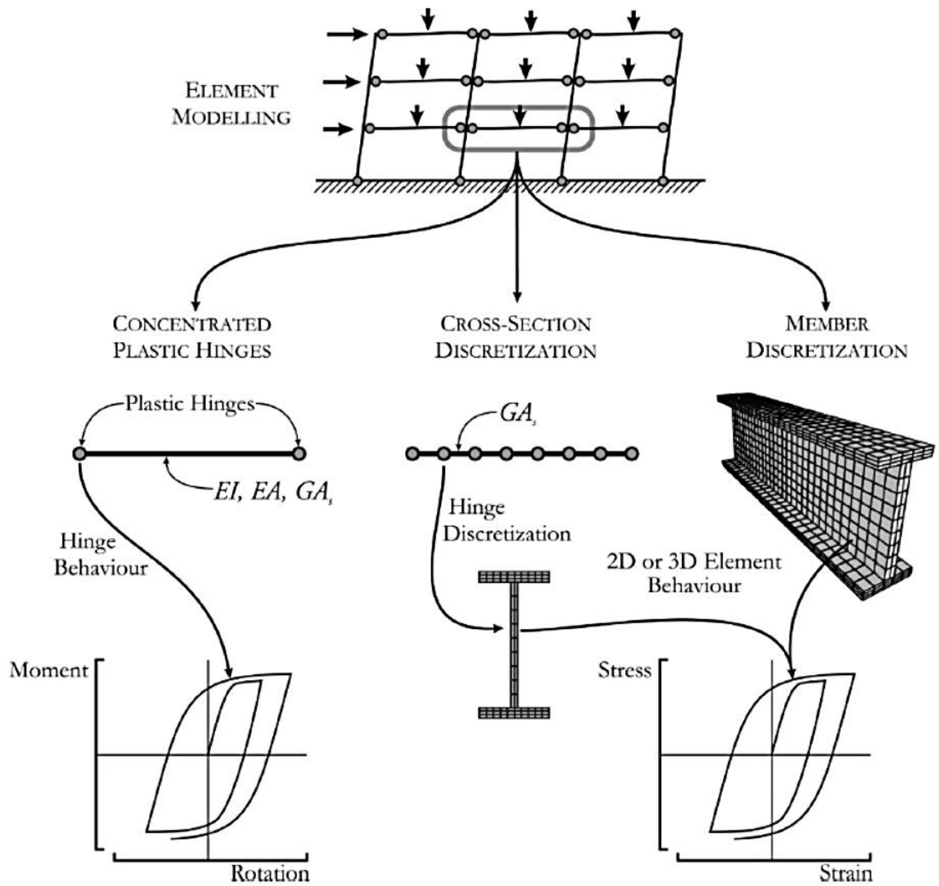

Figure 2-21 - Modelling methods to reproduce the stiffness and hysteretic properties of materials in structural members (Filiatrault et al., 2013)

When the structural response to static loads is sought, the main factors influencing the response are the mechanical properties of the structural components (e.g. frames, joints, walls, foundation) and the boundary conditions of the system (e.g. applied external loads, soil underneath the structure). Meanwhile, in dynamic analysis, the structural response is a function of the essential mechanical properties and boundary conditions, in addition to the temporal effects of these properties.

To produce a numerical model that is in good agreement with the observed behaviour of real structures under dynamic loads, the variation of properties with time such as stiffness, strength, and deformation capacity must be predicted in the shape of a constitutive model. In order to do so, the adoption of idealizations and assumptions becomes inevitable. The extent of simplification adopted should depend on the required accuracy, the available time and computational resources, the parameters of interest in the response, and the level of understanding of the dynamic response of the structure. It is imperative to model the complete hysteretic behaviour of each structural component using properties that rely on experimental evidence. Unloading and reloading stiffnesses and strengths, as well as pinching of the load-deformation hysteresis loops, must be consistent with that observed in experimental tests.

One important outcome of all types of numerical analysis of structures is the load-deformation response. Load-deformation curves illustrate the deformations developed by a structural component with increasing lateral loading. From the curve, the behaviour of the structural component under lateral loading can be evaluated, and the response of the element can be classified as deformation-controlled or force-controlled. ASCE/SEI 41-17 (ASCE, 2017) characterizes structural behaviour based on typical idealized force-deformation curves, illustrated in Figure 2-22. Type 1 curve is composed by an elastic range (from point 0 to point 1), followed by a plastic range (from 1 to 2), which can include strain hardening or softening, and then by a significant degradation of strength (from 2 to 3), which is reduced to only a fraction, but still of substantial value, of the original strength. In all curves from Figure 2-22, loss of lateral force-resisting capacity occurs at point 3, while loss of gravity load-resisting capacity occurs at point 4. The behaviour of structural elements represented by Type 1 curve is typically ductile and, if point $d \geq 2\,g$, the response of the element is deformation-controlled, and force-controlled otherwise. Type 2 curve represents another type of ductile behaviour. This curve contains the same elastic and plastic regions as Type 1 but results in rapid and total loss of strength at point 2. The plastic branch can have either a positive or negative post-elastic slope. Deformation-controlled responses are identified as having point $e \geq 2\,g$ in Type 2 curve. In contrast, Type 3 curve reflects a nonductile or brittle behaviour with absence of a plastic range. Thus, the response of structural elements with Type 3 load-deformation curves evolves from an elastic range directly to a rapid and complete degradation of strength at point 1. Type 3 curve strictly represents elements with force-controlled responses.

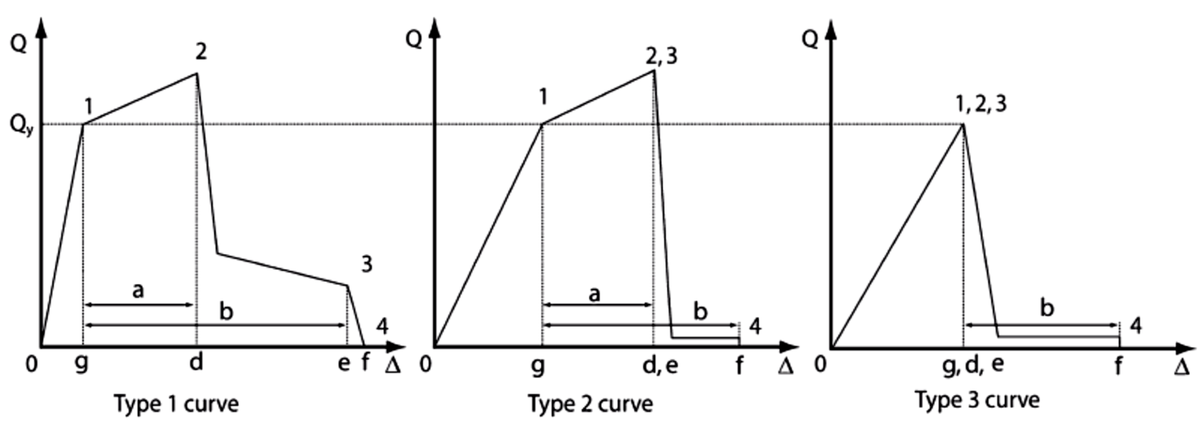

Figure 2-22 - Typical force-deformation curves of structural components (ASCE, 2017)

In ductile types of behaviour, point 1 can be understood as the yield point, where the response transitions from elastic to plastic, originating nonlinear deformation. In reinforced concrete structural elements, nonlinear deformations result in force-deformation relations that may not show a distinct yield point. Examples of situations when this occurs include reinforcement in different depths reaching yielding at different moments in time, plastic hinges being formed in multiple locations of the structural element at different load levels, nonlinear behaviour of materials, to name a few (Park, 1988).

The extent of residual deformation a structure will sustain after reaching a peak displacement during an earthquake is dependent on two aspects of the structure's nature: self-centering capacity and post-yielding stiffness (Yazgan, 2010). For structures with hysteretic behaviour, the self-centering capability will assure negligible displacements. The same is not expected in structures that do not exhibit such hysteresis, and for those the magnitude of residual displacements will be strongly influenced by the post-yielding stiffness (Yazgan, 2010).

In a load-deformation response, pinching of the hysteresis loops significantly influences the sustained residual displacement. The possible range of residual deformations that may be sustained by the plastic hinge region of a structural element is inversely proportional to the degree of pinching of the load-deformation hysteresis loops (Yazgan, 2010).

2.4.3 Seismic response indexes

In order to assess the seismic response of structures, response indexes must be defined, followed by the determination of limit values that the index should respect in order to reflect a fine structural response. Several indexes and limit values proposed by different studies and documents for the seismic performance assessment of structures will be presented in the following sections.

Deformation is an important parameter to be evaluated in the seismic response of structures, as it can implicate an inclination of horizontal members and tilt of vertical members, generating additional and unexpected stresses in structural members and joints. Residual drifts of 1% are referred by the literature as a significant index limit in terms of habitability of buildings. This index limit is reinforced by Kwan and Billington (2003) in their set of criteria proposed to evaluate the functionality of bridge piers, one of which states that residual drifts must be limited to 1%.

The extent of residual drift can hinder the evacuation of the building after an earthquake due to compromised functionality of non-structural elements. Significant damage to door systems, for example, are reported when vertical tilts of door frames and surrounding members exceed 0.005 rad (McCormick et al., 2008). Regarding safety, the residual deformation level of 0.005 rad can be understood as an important index limit for the seismic response assessment of structures. Studies have also suggested that rebuilding becomes a more economic option when residual rotations exceed 0.005 rad if direct and indirect repair costs are considered to evaluate the viability of retrofitting of a structure (McCormick et al., 2008).

Regarding discomfort of occupants in a building, residual inclinations of 0.5% have been reported as the minimum perceptible floor inclination angle for an average person (McCormick et al., 2008). Occupants subjected to residual inclinations above 0.8% reported significant discomfort, with headaches and dizziness after prolonged exposure to the inclined surface.

Using strains in steel and concrete as an index to characterize performance limits, two limit states have been suggested by Kowalsky (2000) based on moment-curvature analysis of circular bridge columns. The first limit is the serviceability limit state, which represents elements that do not require repair after an earthquake, whereas the second limit, the damage control limit state, is suitable for elements that exhibit repairable damage. The first limit state prescribes steel tensile strains limited to 0.015 and concrete compressive strains smaller than 0.004. Meanwhile, limits for the second limit state correspond to strains of 0.06 and 0.018 in steel and concrete, respectively. Limits are also suggested for strains in SMA reinforcement (Wang and Zhu, 2018), which can be taken as 6% (the superelastic strain limit of SMA).

Specifically, for self-centering concrete walls, recent studies have proposed residual drift limits that correspond to multiple hazard levels, based on extensive parametric studies that intend to provide realistic limits for seismic resilient buildings (Henry et al., 2016). The residual drift levels, listed in Table 2-2, aim to allow re-occupancy following a major earthquake given the sufficient recentering of the building.

Table 2-2 - Residual drift performance limits for self-centering systems (adapted from Henry et al., 2016)

Seismic hazard	Residual drift limit (%)
Frequent earthquake	0.1
Occasional earthquake	0.1
Design level earthquake	0.2
Maximum considered earthquake	0.3

2.4.4 Seismic performance levels

With the advancement of performance-based seismic design since the 1990s, the need to evaluate the performance of structures under multiple seismic hazard levels has surfaced. Seismic performance levels are defined, in many methods, according to residual displacement limits. The Federal Emergency Management Agency (FEMA) report FEMA 273: NEHRP (FEMA, 1997) was the first of a series of documents to propose multiple seismic performance levels and the possibility to evaluate the performance of a structure with respect to a particular earthquake scenario or intensity, or even considering all possible earthquakes and corresponding probability of occurrence over a period of time. Thereafter, the document FEMA 356: Prestandard and Commentary for the Seismic Rehabilitation of Buildings (FEMA, 2000) related the seismic performance levels to damage of existing structures. The successor documents, the FEMA P-58-1: Guidelines for the Seismic Rehabilitation of Buildings (FEMA, 2012) and the American Society of Civil Engineers (ASCE) Standard ASCE/SEI 41-17: Seismic Evaluation and Retrofit of Existing Buildings (ASCE, 2017) are the current guidelines for performance-based seismic design in the United States. These guidelines define four target building performance levels, combining the evaluation of the performance of structural and non-structural elements based on maximum and residual drifts and level of damage of the structure, as described in Table 2-3.

Table 2-3 - Building performance levels by the ASCE/SEI 41-17 (ASCE, 2017) defined according to storey drifts prescribed by the FEMA P-58-1 (FEMA, 2012)

Performance level	1-A	1-B	3-C	5-D
Overall damage	Very light	Light	Moderate	Severe
Residual storey drift (Δ/h_s)	0.2% *	0.5%	1.0%	4% (high ductility) 2% (moderate ductility) 1% (low ductility)
Transient storey drift for RC shear walls	1%	2.2%	2.6%	3.6%

* typical out-of-plumb tolerance for new construction

The performance level 1-A, or operational performance level, represents structures that have suffered very limited damage, with vertical and lateral force-resisting systems retaining virtually all the original stiffness and strength. For such structures, the risk of life-threatening injuries is very low. In most cases, the minor repairs required can even be performed after immediate reoccupancy. Damage is restricted to non-structural components, and structural alignment of the building is sound to ensure structural stability.

As an intermediate state of damage, the immediate occupancy performance level 1-B implies that somewhat greater drifts and more spread damage are present in the structure compared to that in the operational level. The structure requires realignment in order to avoid degradation of structural stability, and subsequent repair to structural and non-structural elements. In general, certain cracking will be present in facades, partitions, ceilings, and structural elements of the building, but the fire protection system remains operable and elevators can be restarted. A design aiming for this damage level can minimize costs that could become excessive when designing for the operational level, as well as reduce repair time and operation interruption when compared to that of the conventional life safety state adopted by most design codes. This performance level can also be selected as the design target when protecting valuable equipment and contents, or historic features, is of interest in a building.

The life safety performance level 3-C is characterized by greater structural damage and required realignment due to permanent drift. Although some resistance to partial or total collapse remains and the structure does not represent an immediate risk for life-threatening injuries, the repair necessary to restore safety and functionality, although technically possible, may not be economically feasible.

Ultimately, structures in the collapse-prevention performance level 5-D are near partial or total collapse, which indicates that severe, and probably irreparable, damage is sustained by structural components, including large permanent lateral deformations, significant degradation of lateral stiffness and strength and, in some cases, degradation of the vertical load-carrying capacity. However, the load-bearing columns and walls are still functioning. There is a high risk of collapse induced by aftershocks (FEMA, 2012).

Particularly in reinforced concrete shear walls, expected damage according to each performance level is described by the ASCE/SEI 41-17 (ASCE, 2017) as follows. For the immediate occupancy level, minor cracking of walls can be expected. Limited buckling of reinforcement, some sliding at joints and boundary element distress, some crushing and flexural cracking are characteristic of shear walls in the life safety level, although concrete generally remains in place. In the collapse prevention level, shear walls are expected to have experienced severe boundary element damage, with major flexural and shear cracks and voids, as well as sliding at joints. Transient storey drifts can also be used to classify the damage level of RC shear walls, as presented in the FEMA P-58-1 and summarized in Table 2-3.

2.5 Numerical analysis of structures

Important parameters for the accuracy of numerical analysis are discussed in this section. The discussion involves a review of two studies that included large and reduced-scale experimental testing of conventional concrete shear walls with similar height to the walls investigated in this thesis, which were also modelled in the software VecTor2 (Vecchio et al., 2013). Emphasis is given to the selected material models, modelling decisions, and dynamic analysis parameters, as well as to the efficiency of the models in capturing the behaviour of slender concrete shear walls. First, the main features of finite element analysis in VecTor2 are presented, including that required for dynamic analysis. Ultimately, this section includes a literature review on the procedure for selection and scaling of ground motions records to perform time history analysis of earthquake-prone structures.

2.5.1 Finite element analysis program

The nonlinear finite element analysis program VecTor2 (Vecchio et al., 2013) permits nonlinear static and dynamic analysis to be performed in two-dimensional reinforced concrete membrane structures. The formulation that the program considers for smeared rotating-crack is based on the Modified Compression Field Theory (Vecchio et al., 1986) and the Disturbed Stress Field Model (Vecchio, 2000). The Modified Compression Field Theory calculates average and local strains and stresses in the concrete and in the reinforcement of RC membrane elements subjected to shear and normal stresses, along with crack width and orientation, to determine the failure mechanism of the element, as illustrated in Figure 2-23. The program is considered numerically robust and its solution algorithm, which is based on a secant stiffness formulation using a total load iterative procedure, guarantees a stable performance and good convergence.

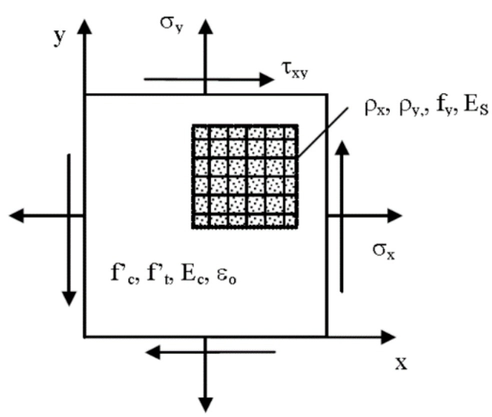

Figure 2-23 - Reinforced concrete membrane element subject to in-plane stresses (Vecchio et al., 2013)

To model solid materials, triangular and quadrilateral elements are available in VecTor2. One particular case of quadrilateral elements is the rectangular element, presented in Figure 2-24 (a). Reinforcement, on the other hand, can be modelled as smeared within the solid elements or as discrete truss bar elements. A truss bar element is shown in Figure 2-24 (b). The bond between truss bars and solid elements can be specified as either 2-node link elements, which have four degrees of freedom and are an exact solution for constant bond slip (depicted in Figure 2-24 (c)), or as 4-node interface elements. The latter have eight degrees of freedom and use a linear displacement function, ensuring exact results for constant and linearly variable bond slips and good approximations for bond slips with nonlinear variation.

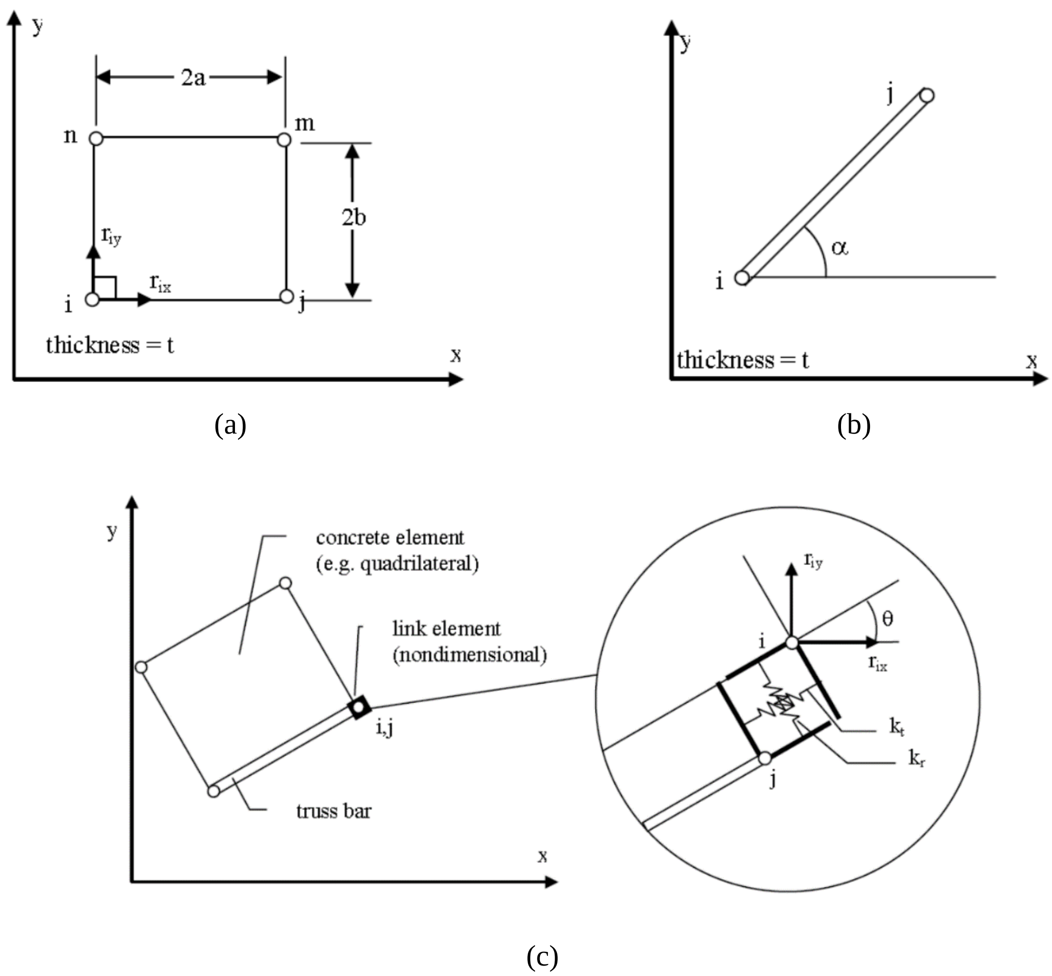

(a) (b) (c)

Figure 2-24 - Elements in VecTor2: (a) rectangular element, (b) truss bar element and (c) link element (Vecchio et al., 2013)

VecTor2 employs the Rayleigh's viscous damping model to introduce damping into dynamic analysis. In the Rayleigh's model, damping values must be assigned to a pair of modes of vibration. The selected modes should be capable of representing the response of the structure. Therefore, as the fundamental mode of vibration dominates the seismic response of the structure, e.g. top displacements and base moments, it should be the first mode to be chosen. The next component of the pair should be selected with careful consideration. If a low mode is selected, the higher modes are likely to be over-damped. Conversely, the definition of a high mode will incur in under-damping of the lower modes (Luu et al., 2013). To aid this decision, it is common to use the mode that corresponds to more than 90% of accumulated modal mass participation. Although not specified by seismic codes, damping values around 5% of the critical damping are commonly employed when modal response spectrum or linear time history analyses are performed. For taller buildings, it is recommended that damping be reduced to 1-2%. Reduced values of damping should also be assigned when nonlinear time history analysis is used, as the energy dissipation that occurs due to the hysteretic response of yielding elements is explicitly considered by this type of analysis (Filiatrault et al., 2013).

2.5.2 Analysis parameters

In order to discuss parameters that are important for the accuracy of the finite element analysis, two studies are subsequently reviewed, which involve large and reduced-scale experimental testing of traditional concrete shear walls with similar height to the walls investigated in this thesis. The studies comprise nonlinear time-history analysis of the walls modelled in VecTor2, with ground motions records representative of western and eastern Canada. Selected material models, modelling decisions, and dynamic analysis parameters are investigated as the benchmark for the analysis conducted herein.

Ghorbani-Renani et al. (2009) investigated the seismic behaviour of a slender ductile RC shear wall, which was built in full-scale with a height of 30 m, and also reproduced in a 1:2.37 scale. The walls were tested under monotonic loading and quasi-static cyclic loading. In addition, the FE program VecTor2 was used to model the walls and conduct nonlinear cyclic and time-history analyses with ground motion records representative of western Canada as input. The experimental results validated the use of the reduced-scale specimen. Moreover, the analysis with VecTor2 was successful in reproducing the shear deformation effects and shear sliding behaviour along the base of the walls (failure mechanism) observed in the experimental tests, as well as the observed initial stiffness, force demand in the transverse steel, and energy dissipation. Ghorbani-Renani et al. emphasized that this type of response could not be captured if simpler frame models with lumped plastic hinges were employed. The FE program overestimated the strength of the walls by 12%, which is associated, according to Ghorbani-Renani et al., to the selected tension stiffening model, i.e. the Bentz model. However, neglecting the tension stiffening effect led to a reduction of 60% in the initial stiffness. The cyclic results were in excellent agreement with the experimental data up to the predicted ductility of the walls, after which strength degradation in the models became more pronounced than that in the experimental tests. Material models adopted by the authors, which are part of the VecTor2 library and are described in detail in Vecchio et al. (2013), included: the Popovic-Thorenfeldt-Collins base curve for concrete, the Kupfer/Richart model for confined concrete, the Vecchio and Collins model for concrete compression softening, the Seckin (Bauschinger) model and the Palermo and Vecchio (with decay) models for the hysteresis of reinforcement and concrete, respectively, the Tassios model for the dowel action of reinforcement, and the Vecchio-Lai model for the slip distortion effect. As a conclusion, Ghorbani-Renani et al. acknowledged that the FE program could effectively predict the inelastic monotonic and cyclic behaviour of ductile shear walls. Good prediction of the response is demonstrated in Figure 2-25. Moreover, the crack pattern provided by the program was compared to that obtained during experimental testing, as demonstrated in Figure 2-26.

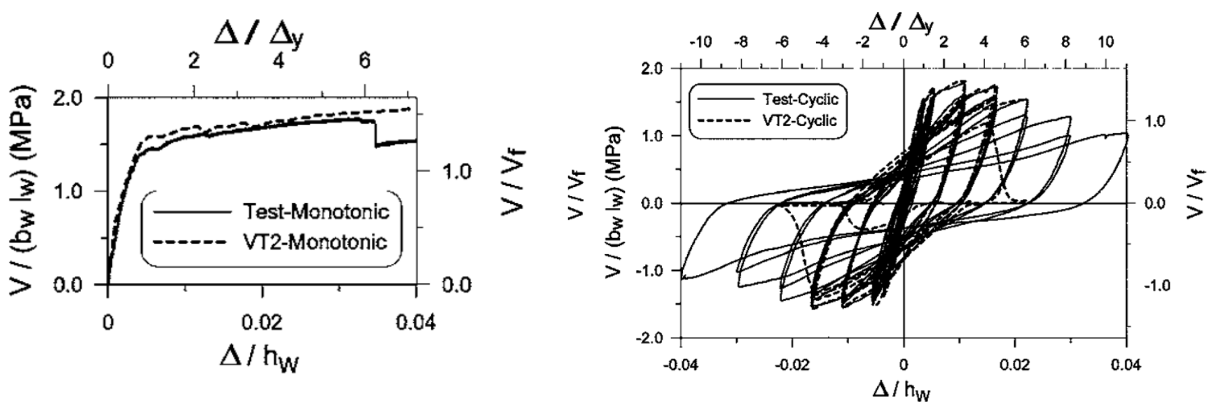

(a) (b)

Figure 2-25 - Responses of specimens from tests and from two-dimensional FE analysis (Ghorbani-Renani et al., 2009): (a) monotonic responses and (b) cyclic responses of model wall

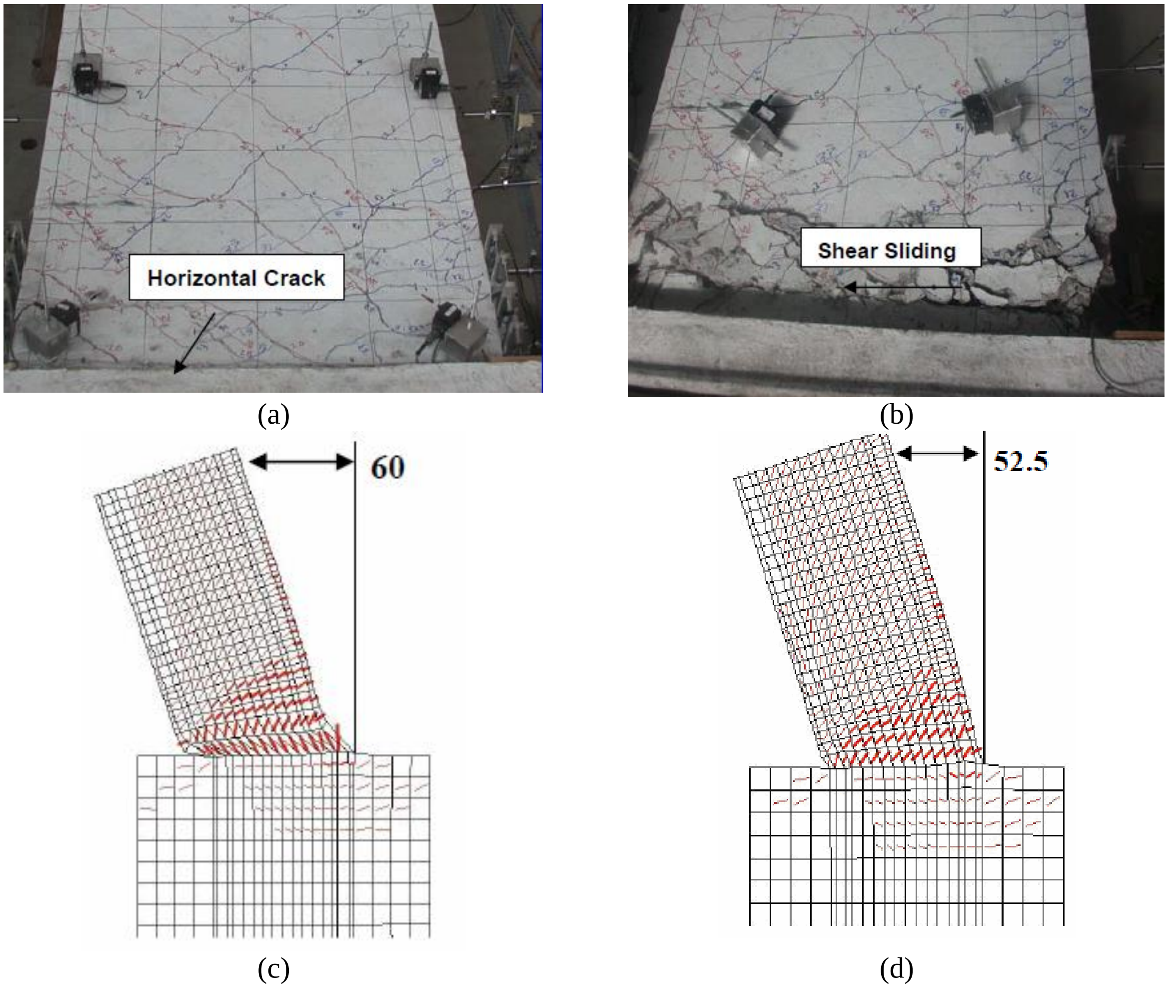

Figure 2-26 - Crack pattern in wall (Ghorbani-Renani et al., 2009): from experimental test of (a) monotonic and (b) cyclic response, and from simulation of (c) monotonic and (d) cyclic response

Luu et al. (2013) tested on an 8-storey, moderately ductile, slender RC shear wall on a shake table at the École Polytechnique in Montreal, Canada. The wall dimensions and the complete setup are illustrated in Figure 2-27 (a) and (b). The wall was 9 m in height due to an applied scale factor of 2.33. The experimental results were used to calibrate a fiber model and a finite element model, the latter created in the software VecTor2. The models were subjected to high-frequency ground motion records, representative of eastern Canada seismicity, and different modelling assumptions were investigated.

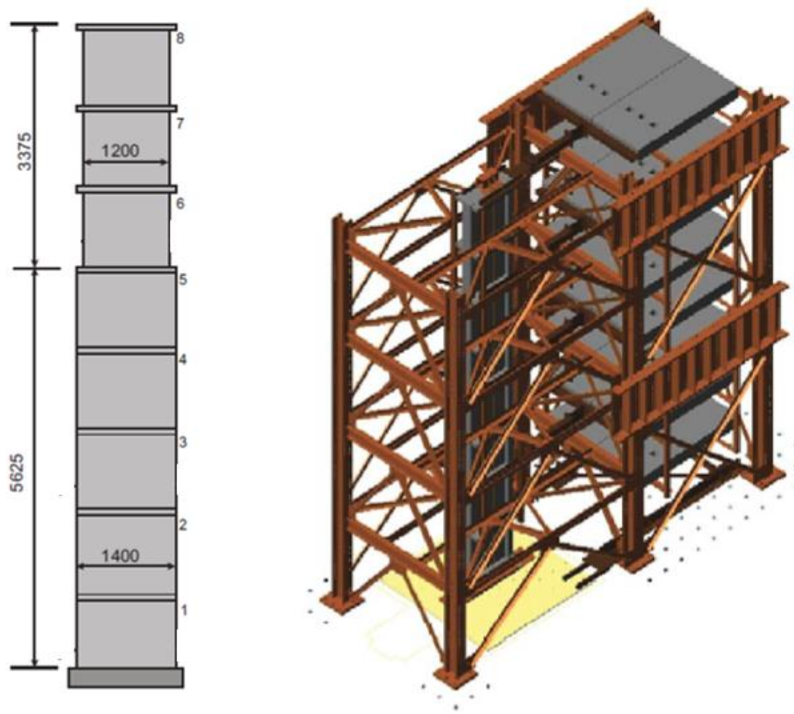

(a) (b)

Figure 2-27- Study by Luu et al. (2013): (a) model wall and (b) complete test setup with stabilizing steel frame

The analysis results indicated that the use of lumped vertical reinforcement in the boundaries of the wall provides better accuracy compared to that of the reinforcement smeared in the concrete elements. With respect to tension stiffening effect, results obtained when this effect was disregarded showed an excellent match to the lateral top displacement time history and to the moment and shear force envelope distributions from the experimental results. However, employing the Bentz 1993 model caused a substantial overestimation of the moment and shear force envelope distributions. When investigating the parameters assigned to the Rayleigh's viscous damping model, better accuracy was provided by selecting the first and third modes of vibration with 1.5% damping, when compared to the selection of the first and second modes with 2.0% damping. Ultimately, the results from the final FE model provided excellent agreement with the experimental results regarding shear force distribution, as well as fair accuracy to crack patterns, top displacements, force demand, rotational ductility, and hysteretic moment-rotation curves. The top displacement time history under the 100% earthquake is displayed in Figure 2-28 as an example. The evolution of the wall period, i.e. elongation with increasing nonlinearity, predicted by VecTor2 indicated increasing level of damage in agreement with that in the tested wall. Larger damping was calculated from the model, which was associated by the authors to accumulated damage in the steel and concrete materials, the dissipated energy at the opening/closing of cracks, and the tangential crack motions modelled in the program. The FE analysis slightly underestimated the base moment. In turn, it provided fine moment distribution in the upper levels of the wall. One interesting aspect of the experimental test was the formation of a secondary plastic hinge at the sixth storey due to higher mode effects, which was properly captured by the FE model. The numerical analysis accurately reproduced both the combined shear-flexural cracks at the base of the wall and the bending cracks at the location of the second plastic hinge.

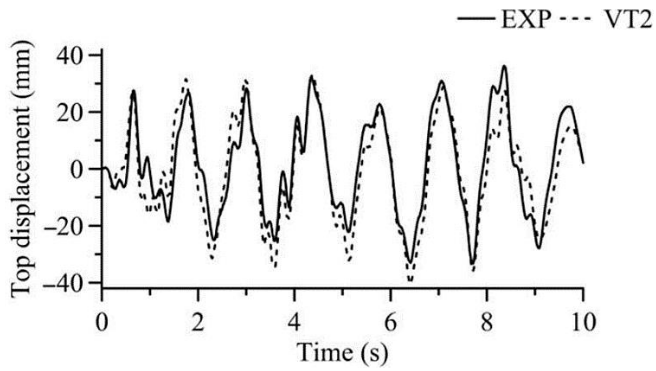

Figure 2-28 - Top displacement time history for wall under 100% earthquake from experiment (EXP) and predicted by VecTor2 (VT2) (Luu et al., 2013)

Relevant material models adopted by Luu et al. (2013) in the FE model of the 8-storey slender RC shear wall include: the Hognestad Parabolic model (concrete pre-peak), the Park-Kent model (concrete post-peak), the Kupfer/Richart model (confined concrete), the Palermo and Vecchio 2002 model with decay (hysteretic response of concrete), the Wong and Vecchio 2002 model (linear tensile softening), the Vecchio and Lai model (crack slip calculation), and the Seckin model with Bauschinger effect (hysteretic response of reinforcement). Mesh size was approximately 100 mm. The seismic mass of each floor was distributed among the nodes of the floor and the self-weight of the wall was considered when determining the axial and seismic loads. The *P-Δ* effects were ignored and the integration of the equation of motion followed the Newmark method.

2.5.3 Selection of ground motion records for dynamic analysis

In order to investigate the seismic performance of structures, the seismic hazard of the regions of interest must be well understood. Different seismic characteristics can drastically alter the way an earthquake affects a structure. To assess the seismic response of a structure at a given site, time-history analysis can be performed with the use of ground motion records, selected to appropriately reproduce the scenarios that contribute most significantly to the seismic hazard of the site. Beyond the characteristic seismic hazard, the seismic risk of a region also depends on the vulnerability of the existing structures on that given region. Even a moderate earthquake can result in dramatic consequences in a location where most structures are not seismic-resistant. In Canada, although the West is subjected to stronger earthquakes, cities in the East are also at risk due to the presence of older masonry buildings, which were designed and constructed before the development of modern seismic provisions (Filiatrault et al., 2013). This way, a proper understanding of the seismicity of both regions is vital for the seismic performance assessment of structures. In fact, the study of the seismic activity in Canada can be subdivided into northern, western and eastern seismic zones. The simplified seismic hazard map of Canada, developed by Natural Resources Canada, can be observed in Figure 2-29.

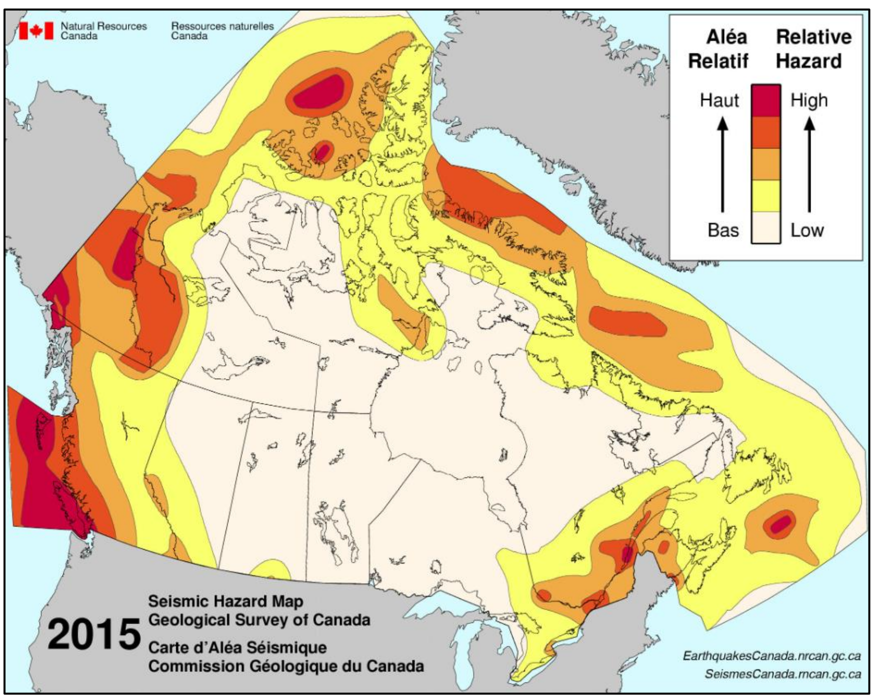

Figure 2-29 - Simplified seismic hazard map of Canada (NRC, 2017)

Although active, the seismic zone of northern Canada is not a major concern for earthquake engineering given the low population in the affected areas. In general, the seismic hazard of western Canada is characterized by high magnitude earthquakes, with long return periods and low frequency content. The region is part of the Pacific Ring of Fire. Sources of earthquakes are active plate boundary regions. For this reason, the rate and size of the generated ground motions are directly linked to plate interaction. The main plate interactions in the region are as follow: the subduction of the Juan de Fuca Plate beneath the North American Plate (called Cascadia subduction zone), the lateral movement (strike-slip movement) between the North American Plate and the Pacific Plate, and the interaction between the Pacific Plate and the Juan de Fuca Plate (Filiatrault et al., 2013). The schematic movements of the tectonic plates in western Canada are illustrated in Figure 2-30.

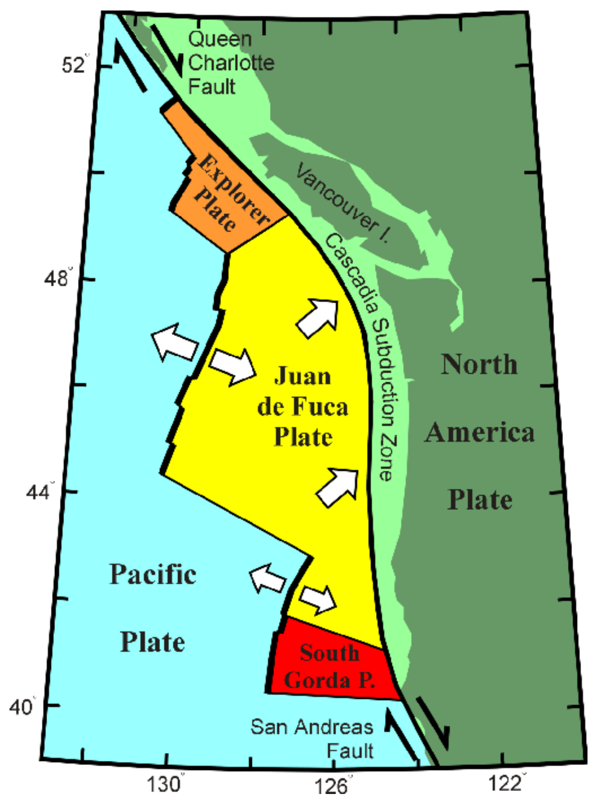

Figure 2-30 - Tectonic plates in western Canada (NRC, 2017)

Eastern Canada is subjected to earthquakes with high frequency content, shorter return periods, and that propagate further away due to the integrity of the rock in the surroundings, compared to that of western Canada. Attenuation of the seismic waves is slow, and ground motions can be felt hundreds of kilometers away from their epicenter, potentially affecting major cities in eastern North America. This area is located on a very large, dense and relatively stable continental plate, the Canadian Shield. No evident sources of seismic motions can be pointed out, as there are no faults reaching the surface. It is believed that the reactivation of an ancient system of rift faults is associated to most of the seismic activity recorded in the area (Filiatrault et al., 2013). Figure 2-31 illustrates the historical and instrumentally-recorded earthquakes of eastern Canada. The characteristics of eastern Canada's seismicity are associated with a weak availability of historical ground motion records, due to either low-energy or low sensitivity of the recording instruments (Sadeghian, 2018).

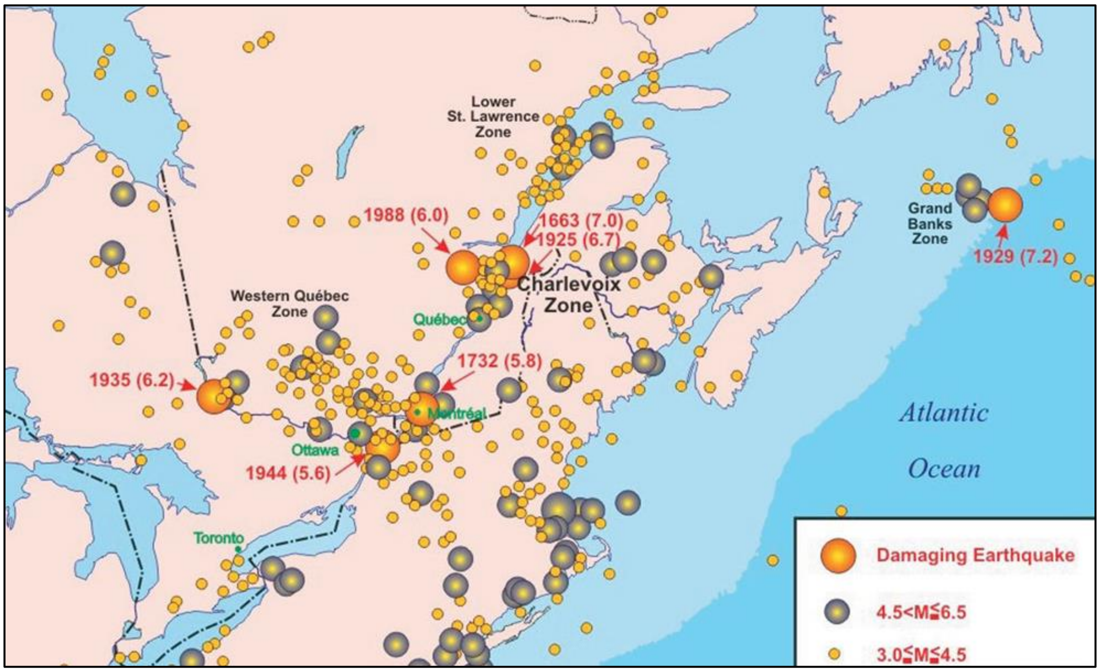

Figure 2-31 - Historical and instrumentally-recorded earthquakes of eastern Canada (Lamontagne et al., 2004)

More attention has been given to monitoring and investigating the causes of earthquakes in the West given the higher seismic activity of the region. In contrast, no significant ground motions were recorded in the East for the past two hundred years, which has led to a poor understanding of the sources that contribute to induced earthquakes in the region. Despite the lack of official records during the last couple of centuries and since the seismograph was developed, large and damaging earthquakes have occurred in the region in the past and, therefore, will inevitably occur in the future (NRC, 2017).

The process to select and scale historical and simulated ground motion records to properly represent the seismic hazard of a region involves several procedures. First, the seismic scenarios should be characterized in terms of source type, and magnitude and distance (M-R scenarios). A period range of interest (T_R) must then be defined according to the structure under consideration. It is important that this range covers the periods of vibration that have a strong impact on the dynamic response of the structure. Earthquake records are then sought to match the target acceleration response spectra defined for the M-R scenarios over T_R.

Given the inherent variability and uncertainty of future earthquakes, an ensemble of earthquake records must be used to ensure reliability of the results (Tremblay et al., 2015).

The period range defined for analysis should encompass the period of the structure in the elastic uncracked state, as well as the potential increased period due to inelastic response (Sadeghian, 2018). To establish the period range, the Structural Commentary J of the NBC 2015 (NRC, 2015b) sets a minimum and a maximum periods, as expressed in Equation 2-16. The lower limit in Equation 2-16 corresponds to the period of the highest mode of vibration necessary to accumulate 90% of the structural mass ($T_{90\%}$), which cannot exceed 15% of the period of the fundamental mode of vibration of the structure (T_1). The upper limit must be greater than 1.5 s to ensure the analysis of stiff structures includes the period range where a significant amount of the energy of typical seismic motions is concentrated, and corresponds to two times T_1. When 3-D models are used to conduct dynamic analysis, T_1 should be taken as the shorter of the two periods relative to the first translational modes of the structure.

$$T_R = \begin{cases} T_{min} = [0.15T_1, T_{90\%}] \\ T_{max} = [2.0T_1, 1.5\ s] \end{cases} \qquad \text{2-16}$$

The Structural Commentary J of the NBC 2015b proposes two methods to determine the target response spectrum ($S_t(T)$) that will be used to seek for ground motion records, Method A and Method B. Method A is a simpler version that considers an unique $S_t(T)$ along the entire period range T_R. This method is a general version of the method proposed by Atkinson (2009), which will also be discussed in this section. Method A results in satisfactory analysis provided that the earthquake records are appropriately selected and scaled to reflect the dominant M-R scenarios of the location (Tremblay et al., 2015). Method B, conversely, proposes $S_t(T)$ to be broken down into multiple target spectra, each one developed according to a relevant M-R scenario and to the portion of T_R where the scenario is most influent. Ground motion prediction equations can be used to generate spectral shapes for specific scenarios, and mean spectral ordinate predictions can be used to build the target spectra. When Method B is chosen, attention must be paid so that the envelope of all target spectra remains above 75% of the uniform hazard spectrum (UHS) over the entire period range T_R. In addition, linear scaling of the individual target spectra should be performed so that $S_t(T)$ matches or exceeds the UHS over the individual scenario period range. In general, Method B provides more thorough representation of the seismic demand imposed by natural earthquakes at given periods (Tremblay et al., 2015). In both methods, at locations where significant contribution to the seismic hazard arises from multiple sources of ground motions, the number of scenarios established should individually address all earthquake types or fault mechanisms that influence the seismic hazard. Example of such locations are those of western Canada, more specifically in the southwest part of British Columbia, where the seismic hazard is composed by three different types of earthquakes: crustal, in-slab (or sub-crustal) and interface (or subduction) earthquakes (Tremblay et al., 2015).

To ease the comparison between the spectral acceleration of the earthquake records and the UHS given the peaks at shorter periods typically present in the response of natural earthquakes, the NBC 2015 prescribes that the plateau in the UHS, defined between the periods of zero and 0.2 s, can be replaced by discrete values of pseudo-acceleration at 0 s (Peak Ground Acceleration (PGA)), 0.05 s, 0.1 s, and 0.3 s, adjusted according to the soil type.

There are no explicit guidelines on how to determine the dominant M-R scenarios of a site's seismic hazard in the NBC 2015. Typically, the process involves examining deaggregations of the seismic hazard at periods within T_R. Seismic hazard deaggregations for the city of Vancouver – BC corresponding to the seismic hazard with probability of exceedance of 2% in 50 years are provided in Figure 2-32 for short and long periods (0.2 s, 0.5 s, 1.0 s, and 5.0 s). Once the relevant M-R scenarios are established, the search for suitable earthquake records should consider an acceptable magnitude and distance ranges. Note that magnitude and distance in the UHS from the NBC 2015 are measured using moment magnitudes and hypocentral distances (distance from the site to the point in the rock where the energy is first released), respectively, and the pseudo-acceleration spectrum considers 5% damping. As a consequence, adjustments to the data retrieved from seismic hazard deaggregations could be necessary prior to the selection of ground motions records to ensure compatibility.

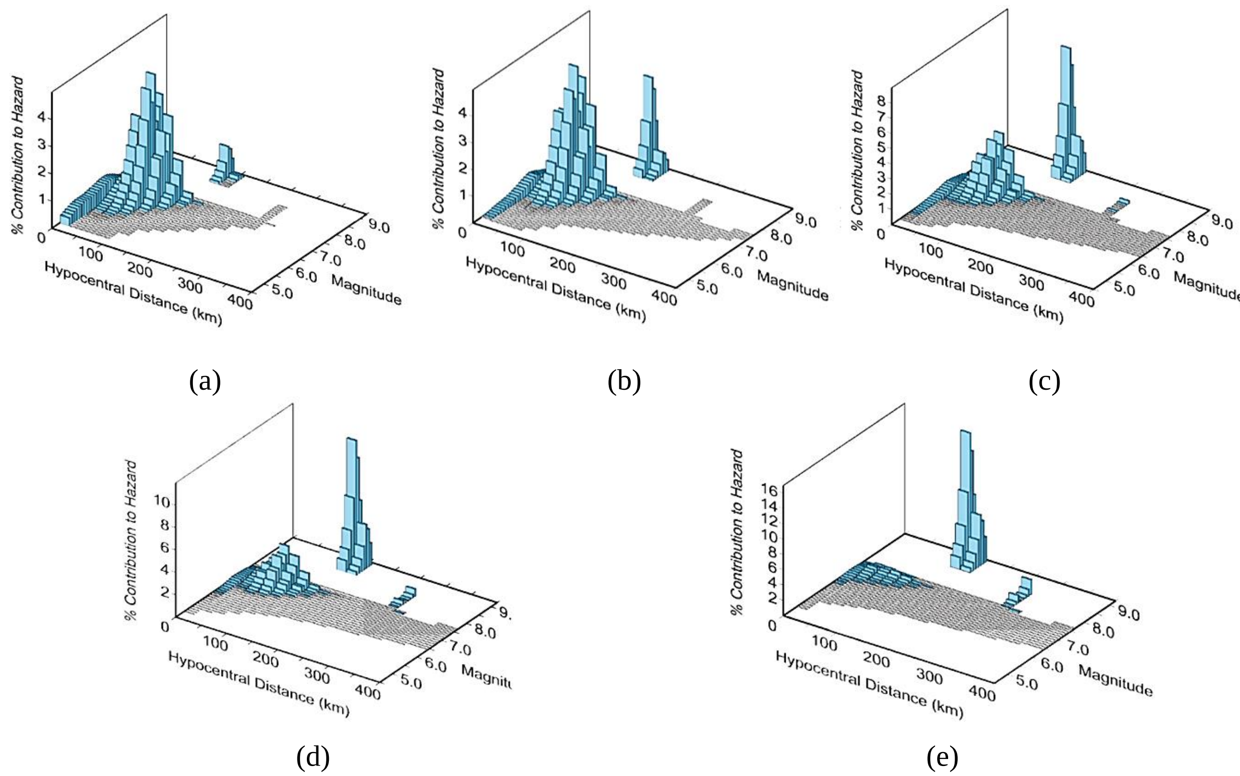

Figure 2-32 - Seismic hazard deaggregations for Vancouver – BC associated to (a) 0.2 s, (b) 0.5 s, (c) 1.0 s, (d) 2.0 s and (e) 5.0 s (Tremblay et al., 2015).

Several databases can be accessed as a resource for the selection of ground motion records. For North America, the Pacific Earthquake Engineering Research (PEER) Center provides two databases of historical earthquake records that fit the main seismic zones of Canada. The NGA-West2 (Ancheta et al., 2013) can be used to search for shallow crustal earthquake records, whereas the NGA-East (Goulet et al., 2014) contains stable continental earthquake records.

Spectral matching techniques can be used to provide a better match between the target spectrum and historical records over a determined period range (Atkinson, 2009). As the process permits the use of natural earthquake records, more realistic information regarding seismological characteristics, such as phasing, will be available for the analysis. Conversely, it is argued that spectral matching might soften the effects of earthquakes as it artificially smooths out peaks and troughs present in real records (Tremblay et al., 2015). As an alternative, ground motion records can be generated by simulation of the desired seismic characteristics, such as frequency content and duration, as it was done by Atkinson (2009). Atkinson applied the stochastic finite-fault method to generate earthquake time histories that match the UHS from the NBC for a range of Canadian sites, which can be useful for various applications. The database provided by Atkinson (2009) includes records of magnitude of 9, which simulate megathrust events on the Cascadia subduction zone at distances of 100-200 km in western Canada. Atkinson states that subduction records may be significant for the response of long-period structures (1.0 to 5.0 s), as they have long durations and rich energy content at long periods (due to the attenuation of the higher frequencies by the larger distances). To match target spectra representative of eastern Canada, Atkinson (2009) advises that the lower magnitude records (magnitude 6) provided in the catalog be used within the period range of 0.5 to 0.1 s (plus PGA). In contrast, the higher magnitude records (magnitude 7) should be used to match the 0.5 to 2.0 s period range of $S_t(T)$.

Simulated ground motion records provided by Atkinson (2009), and the NGA-West2 (Ancheta et al., 2013) and the NGA-East (Goulet et al., 2014) databases are given in moment magnitude and closest distance to fault plane, and the response spectra are 5% damped. Although the NBC 2015 states that historical earthquake records are preferred for time-history analysis, the use of simulated records can ensure efficiency and flexibility to the analysis, becoming appealing when natural records of a particular site are unavailable.

When time-history analysis is used for design, an ensemble containing at least eleven ground motion records is suggested by the NBC 2015. In addition, at least five records should be selected for each scenario. However, when multiple scenarios represent distinct tectonic sources of seismic activity, a suite of not less than eleven records should be used for each source. When possible, no more than two records from the same earthquake event should be used.

Once several records are pre-selected, scaling of the corresponding acceleration response spectra should be performed in two stages. The NBC 2015 does not define specifically how the scaling should be performed. Atkinson (2009) orients that the ratio of the target spectral amplitude $S_t(T)$ to the spectral amplitude of the ground motion record $S_g(T)$ should be calculated over the desired period range. Thereafter, the mean and the standard deviation of the computed ratio of each candidate record should be calculated over the period range. Atkinson (2009) suggests that records with mean varying from 0.5 to 2.0 be preferred, whereas Tremblay et al. (2015) suggests the upper limit can be extended to 5.0 in cases where historical records exhibit significant variability in shape. Among that, the best records will be those with the lowest standard deviation. The mean of $S_t(T)/S_g(T)$ can then serve as a scaling factor for the selected record, used to satisfy the NBC 2015 requirement that the selected response spectra on average equals or exceeds of $S_T(T)$ over the defined period range. Another method to scale the ground motion records is the Mean Square Error (MSE), which minimizes the error between the spectral acceleration of the record and the target spectrum (Abraik and Youssef, 2016). However, the NBC 2015 recommends the use of linear methods of scaling in order to preserve the signature and frequency distribution of energy of the ground motion record. A second round of scaling, applied to all records in a suite, might be necessary to ensure the mean response spectrum of the suite does not have any point below 10% of $S_t(T)$ over the appropriate scenario-specific period range.

In a design process, the structure is ultimately subjected to the selected and scaled ground motion records separately. Every parameter of interest of the seismic response of the structure, such as drifts and forces, must be determined as the mean of the results obtained in each analysis. When multi-suite ground motion ensembles are employed but at least one of the suites contains less than 11 records, the NBC 2015 recommends that the mean of the n highest values be used, where n is the average number of records in all suites. Other recommendations indicate the use of the mean plus one standard deviation value or the 84th or 90th percentile values, therefore pursuing higher percentiles of the response in order to mitigate the effect in the mean response of potential lower demand arising from some of the records (Tremblay et al., 2015). Tremblay et al. (2015) state that the acceptance criteria for multi-suite ground motion ensembles remains open for research work, and more detailed guidelines should be adopted by the NBC in the future.

Due to the lack of reliable historical records, researchers typically select artificial records to conduct time-history analyses of structures in eastern Canada. To name a few, Luu et al. (2013) and Abraik and Youssef (2017) used artificial records developed for eastern North America in their dynamic analyses. To analyze structures in the West, Abraik and Youssef (2016) are examples of researchers who utilized historical earthquake records, which were scaled based on the mean squared error (MSE) method. Alam et al. (2012) included one simulated record in a suite containing nine other historical records representative of western Canada, which were scaled according to the fundamental period from the effective stiffness of the structures.

3. DESIGN OF SHEAR WALLS

In this chapter, the design of the reinforced concrete shear walls, which act as the vertical component of the Seismic Force-Resisting System (SFRS) for the building under investigation, will be presented. The design procedure initiated with the determination of the seismic forces acting on the building following the provisions of the 2015 edition of the National Building Code of Canada (NRC, 2015). Dynamic analysis based on 3-D models of the building were used to determine the seismic forces in the two design locations, corresponding to Vancouver, BC and Montreal, QC. Thereafter, the design of the steel-reinforced shear walls for flexural and shear demands was completed according to the provisions of the Canadian Standards Association Standard A23.3-14, Design of Concrete Structures (CSA, 2014) provisions. The main features of the design of reinforced concrete shear walls in the CSA A23.3-14 were presented in Section 2.3. Ultimately, the design adopted for the hybrid SMA-steel reinforced concrete shear walls is presented and justified, along with the material properties considered for the Ni-Ti SMA reinforcing bars.

3.1 Seismic demands and design

Figure 3-1 illustrates the prototype building investigated in this thesis. The building has a typical floor plan of 42 m × 36 m, a 3.5 m-high first storey, and nine 3.0 m-high storeys from level 2 to 10. Lateral resistance to earthquakes is provided by four rectangular RC shear walls in each orthogonal direction. The floor plan and arrangement of the walls led to larger torsional effects in one principal direction. Thus, a typical shear wall was designed for the critical direction and adopted for the other walls. The shear walls were designed as the seismic force-resisting system of the building. The columns were considered part of the gravity-load-carrying system, and not to experience inelastic response when subjected to the seismic displacements. Thus, the response of the columns was assumed to be force-controlled. The flat slabs in the building have thickness of 225 mm. The selection of this building configuration was intended to provide a prototype structure to understand the performance of SMA-reinforced elements in full-scale structures as a first study. The building provides a simplified SFRS layout such that the SFRS is easily identified. Future studies will investigate other building configurations and SFRS.

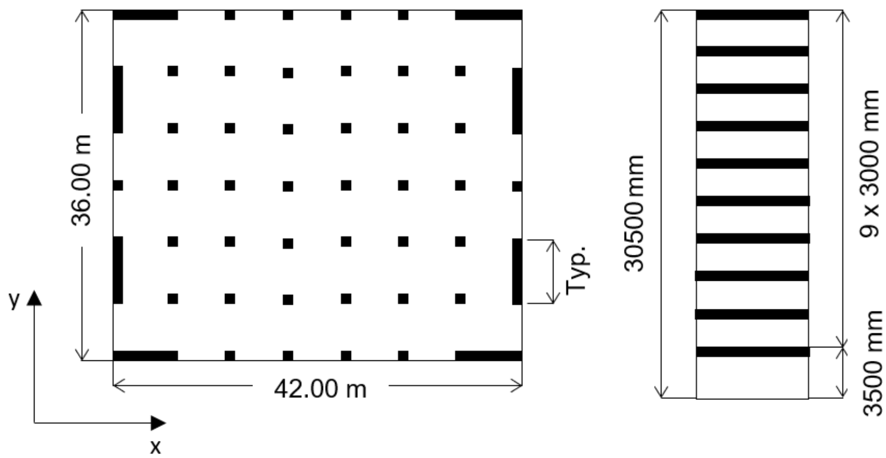

Figure 3-1 - Plan view and wall elevation of the building under investigation

The building in Figure 3-1 was initially assumed to be regular for design purposes. According to the structural irregularities specified in the NBC 2015, the building does not present an in-plane discontinuity of the vertical SFRS, out-of-plane offsets, or non-orthogonality between SFRS components. Moreover, vertical geometric irregularities were avoided in the SFRS by the adoption of constant wall dimensions among every storey. Further verification of structural irregularities are presented following the detailed design of the walls, which will confirm that the building under study is structurally regular.

To verify the fundamental period of the structure and carry out the design process, a 3-D model of the building was developed using the structural analysis program SAP2000® (CSI, 2016). Figure 3-2 illustrates the 3-D model of the building. The seismic weight and the hazard spectrum corresponding to each design location were input in the program, generating one model for each design location. In the models, the slabs were modelled as rigid diaphragms. The seismic weight of each storey was lumped to the storey level. Therefore, the slabs contained the centre of mass and the corresponding inertial forces generated by the ground acceleration. Thus, it was assumed that the seismic forces would be fully transmitted by the slabs to the vertical components of the SFRS, i.e. the shear walls. In SAP2000®, the shear walls were modelled as membrane finite elements. Columns were pinned at the base in order to prevent them from engaging in the response to the earthquake loads. Although the building under study satisfied the requirements for the use of the equivalent static procedure prescribed by the NBC 2015, dynamic analysis was preferred as it permits a more accurate consideration of the effects of the seismic loading, including torsional effects. The models were thus subjected to dynamic modal response spectrum analysis in SAP2000® to determine the seismic force demands and the resulting displacements of the structure.

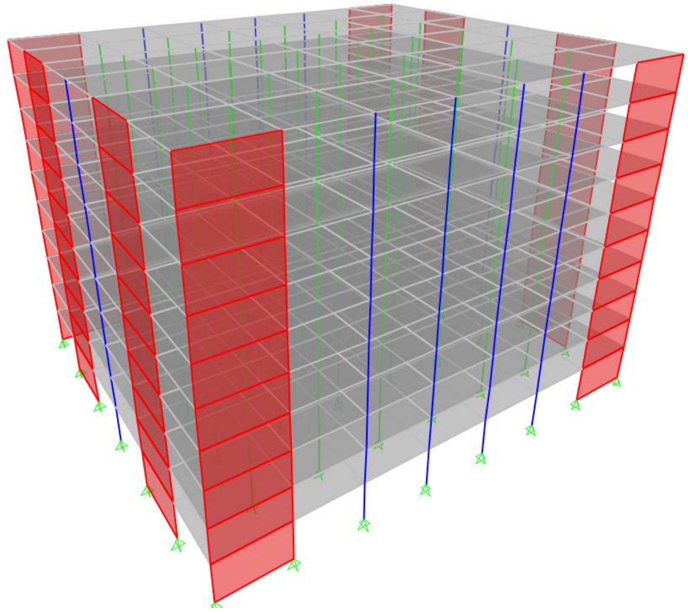

Figure 3-2 - 3-D model of the building developed with SAP2000® (CSI, 2016)

Table 3-1 lists the gravity loads acting on the building at each design location, which were used to determine the seismic weight (W) of the building according to Equation 2-4. The storey W for levels 1 to 9 in both directions was equal to 11019 kN, while the storey W for level 10 was calculated as 10130 kN for Vancouver and as 10444 kN for Montreal. The variation of mass among consecutive storeys was smaller than 150% in all cases, therefore the buildings did not present mass irregularity. The gravity loads were uniformly distributed as area loads on the slabs. To avoid duplication of the self-weight of the structure, all materials were assigned a density equal to zero. The program was set to convert the applied loads into masses and to use them as the mass source for dynamic analysis, which resulted in a total of 590 modes of vibration in the model.

Table 3-1 - Gravity loads acting on the building

	Dead Loads	(kPa)	Companion loads	(kPa)
Roof	Slab (225 mm-thick)	5.29	Live load (roof)	1.00
	Mechanical, ceilings and electrical (MCE)	1.00	Snow load (Vancouver)	1.64
			Snow load (Montreal)	2.48
Storeys	Partitions	1.00	Live load (office)	2.40
	Slab (225 mm-thick)	5.29		
	Mechanical, ceilings and electrical (MCE)	1.00		

In this study, the design locations were selected to be representative of seismic zones in western and eastern Canada, as Vancouver, BC and Montreal, QC, respectively. The building was assumed to be located on firm ground, corresponding to Site Class C in the NBC 2015. Based on this Site Class, the response spectra were defined for each location and presented in Figure 3-3. The design PGA corresponds to 0.369 g and 0.379 g, respectively for Vancouver and Montreal.

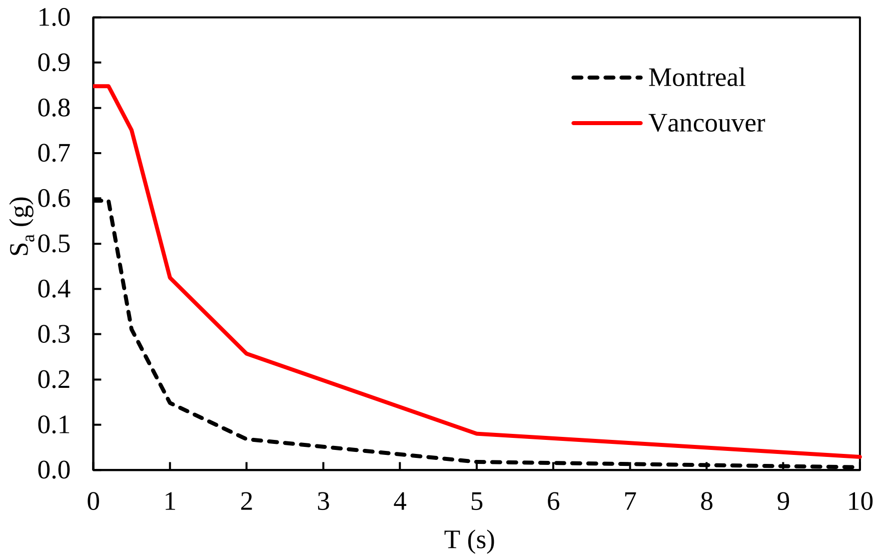

Figure 3-3 - Pseudo-acceleration response spectra of the design locations for Site Class C

To conduct dynamic modal response spectrum analysis, the seismic coefficients from the NBC 2015 were used as input to define a response spectrum function in SAP2000®. This function was assigned to a Response Spectrum Analysis (RSA) load case for each principal orthogonal direction. Modal analysis indicated that 73 modes should be considered for the response of the RSA in order to accumulate for 95% of modal mass participation at each degree of freedom (x and y), as required by the NBC 2015. All shear walls were considered to be cracked for the dynamic analysis, with degraded stiffness determined by the application of stiffness reducing factors equal to 0.5 for the ductile walls, defined according to Equation 2-6 for the building in Vancouver, and to 0.7 for the moderately ductile walls used in the building in Montreal.

Initially, the analyses were run with the models restrained to move in one in-plan direction. In this configuration, independent x and y modal analyses were conducted to capture the modal periods of vibration of the structure. Figure 3-4 (a) depicts the model of the building after the application of the RSA function in the x-direction, with the structure restricted to move in the y-direction, and the shape resulting from analysis along the y-direction Figure 3-4 (b), with the structure restrained in the x-direction. The fundamental period and base shear obtained from the dynamic analyses are listed in Table 3-2 and Table 3-3. These values were assessed against the values calculated using the code equations. The governing base shear used for design, as well as the resulting scaling factors to be applied to the output forces and displacements from dynamic analysis, calculated according to Equation 2-7, are also presented in Table 3-2 and Table 3-3.

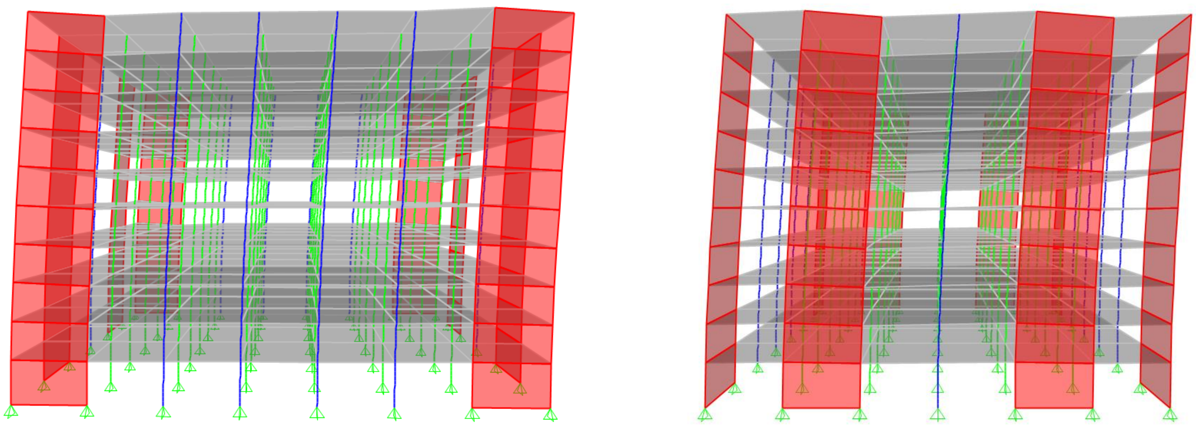

(a) (b)

Figure 3-4 - Deformed shape of building resulting from response spectrum analysis restricted in the (a) y-direction and (b) x-direction

Table 3-2 - Results from restrained analyses of Vancouver building along X and Y direction

Parameter	X direction		Y direction	
I_E	1.00		1.00	
W	109295 kN		109295 kN	
R_d	3.5		3.5	
R_o	1.6		1.6	
V_{el}	40942 kN		40942 kN	
$V_{st} = V_{el} / R_d R_o$	7311 kN		7311 kN	
V_{min} for T = 4.0 s	2713 kN		2713 kN	
$V_{max} = 2/3\ V_{max}\ (T = 0.2\ s)$	11034 kN		11034 kN	
Requirements for	Strength	Drift	Strength	Drift
T_a	0.649 s	0.649 s	0.649 s	0.649 s
T_{lim}	1.30 s	4.00 s	1.30 s	4.00 s
T_{RSA}	1.946 s	1.946 s	1.947 s	1.947 s
T that governs	1.30 s	1.95 s	1.30 s	1.95 s
$0.8 \times V_{st}$	5849 kN	3963 kN	5849 kN	2170 kN
$V_{RSA} / R_d R_o$	4967 kN	4967 kN	4961 kN	4961 kN
V_d	5849 kN	4967 kN	5849 kN	4961 kN
Scale factor (V_d/V_{RSA})	1.178	1.000	1.179	1.000

Table 3-3 - Results from restrained analyses of Montreal building along X and Y direction

Parameter	X direction		Y direction	
I_E	1.00		1.00	
W	109612 kN		109612 kN	
R_d	2.00		2.00	
R_o	1.40		1.40	
V_{el}	14117 kN		14117 kN	
$V_{st} = V_{el} / R_dR_o$	5042 kN		5042 kN	
V_{min} for T = 4.0 s	1408 kN		1408 kN	
$V_{max} = 2/3\ V_{max}\ (T = 0.2\ s)$	16106 kN		16106 kN	
Requirements for	Strength	Drift	Strength	Drift
T_a	0.649 s	0.649 s	0.649 s	0.649 s
T_{lim}	1.30 s	4.00 s	1.30 s	4.00 s
T_{RSA}	1.96 s	1.96 s	1.96 s	1.96 s
T that governs	1.30 s	1.96 s	1.30 s	1.96 s
$0.8 \times V_{st}$	4033 kN	2313 kN	4033 kN	2313 kN
V_{RSA} / R_dR_o	4560 kN	4560 kN	4551 kN	4551 kN
V_d	4560 kN	4560 kN	4551 kN	4551 kN
Scale factor (V_d / V_{RSA})	1.00	1.00	1.00	1.00

The code upper limit for the fundamental period of the structure, equal to $T = 2 \times T_a = 1.3\ s$, governed in Vancouver, as modal analysis indicated a fundamental period equal to 1.95 s. Although the base shear obtained from the analysis (V_{RSA}) corresponded to 68% of the static base shear V_{st}, it could not be taken as lower than 80% of V_{st} as per the NBC 2015. As a result, every analysis result used for the design of elements for strength requirements had to be amplified by a factor of 1.18. Conversely, resulting displacements did not require scaling due to the relaxed upper limit of 4.0 s allowed for displacement requirements. In the case of Montreal, the upper limit of $T = 1.3\ s$ governed the period and V_{RSA} was found to be equal to 90.4% of V_{st}. Thus, scale factors were not required for the analysis of the building in Montreal.

Subsequently, the models were unrestrained and subjected to the RSA load case amplified by the respective scale factors (1.18 in Vancouver and 1.0 in Montreal), applied independently in each direction. To introduce torsion to the analysis, the seismic forces in this load case were applied considering 10% eccentricity regarding the centre of rigidity of each storey level, as illustrated in Figure 3-5. Maximum and minimum lateral displacements (Δ) at each storey level were recorded and the average displacements were calculated. It was then possible to evaluate the torsional sensitivity by calculating the B factor. Lateral displacements and values of B_x in the x and y direction are listed in Table A-1 in Appendix A. Values of B_x did not exceed 1.08 and 1.12, respectively, in both design locations. As the B factor did not surpass the code limit of 1.7, the building was deemed structurally regular, permitting the eccentricity to be reduced to 5%.

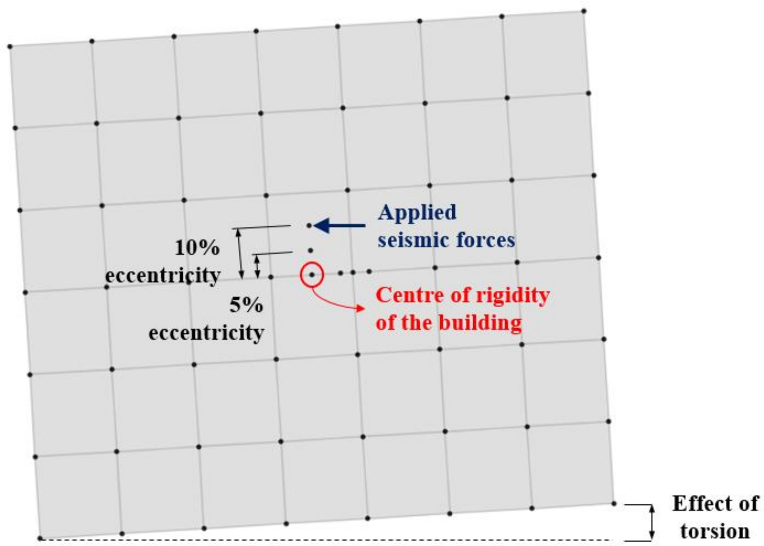

Figure 3-5 - Schematic plan view of the consideration of torsion in the 3-D analysis of the building

In order to take advantage of the relaxed period allowed by the NBC 2015 for displacement requirements, the model was run considering the reduced eccentricity and the unscaled RSA load case. The resulting displacements and storey shear forces were used to check the stability coefficient θ, according to Equation 2-5, and the limit of 2.5% for the interstorey drifts (δ_i). Table A-2, in Appendix A, presents the results from this analysis, as well as the calculated values of θ and δ_i. The maximum stability coefficient recorded was equal to 0.23 in Vancouver and to 0.09 in Montreal. Both values are within the code limit of 0.4. Since θ was smaller than 0.1, the *P-Δ* effects were neglected for the building in Montreal, whereas the lateral forces were amplified by the factor $\theta +1$ for the building in Vancouver at the storey levels where $\theta >0.1$. In terms of δ_i, level 10 corresponded to the largest interstorey drift in both design locations, which was equal to 2.05% for the building in Vancouver and to 0.83% for the building in Montreal, while the lateral drift corresponding to the total height of the buildings was equal to 1.5% and 0.6% for the buildings in Vancouver and Montreal, respectively. A final analysis was conducted considering the scaled RSA load case and the eccentricity of 5%, which provided the design shear forces used to design elements for strength. Table 3-4 presents the design shear forces for the shear walls in each design location.

Table 3-4 - Design shear forces and moments in shear wall

	Vancouver		Montreal	
Level	X direction V_{d-i} (kN)	Y direction V_{d-i} (kN)	X direction V_{d-i} (kN)	Y direction V_{d-i} (kN)
10	407	412	339	377
9	646	654	439	473
8	748	757	453	487
7	803	813	496	528
6	880	892	506	538
5	994	1008	544	579
4	1138	1154	694	730
3	1301	1320	890	928
2	1417	1437	1057	1094
1	1549	1571	1202	1227
Overturning moment at the base	30361 kNm	30777 kNm	20224 kNm	21258 kNm

3.2 Flexural design of steel-reinforced concrete shear walls

The flexural demand for the design of the shear walls corresponds to the overturning moments provided in Table 3-4, which were determined from the dynamic analyses with the earthquake load combination and the axial loads from the tributary area of the walls calculated according to Table 3-1. Due to the in-plan distribution of the walls in the building, the walls in the y-direction were more sensitive to torsion, and consequently the demand was found to be greater in this direction. In each design location, the design was therefore performed for a typical wall in the y-direction and adopted for all eight walls. With that, the demand corresponded to an overturning moment of 30780 kNm and an axial load of 4340 kN for the wall in the building located in Vancouver, and to an overturning moment of 21260 kNm and an axial load of 4380 kN for the wall in the building located in Montreal. Considering the level of demand and the common practice in each design location, a conventional, steel-reinforced ductile shear wall was adopted for the design location of Vancouver, BC, named Wall DSRW (Ductile Steel-Reinforced Wall), whereas a moderately ductile type of wall was selected for the design location of Montreal, QC, referred to as Wall MDSRW (Moderately Ductile Steel-Reinforced Wall). The mechanical properties adopted in design and modelling of the shear walls are listed in Table 3-5. The properties correspond to typical properties for the steel and concrete and were selected to match the walls previously tested and modelled by Abdulridha and Palermo (2017) and Maciel et al. (2016). Results from these studies were used to validate the numerical analysis in this thesis.

Table 3-5 - Mechanical properties of concrete and steel

Material property	Value
Compressive concrete strength (f'_c)	30 MPa
Modulus of elasticity of concrete (E_c)	24647.5 MPa
Concrete specific weight (γ_c)	23.5 kN/m^3
Factor to account for low-density concrete (λ)	1.0
Concrete Poisson's ratio (ν)	0.2
Yielding strength of steel (f_y)	400 MPa
Ultimate strength of steel (f_u)	600 MPa
Modulus of elasticity of steel (E_s)	200000 MPa
Strain hardening strain of 10M steel bars (ε_{sh})	1%
Ultimate strain of 10M steel bars (ε_{su})	8%
Strain hardening strain of 15M and 25M steel bars (ε_{sh})	2%
Ultimate strain of 15M and 25M steel bars (ε_{su})	12%

Although the concrete design standard A23.3-14 permits reducing the wall thickness and the reinforcement ratio above the plastic hinge region of the walls, the cross-section at the base of the walls were extended to the other storey levels. Following this approach, irregularities in vertical stiffness were avoided and the correlation between the response of the walls and the presence of SMA was simplified. The plastic hinge was expected to form at the base of the walls and to extend over a height of 6.05 m according to Equation 2-8.

Details of Wall DSRW are illustrated in Figure 3-6 (b) and Figure 3-7 (b). The minimum thickness required for Wall DSRW was 350 mm, according to Equation 2-9. To develop the desired rotational capacity in Wall DSRW, concentrated reinforcement was provided along a distance equal to 500 mm from the edges of the wall; this distance was determined according to Equation 2-15. The concentrated reinforcement was tied with confinement reinforcement, permitting the ultimate concrete strain (ε_{cu}) at crushing to be taken as 0.006. In each of these boundary regions, sixteen-25M (25.2 mm diameter) bars were specified as longitudinal reinforcement, resulting in a reinforcement ratio of 4.6%. Ties were specified as three sets of 10M (11.3 mm diameter) closed stirrups spaced vertically at 140 mm. In the web zone of the wall, vertical distributed reinforcement consisted of 15M (16 mm diameter) bars spaced at 230 mm, resulting in a longitudinal reinforcement ratio (ρ_l) of 0.5%. The ratio of distributed horizontal reinforcement (ρ_t) was selected as the minimum requirement of 0.25% (from Equation 2-10) in both Walls DSRW and MDSRW. All distributed reinforcement was arranged in two layers in both walls.

Final design of Wall MDSRW can be observed in Figure 3-6 (a) and Figure 3-7 (a). For this wall, the minimum thickness was 250 mm. Although increased concrete strain capacity was not required to develop sufficient rotational capacity, the length of the boundary zones was maintained at 500 mm to aid comparison of the walls. Distributed vertical reinforcement was prescribed as 15M bars spaced at 400 mm, resulting in a ratio ρ_l of 0.4%. Ten-25M bars were used as longitudinal reinforcement in the boundary zones, resulting in a reinforcement ratio of 4%. The latter was tied with two sets of 10M closed stirrups spaced vertically at 125 mm.

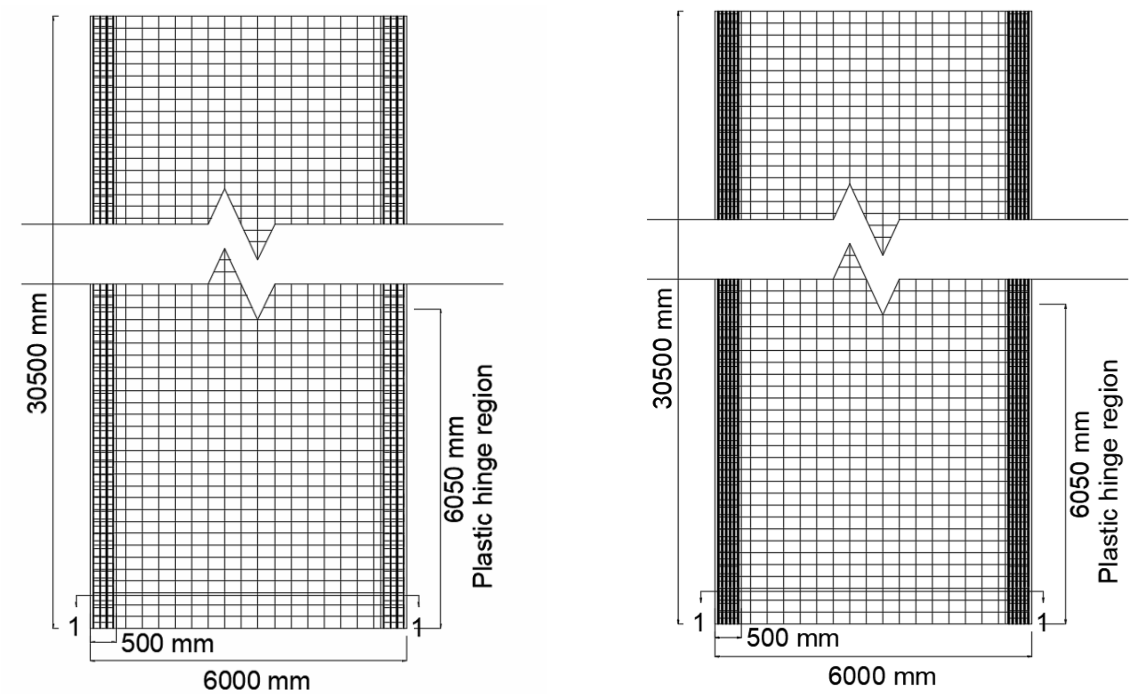

(a) (b)

Figure 3-6 - Elevation of steel-reinforced concrete shear walls: (a) Wall MDSRW and (b) Wall DSRW

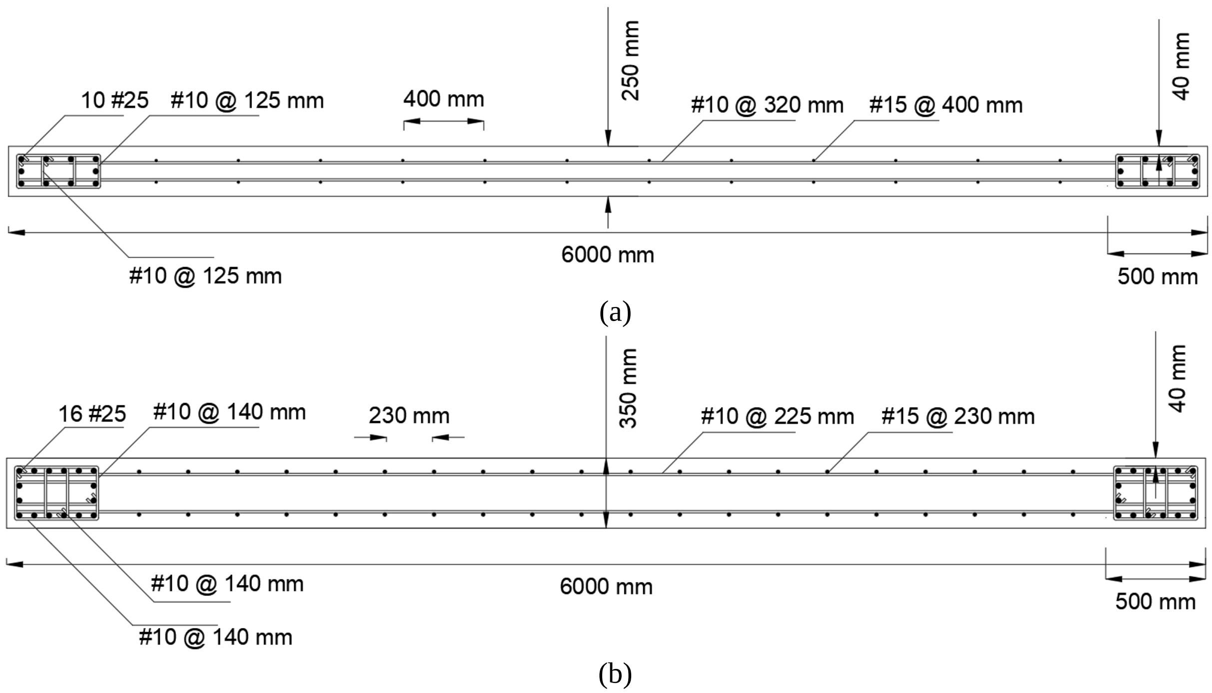

Figure 3-7 - Section 1-1 of steel-reinforced concrete shear walls: (a) Wall MDSRW and (b) Wall DSRW

The demand considered for the design process required the use vertical distributed reinforcement in walls DSRW and MDSRW in a ratio equal to 0.38% and 0.2%, respectively. However, sensitivity analysis (presented in subsequent chapters) illustrated that the response of the hybrid walls, with cross-sections defined following the final design of the conventional steel-reinforced walls, is highly influenced by the quantity of ρ_l in the web zone. Therefore, in order to ensure stability of the analysis and adequate simulation of the behaviour of the walls at late stages of loading, ρ_l was increased to 0.5% and 0.4% in Walls DSRW and MDSRW, respectively.

To check the resistance against the combined effects of bending and axial load, cross-sectional analysis was conducted using the sectional analysis program Response2000© (Bentz and Collins, 2001). Moment interaction diagrams were generated for each wall to assess the critical load combinations against the envelopes of resistance provided by the designed cross-sections. The moment interaction diagrams are depicted in Figure 3-8 (a) for Wall DSRW and Figure 3-8 (b) Wall MDSRW. Sectional analysis was also used to determine the nominal and probable moment resistances of the walls, as well as the depth of the compression zone (*c*). With the values of *c*, the final check of the rotational capacity of the walls was performed. Using Equation 2-13, the rotational demand was found to be equal to 0.012 in Wall DSRW, whereas the rotational capacity was calculated as 0.013 using Equation 2-14. For Wall MDSRW, the rotational demand and rotational capacity were found to be equal to 0.004 and 0.005, respectively. Hence, the design of the walls provided sufficient rotational capacity to overcome the rotational demand and to allow the expected ductility of the walls to be developed.

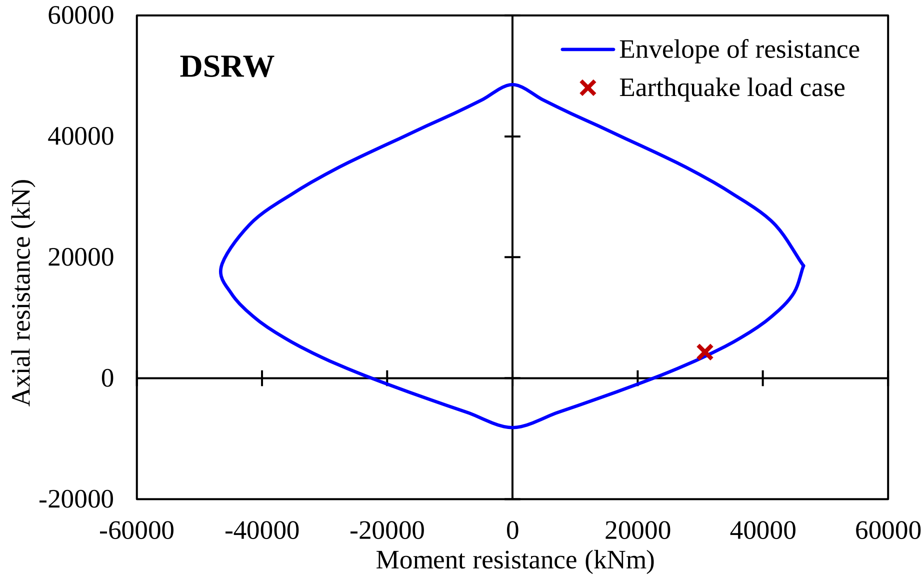

(a)

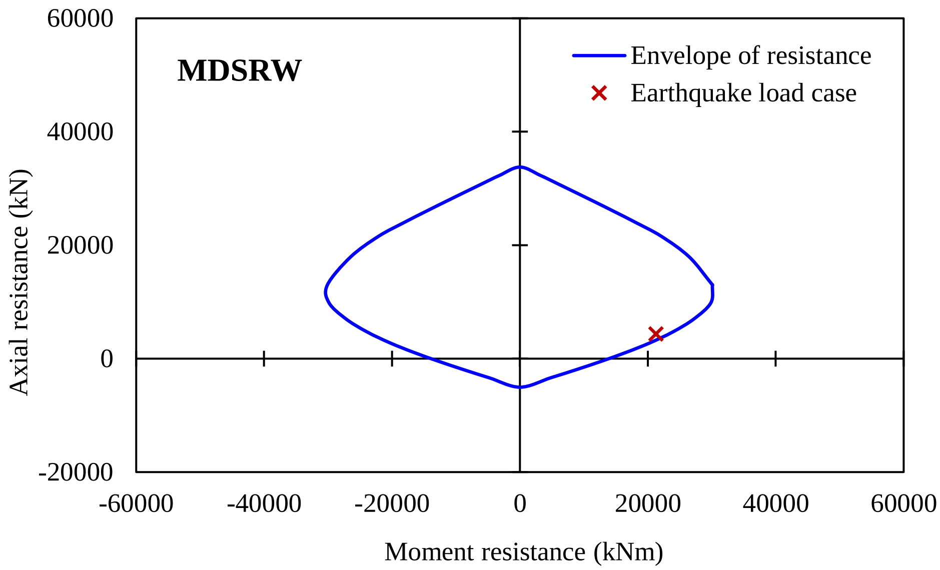

(b)

Figure 3-8 - Moment interaction diagrams from sectional analysis on Response2000© (Bentz and Collins, 2001): (a) Wall DSRW and (b) Wall MDSRW

3.3 Shear design of steel-reinforced concrete shear walls

The shear demand on the walls was determined using response spectrum analysis on SAP2000® (CSI, 2016). Resulting shear forces are listed in Table 3-4. The greater value of base shear corresponded to the y-direction. To account for the increase in the demand due to the development of inelasticity in the fuse elements (the plastic hinge at the wall base), the shear demand was amplified by the factor for flexural overstrength, calculated as the ratio of the probable moment capacity to the factored bending moment at the base of the wall. A second scaling factor was applied subsequently to account for inelastic effects associated with higher modes of vibration of the structure. For Wall DSRW, the base shear was equal to 1570 kN, and the mentioned factors resulted in 1.40 and 1.15, respectively. Thus, final base shear in Wall DSRW was computed as equal to 2540 kN.

As discussed in Section 2.3.4, the shear resistance of concrete shear walls was calculated based on the existing axial load (4340 kN), which led to a θ of 45° in Wall DSRW, and on the inelastic rotational demand of the wall (0.013), resulting in a β of 0.05. Using these parameters, it was found that the minimum distributed horizontal reinforcement of 0.25% provided a shear resistance of 2900 kN in Wall DSRW, which was sufficient to resist the shear demand through the height of the wall, since the maximum shear occurred at the base of the wall.

For Wall MDSRW, the design base shear was determined as 1280 kN. The factor for flexural overstrength of moderately ductile shear walls was calculated as the ratio of the nominal moment capacity to the factored bending moment, which resulted in a factor equal to 1.26. The amplification factor due to inelastic effects on higher modes was computed as 1.07. Hence, the base shear was magnified to 1730 kN. In order to calculate the shear resistance of the wall, θ was taken as 45° due to the axial load acting at the base of the wall (4380 kN), and β was taken as equal to the upper value of 0.18 due to the inelastic rotational demand on the wall (0.005). Shear resistance of Wall MDSRW was therefore estimated as 2040 kN. The minimum distributed horizontal reinforcement of 0.25% provided a shear resistance that was greater than the calculated shear demand.

3.4 Design of hybrid SMA-Steel RC shear walls

A hybrid ductile wall was defined for Vancouver, which will be referred to as Wall DHW (Ductile Hybrid Wall), whereas a hybrid moderately ductile wall was defined for Montreal and will be named Wall MDHW (Moderately Ductile Hybrid Wall). For the hybrid walls, comparable dimensions and reinforcement details were adopted, with the exception of the deformed-steel longitudinal reinforcement in the plastic hinge zone within the boundaries of the walls, which was replaced by Ni-Ti superelastic SMA bars with diameter similar to the longitudinal reinforcement in the steel-reinforced walls. The SMA bars were connected to steel bars above the plastic hinge region through mechanical couplers, which were modelled as stiff reinforcing elements. The remaining reinforcement details were consistent with that of the steel-reinforced walls. Details of the hybrid walls are illustrated in Figure 3-9 and Figure 3-10. The mechanical properties of Ni-Ti SMA considered in this thesis are listed in Table 3-6. The stress and strain values correspond to that employed in the numerical simulations of the benchmark study (Abdulridha and Palermo, 2017), with the exception of the ultimate values, which were not properly captured in the coupon test performed by Abdulridha and Palermo (2017). The ultimate stress and strain values of the 25.4 mm Ni-Ti SMA bars were defined assuming similar properties to that obtained by Cortés-Puentes and Palermo (2018) through tension testing of Ni-Ti superelastic SMA rods of 12.7 mm in diameter.

Table 3-6 - Mechanical properties of Ni-Ti SMA

Material property	Value
Bar diameter	25.4 mm
Strain hardening strain (ε_{sh})	6%
Ultimate strain (ε_{su})	20%
Yielding strength (f_y)	400 MPa
Ultimate strength (f_u)	1000 MPa
Modulus of elasticity (E_{SMA})	38000 MPa

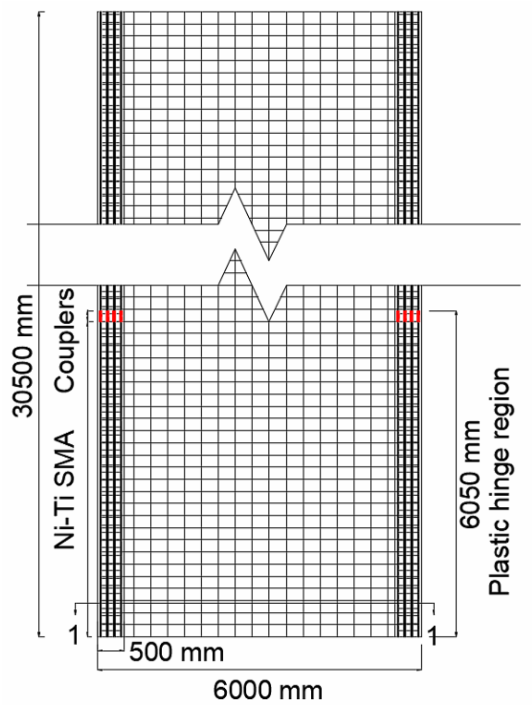

(a)

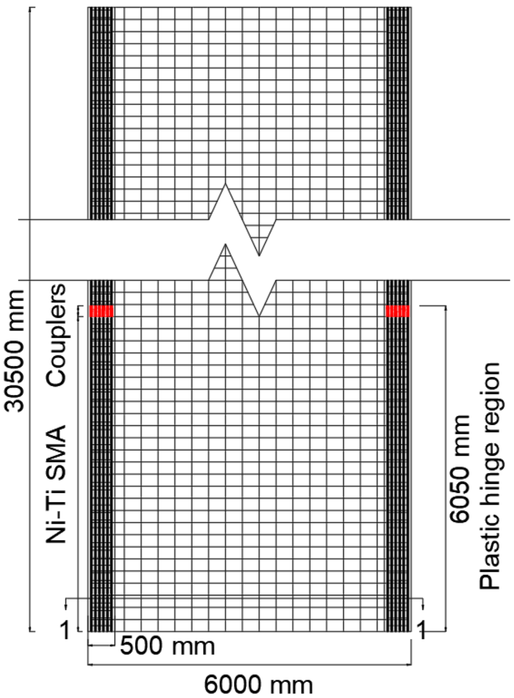

(b)

Figure 3-9 - Elevation of hybrid SMA-steel reinforced concrete shear walls: (a) Wall MDHW and (b) Wall DHW

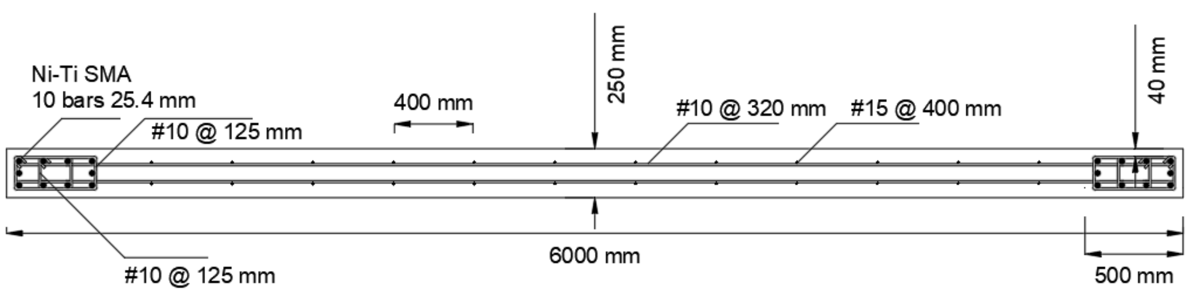

(a)

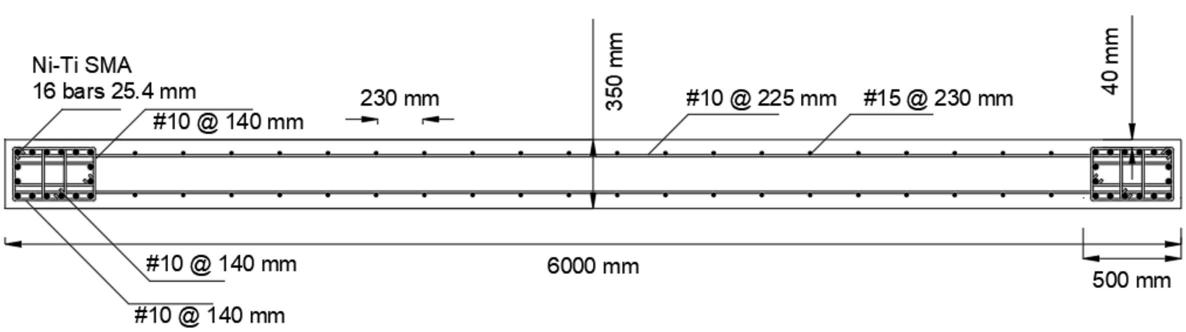

(b)

Figure 3-10 - Section 1-1 of hybrid SMA-steel reinforced concrete shear walls: (a) Wall MDHW and (b) Wall DHW

4. NUMERICAL ANALYSIS

This chapter presents the methodology of the numerical analyses conducted in this thesis. For the numerical analyses, the designed walls were modelled as full-scale 2-D finite element models in the preprocessor FormWorks. The analysis results were obtained from the post-processor Augustus. [Note that programs FormWorks and Augusts are part of the VecTor2 software package (Vecchio et al., 2013)]. The walls were initially subjected to pushover and reverse cyclic analyses at multiples of the yield displacement. The static nonlinear analyses were performed to determine the lateral capacity, failure mechanism, residual drifts, recentering, and energy dissipation of the walls. Thereafter, time history analyses were carried out to evaluate the seismic performance of the different types of walls in terms of peak interstorey drift, peak roof drift, permanent interstorey drift, and permanent roof drift.

The static analyses were validated against numerical results from a previous numerical study (Maciel et al., 2016), which investigated the effect of varying axial load ratio on slender hybrid SMA-steel and conventional steel reinforced concrete shear walls, previously tested by Abdulridha and Palermo (2017). The walls in this study are comparable with the walls tested by Abdulridha and Palermo given the adopted arrangement of SMA bars (Ni-Ti bars replacing the longitudinal reinforcing steel in the boundary zones within the plastic hinge region) and the aspect ratio (slender walls with aspect ratio greater than 2.0). The study by Abdulridha and Palermo (2017) also served as the benchmark for the material models adopted in the finite element models.

This chapter also includes an investigation of modelling decisions and material models adopted by two other studies in which VecTor2 FE analysis and fiber-model analysis were employed to simulate mid-rise RC shear walls (Ghorbani-Renani et al., 2009; and Luu et al., 2013). The analyses run by Ghorbani-Renani et al. and Luu et al. were corroborated with experimental test results. Further discussion on the analysis parameters and modelling aspects adopted in this thesis is available in Chapter 5 - Sensitivity Analysis.

4.1 Finite element model

Figure 4-1 illustrates the finite element models of Walls MDSRW (a), MDHW (b), DSRW (c), and DHW (d). Three concrete regions (1, 2 and 3) were defined and modelled with plane stress, four-noded rectangular elements. Region 1 includes the rigid base foundation (800 mm deep × 1500 mm wide) and the top slab (225 mm thick × 1500 mm wide), where all reinforcement was considered smeared in the concrete elements.

The width of the top slab corresponds to the width tributary to the walls. Support conditions are applied through vertical and horizontal restraints assigned to the nodes at the base of the foundation. Region 2 defines the web zone of the walls where distributed reinforcement is located. In region 2, the transverse shear reinforcement is smeared in the concrete elements, while the longitudinal reinforcement is represented by discrete, two-noded truss bar elements. Region 3 corresponds to the boundary zones of the walls, where truss elements are adopted to discretize the SMA and the steel longitudinal reinforcing bars, whereas the transverse shear reinforcement and confinement reinforcement are smeared. The connection between the SMA and steel bars in walls MDHW and DHW is modelled via a stiff steel coupler with diameter greater than that of the bars. In all walls, elements representing steel reinforcing bars are defined as fully bonded with the surrounding concrete, whereas the SMA bars are modelled as embedded smooth bars interacting with concrete through bond-link elements. Meshing of the foundation and top slab conformed to the mesh of the walls.

For Walls DSRW and DHW, the mesh aspect ratio is approximately 1.2 in Region 2, with elements of approximately 250 mm × 300 mm, and aspect ratio of 4.7 in Region 3, with element dimensions of 65 mm × 300 mm, imposed by the closely spaced longitudinal reinforcement. A 300 mm length is used for the truss bar elements such that the nodes coincide with the nodes of the rectangular concrete elements. The mesh aspect ratio in Region 2 of walls MDSRW and MDHW is the same as that of the ductile walls. In Region 3, the largely spaced longitudinal reinforcement is modelled with truss bar elements of 250 mm in length, resulting in concrete elements of 125 mm × 250 mm and in mesh aspect ratio of 2.0. Elements in Region 1 conform to the element size of the other regions. The total number of elements composing each model is listed in Table 4-1.

Table 4-1 - Number of elements composing FE model of each wall

	Concrete elements	Truss elements	Bond-link elements	Total number of elements
MDSRW	4402	2540	-	6942
MDHW	4402	2540	200	7142
DSRW	3866	3456	-	7322
DHW	3866	3456	264	7586

An axial load ratio ($P/A_g f'_c$) of 6.90% was applied along the top slab of the ductile walls, which corresponds to the gravity loads acting on the tributary area of the walls of the building located in Vancouver. The axial load ratio applied to the moderately ductile walls corresponds to 9.70%, which is greater than that of the ductile walls due to the smaller gross section area (A_g) of these walls.

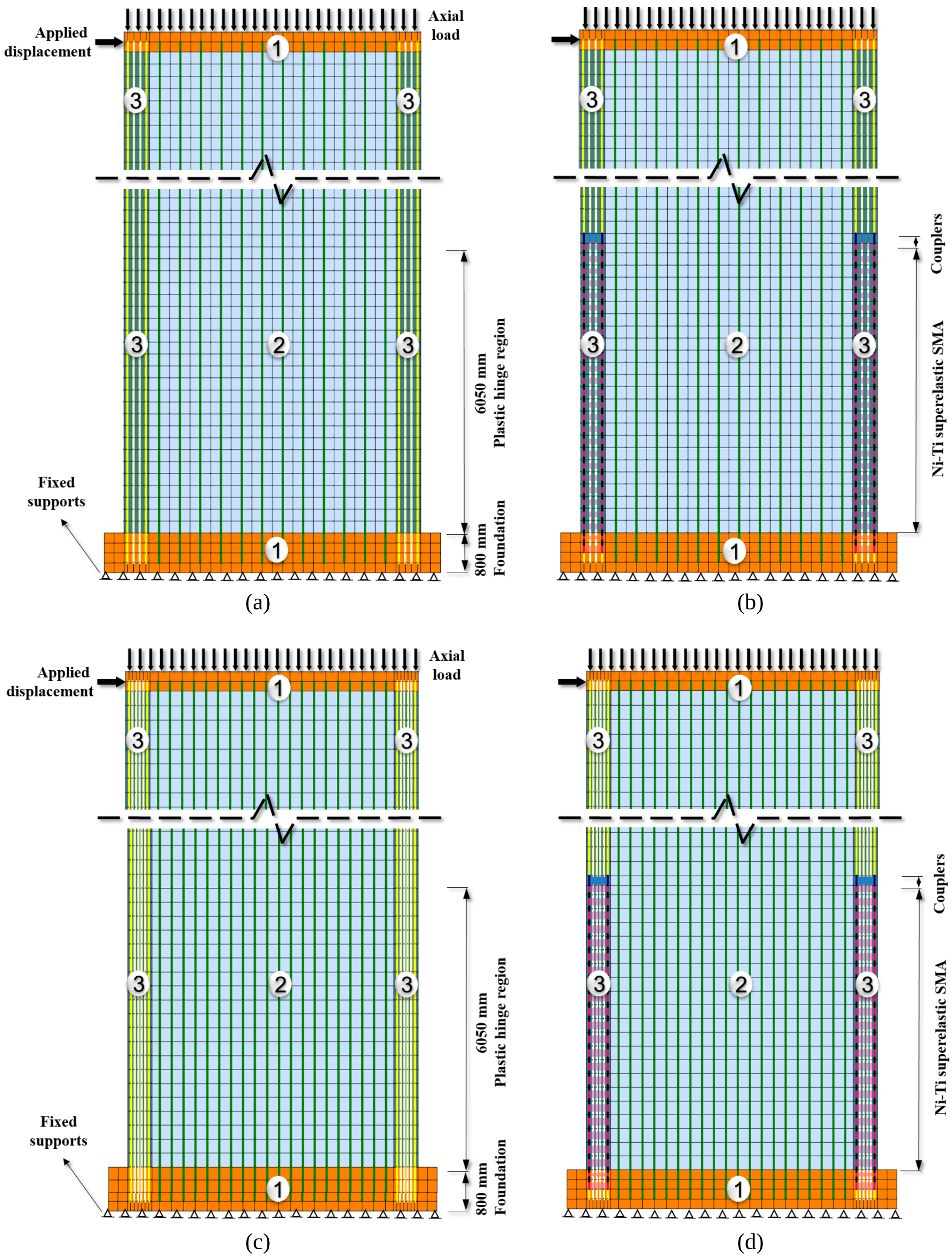

Figure 4-1 - Finite element models in FormWorks (Vecchio et al., 2013) for static analysis of the walls: (a) Wall MDSRW, (b) Wall MDHW, (c) Wall DSRW and (d) Wall DHW

4.2 Material models and properties

Among the various constitutive material models available in VecTor2, the models selected for the analyses in this study are summarized in Table 4-2. Detailed description of each model can be found in Vecchio et al. (2013).

Table 4-2 - Material models adopted in the finite element analysis

Material Property	Material Model
Concrete Compression Base Curve	Hognestad Parabola
Concrete Compression Post-Peak	Modified Park-Kent
Concrete Compression Softening	Vecchio 1992-A (E1/E2-Form)
Concrete Tension Stiffening	Modified Bentz 2003
Concrete Tension Softening	Bilinear
Concrete Confinement Strength	Kupfer/Richart
Concrete dilation	Variable - Isotropic
Concrete Cracking Criterion	Mohr-Coulomb (Stress) Model
Concrete Crack Stress Calculation	Basic (DSFM/MCFT)
Concrete Crack Width	Agg/2.5 Max Crack Width
Concrete Crack Slip	Walraven
Concrete Hysteretic Response	Non-Linear with Plastic Offsets
Concrete Bond	Eligehausen
Reinforcement Hysteretic Response	Bauschinger Effect - Seckin
Reinforcement Dowel Action	Tassios - Crack Slip
Reinforcement Buckling	Akkaya - 2012
Crack Spacing	CEB-FIP 1978 Deformed Bars

In general, default material models should be preferred, unless a user-selected model is known to better represent the behavioural response of a material (Abdulridha, 2013). In the analyses of this thesis, all material models were adopted as the default options in VecTor2, with the exception of the model for the hysteretic response of SMA reinforcement. This material property was modelled according to the constitutive model presented in Figure 1-1 (b), which has been incorporated into VecTor2 though the reinforcement type *Shape Memory Alloy 2*.

The analyses were set to consider the previous loading strain history but not the strain rate effects, which increase the dynamic strength of materials when considered. Creep and relaxation were not considered. Structural damping, which decreases the amplitude of the vibration of structures, was disregarded. Geometric nonlinearity was considered since large deformations can alter the manner loads are applied and resisted. For concrete, the compression pre-peak curve followed the Hognestad parabola, which is suitable for normal strength concrete. The descending portion of the stress-strain response (compression post-peak) was set to follow the Modified Park-Kent model. Secondary effects of concrete were also modelled in VecTor2. The reduction in compressive strength and stiffness due to co-existing transverse cracking and tensile straining, i.e. compression softening, was considered according to the model by Vecchio 1992-A (e1/e2-Form). The tensile stresses in concrete between cracks that result from the bond action between reinforcement and concrete, i.e. tension stiffening, was modelled with the Modified Bentz 2003 model. The post-cracking tensile stresses in plain concrete (tension softening) were modelled with a bilinear descending response. The confined strength of concrete due to out-of-plane reinforcement confinement was set according to the Kupfer/Richart model. Concrete dilation, i.e. the expansion of concrete due to internal microcracking resulting from compressive stress, was defined as isotropic. The Mohr-Coulomb (Stress) model was assigned to the cracking strength of concrete, as it accounts for cracking strength decreasing as the compressive stresses acting transversely increase. The basic (DSFM/MCFT) model was chosen for the calculation of the crack shear stress transferred through the aggregate interlock. Crack width check was considered; this parameter accounts for a reduction in the compressive stresses when crack width exceeds a specified limit. The crack shear-slip check was considered as following the Walraven model to explicitly account for strains due to shear slip along the cracks. For the hysteretic response of concrete, the non-linear model with plastic offsets was selected. For the hysteretic response of reinforcement, the Seckin model with Bauschinger effect was chosen. This model is composed by a linear elastic region, a subsequent yield plateau, and ultimately a curvilinear branch representing strain hardening. To model the dowel action of reinforcement, i.e. the shear resistance developed when cracks slip transversely to the axis of the rebars, the Tassios crack-slip model was selected. At last, the crack spacing was selected as following a uniform allocation, which is suitable for most modelling purposes, given by the CEB-FIP 1978 Deformed Bars model. Perfect bond conditions were assumed between steel reinforcement and concrete. With respect to the SMA reinforcement, the concrete bond was modelled by the Eligehausen model. This model defines the bond relationship as a series of bond stresses and bond slips, which were set to represent that emerging on smooth embedded bars.

VecTor2 requires several mechanical properties to be defined by the user and derives others automatically. For concrete, only the compressive strength is necessary. For the reinforcement, the input includes the bar diameter and cross-sectional area (for discrete reinforcement) or reinforcement ratio (for smeared reinforcement), elastic modulus, yield strength and ultimate strength, strain hardening strain and ultimate strain. The bond properties that the program requires are the confinement pressure factor, which is used to interpolate the response between unconfined splitting failure and confinement pull-out failure, and information about the distribution of the reinforcement. The concrete and reinforcement properties were defined according to the properties used for design and presented in Table 3-5 and Table 3-6.

4.3 Nonlinear static analysis

Employing the material models and properties discussed above, the finite element models from Figure 4-1 were subjected to two types of nonlinear static analysis in VecTor2. The lateral capacity of the walls was investigated using pushover analysis, while the hysteretic response of the walls was evaluated using reverse cyclic analysis.

4.3.1 Pushover analysis

Static nonlinear pushover analyses were conducted through the application of incremental lateral displacements, by increments of 5 mm, at the centre of the top slab of the walls. The resulting pushover curves were used to determine the lateral capacity of the walls in terms of secant stiffness, lateral strength, yield point, ultimate displacement, and displacement ductility.

4.3.2 Reverse cyclic analysis

Reverse cyclic analyses were performed for each type of wall respecting the load protocol illustrated in Figure 4-2. The peak displacement of each cycle was selected based on the yield displacement of the respective wall and normalized as drift ratios, where drifts corresponded to lateral displacements divided by the height of the wall. Increment between cycles corresponded to 0.1% until 0.5% drift, and to 0.5% from 0.5% drift up to failure. The predicted load-displacement hysteretic responses were used to determine the lateral capacity, failure mechanism, wall rotation, and the recovery and energy dissipation capacities of the walls.

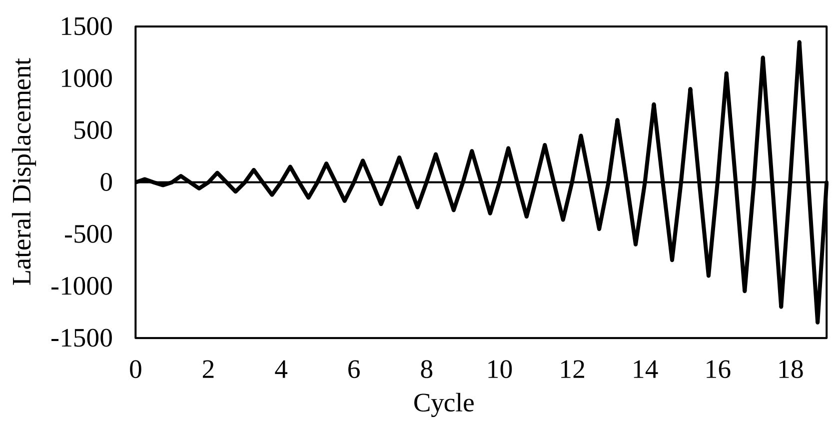

Figure 4-2 - Load protocol for reverse cyclic analysis

4.4 Nonlinear dynamic analysis

4.4.1 Parameters for dynamic analysis

To perform the dynamic analyses, the portion of the seismic weight of the building corresponding to each shear wall was converted into mass and applied to a central node at each storey level. Modifications of the finite element models were required given the limitations imposed by VecTor2 on the size of the stiffness matrix for dynamic analysis. The new models employed in the dynamic analyses are depicted in Figure 4-3. The mesh size was increased, as minimally as possible, to reduce the number of nodes in the models, consequently reducing the degrees of freedom for analysis. Stiff elements were introduced at the storey levels to ensure a stable dynamic response when masses were assigned to these locations. The use of truss bar elements to represent the longitudinal reinforcement throughout the walls limited the element width, incurring in greater aspect ratios as element size was increased, specifically in the models of the heavily reinforced ductile walls. For the moderately ductile walls, the mesh aspect ratio in the new model was equal to 1.3 in the web region and 2.5 in the boundaries. In the same regions, the mesh aspect ratio was increased to approximately 2.2 and 7.4 for the ductile walls. The regions included to represent the building slabs were assigned the same material as that of the top slab, and have aspect ratios of 1.4 and 1.2 for the moderately ductile and ductile walls, respectively. The mesh size of the top slab and foundation were maintained from the original model.

The material properties used in dynamic analysis were the same as those used in static analysis, with the addition of the consideration of ground motion acceleration in the horizontal direction, input as ground motion records. Damping of 1.5% was assigned to the first and third modes for the Raleigh's viscous damping model, as suggested by Luu et al. (2013). The third mode of vibration was selected as it is the mode that accumulates more than 90% of the structural mass. The same axial load ratios considered for the design of each wall were included in the dynamic analysis. The analyses were carried out for a duration of 20 s beyond the duration of each ground motion record, resulting in total duration of analysis that varies from 40 s to 150 s. The additional time permitted the response of the structure to decay through free vibration, which resulted in better estimates of the residual. The dynamic analyses corresponding to the building in Vancouver used an integration time step of 0.005 s when records from Scenarios 1 and 2 were employed, and 0.001 s for the records from Scenario 3. For the building in Montreal, the integration time step was adopted as 0.002 s. Further discussion regarding time steps for dynamic analysis is presented in Section 0. The dynamic analysis employed the Newmark constant average acceleration solution method, which is considered to provide accurate and stable results (Vecchio and Saatci, 2007).

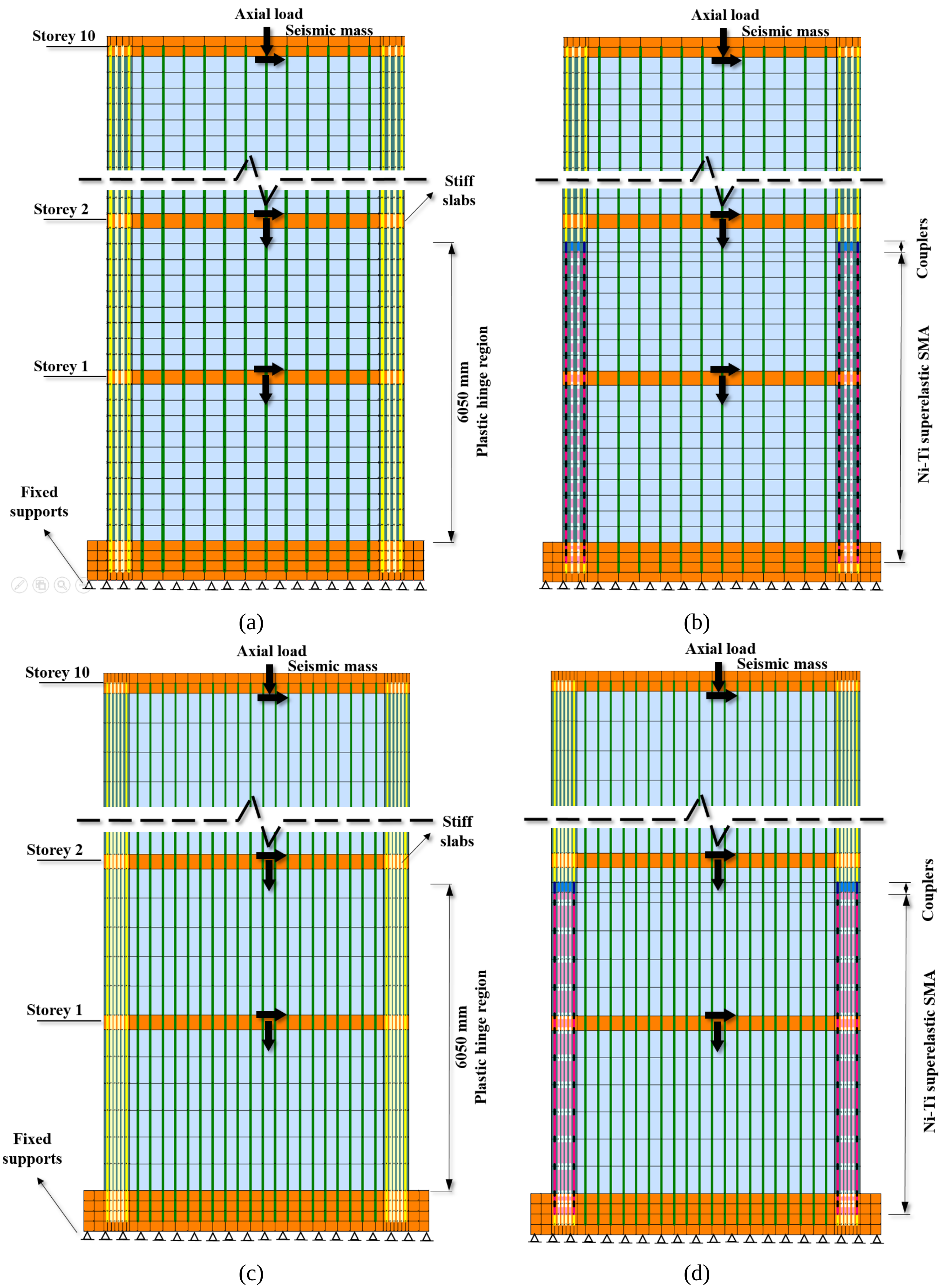

Figure 4-3 - Finite element models in FormWorks (Vecchio et al., 2013) for dynamic analysis of the walls: (a) Wall MDSRW, (b) Wall MDHW, (c) Wall DSRW and (d) Wall DHW

4.4.2 Selection of ground motion records for Montreal - QC

To assess the seismic response of the shear walls, time history analyses were performed with the use of ground motion records, which were selected to appropriately reproduce the M-R scenarios that contribute most significantly to the seismic hazard of the seismic zone. In addition, a period range of interest (T_R) was defined to target ground motion records which response spectra better match the UHS. To define T_R, the fundamental period of the building located in Montreal was considered as equal to 1.3 s. From modal analysis of the building, the period of the highest mode necessary to accumulate 90% of the structural mass (third mode of vibration) was found to be equal to 0.13 s. Therefore, according to Equation 2-16, the period range of interest for dynamic analysis of the structure is from 0.13 s to 2.60 s.

The seismic hazard of locations with higher seismicity in eastern Canada, such as Montreal, according to Atkinson (2009), is dominated by two scenarios: magnitude 6 earthquakes at distances ranging from 10 to 30 km, which are significant for the period range of 0.13-1.0 s; and magnitude 7 earthquakes that occur at longer distances (20 to 70 km) and influence the period range of 1.0-2.6 s. Method A, presented in Section 2.5.3, was adopted for the selection and scaling of the ground motion records in Montreal. Therefore, a single target response spectrum was defined for each M-R scenario, corresponding to the UHS of the seismic hazard with a 2% probability of exceedance in 50 years defined by the NBC 2015 (NRC, 2015) for the city of Montreal. The UHS, i.e. the design hazard, was previously presented in Figure 3-3. The spectrum was modified according to recommendations from the NBC 2015 to permit a better match of the spectral acceleration of the ground motion records at shorter periods. The resulting target response spectrum, $S_t(T)$, and the defined period range of interest of each scenario, T_{RS1} and T_{RS2}, are plotted in Figure 4-4.

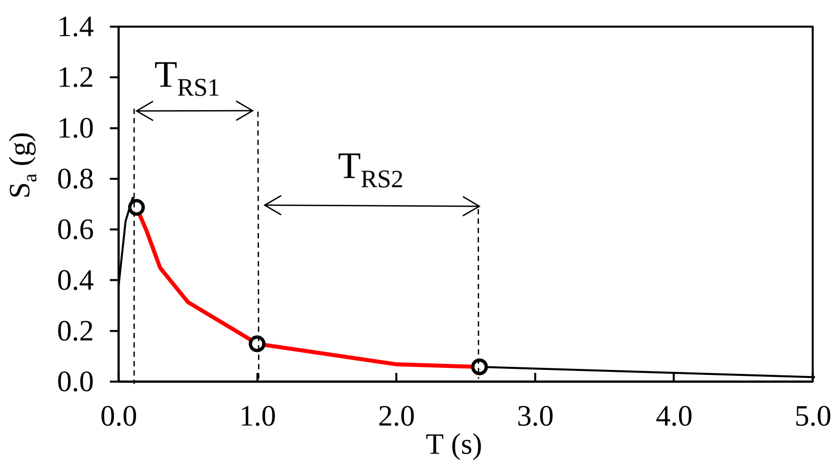

Figure 4-4 - Target acceleration spectrum corresponding to 2% hazard in Montreal along period range of interest

To match $S_t(T)$, appropriate records were sought from the Engineering Seismology Toolbox (Atkinson, 2009) database of simulated ground motion records. Simulated records were preferred given the lack of historical earthquake records characteristic of eastern Canada. The search was limited to records corresponding to simulated soil Site Class C. Eleven records in total, with at least five for each scenario, should be selected if the objective of the analysis was to design the building. Consequently, the results presented in Section 6.3, e.g. displacements and drifts, are taken as the mean results from the analyses employing each of the eleven ground motion records. Table 4-3 presents the composition of the ensemble of ground motion records determined for the analysis of the building in Montreal.

Table 4-3 - Ensemble of ground motion records for dynamic analysis in Montreal

	Scenario 1 (0.13-1.0 s)	Scenario 2 (1.0-2.6 s)
M6 at 10-30 km	5 records	
M7 at 20-70 km		6 records
Total	11 records	

The pre-selection resulted in 90 records for each scenario. The ratio $S_t(T)/S_g(T)$ and the mean of the computed ratio corresponding to each pre-selected record were calculated over the corresponding scenario-specific period range. The mean of the ratio was employed, along with the standard deviation of the mean of the ratio, to refine the selection, restricting the selected records to those with mean between 0.5 and 2.0 and lower standard deviation. Table 4-4 lists important characteristics of the selected eleven ground motion records, including magnitude and distance, duration of the excitation, and PGA, while Figure 4-5 illustrates the spectral acceleration of the unscaled ground motion records.

Table 4-4 - Characteristics of the ground motion records selected for the analysis in Montreal

	Record number*	Magnitude	Distance (km)	Duration (s)	PGA (g)	Mean $S_t(T)/S_g(T)$
S1	5	6	21.5	5.0	0.28	1.34
	7	6	12.8	3.0	0.52	0.59
	9	6	12.8	3.0	0.41	0.82
	19	6	26.3	6.0	0.17	1.81
	30	6	14.3	4.0	0.50	0.82
S2	6	7	50.3	18.0	0.12	1.69
	15	7	50.3	18.0	0.13	1.84
	18	7	20.6	15.0	0.49	0.78
	20	7	51.9	19.0	0.12	1.60
	34	7	25.2	16.0	0.39	1.20
	36	7	25.2	15.0	0.47	0.96

*record number as listed in the source database

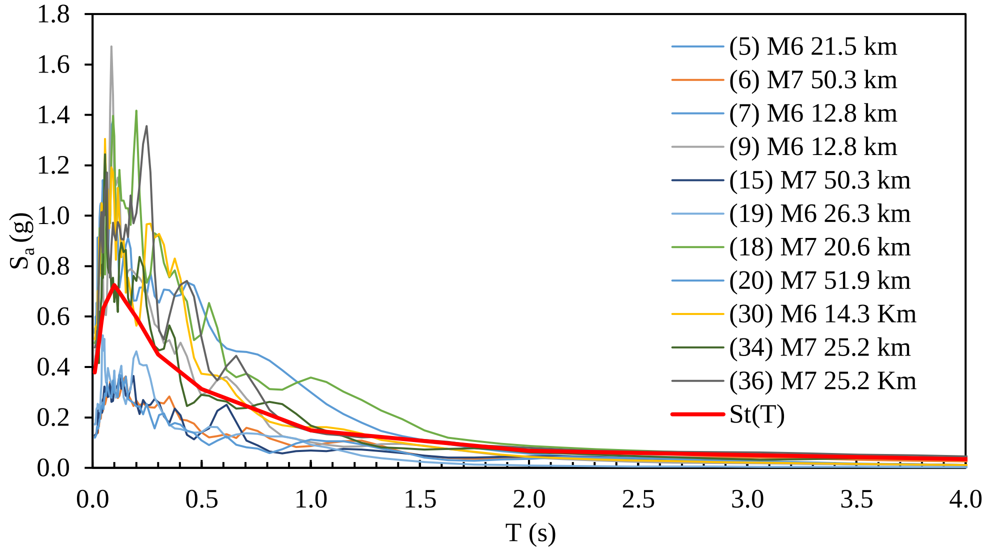

Figure 4-5 - Spectral acceleration of unscaled ground motion records selected for the analysis in Montreal

The spectral accelerations of the selected ground motion records were scaled employing the mean of $S_t(T)/S_g(T)$ along the scenario-specific period range. The resulting scaled acceleration spectra were found to require a secondary scaling factor in order to be matching or exceeding 90% of $S_t(T)$ over the entire scenario-specific period ranges. A secondary scaling factor equal to 1.3 was applied to the records of Scenarios 1 and 2. The final $S_g(T)$ of the eleven records are plotted in Figure 4-6, divided into Scenario 1 (Figure 4-6 (a)) and Scenario 2 (Figure 4-6 (b)). Figure 4-7 illustrates the mean of the spectral acceleration of the selected ground motion records per scenario, plotted against the target spectrum.

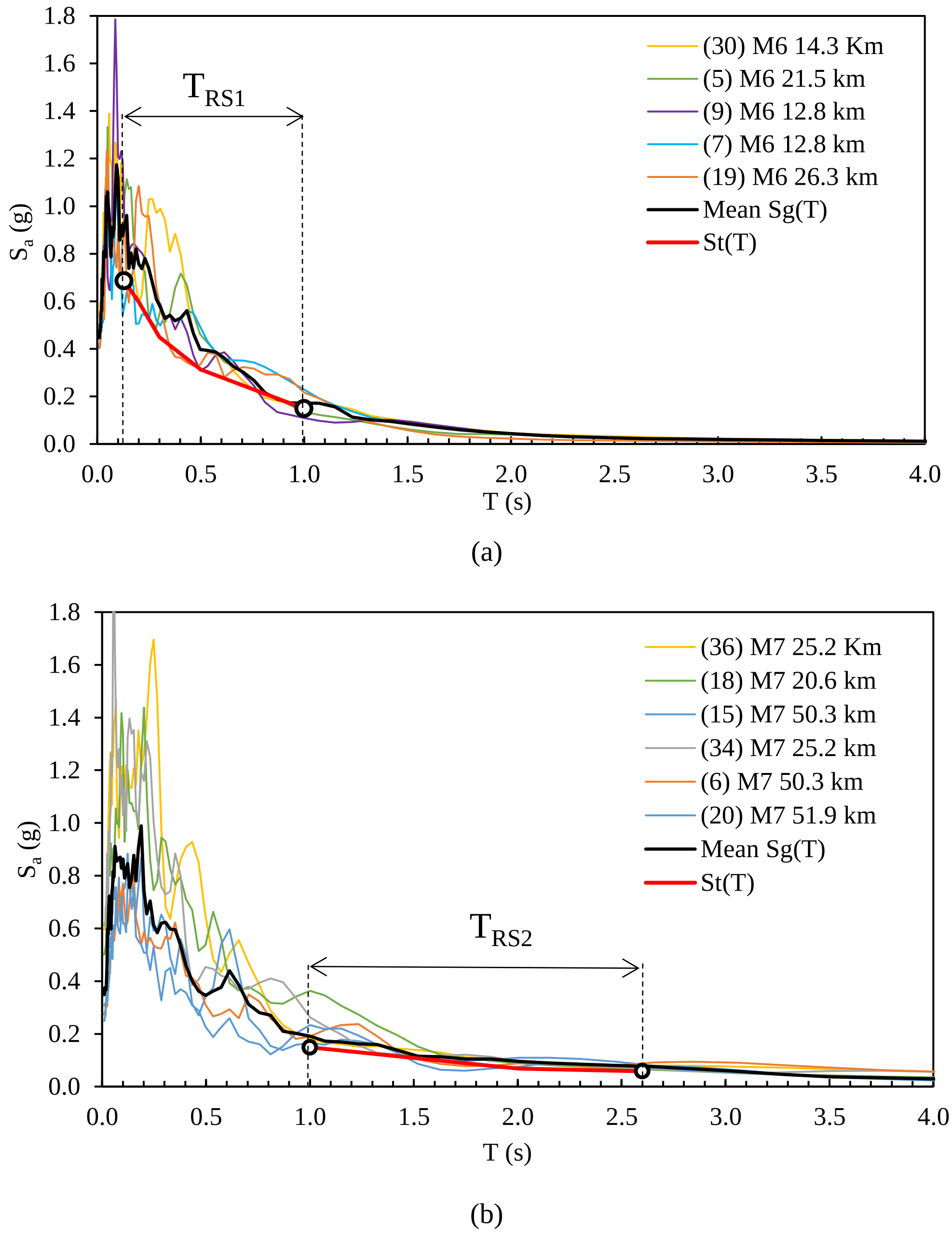

Figure 4-6 - Spectral acceleration of ground motion records selected and scaled to match the target spectrum $S_t(T)$ over: (a) T_{RS1} and (b) T_{RS2}

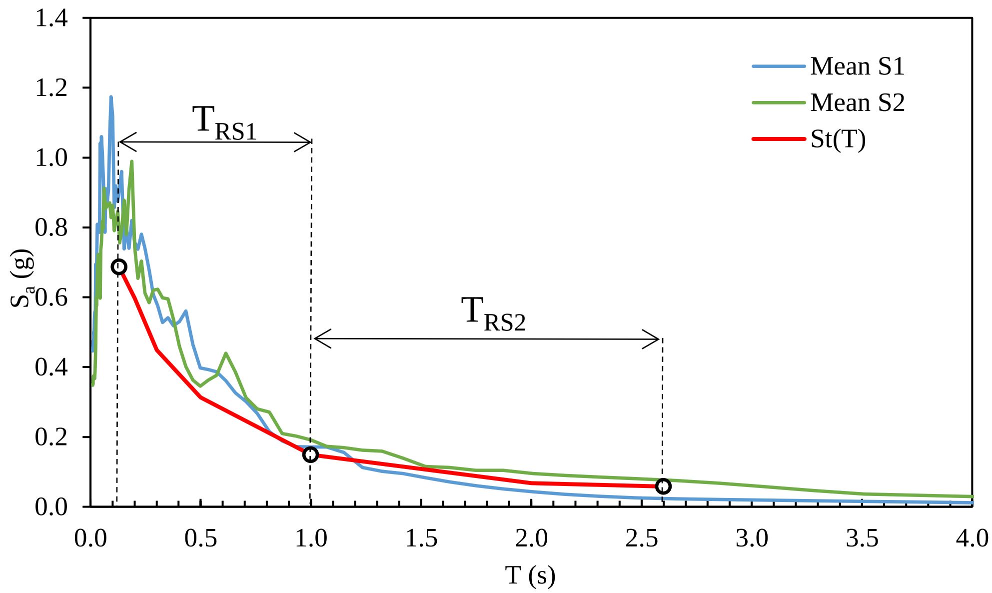

Figure 4-7 - Spectral acceleration of the mean of records selected and scaled for Scenarios 1 and 2 compared to the target spectrum $S_t(T)$ for Montreal

Ultimately, the same primary and secondary scaling factors applied to the acceleration response spectra were applied to the acceleration time histories of the selected ground motion records, which are plotted in Figure 4-8 (a) for Scenario 1, and in Figure 4-8 (b) for Scenario 2. Although all the records provided by Atkinson (2009) for eastern Canada are 20 s-long, the excitation within the records is concentrated in durations that vary from 3 s to 19 s. Individual acceleration time histories of the records are available in Appendix B, Table B-1.

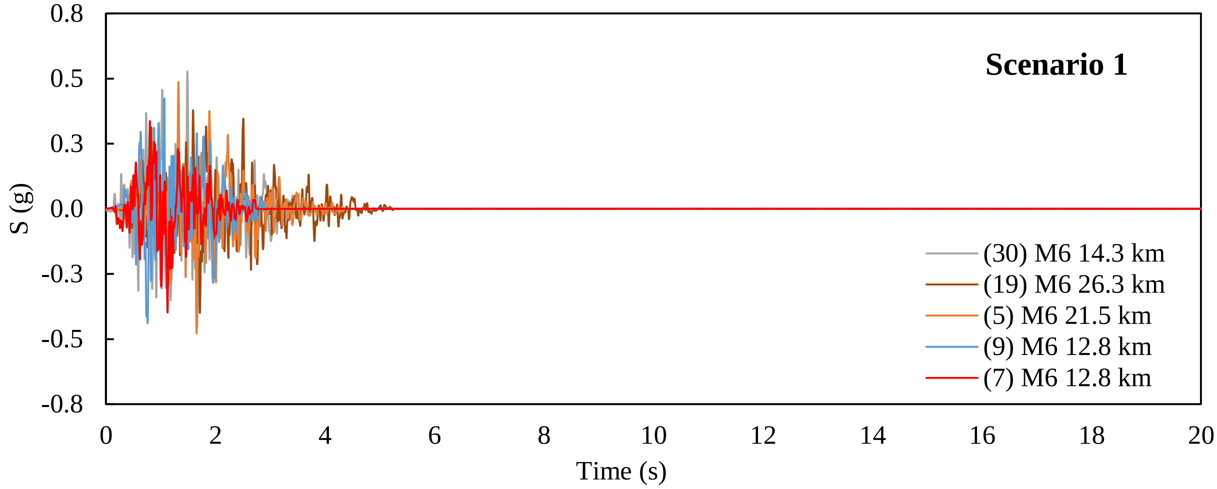

(a)

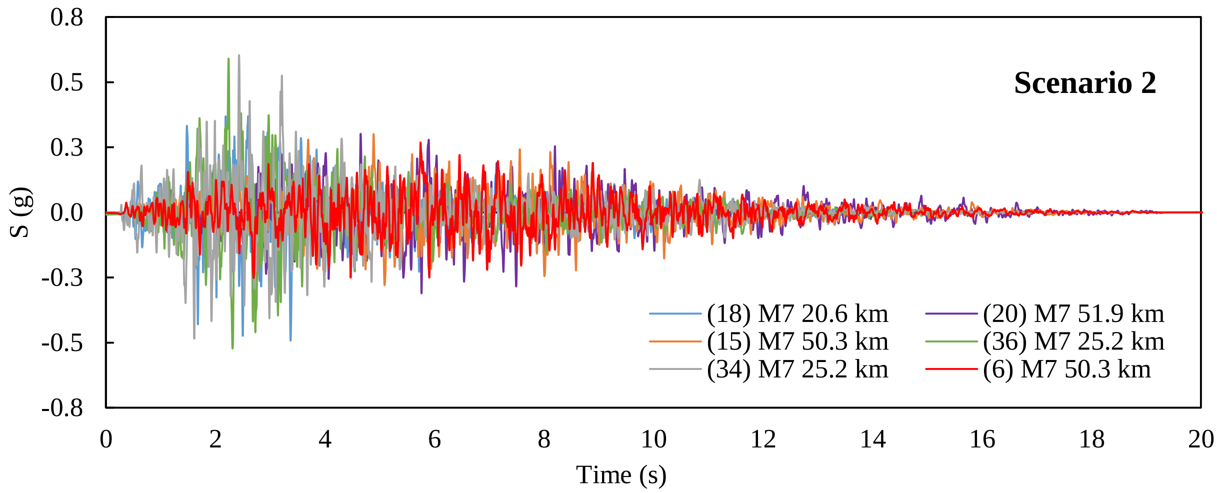

(b)

Figure 4-8 - Acceleration time history of scaled ground motion records in Montreal: (a) Scenario 1 and (b) Scenario 2

4.4.3 Selection of ground motion records for Vancouver - BC

The fundamental period of the building located in Vancouver, BC, bounded by the code upper limit of $2T_a$, is equal to 1.3 s, while the period of the highest mode contributing to 90% of the structural mass, determined by modal analysis of the building as the third mode of vibration, is equal to 0.1 s. As a result, the period range of interest for the time history analysis of this building starts at 0.1 s and ends at 2.6 s, as per Equation 2-16.

The seismic hazard of southwestern British Columbia, where Vancouver is located, was defined based on the hazard deaggregations previously presented in Figure 2-32. In general, the seismic hazard of the region can be divided into three different types of earthquakes: shallow earthquakes in the North American plate (crustal), deep sub-crustal (depths of 50 km or more) events at the Juan de Fuca plate, and interface (or subduction) earthquakes of large magnitude (M9) at the boundary of the two plates, occurring away from the coast and at depths of around 20 km (Tremblay et al., 2015). The shorter periods of the spectrum are mostly influenced by intermediate magnitude events occurring at distances of less than 50 km (crustal earthquakes) and at distances greater than 50 km (crustal and sub-crustal events). In contrast, the spectrum is dominated by the larger magnitude interface earthquakes at longer periods.

Method A, presented in Section 2.5.3, was employed for the selection and scaling of the ground motion records. Given the complexity of the seismicity of this region, three scenarios were defined, following the division of T_R and the M-R mean values proposed by Tremblay et al. (2015) for the city of Vancouver, BC. The M-R values presented are given in moment magnitudes and closest distance to fault. The lower limit of T_{RS1} and the upper limit of T_{RS3} were adjusted to account for the period range of interest of this study. As a consequence, the following scenarios were defined: Scenario 1, for crustal earthquakes, corresponding to 0.1 s to 0.8 s, with mean magnitude of 6.7 and mean distance of 14 km; Scenario 2, for sub-crustal earthquakes, with a range of 0.3 s to 1.5 s, magnitude 7.0 and distance of 52 km; and Scenario 3, for interface earthquakes, ranging from 1.0 s to 2.6 s, with magnitude 8.6 and distance of 141 km. Figure 4-9 illustrates the target acceleration response spectrum for the 2% probability of exceedance in 50 years seismic hazard in Vancouver, which includes the replacement of the plateau at shorter periods by discrete pseudo-acceleration values available at the Geological Survey of Canada (NRC, 2017) and highlights the scenario-specific period ranges.

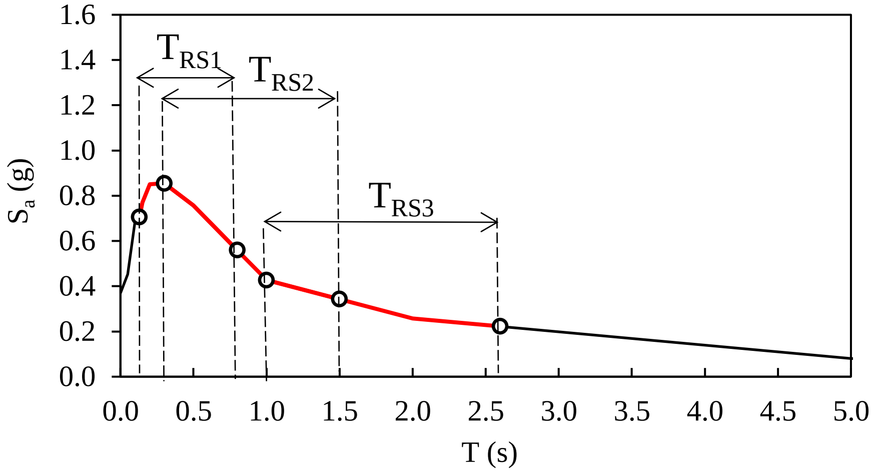

Figure 4-9 - Target acceleration spectrum for the 2% hazard in Vancouver along T_R

The NGA-West2 (Ancheta et al., 2013) database was used as the source of natural earthquake records to match the target spectrum along Scenarios 1 and 2. Acceptable ranges were defined for magnitude and distance respecting the criterion proposed by Tremblay et al. (2015), which suggests a variation equal to 40 km for crustal events and 60 km for sub-crustal and interface events. The selections was limited to records from sites with average shear wave velocity ranging from 360 m/s to 760 m/s, corresponding to Site Class C. In contrast, the Engineering Seismology Toolbox (Atkinson, 2009) database was used as source of simulated ground motion records representative of the megathrust events of the Cascadia subduction region, which correspond to Scenario 3. If the dynamic analysis was used to design the building, at least eleven records for each of the three scenarios should have been selected, given that they represent distinct earthquake sources. As the objective of this study is to investigate the feasibility of the implementation of SMA-reinforced shear walls in terms of seismic performance, a simplification was adopted so the total number of records matches eleven. A set of 25 earthquake records were pre-selected for each of the Scenarios 1 and 2, whereas 45 simulated records were pre-selected for Scenario 3. Four records were thereafter selected for each of the Scenarios 1 and 2, and three records were selected for Scenario 3, reaching a total of eleven records for the ensemble of ground motion records, as described in Table 4-5. The results presented in Section 6.3 are therefore taken as the mean results from the analyses employing each of the eleven earthquake records.

Table 4-5 - Ensemble of ground motion records for dynamic analysis in Vancouver

Type of event	Range of magnitude	Range of distance	Scenario 1 (0.1-0.8 s)	Scenario 2 (0.3-1.5 s)	Scenario 3 (1.0-2.6 s)
Crustal	5.7-7.7	0-54 km	4 records		
Sub-crustal	6.0-8.0	0-112 km		4 records	
Interface	7.6-9.6	81-201 km			3 records
Total				11 records	

For each of the pre-selected ground motion records, the ratio $S_t(T)/S_g(T)$ and the mean of the computed ratio corresponding to each pre-selected record were calculated over the corresponding scenario-specific period range. To refine the selection, the records were maintained if the respective mean of the ratio was between 0.5 and 5.0, and lower standard deviation of the mean of the ratio was preferred. The relaxed upper limit for the mean employed herein is due to the great variability in shape found among natural earthquake records. Table 4-6 presents important characteristics of the ensemble of ground motion records chosen to represent the 2% in 50 years seismic hazard in Vancouver, and Figure 4-10 illustrates the unscaled spectral accelerations of the eleven ground motion records.

Table 4-6 - Characteristics of the ground motion records selected for the analysis in Vancouver

	Record number*	Record name	Distance (km)	5-95% Duration	PGA (g)	Mean $S_t(T)/S_g(T)$
S1	150	Coyote Lake, 1979	3.11	3.5	0.42	1.21
	250	Mammoth Lakes, 1980	16.00	7.1	0.95	0.78
	265	Victoria, Mexico, 1980	14.37	8.2	0.65	1.23
	313	Corinth, Greece, 1981	10.27	15.4	0.24	1.28
S2	14	Kern County, 1952	82.19	33.6	0.09	2.52
	359	Coalinga, 1983	26.38	10.9	0.18	1.48
	472	Morgan Hill, 1984	31.88	21.8	0.08	4.84
	496	Nahanni, Canada, 1985	4.93	4.5	0.52	1.41
S3	14	M9 Cascadia 14	112.40	-	0.14	1.62
	15	M9 Cascadia 15	112.40	-	0.17	1.78
	23	M9 Cascadia 23	156.70	-	0.08	2.06

*record number as listed in the source database

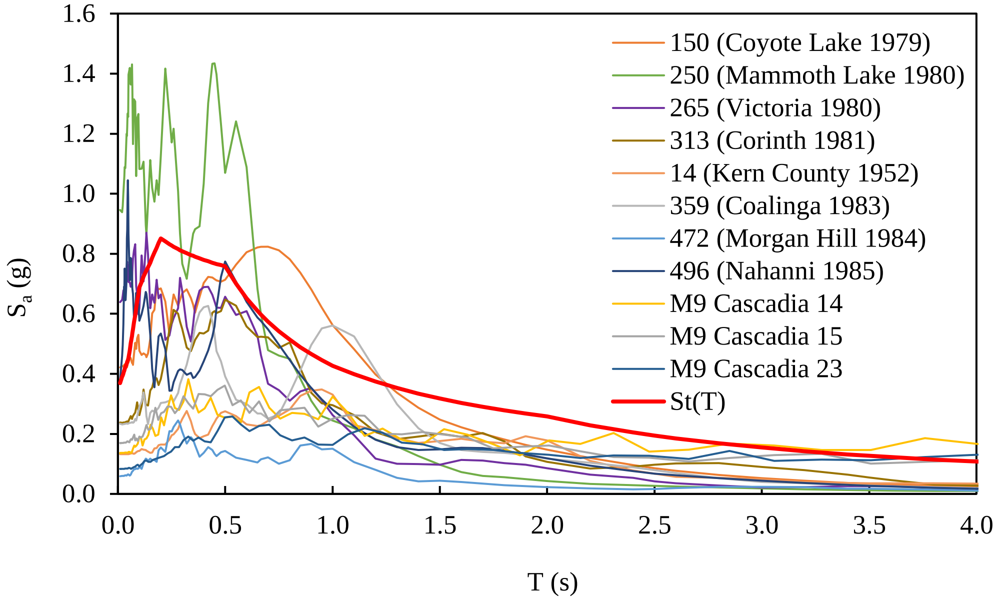

Figure 4-10 - Spectral acceleration of unscaled ground motion records selected for the analysis in Vancouver

The mean spectra were determined for each scenario based on the records scaled employing the mean of the ratio $S_t(T)/S_g(T)$ as scaling factor. In order for the mean spectra to match or exceed 90% of $S_t(T)$ over the entire scenario-specific period range, secondary scaling factors of 1.25 for Scenarios 1 and 2 and 1.1 for Scenario 3 were applied. Figure 4-11, Figure 4-12 and Figure 4-13 illustrate the spectral accelerations of the selected and scaled ground motion records of Scenario 1, 2 and 3, respectively, along with the target spectra for the 2% in 50 years hazard corresponding to the scenario-specific period range. The mean spectral acceleration of the selected and scaled records representing Scenarios 1, 2, and 3 is compared with the target response spectrum over T_R in Figure 4-14.

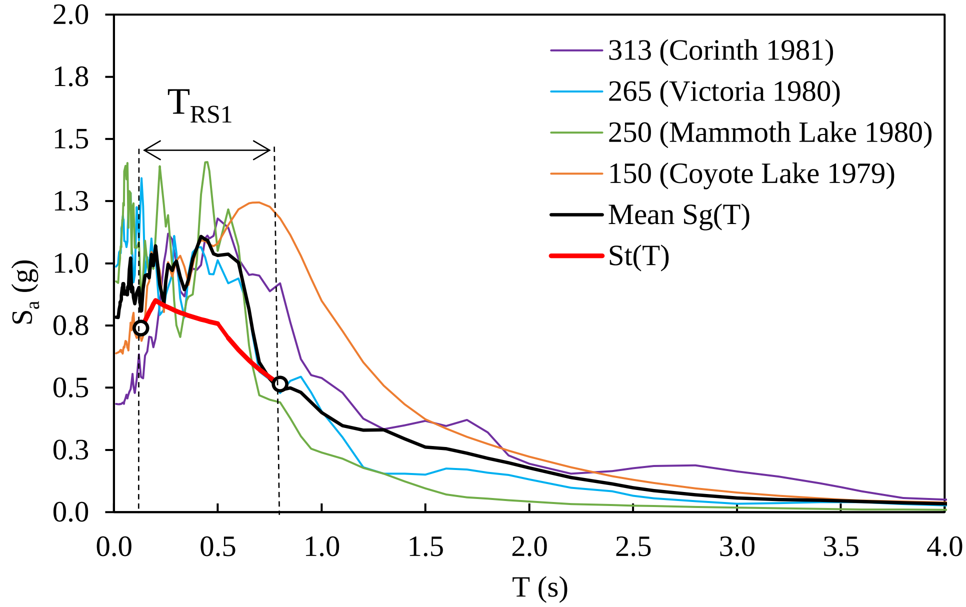

Figure 4-11 - Spectral acceleration of ground motion records selected and scaled to match the target spectrum $S_t(T)$ over T_{RS1}

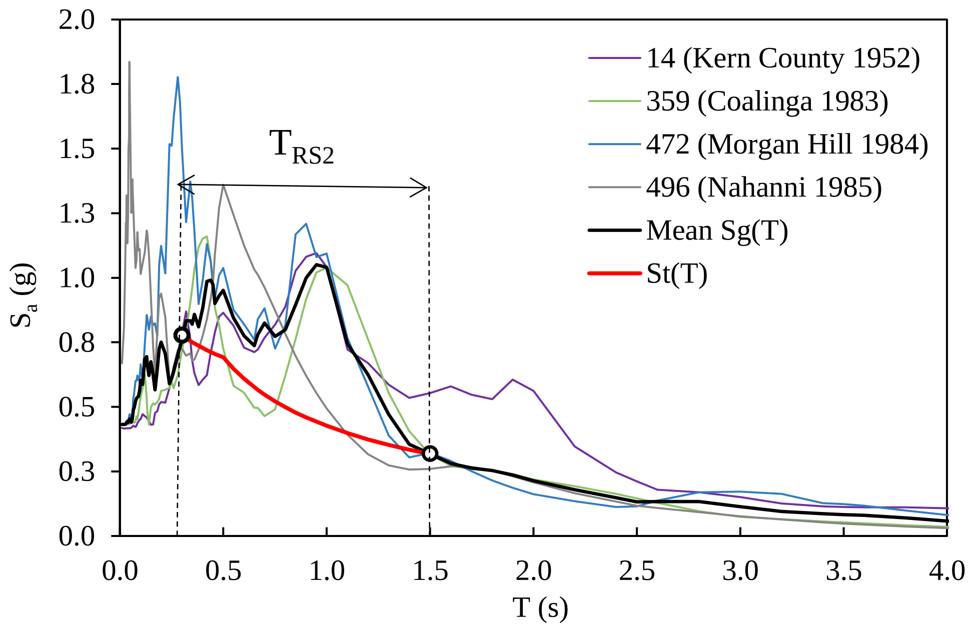

Figure 4-12 - Spectral acceleration of ground motion records selected and scaled to match the target spectrum $S_t(T)$ over T_{RS2}

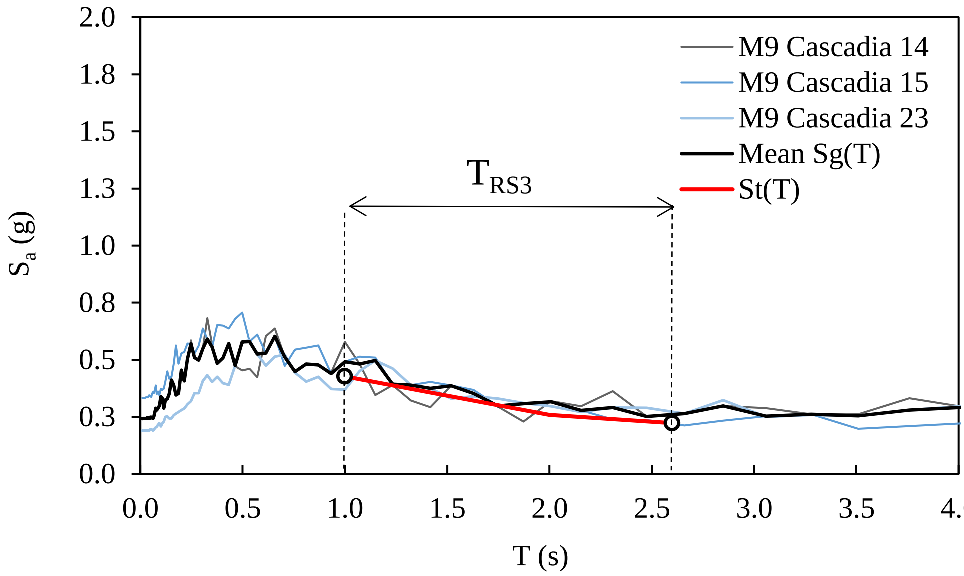

Figure 4-13 - Spectral acceleration of ground motion records selected and scaled to match the target spectrum $S_t(T)$ over T_{RS3}

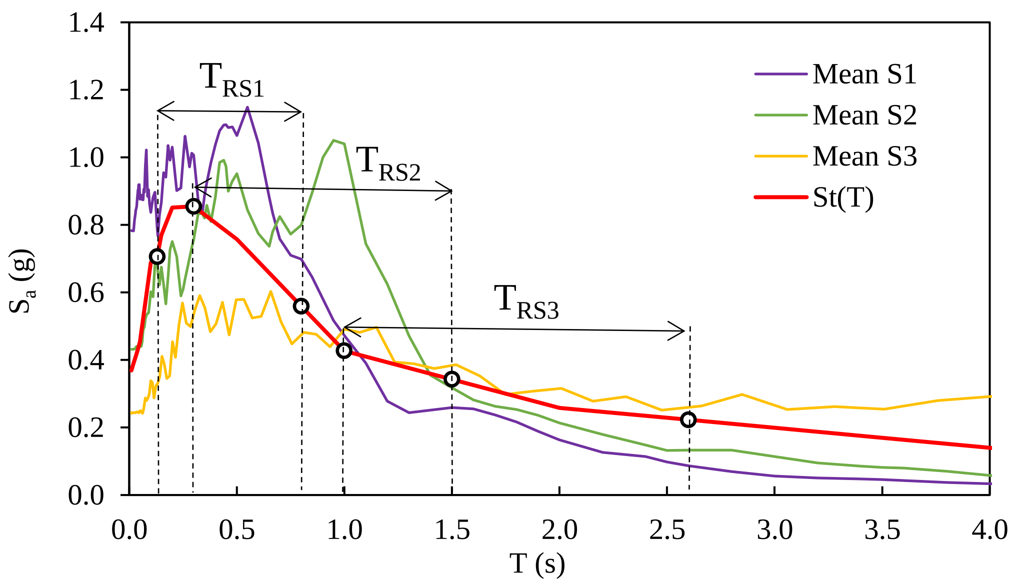

Figure 4-14 - Spectral acceleration of the mean of records selected and scaled for Scenarios 1, 2 and 3 compared to the target spectrum $S_t(T)$

The scaled acceleration time histories of the selected ground motion records for Scenarios 1, 2, and 3 are plotted in Figure 4-15 (a), Figure 4-15 (b), and Figure 4-15 (c), respectively. Individual acceleration time histories of the records are available in Appendix B, Table B-2. Duration of the records employed in Scenarios 1 and 2 varies from 25 s to 70 s. Although the simulated records that represent the Cascadia events in Scenario 3 have longer duration (260 s), the analyses were run for a duration of 150 s to mitigate the required computational time.

Ultimately, one record from the suite was selected to be amplified and used to further investigate the behaviour of the ductile walls of the building located in Vancouver. The scaled acceleration time history of Record 150 - Coyote Lake, 1979 (initially scaled by 1.51) was further amplified with the use of scaling factors equal to 1.5 and 2.0. The resulting 150% and 200% amplified acceleration time histories of Record 150 are provided in Table B-3 of Appendix B.

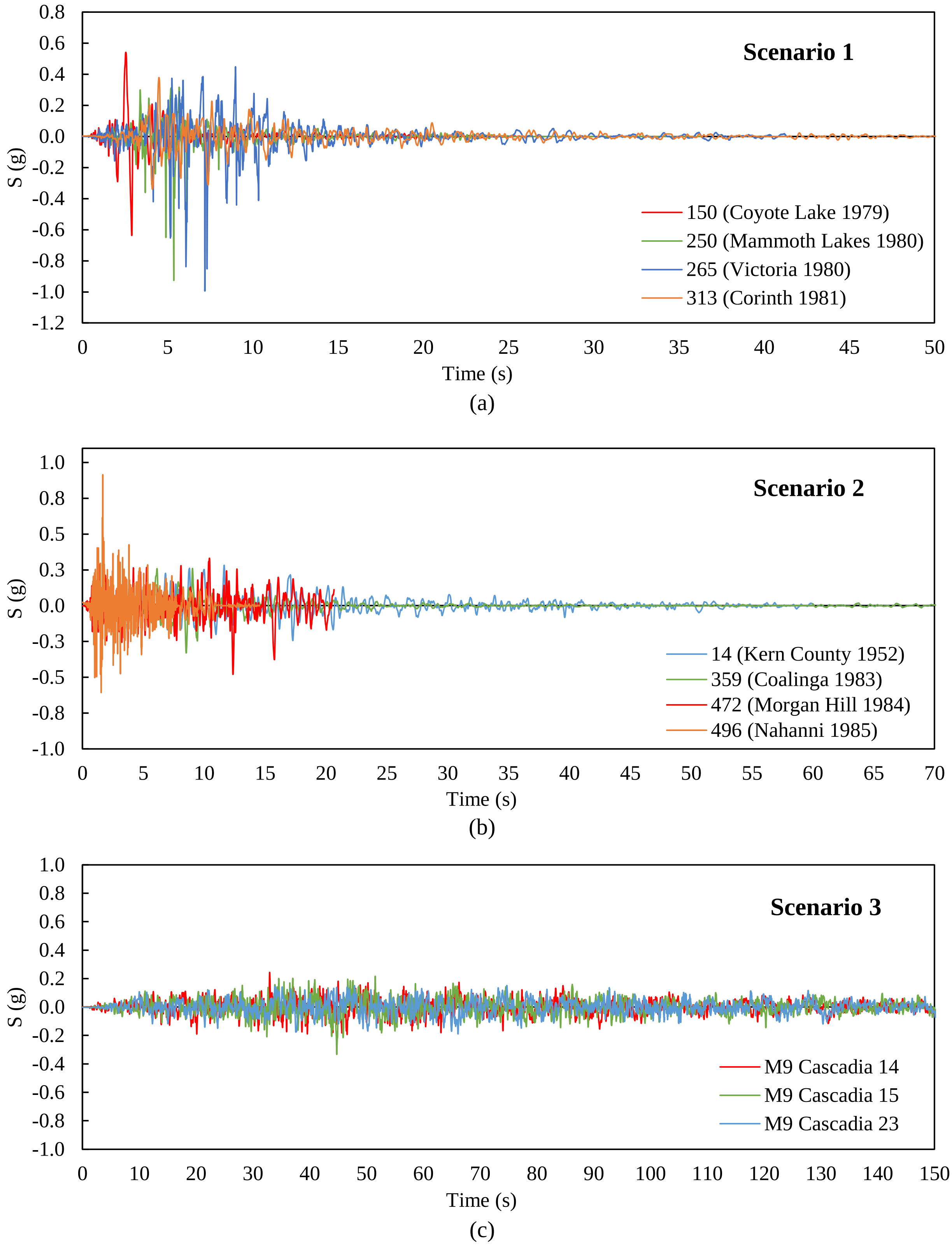

Figure 4-15 - Acceleration time history of the ground motion records for Vancouver: (a) Scenario 1, (b) Scenario 2 and (c) Scenario 3

5. SENSITIVITY ANALYSIS

In this chapter, the parameters that were investigated to improve the accuracy of the numerical analyses will be presented. The variation in the response of the walls triggered by each parameter, as well as the modelling aspects that were found to have a significant influence in the numerical results, will be discussed. Thereafter, the decision regarding the parameters employed in the final models will be justified. Several variations in the design of the hybrid wall, specifically for the layout of the SMA bars, will also be investigated. The ductile walls DSRW and DHW were used as reference for the sensitivity analyses.

5.1 Modelling aspects

5.1.1 Steel reinforcing bars

The consideration of longitudinal reinforcement smeared in the concrete elements was assessed against the use of discrete truss bar elements for both the edge and web zones of the walls. The use of truss bar elements in the edge zones of reinforced concrete shear walls has been acknowledged to lead to more accurate results (Luu et al., 2013). In addition, modelling the Ni-Ti SMA reinforcing bars and the couplers to the steel bars required the use of discrete elements in the edge zones of the hybrid SMA-steel walls. Therefore, the concentrated longitudinal reinforcement in the edges of the walls was modelled with discrete, two-noded truss bar elements.

Initially, the analyses were run with the vertical reinforcement in the web zone of the walls smeared in the concrete elements. During a review of the design of the ductile walls, it was found that the ratio of vertical reinforcement (ρ_l) in the web zone could be reduced from 0.5% to 0.38% according to the seismic demand. However, when this modification was implemented in the finite element model of Wall DHW, the wall exhibited a significant reduction in lateral capacity, as is evident in the hysteretic response of the wall provided in Figure 5-1. This large drop in capacity was incompatible with the relative small change in design. The predicted failure mechanism of this wall reveled that fracture of the bars in the web zone controlled the response of the hybrid wall when ρ_l was lower than 0.5%. The displaced shape and cracking pattern of the lower portion of Wall DHW with ρ_l of 0.38%, on the verge of failure (1.5% drift), can be observed in Figure 5-2. Localized large cracks that surfaced at the base of the hybrid wall due to poor bond between the smooth SMA bars and concrete caused fracture of the steel bars in the web zone prior to failure of the SMA bars, reducing the capacity of the wall.

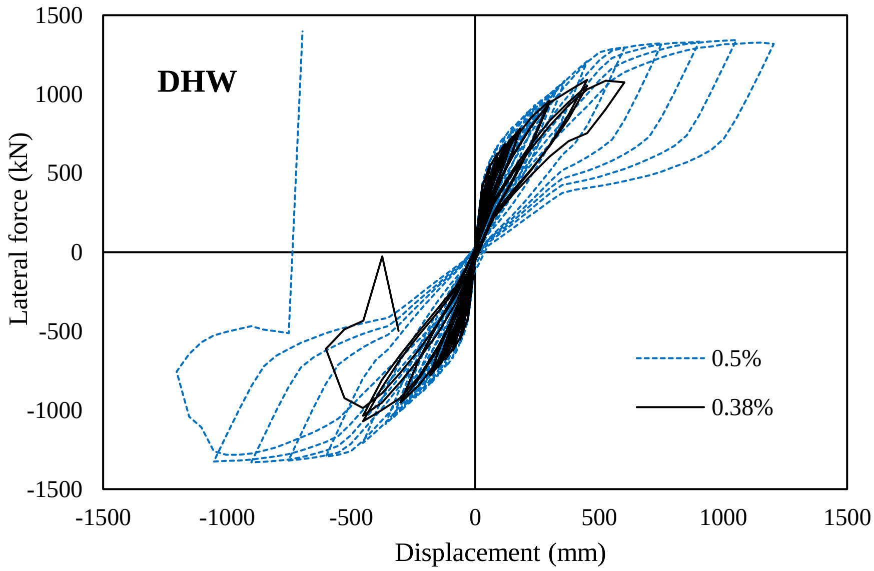

Figure 5-1 - Hysteretic responses of Wall DHW with ρ_l equal to 0.38% and 0.5%

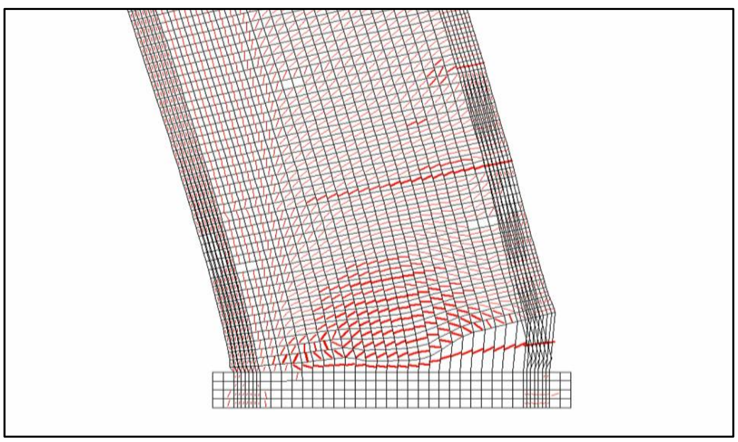

Figure 5-2 - Displaced shape and cracking pattern of Wall DHW on the verge of failure (1.5% drift)

Varying ρ_l significantly affected the response of the hybrid wall beyond 3% drift due to the localized cracks characteristic of SMA-reinforced concrete elements. To better investigate this behaviour, the smeared reinforcement in the web zone was replaced with discrete truss bar elements, spaced according to the specifications in design for the distributed vertical reinforcement of the walls.

Figure 5-3 illustrates the hysteretic response of Walls DSRW and DHW, modelled with smeared and discrete truss bars in the web zone. The ultimate lateral capacity of the walls was substantially modified with the change in the model, while the lateral stiffness remained unaltered. The discrete reinforcement in Wall DHW resulted in a slightly reduced lateral capacity, with visible strength degradation, and similar failure mechanism due to fracture of longitudinal bars in the web zone. The response of the model containing truss bar elements in the web zone was deemed more accurate as it better represents the actual configuration of the walls and captured strength degradation in Wall DHW not captured by the smeared reinforcement.

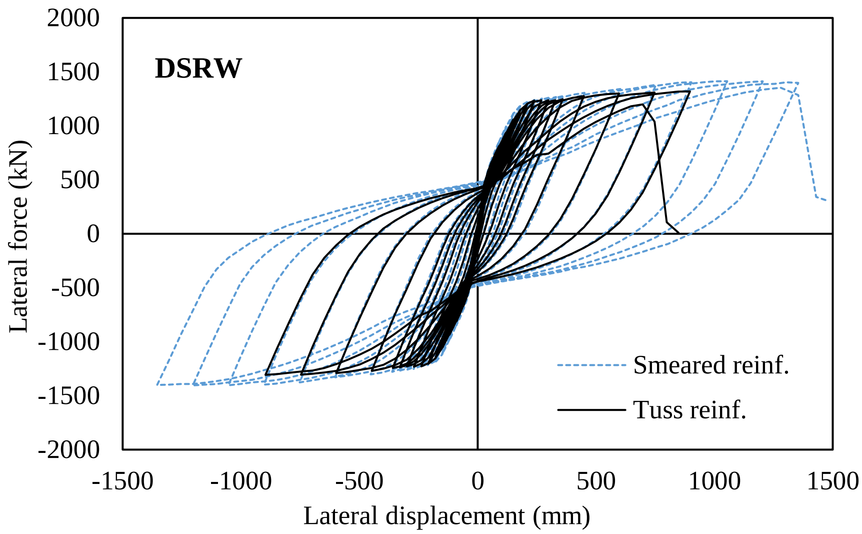

(a)

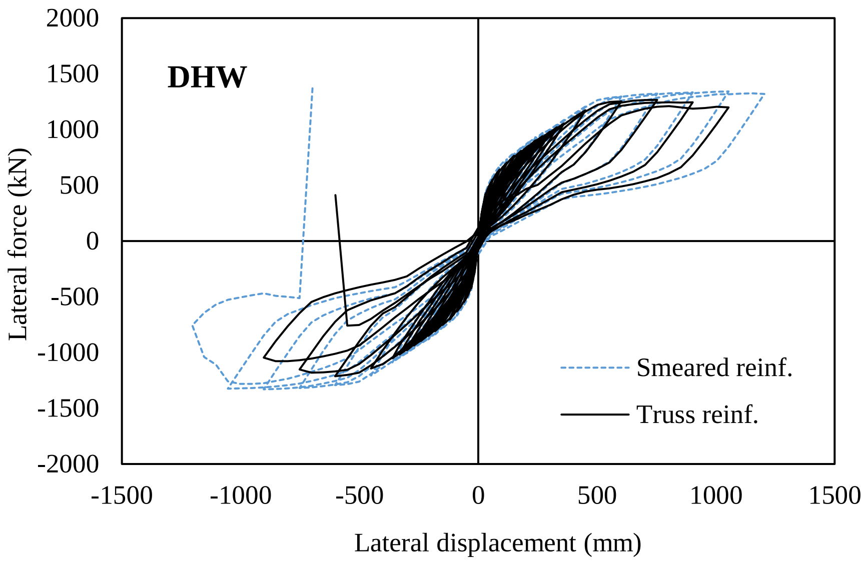

(b)

Figure 5-3 - Hysteretic response of ductile walls with longitudinal reinforcement in the web zone modelled as smeared in the concrete elements and as discrete truss bar elements: (a) Wall DSRW and (b) Wall DHW

To further investigate the relationship between the lateral capacity of the hybrid walls and the longitudinal reinforcement ratio, different values of ρ_l (0.25%, 0.35%, 0.40%, 0.45%, and 0.50%) were modelled with truss bar elements in Walls DSRW and DHW. The upper limit of 0.50% represents the maximum amount of steel allowed by the code to be placed without requiring ties. The reinforcement ratio of 0.25% corresponds to the code's minimum amount of steel for distributed reinforcement in shear walls. The walls were subjected to reverse cyclic analysis, and the resulting hysteretic responses of the various models are exhibited in Figure 5-4.

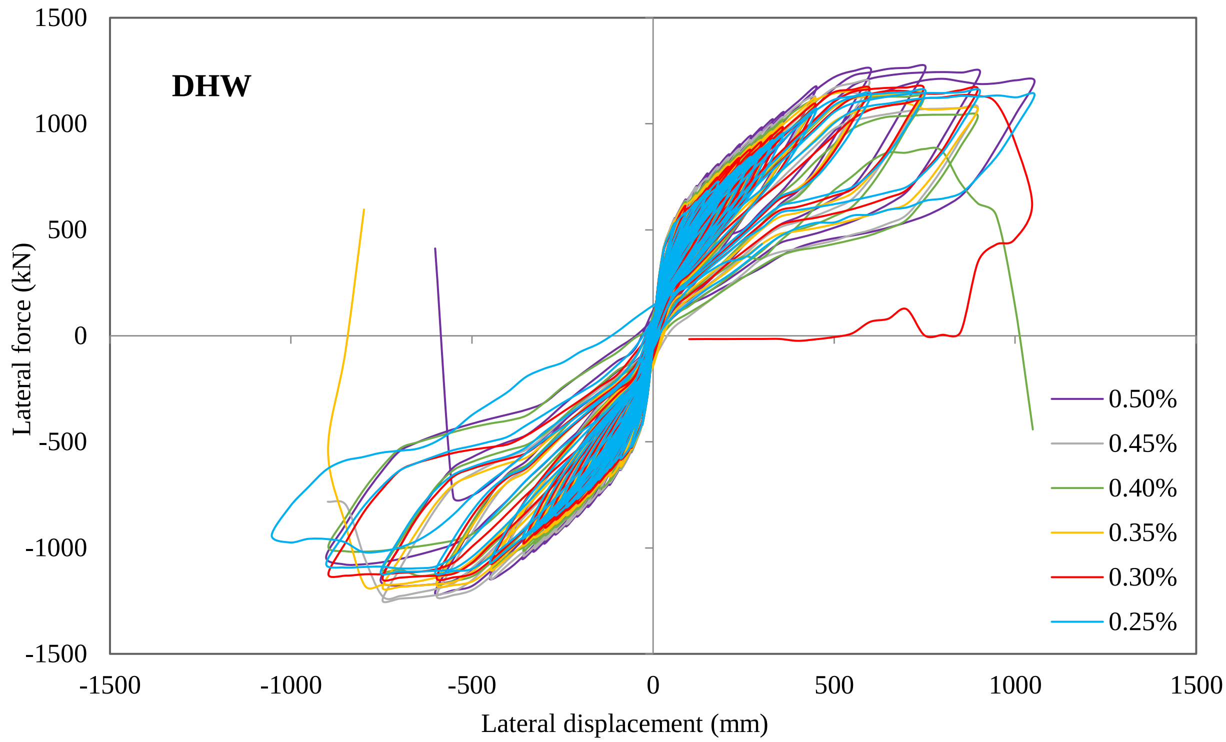

Figure 5-4 - Hysteretic response of Wall DHW modelled with varying ρ_l

Decreasing the value of ρ_l reduced the lateral strength and lateral displacement capacities. This reduction was expected and did not cause major variations on the response. The lateral strength of the wall with ρ_l ranging from 0.25% to 0.45% was reduced by 5%, on average, with respect to the wall with ρ_l of 0.50%. The maximum lateral displacement was reduced by a maximum of 15%. The response of all models was stable and did not exhibit the premature failure predicted for the wall with the smeared reinforcement in the web zone (Figure 5-1). This behaviour indicates that the use of discrete truss bar elements to model the longitudinal steel reinforcement is paramount for the modelling of hybrid SMA-steel reinforced concrete walls.

5.1.2 SMA reinforcing bars

To adequately model the anchorage of the smooth SMA bars in the concrete, different bond stress-slip relationship were investigated. The mutual presence in the finite element models of smooth SMA bars, bond elements, couplers, applied axial load, and the large number of elements due to the dimensions of the walls significantly increased the level of complexity of the finite element analysis, requiring iterative modelling procedures to converge into a stable and reliable response.

VecTor2 (Vecchio et al., 2013) permits truss bar elements to be modelled as perfectly or imperfectly bonded to concrete at different nodes along the truss element. When imperfect bond is chosen, an element is created between two overlying nodes, which can be selected as either a link or an interface element. The difference between the two types of bond elements is the complexity of the stress-slip relationship they employ. In addition, bond models and bond properties are defined by the user. Bond properties include consideration of hooked/straight bars, and the bond confinement pressure factor. This factor varies between 0 and 1 and assigns to the bar a specific fraction of the bond stress calculated internally by the program. The effects of assigning bond confinement pressure factors equal to 0, 0.5 and 1.0 in reverse cyclic analysis were investigated in Wall DHW. The resulting hysteretic responses are illustrated in Figure 5-5. As it can be observed, the superposition of the hysteretic loops from the three different models indicates that the response of SMA-reinforced walls are independent of the bond confinement pressure factor, which is possibly due to the selection of smooth bars for the shape memory alloy bars.

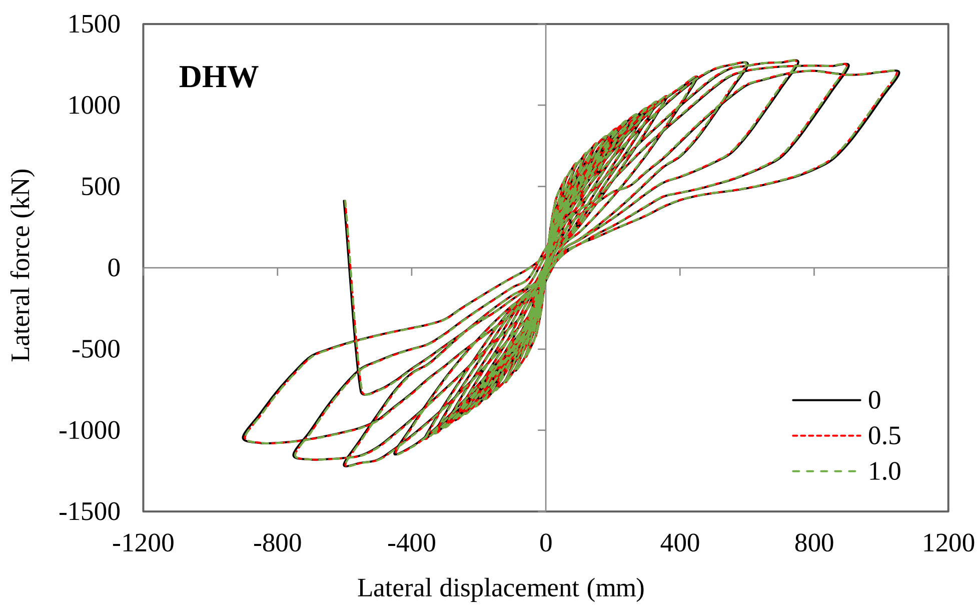

Figure 5-5 Hysteretic response of Wall DHW modelled with different bond confinement pressure factors

Different options for modelling the SMA bars were investigated in the search for a stable and reliable model. The investigation included varying the sequence of elements, the bond conditions of nodes, the length of the bars within the foundation, and the hooked/straight condition of the bars. In the final models, the SMA bars were modelled as embedded in the wall foundation, and defined as hooked in the bond properties. This modelling approach, previously used by Abdulridha and Palermo (2017), predicted the most reliable response. A steel element was used to initiate the bar to ensure stability of the model, i.e. ensure that the SMA bars would not be pulled out of the foundation during analysis. The SMA bars were modelled with perfectly bonded nodes at the extremes and imperfectly bonded nodes along the length of the bar. From the last node of the top, an element was defined as perfectly bonded to concrete and assigned the coupler reinforcement material. The top of the coupler marked the end of the plastic hinge length, from where the deformed steel truss bar elements initiated.

Next, several variations in the arrangement of SMA bars in the hybrid wall were investigated, motivated by the findings from the static analyses presented in Section 6.2. Although not economical, a wall entirely reinforced with SMA bars within the plastic hinge region could overcome the reduced lateral capacity observed in analysis due to the fracture of the steel bars in the web zone of the hybrid walls. The finite element model of this reinforcement layout is illustrated in Figure 5-6.

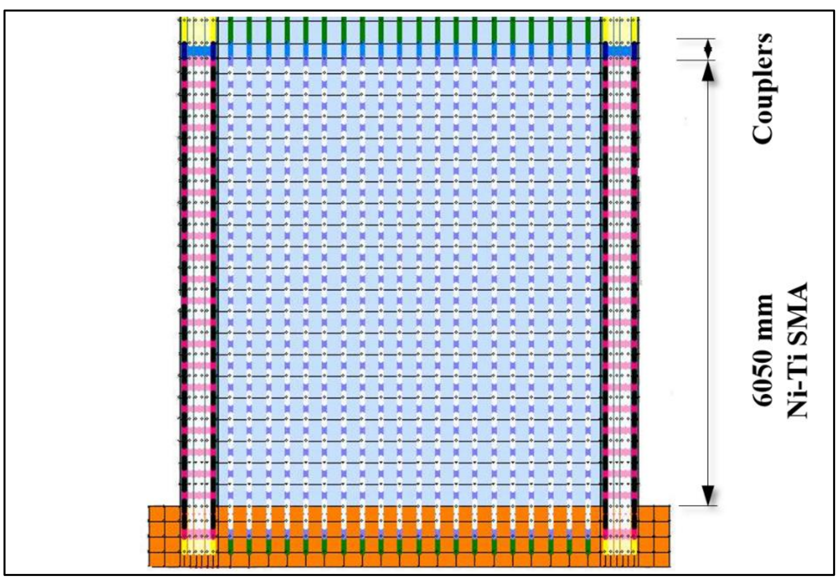

Figure 5-6 - Lower portion of the finite element model of Wall DHW with SMA bars in the boundaries and web zones

Comparison of the hysteretic response of Wall DHW with SMA bars across the entire cross-section within the plastic hinge region and Wall DHW with steel bars in the web zone is shown in Figure 5-7. The model with SMA bars across the entire cross-section exhibited a reduction in the lateral strength of 11%, and similar lateral displacement capacity. Pinching of the hysteresis loops is more pronounced, and the response is closer to the idealized flag-shaped response of self-centering systems. As a result, the energy dissipation capacity, given by the area within the hysteresis loops, is reduced. The gain in behavioural response is not as significant as the increase in cost due to the SMA.

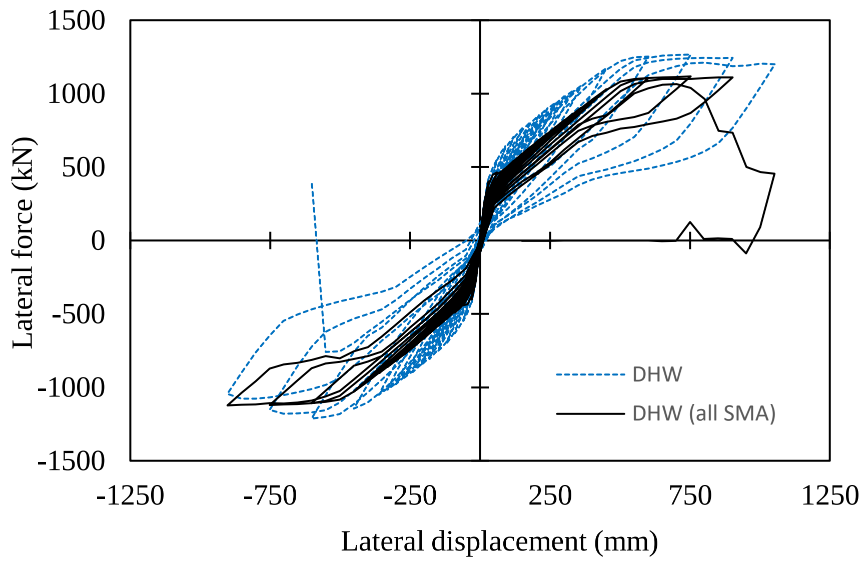

Figure 5-7 - Hysteretic response of Wall DHW with web zone reinforcement composed of steel and SMA

The effects of shortening the SMA bars in the hybrid wall was also investigated. The hysteretic response of Wall DHW revealed that 85% of the wall rotation was concentrated within a height of 1200 mm from the base of the wall. The wall developed a rocking movement at this height, where a large crack surfaced due to the poor bond of SMA to concrete. This concentration of the inelastic demand in the hybrid wall indicated that the plastic hinge length could be shorter than anticipated by the code procedure, which was developed for conventional steel-reinforced shear walls. Therefore, two additional plastic hinge lengths were investigated, corresponding to 3000 mm and 1200 mm. The finite element models developed with SMA bars extending up to 3000 mm and 1200 mm from the base of the wall in the edge zones are depicted in Figure 5-8 (a) and Figure 5-8 (b), respectively. Figure 5-9 illustrates the hysteretic response of the models of Wall DHW, plotted against the response of the original model (plastic hinge length of 6050 mm).

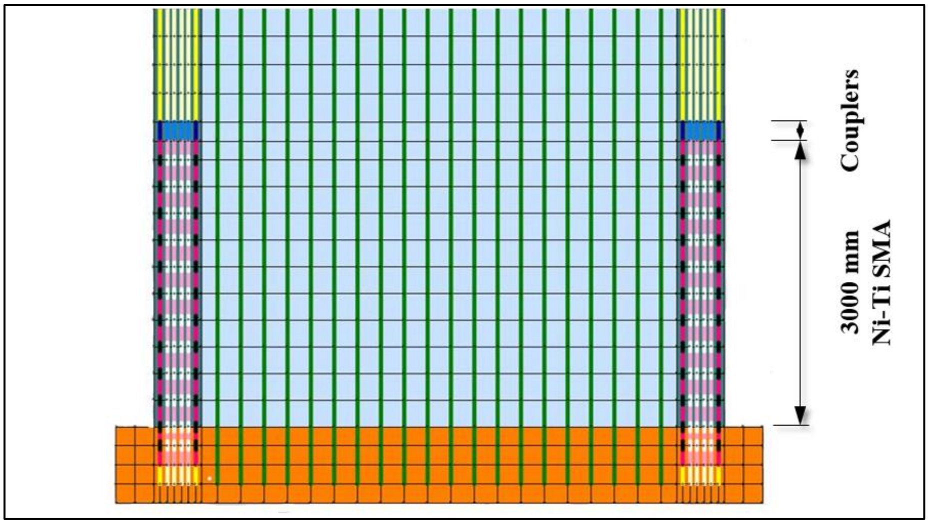

(a)

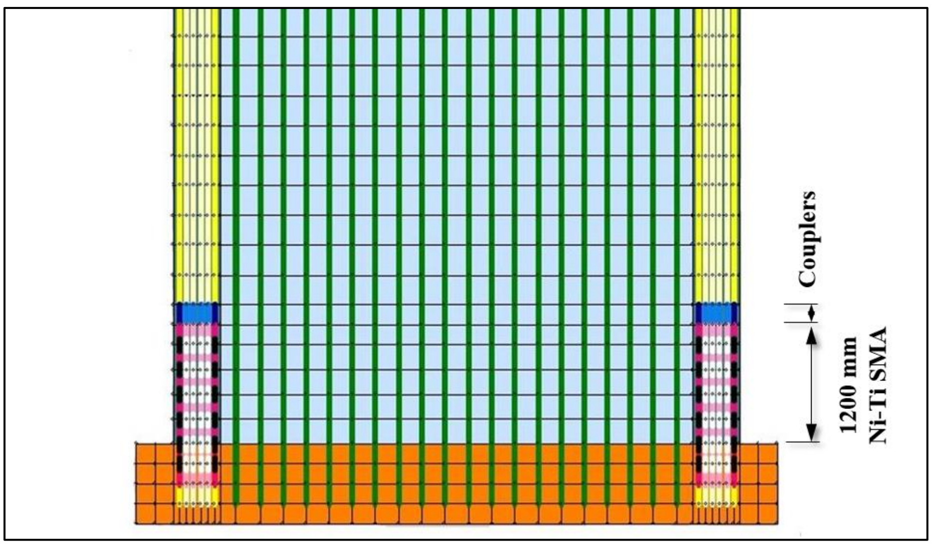

(b)

Figure 5-8 - Lower portion of the finite element model of Wall DHW with SMA bars within: (a) 3000 mm and (b) 1200 mm

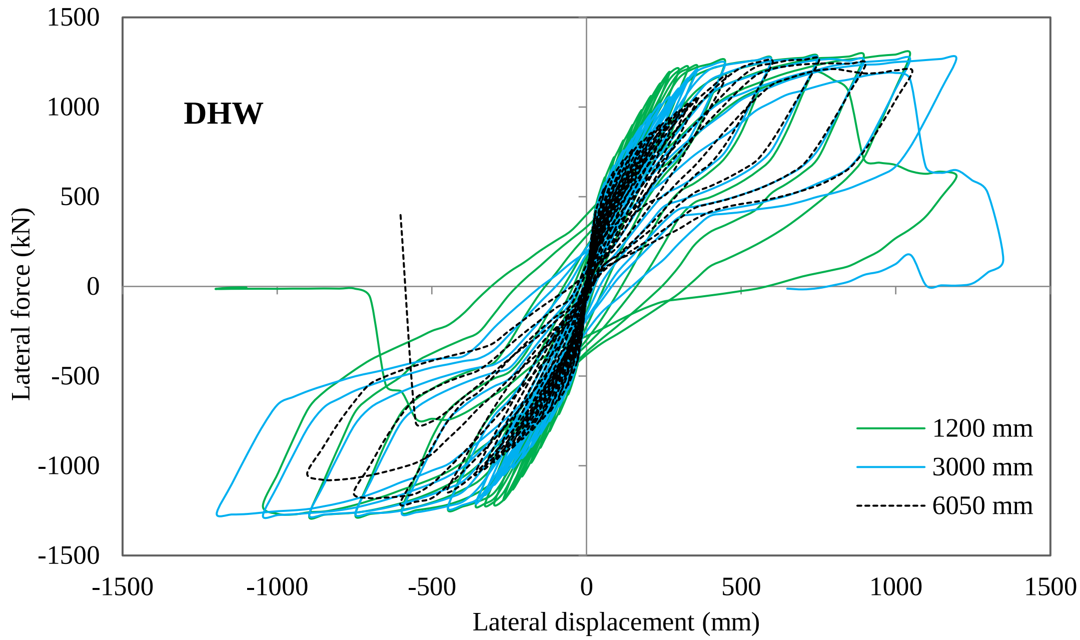

Figure 5-9 - Hysteretic response of Wall DHW with different lengths of SMA bars

Reduction in lateral strength of 1% and to 3% for the walls with SMA lengths of 3000 mm and 1200 mm, respectively. The lateral displacement capacity of the new models was larger, corresponding to an increase of 28% and 14% in the maximum lateral displacement experienced by the models with 3000 mm and 1200 mm SMA lengths, respectively, compared to the original model. The reduced amount of SMA increased the effective stiffness of the walls by 34%, in the model with 3000 mm, and by 68% in the model with 1200 mm. The main impact on the response occurred with the residual displacements exhibited by the wall upon unloading of each cycle, which is demonstrated by the wider hysteresis loops in Figure 5-9. Beyond 2.5% drift, Wall DHW recovered 96% of the lateral drifts when 6050 mm-long SMA bars were used. The recovery capacity at 2.5% drift was not altered when the bars were shortened to 3000 mm (96%), and was reduced to 82% when the 1200 mm-long bars were used. The hysteresis loop corresponding to the drift demand of 2.5% for the three lengths of SMA bars is provided in Figure 5-10. The smaller recovery capacity of the wall with 3000 mm was only present at higher drift demands. The higher energy dissipation of the walls with plastic hinge length of 3000 mm and 1200 mm is associated with the more cycles sustained. At 2.5% drift demand, the cumulative energy dissipation in the model with 3000 mm was 1.22 times that dissipated by the original model, while the model with 1200 mm dissipated 1.64 times the energy. The results indicate that shorter plastic hinge lengths could improve the cost-effectiveness of SMA-reinforced shear walls, without significant loss in performance of the self-centering system. However, the combined effect of increased stiffness, which would attract higher seismic loads, greater energy dissipation capacity, and reduced self-centering requires further investigation with the use of dynamic analysis. The complete assessment of the response of hybrid shear walls with shorter plastic hinge lengths is out of the scope of this thesis and will be addressed in future studies.

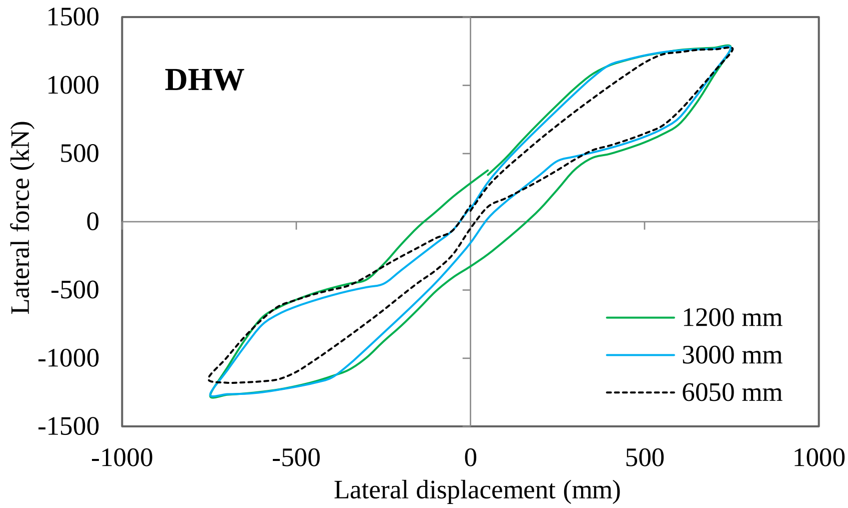

Figure 5-10 - Hysteresis loop of Wall DHW corresponding to 2.5% cycle with different lengths of SMA bars

5.1.3 Location of axial load

The distribution of the axial load acting on the walls was investigated assuming two arrangements: the distribution among the nodes on the top of the walls and among the nodes of the storey levels. Although the distribution among the storey levels is a better representation of the loads on the building, this arrangement led to complexities in the model, such as the need for stiffening the elements to prevent local crushing of concrete due to high axial loads. Within the plastic hinge region of the hybrid walls, this distribution added specific complexity due to the interaction of the axial loads with the SMA bars and the bond elements. Reverse cyclic analysis of Wall DHW with axial load distributed at the storey levels demonstrated a reduction in the lateral displacement capacity of the wall, as provided in Figure 5-11. Maximum displacement was reduced by 29% when compared to the maximum displacement sustained by the model with axial load concentrated at the top of the wall. The lateral strength, stiffness and residual displacements were not affected by the change. This reduced lateral displacement capacity is counter-intuitive, since concentrating all the axial load at the top should magnify the *P-Δ* effects, and could be related to the complexity of the model. As a result, the simplification of concentrating the axial load at the top of the walls was understood as acceptable.

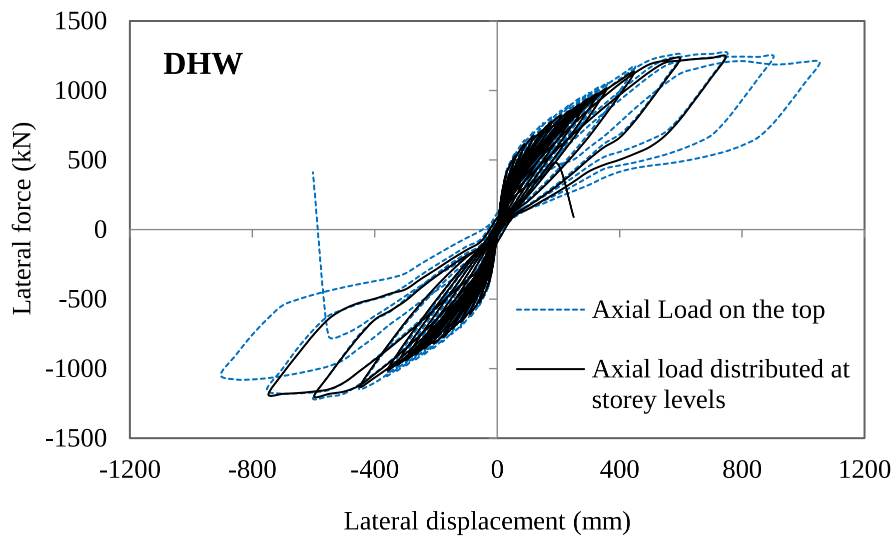

Figure 5-11 - Hysteretic response of Wall DHW modelled with different distribution of axial loads

5.1.4 Stiffer elements due to the presence of slabs

Investigation of the effects of different forms of distributing the axial load on the walls exposed that applying the axial load as nodal loads among the elements at the storey levels led to instability of the analysis and, therefore, required the implementation of stiffer elements at these locations. In the building under study, the shear walls were laterally supported by 225 mm-thick flat slabs at each of storey levels. The presence of the slabs in the models would potentially increase the strength of the walls due to the overlap of reinforcement. In order to investigate this effect, a model was developed with a concrete region defined for the elements at the storey levels, with out-of-plane width corresponding to the tributary width of the shear walls (1500 mm) and with reinforcement smeared in the 0°, 90° and out-of-plane directions. The model of Wall DHW is shown in Figure 5-12.

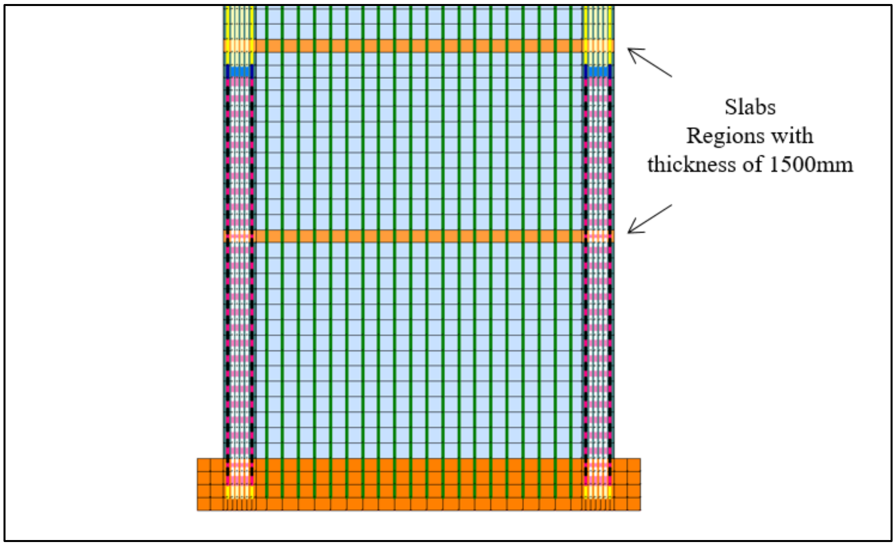

Figure 5-12 - Lower portion of the finite element model of Wall DHW, highlighting the concrete regions defined to represent the slabs

The variation on the hysteretic response due to the addition of the slabs and the distribution of the axial load at the storey levels was deemed insignificant to justify the adoption of a more complex model for the static analyses. The need for stiffer elements imposed by the distribution of the seismic masses among the storey levels governed the modelling decisions for the dynamic analyses. The slabs were consequently introduced in the models of the walls employed for dynamic analysis.

5.1.5 Concrete cover

As the horizontal reinforcement, from both in-plane and out-of-plane directions, was smeared in the concrete elements in all regions of the models, a potential overstrength was present at the concrete cover of the walls. The increased confinement due to the presence of reinforcement could delay spalling of the cover, potentially overestimating the lateral capacity of the wall if the loss of the concrete cover triggered other failure mechanisms in the walls. To investigate this issue, a model was developed with a plain, unconfined, concrete region for the concrete cover at the boundaries of the walls. The detail of the cover in the finite element model of Wall DHW can be observed in Figure 5-13. When subjecting the model to reverse cyclic analysis, the discretization of the concrete cover was found to have negligible impact on the response of the walls. Therefore the models with uniform concrete properties in the boundary zones were preferred for simplicity. The simple use of plain concrete in the cover may not be sufficient for VecTor2 to capture the effects of cover spalling. More sophisticated procedures could be investigated in order to introduce this effect in the models, such as the use of the element erosion tool recently added to the latest version of the program.

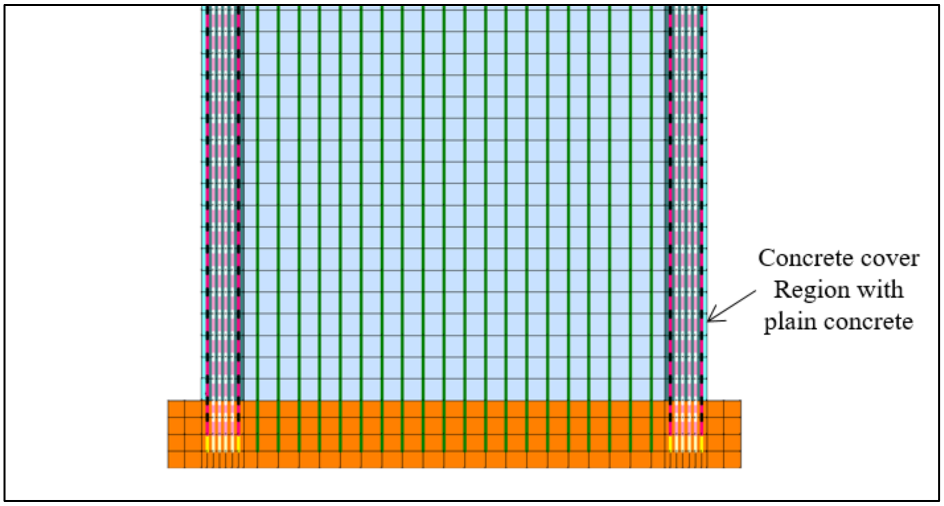

Figure 5-13 - Lower portion of the finite element model of Wall DHW, highlighting the region defined for the concrete cover

5.1.6 Finite element mesh

The limit in number of elements and nodes existing in the version of FormWorks (Vecchio et al., 2013) employed in this thesis governed the finite element mesh size used in the models. Given the large dimensions of the walls, which are 6 m-wide and 30.5 m-high, the size of the elements could not be refined below the sizes presented in Section 4.1. For that reason, accuracy of the finite element mesh could not be tested through incremental mesh refinement. However, a comparison of the numerical results with that from the benchmark studies, which will be presented in Section 7.1, validated the adopted models and their respective finite element mesh.

As the study progressed to the dynamic analysis phase, a new meshing constraint surfaced, i.e. the size of the matrices for stiffness, mass and damping that VecTor2 is capable of handling. To address this constraint, the size of the elements was increased in order to reduce the total number of nodes in each model. The modified models used for dynamic analyses are presented in Figure 4-3. To ensure that this modification did not affect the accuracy of the analysis, reverse cyclic analyses were performed with the modified models, and results were compared to those obtained using the original models with refined finite element mesh. As an example, the comparison of the hysteretic response of Wall MDHW between the two models is illustrated in Figure 5-14, where it is evident that the hysteretic loops from both models almost coincide, indicating similar lateral strength, stiffness, and recentering capacity. However, capturing the failure mode is a very sensitive task in simulations, and the lack of a comparable experimental test hinders the decision of which modelling aspects result in the more realistic response. The variation in the response of the walls at high levels of drift demand (above 3%) caused by the modification in the models was not considered critical. In addition, most of the dynamic analyses conducted using the modified models did not subject the walls to this level of drift demand. Therefore, within the code limit of 2.5%, the response of the modified models is deemed acceptable and accurate in terms of the previously conducted reverse cyclic analysis.

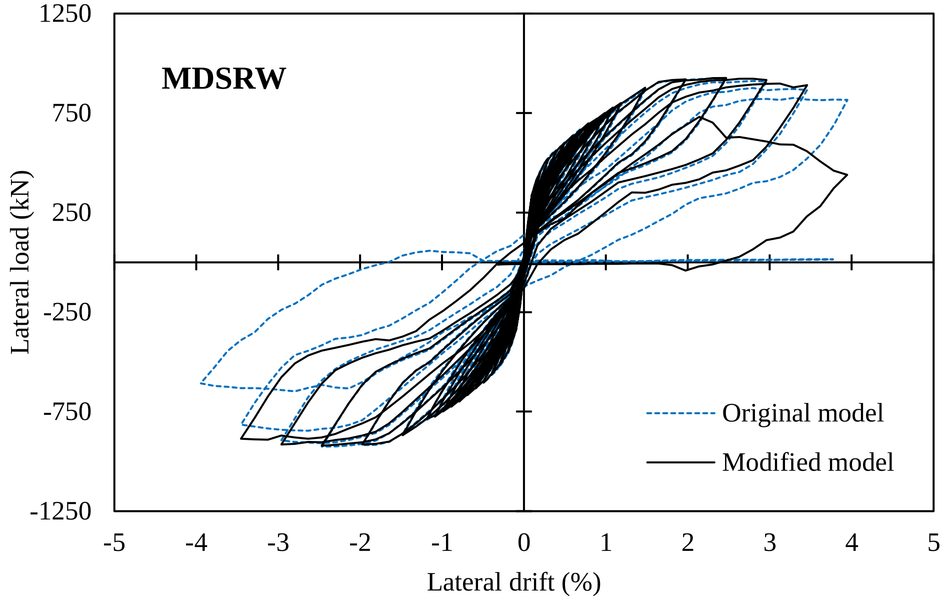

Figure 5-14 - Hysteretic response of Wall MDSRW resulting from original model used in static analysis and modified model with increased mesh size

5.2 Material properties

5.2.1 Limit strains in reinforcement

Figure 5-15 illustrates the hysteretic response of Wall DHW modelled with different values of ε_{sh} and ε_{su} of steel and subjected to reverse cyclic analysis. The effects of different values of strain hardening strain (ε_{sh}) and ultimate strain (ε_{su}) of steel were investigated, where the combinations of ε_{sh} and ε_{su} listed in Table 5-1 were assigned to all reinforcing steel in the models. The objective of this sensitivity analysis was to investigate the influence of the steel properties in the fracture of the longitudinal steel reinforcement in the web zone of the hybrid walls observed in analysis. In the model named *Benchmark model* in Figure 5-15, typical properties for steel and concrete were used, following that used by Abdulridha and Palermo (2017), where the strain limits adopted for the larger diameter steel bars corresponded to ε_{sh} of 20 mm/m and ε_{su} of 120 mm/m. The strain limits for the 10M steel bars, which were all modelled as smeared in the concrete elements, were equal to a ε_{sh} of 10 mm/m and a ε_{su} of 80 mm/m.

Table 5-1 - Strain combinations investigated

Strain combination	ε_{sh} (mm/m)	ε_{su} (mm/m)
1	20	80
2	20	120
3	10	80
4	10	120

Varying the strain limits did not significantly influence the response of Wall DHW. The ultimate displacement of the wall was shortened by one cycle when smaller values of ultimate strains were considered. The strain combination from the benchmark model resulted in the largest lateral displacement capacity. The results from this sensitivity analysis indicated that the fracture of the steel bars in the web zone of the hybrid walls was not related with the strain limits adopted for the longitudinal steel reinforcing bars.

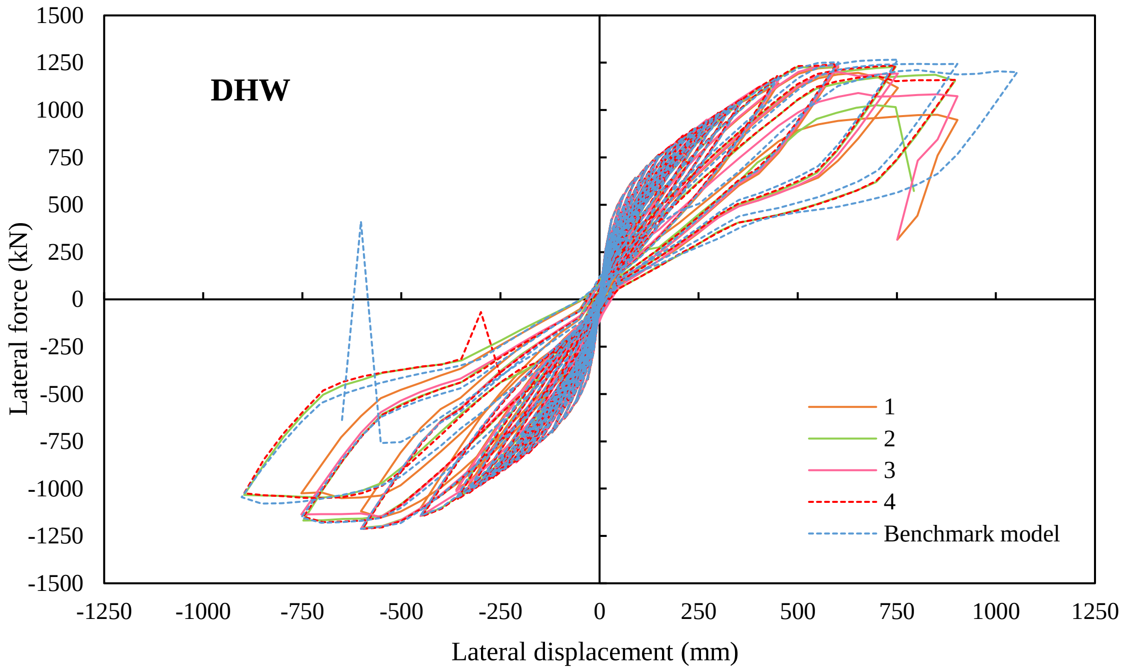

Figure 5-15 - Hysteretic response of Wall DHW modelled with different combinations of strain limits of steel

5.3 Material models

5.3.1 Hysteretic response of steel reinforcement

For the hysteretic response of the steel reinforcement, the default model in VecTor2 (Vecchio et al., 2013) was employed, which corresponds to the Seckin model with Bauschinger effect. The same model was employed in the benchmark study by Abdulridha and Palermo (2017). In addition, the effects of accumulation of damage in the reinforcing bars were investigated with the use of the Seckin model with local accumulation. The hysteretic response of the ductile walls is exhibited in Figure 5-16, where the response obtained with the use of the default model is superimposed over the response of the model under investigation. The use of the Seckin model with local accumulation in Wall DSRW (Figure 5-16 (a)) resulted in similar lateral strength and lateral displacement capacity, but in larger residual displacements after each cycle. In Wall DHW (Figure 5-16 (b)), the use of the new model amplified the strength degradation of the wall at late stages of loading and resulted in slightly larger residual displacements. The lack of experimental results from testing of walls with comparable height to that investigated herein hinders the assessment of which model is more accurate when assessing the response of the walls. Therefore, the models used by Abdulridha and Palermo (2017) in the numerical analysis of the walls, which were corroborated with experimental results, were preferred for both the hysteretic response of steel and concrete, discussed in the following sections.

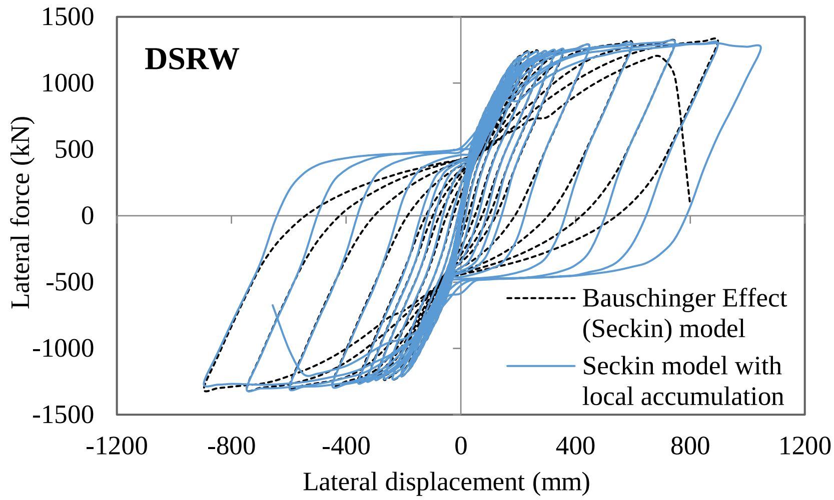

(a)

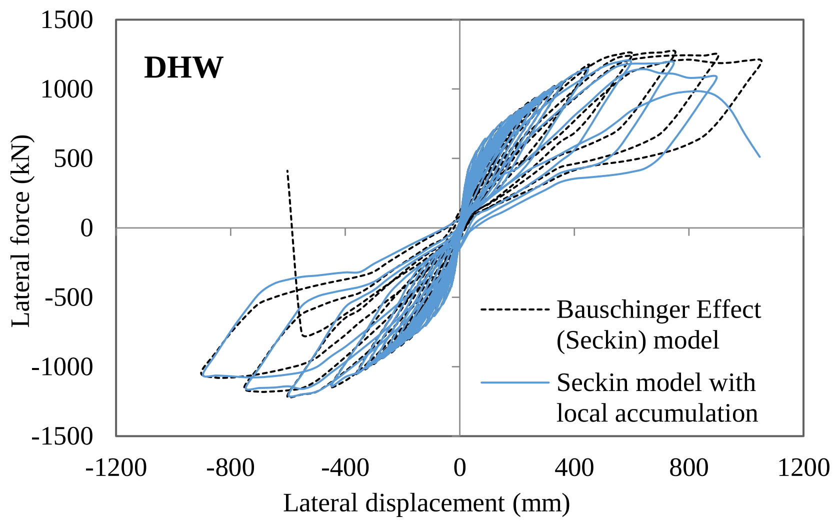

(b)

Figure 5-16 - Hysteretic response of ductile walls with hysteretic response of steel reinforcement defined according to different material models: (a) Wall DSRW and (b) Wall DHW

5.3.2 Hysteretic response of concrete

The effects of two material models were investigated for the hysteresis of concrete: the nonlinear model with plastic offsets and the Palermo 2002 model with decay. Figure 5-17 (a) and (b) present the hysteretic response of Walls DSRW and DHW, respectively, when the two material models were adopted. The use of the Palermo 2002 model had opposite effects on the two walls, increasing the lateral displacement capacity of Wall DSRW and reducing that of Wall DHW. However, the effects of the model were only noticeable at late stages of loading and did not affect the strength, stiffness or residual displacements of the walls. The lack of experimental results hinders the confidence in adopting material models different from that validated by previous studies, and the hysteresis of concrete was therefore modelled according to the default model in the program, i.e. the nonlinear model with plastic offsets, as adopted by Abdulridha and Palermo (2017).

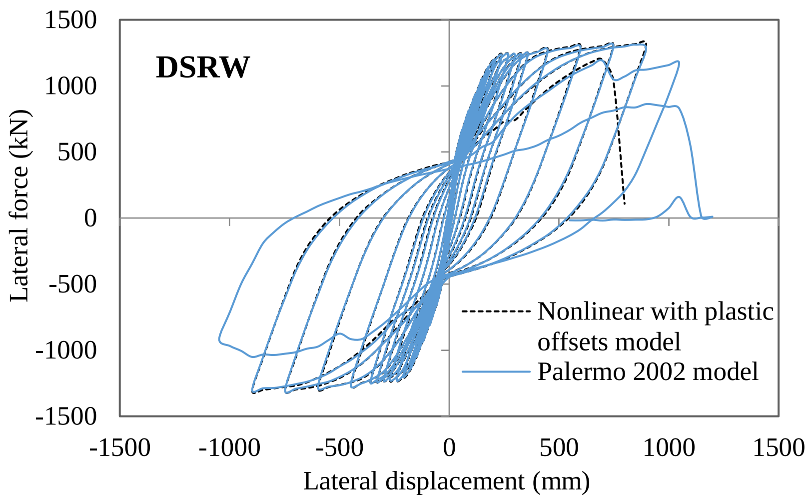

(a)

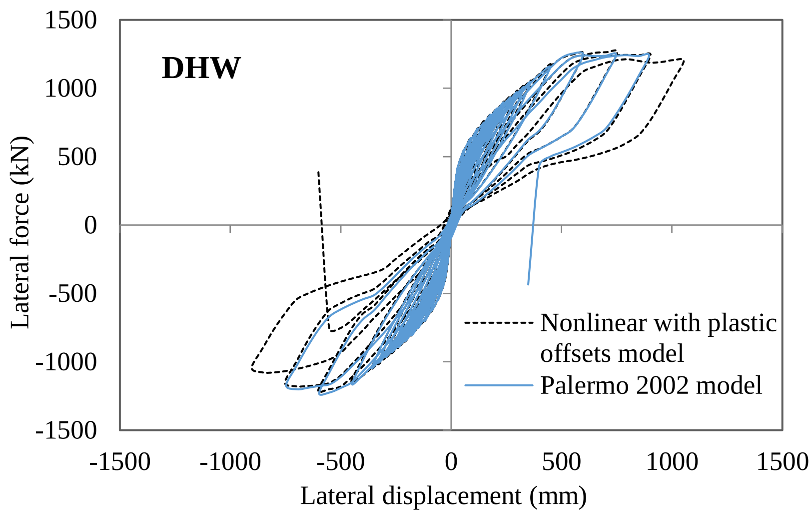

(b)

Figure 5-17 - Hysteretic response of ductile walls with hysteretic response of concrete defined according to different material models: (a) Wall DSRW and (b) Wall DHW

5.4 Analysis parameters in static analysis

5.4.1 Loading protocol for reverse cyclic analysis

The reverse cyclic analyses in this thesis were conducted with the application of incremental lateral displacements at the top of the walls. The parameters of the loading protocols for this type of analysis include the increment size, the initial and final factors for the first cycle, the number of cycles, the number of repetitions for each cycle, and the total number of cycles. The increment size directly impacts the required computational time. The number of repetitions is also an important parameter, as the repetition of cycles contributes to the accumulation of damage, potentially affecting the ultimate lateral displacement capacity of the walls. Multiple load protocols were investigated with the use of different parameters in the search for an acceptable level of accuracy combined with optimal computational time. The number of repetitions varied from 1 to 3. Figure 5-18 illustrates some of the load protocols investigated, which employ various cyclic increments, number of repetitions, and total number of cycles.

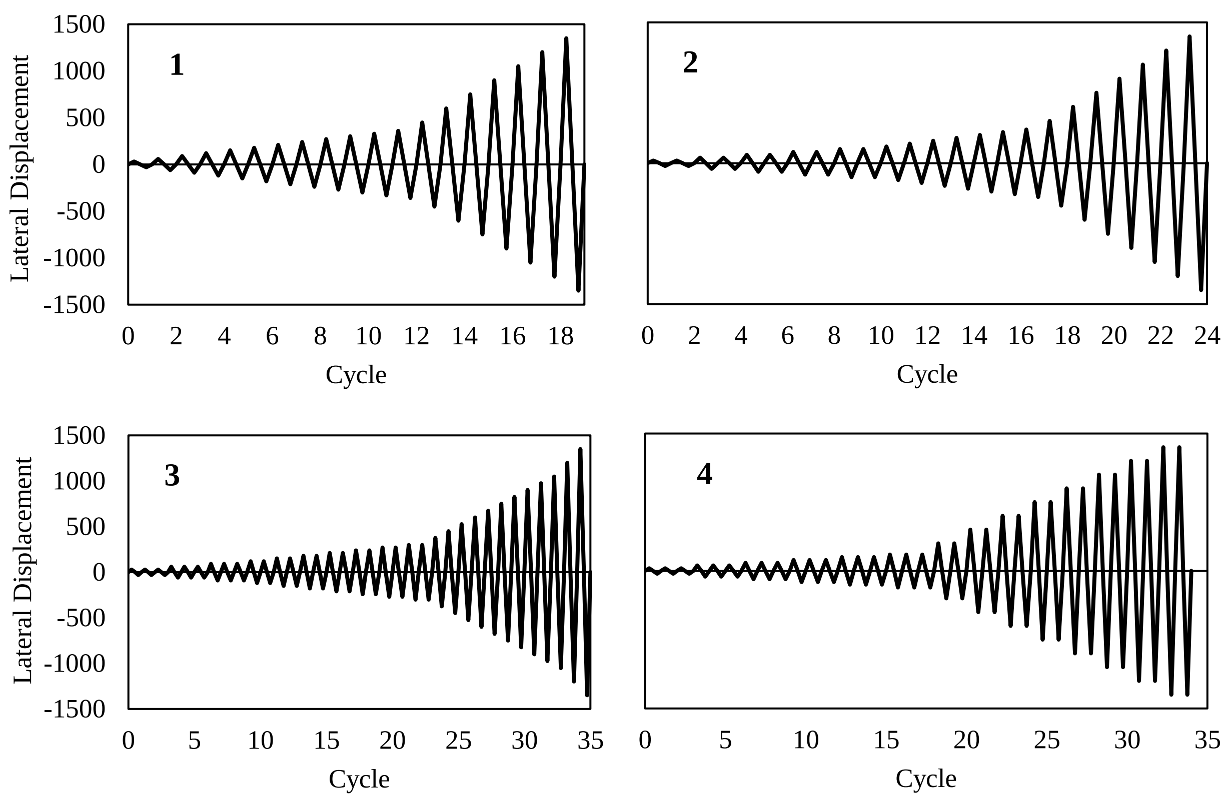

Figure 5-18 - Samples of load protocols investigated for reverse cyclic analyses

The hysteretic responses resulting from the use of the different load protocols are illustrated in Figure 5-19. The variation in the response of both walls is small, with the exception of the response of Wall DSRW to load protocol 4, where the use of multiple repetitions resulted in some strength degradation, but also in an increased lateral displacement capacity.

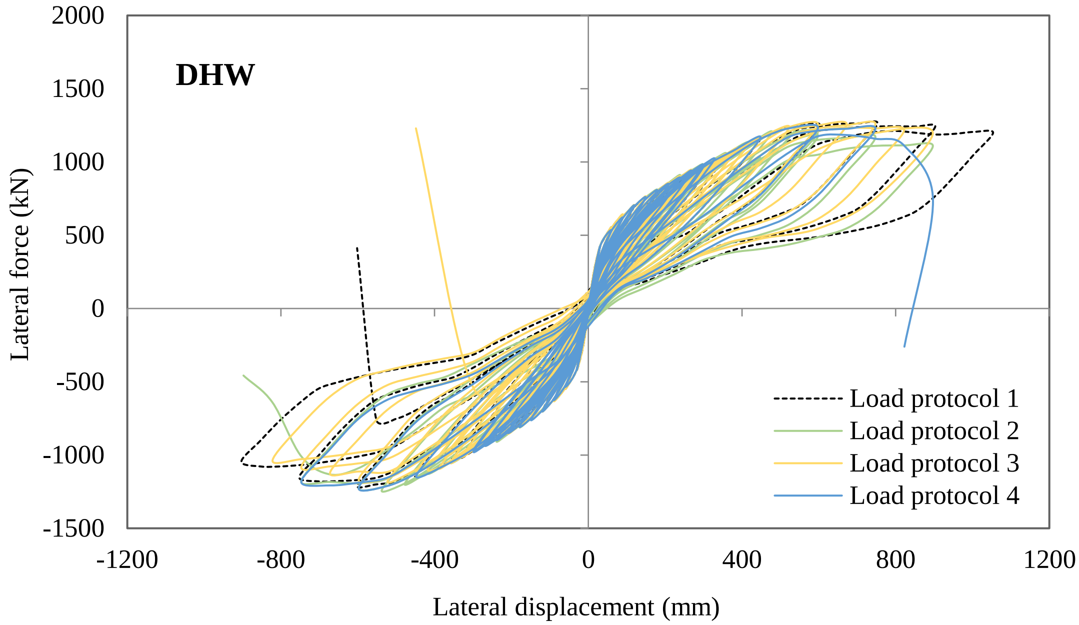

(a)

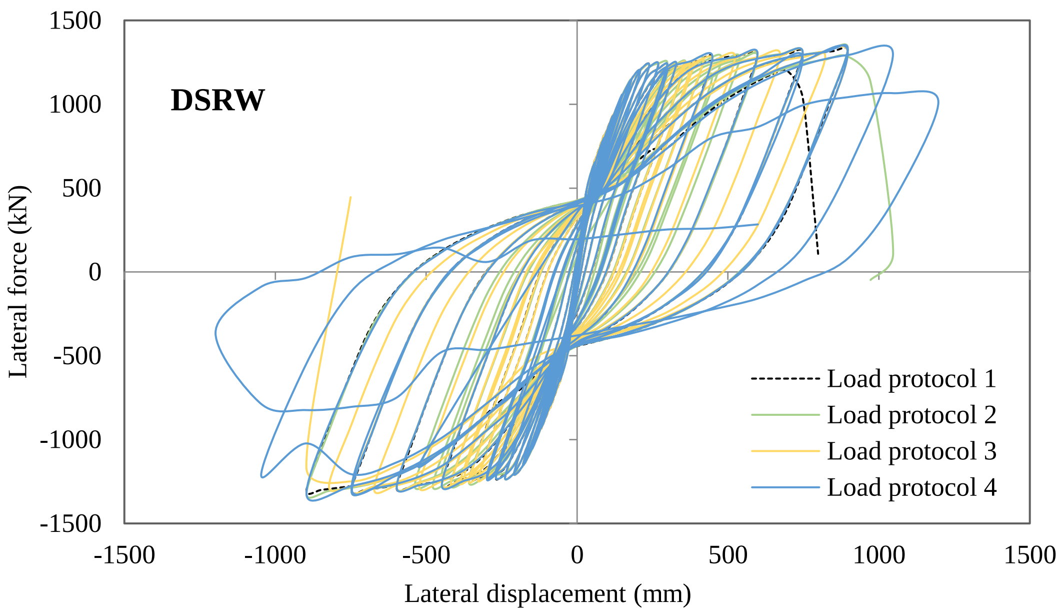

(b)

Figure 5-19 - Hysteretic response of ductile walls with various load protocols: (a) Wall DSRW and (b) Wall DHW

The post-processor Augustus (Vecchio et al., 2013) was found to have deficiencies regarding the number of output files it could process. This is attributed to the complexity of the finite element model, with the number of elements close to the limits imposed by the program. Because of that, the number of repetitions adopted was limited to 1, and the load protocol selected to run the reverse cyclic analyses in this thesis, considering the desired level of accuracy and the optimization of the analysis, is that represented by protocol 1 in Figure 5-18. In this loading protocol, the final factor of each cycle corresponded to incremental fractions of the drift at yielding of the steel-reinforced walls, and at pseudo-yielding of the SMA-reinforced walls. Prior to yielding/pseudo-yielding, the cycles were run in increments of 0.1% drift, and reduced step sizes within the cycles were used to better capture the evolution of the stiffness of the walls. Beyond yielding, the final factor for the cycles had increments of 0.5% up to failure of the walls. Within the cycles with larger final drifts, the step size was increased to minimize the required computational time.

5.5 Analysis parameters in dynamic analysis

5.5.1 Location of seismic masses

The distribution of the seismic mass corresponding to the wall was investigated following different criteria, including: distribution among every node in the model (Model 1); distribution among the nodes corresponding to each storey level (Model 2); lumping of the masses at one central node per storey level (Model 3); and at a single node at a height corresponding to the resultant M_f / V (19600 mm) of the wall (Model 4). Model 1 led to instability of the analysis, resulting in termination of the analysis and in a displaced shape of Wall DSRW upon failure as depicted in Figure 5-20 (a). Model 2, prior to the addition of stiffer slab elements, also incurred instability, with localized distortion of elements occurring where masses were assigned in Wall DSRW, as illustrated in Figure 5-20 (b). Model 2, with stiffer slab elements, and Model 3 resulted in stable analyses. Eigenvalue analysis of Model 3 was used to capture the modal periods of vibration of the walls since this model has ten degrees of freedom and would provide ten modes of vibration (details of the eigenvalue analysis is presented in Section 6.3). The use of one central mass per storey (Model 3) or one mass per node of the storey level (Model 2) did not modify the dynamic response of the walls. To be in accordance with the 3-D model of the building developed in SAP2000® (CSI, 2016), the consideration of mass as lumped at the storey levels (Model 3) was preferred. This model also had a reduced number of degrees of freedom compared to Model 2. Model 4 was solely used to define an equivalent single degree of freedom system in order to validate the masses and periods obtained with the other models, and also resulted in stable analysis.

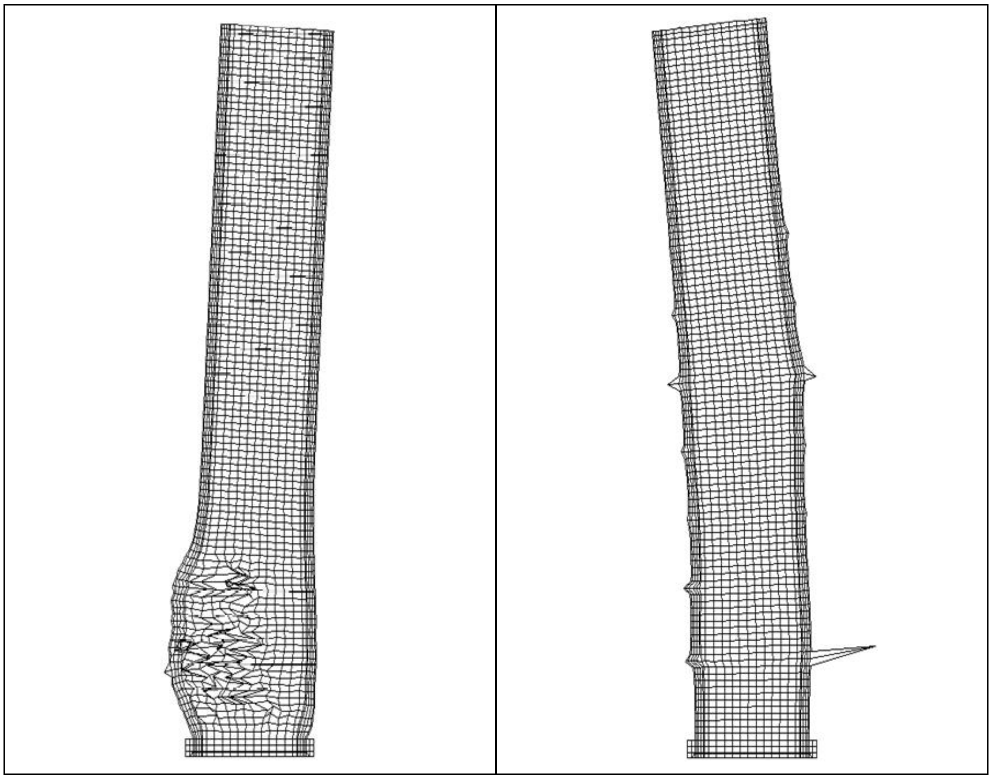

(a) (b)

Figure 5-20 - Displaced shape of Wall DSRW upon failure when modelled according to: (a) Model 1 and (b) Model 2

5.5.2 Application of axial load

In the finite element models employed for dynamic analysis, the use of stiffer elements at the storey levels was found to be mandatory. Therefore, the axial loads could be distributed at the storey levels without further complications. In dynamic analysis, VecTor2 (Vecchio et al., 2013) also permits axial loads to be assigned by the conversion of the considered seismic masses through the application of a load factor. With axial loads applied as nodal loads, two possibilities exist in VecTor2: to assign the loads to the same load case that contains the dynamic analysis, or to define a second load case with monotonic loading just for the axial loads. The attempt to model the first case failed because of numerical convergence problems with VecTor2. The second possibility resulted in the same response of that obtained when portions of the mass were converted into axial loads. Therefore, axial loads were not applied as nodal loads, but considered at every storey level with the use of a factor to convert the applied masses into static loads. In this case, no specific load case was defined for the axial loads.

5.5.3 Damping

Viscous damping is introduced to the dynamic response calculated by VecTor2 using the Rayleigh's damping model, according to which specific damping ratios are assigned to designated modes of vibration of the structure. Suggested values of damping ratio found in the literature range from 1% to 2%, and references to modes of vibration range from the first to the third modes. For the analyses in this thesis, the following damping parameters were investigated: 0%, 1%, 1.5%, and 2% damping ratios, applied to the first and second modes, and to the first and third modes of vibration.

Little variation was predicted in the top-displacement time history of the walls when the damping parameters were altered. Minor variation was evident when comparing the response obtained using 1% or 1.5% damping in the first and third modes for Wall DSRW when subjected to the earthquake record 313 (Corinth, Greece), as shown in Figure 5-21. This might be due to the fact that the majority of the damping in the dynamic response generated by VecTor2 has been acknowledged to be supplied by other behavioural mechanisms, such as concrete cracking and material hysteresis (Saatci, 2007), while minor amounts of viscous damping are incorporated by the Rayleigh's method. Therefore, the pair of reference modes adopted for the dynamic analyses were the first and third modes, as the third mode is the one that accumulates more than 90% of mass participation in the dynamic response of the walls, while the damping ratio was set as 1.5%, in accordance with the literature review, as presented in Section 2.5.2.

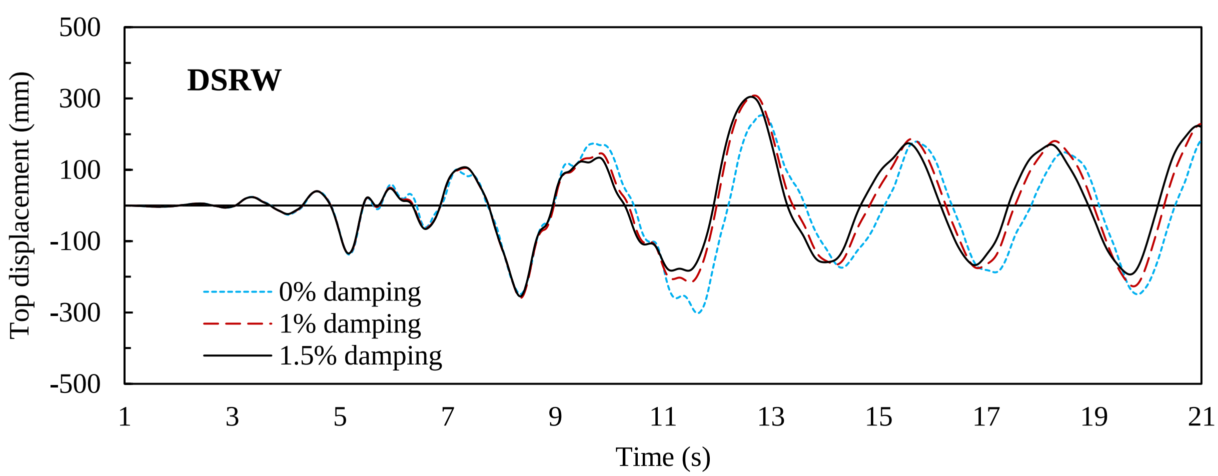

Figure 5-21 - Top displacement time history of Wall DSRW with different damping ratios

5.5.4 Time interval for numerical integration

In VecTor2 (Vecchio et al., 2013), the time step adopted to generate output files, which defines when the results are recorded, divided by the user-defined number of repetitions determines the time interval the program uses for the numerical integration. VecTor2 allows the time step between output files to be different than that employed internally to calculate results, in order to optimize the analysis, if desired. The time interval employed by the program for the Newmark's direct integration procedure directly affects the accuracy of the results and the stability of the analysis, as well as the computational time required to run each stage. When stability is not ensured, unbounded oscillation occurs and the results will exhibit limitlessly increasing displacements (Saatci, 2007). Multiple values for time step and number of repetitions were investigated in this thesis. The convergence of the results with the refinement of the analysis parameters was evaluated, permitting the selection of an optimal combination of time step and repetitions to obtain accurate results and less time-consuming analyses.

To attest the accuracy of the mentioned parameters, further analyses were conducted. Analyses of Wall DSRW, subjected to a sample simulated ground motion record, were performed employing a numerical integration time step of 0.005 s with 20 repetitions (output files at every 0.1 s), 10 repetitions (output files at every 0.05 s), and 4 repetitions (output files at every 0.02 s). Further analyses of Wall DSRW, subjected to a sample historical earthquake record, employing a numerical integration time step of 0.0029 (with 10 repetitions and output files at every 0.029 s) and of 0.00029 (with 100 repetitions and output files at every 0.029 s) were conducted. The top displacement time histories of these analyses, provided in Figure 5-22 (a) for 15 s and Figure 5-22 (b) for 20 s, indicated that integration time steps smaller than 0.001 s had minor influence on the results. As a result, the time steps for numerical integration were selected to match the time step of the ground motion record employed in each analysis. The simulated records for eastern Canada had a time step equal to 0.002 s, thus the time step for the output files was set as 0.02 s with 10 repetitions, resulting in a time step for numerical integration of 0.002 s. The time step varied among different historical earthquake records for western Canada. In general, numerical integration time steps of 0.005 and 0.001 were obtained with the use of 2 or 10 repetitions, generating output files at every 0.01 s.

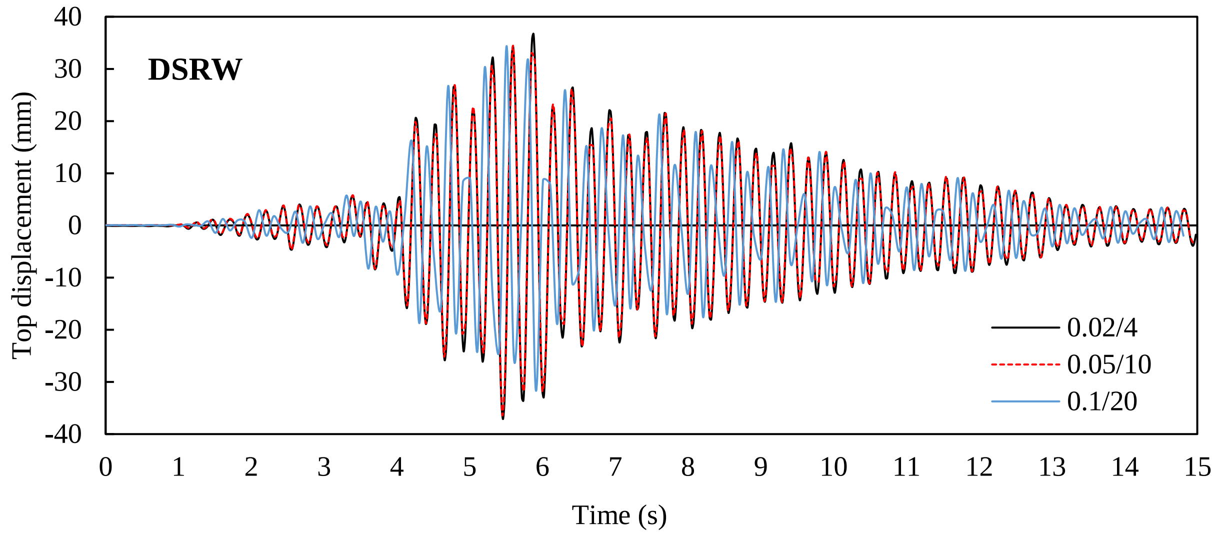

(a)

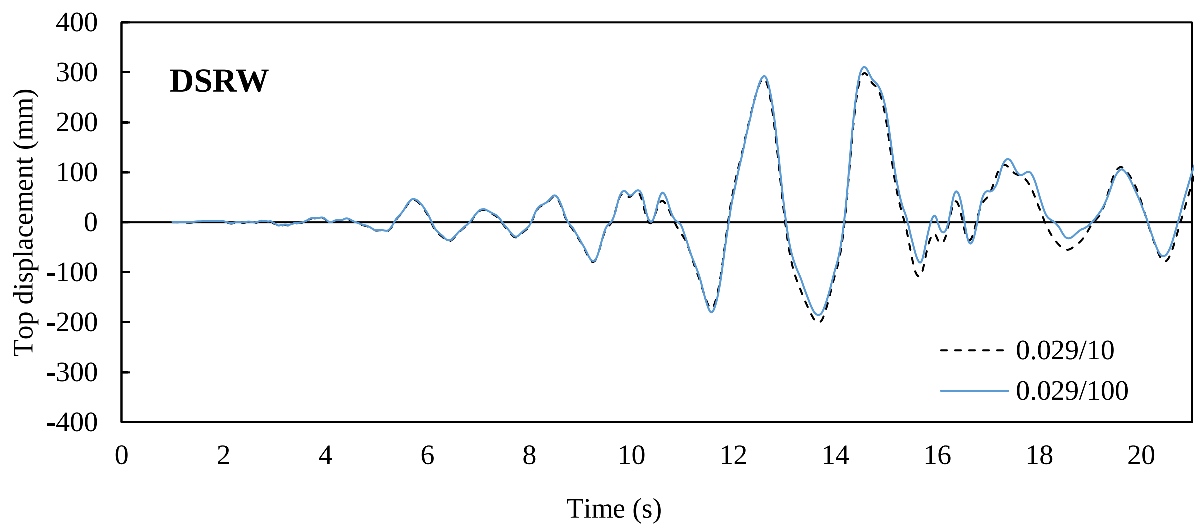

(b)

Figure 5-22 - Top displacement time histories of Wall DSRW: (a) initial 15 s of analyses the same incremental step but different repetitions and (b) initial 20 s of analyses using different incremental steps

5.5.5 Duration of analysis

The duration of the seismic excitation varies among different historical earthquake records. Among the simulated ground motion records from the Engineering Seismology Toolbox (Atkinson, 2009), the main excitation is concentrated at variable intervals, although most records last for 20 s. For this reason, and to capture the decay of the response and the permanent displacements in the walls, time history analyses were carried out by different time spans, such as 40 s, 60 s, and 80 s. The exception was the simulated records that represent the Cascadia earthquakes, which occur at longer distances and have longer periods, with consequent longer durations. Records of this type of event are provided with a duration of 260 s. The analyses representing Scenario 3 in Vancouver, which employed Cascadia simulated records, were run for 150 s. It was found that those time spans are sufficient to ensure that the main energy content of the earthquake was considered and the decay of the response was captured.

The computational time required to conduct the time history analyses depended on the size of the ground motion record and on the selected time increment. The time history analyses of eastern Canada, where all records had duration of 20 s and employed a numerical integration time step of 0.002 s, required approximately 26 h to be concluded. In western Canada, the variability between the earthquake records of Scenarios 1 and 2 resulted in different analysis time requirements. On average, 40 s of analysis required 24 h to run with numerical integration time step of 0.005 s, while 80 s of analysis required around 48 h. To run the 150 s of analysis defined for the ground motion records of Scenario 3, computational time was close to 65 h. Analyses were performed in computers with 3.5 GHz processor and 64.0 GB installed memory (RAM).

5.5.6 Support reactions

The lateral strength of the walls from the dynamic analyses was corroborated against that predicted with static analyses, as presented in Section 7.1. The lateral strength predicted with the dynamic analyses were overestimated. Given the multiple analysis parameters tested and the consistency of this overestimation throughout all models and all earthquake records, there is confidence that the modelling decisions were not the cause of this issue. Over-prediction of the peak support reactions in dynamic analysis with VecTor2 has been reported by Saatci (2007), which was attributed to unrealistic contribution of high frequency response components to the numerical solution. Saatci (2007) stresses that further investigation is required in order to determine the exact mechanisms involved in the calculated extremely high peak support reactions.

6. NUMERICAL RESULTS

This chapter presents the numerical results from static and dynamic analyses performed on the ductile and moderately ductile shear walls investigated in this thesis. Results are divided into three types of response: the monotonic response (resulting from pushover analysis), the hysteretic response (obtained from reverse cyclic analysis), and the seismic response (from time history analysis). From the monotonic and hysteretic responses of the walls, the lateral strength, ultimate displacement, effective stiffness, yield point, and displacement ductility were evaluated. The assessment of the hysteretic response of the walls also included vertical displacements and failure mechanism. Lastly, the seismic response of the walls is presented in terms of modal vibration periods, top displacement time histories, transient and permanent roof drifts and interstorey drifts, progress of damage, and failure mechanisms. The numerical results were collected with the use of the post-processor Augustus (Vecchio et al., 2013), which provides values for a range of parameters that are recorded at each load step/time step and at every finite element.

6.1 Monotonic response

The monotonic response of the walls was investigated using displacement-controlled pushover analysis. Results permitted the assessment of the lateral capacity of the walls, as well as the effective stiffness and the displacement ductility.

6.1.1 Ductile walls

Figure 6-1 illustrates the monotonic response of Wall DSRW. To determine the yielding point of the shear walls in this study, the Reduced Stiffness Equivalent Elasto-Plastic Yield Method (Park, 1988) was applied. The methodology is detailed in Figure 6-1. A secant stiffness is defined at 75% of the peak lateral strength of the walls (F_{max}). The intersection between the secant stiffness and the peak strength determines the yield displacement (Δ_y). The yield strength (F_y) is the corresponding ordinate in the curve to Δ_y. According to Park (1988), this method is the most realistic to determine the yield deformation of reinforced concrete structures, since the applied secant stiffness introduces a reduction in stiffness due to cracking near the end of the elastic range.

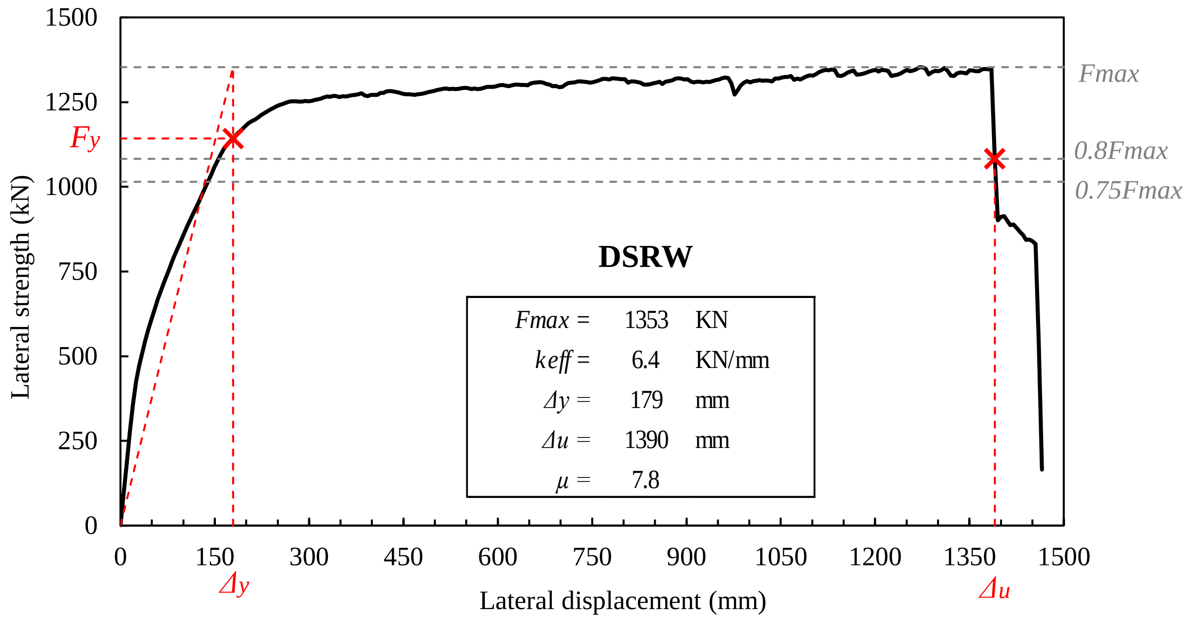

Figure 6-1 - Monotonic response of Wall DSRW

The yield point of Wall DSRW was determined at a displacement of 179 mm and a strength of 1143 kN. Wall DSRW experienced a maximum lateral strength of 1353 kN and an effective stiffness of 6.4 kN/mm. The effective stiffness (k_{eff}) was computed as the slope of the loading branch going through the yield point. The lateral displacement capacity of the walls is evaluated in terms of ultimate displacement (Δ_u), which is defined as that corresponding to 80% of F_{max} in the post-peak regime, resulting in 1390 mm in Wall DSRW. The ratio of the ultimate displacement (Δ_u) to the yield displacement (Δ_y) defines the displacement ductility (μ), equal to 7.8 in this ductile steel-reinforced wall.

Figure 6-2 illustrates the monotonic response of Wall DHW. The reduced stiffness equivalent elasto-plastic yield method resulted in a Δ_y of 379 mm and a F_y of 1086 kN for this wall. Note that yielding in hybrid concrete elements containing superelastic SMA does not imply permanent inelastic deformations. Therefore, the term *pseudo-yielding* will be used hereafter to refer to the point in the response of the hybrid walls equivalent to the yield point of the steel-reinforced walls. Wall DHW experienced a k_{eff} of 2.9 kN/mm and sustained loads up to an ultimate displacement of 1194 mm. The resulting displacement ductility is equal to 3.2.

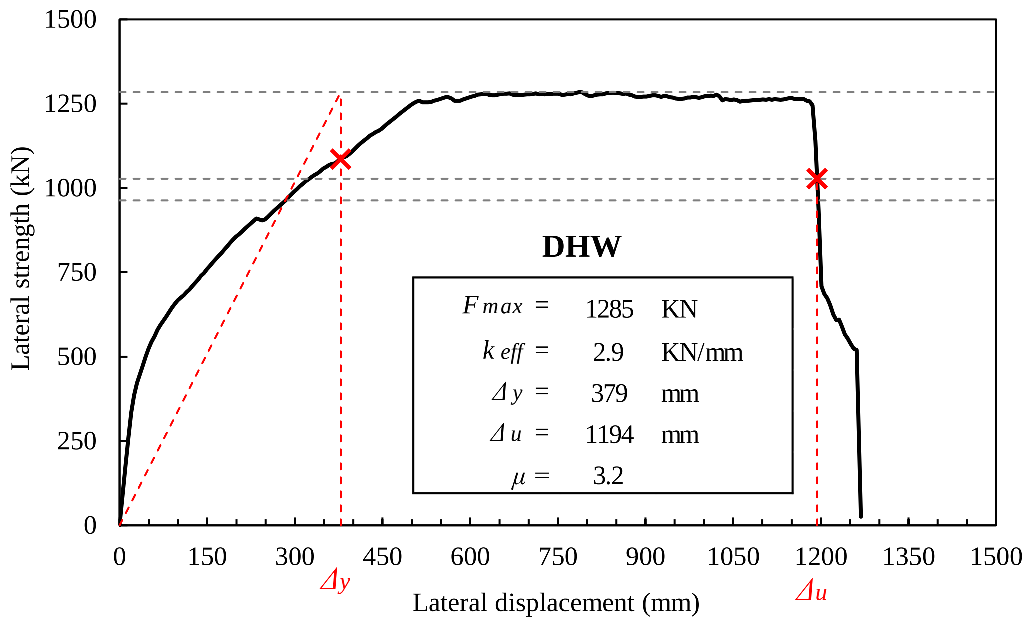

Figure 6-2 - Monotonic response of Wall DHW

6.1.2 Moderately ductile walls

The monotonic response of Wall MDSRW is depicted in Figure 6-3. This moderately ductile steel-reinforced wall experienced a maximum lateral strength of 978 kN and an ultimate displacement of 1205 mm. The yield point corresponds to 154 mm displacement and 832 kN force. Based on this yield point, the effective stiffness is 5.4 kN/mm. The displacement ductility of Wall MDSRW is equal to 7.8.

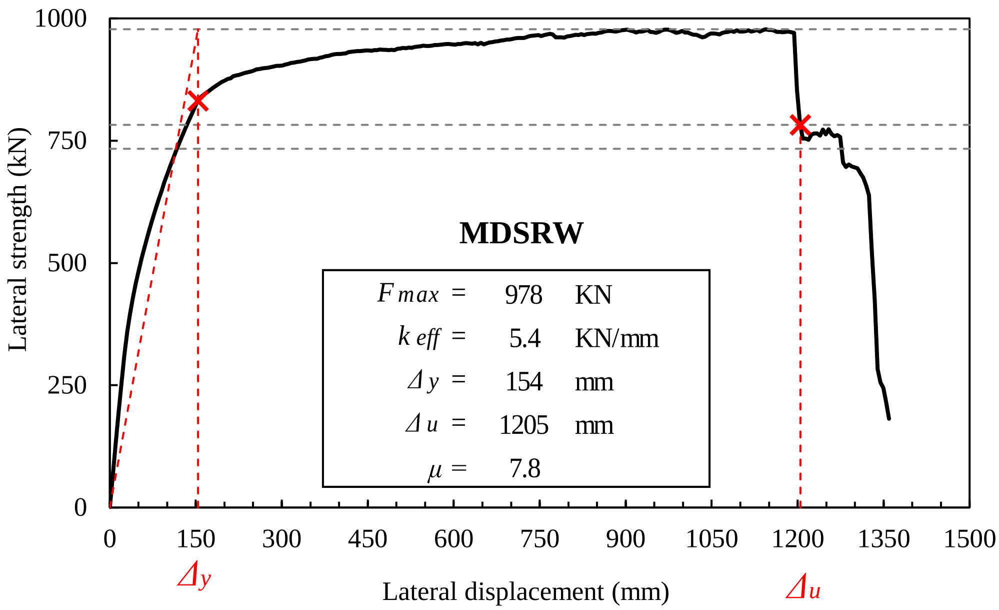

Figure 6-3 - Monotonic response of Wall MDSRW

Figure 6-4 illustrates the response of Wall MDHW. The pseudo-yielding point of the moderately ductile hybrid SMA-steel reinforced concrete wall occurs at Δ_y of 321 mm and F_y of 767.5 kN. Maximum lateral strength is equal to 926 kN and the wall could sustain the imposed displacements up to Δ_u of 1162 mm. As a result, k_{eff} and μ were determined as equal to 2.4 kN/mm and 3.6, respectively.

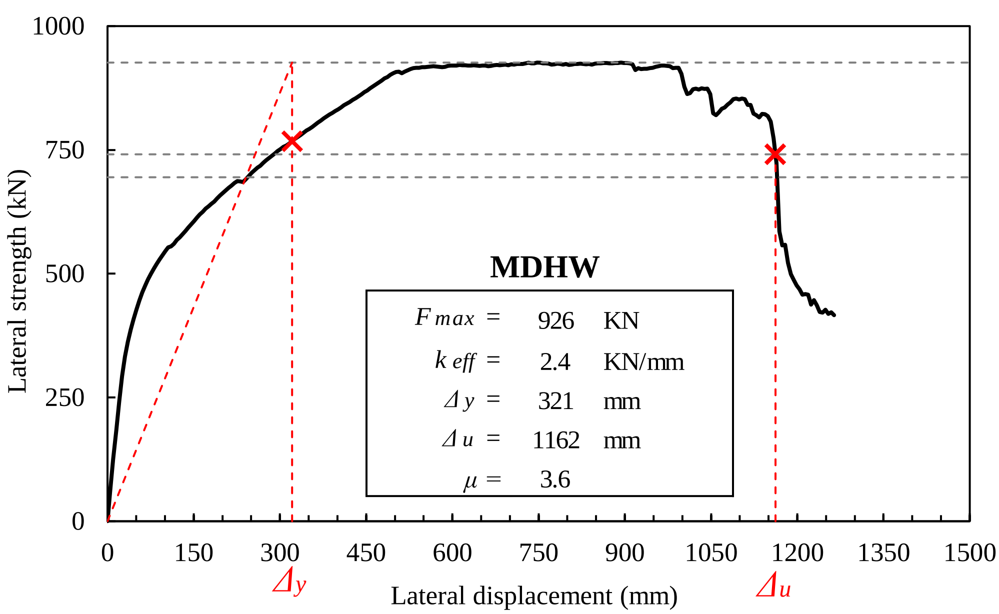

Figure 6-4 - Monotonic response of Wall MDHW

6.2 Hysteretic response

The hysteretic response of the walls resulting from nonlinear reverse cyclic analyses is presented in this section. In general, the hysteretic response of the walls was stable and symmetric, dominated by flexure, and without signs of brittle failure. Subsequently, the load-displacement response of the ductile and the moderately ductile walls will be addressed in detail, including the lateral load-lateral displacement and lateral load-vertical displacement hysteretic responses. In addition, the failure mechanism and cracking pattern of the walls will be presented. Failure of the walls was evaluated based on the stresses and strains in the SMA and the steel reinforcement and in the concrete.

6.2.1 Hysteretic response of ductile walls

The hysteretic response of the ductile walls is illustrated in Figure 6-5 (Wall DSRW) and Figure 6-6 (Wall DHW). Wall DSRW sustained a peak strength (F_{max}) of 1319 kN. The calculated effective stiffness (k_{eff}) was 6.4 kN/mm, which corresponds to the slope of the loading branch going through the yield point determined by the reduced stiffness equivalent elasto-plastic yield method (Park 1988), illustrated in Figure 6-6. Wall DSRW experienced a displacement ductility (μ) of 4.7, which is associated to a yield displacement (Δ_y) of 179 mm and an ultimate displacement (Δ_u) of 847 mm. The ultimate displacement was determined as the displacement corresponding to a drop of 20% in the lateral strength of the wall, or 0.8 F_{max}.

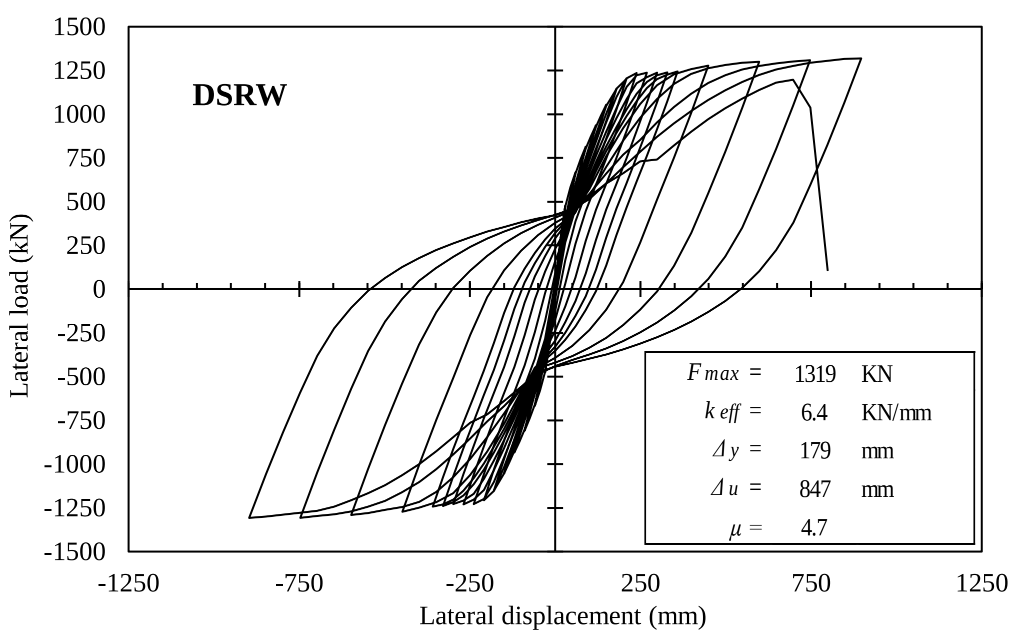

Figure 6-5 - Lateral load-displacement hysteretic response of Wall DSRW

Wall DHW sustained F_{max} of 1266 kN and Δ_u of 991 mm. The pseudo-yield point was determined at Δ_y of 375 mm, resulting in an effective stiffness of 2.8 kN/mm and a displacement ductility of 2.6.

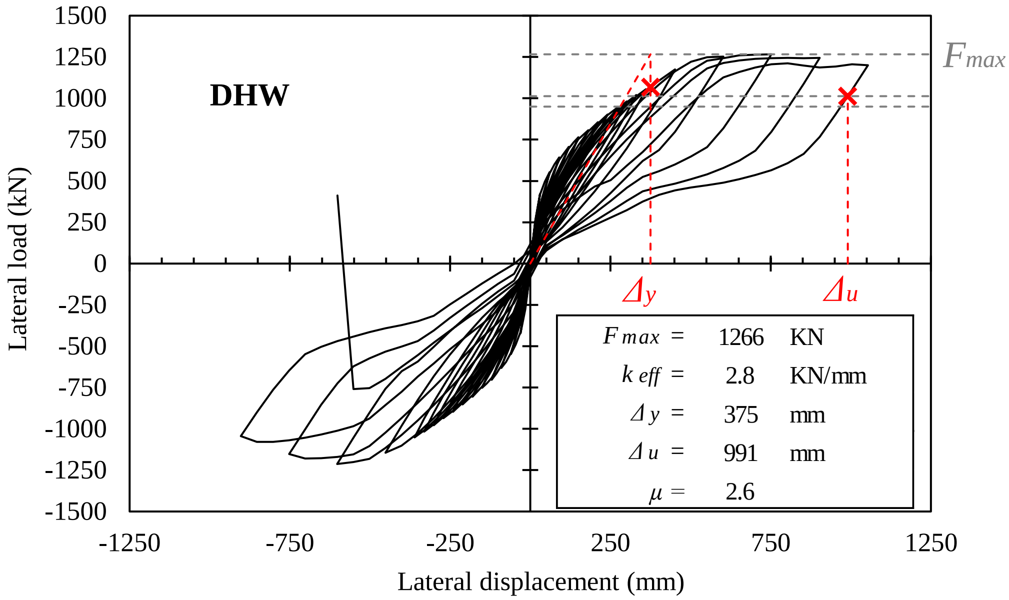

Figure 6-6 - Lateral load-displacement hysteretic response of Wall DHW

Figure 6-7 and Figure 6-8 illustrate the lateral load-vertical displacement (Δ_v) response of the ductile walls recorded at the top and the lower portion of the walls, respectively. Top displacements were measured at the right and left sides of the walls and correspond to the total vertical displacement of the walls at each cycle. Measurements at the lower portion of the walls were taken at the 5th element from the base (at approximately 1200 mm). In this way, it was possible to avoid irregularities in the values caused by the influence of the restricted nodes at the base of the models. The height of 1200 mm corresponded to the critical section identified in the hybrid walls, where a large horizontal crack was developed, as it will be discussed later. The walls experienced larger vertical displacements in one direction due to the elongation of the longitudinal reinforcement in tension. The response of Wall DSRW (Figure 6-7) is symmetric between the left and right sides of the wall, except at the onset of failure. The maximum vertical displacement at the top of Wall DRSW, from Figure 6-7 (a), is approximately 150 mm, from which approximately 40 mm correspond to displacement of the lower portion of the wall, as evident in Figure 6-7 (b). Significant levels of residual vertical displacements can be observed in Wall DSRW, which is shown by the large vertical displacements corresponding to zero lateral load in Figure 6-7. On average, 60% of the maximum vertical displacement of 153 mm at the top of the wall is present upon unloading as residual displacement.

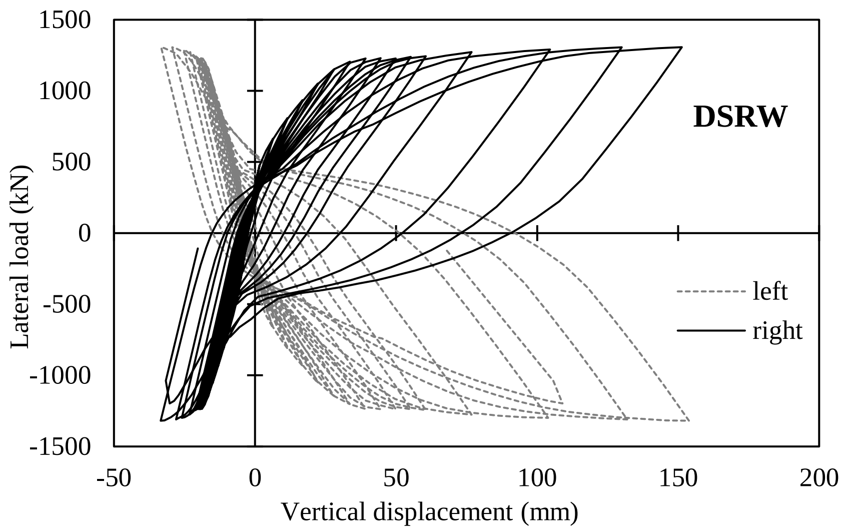

(a)

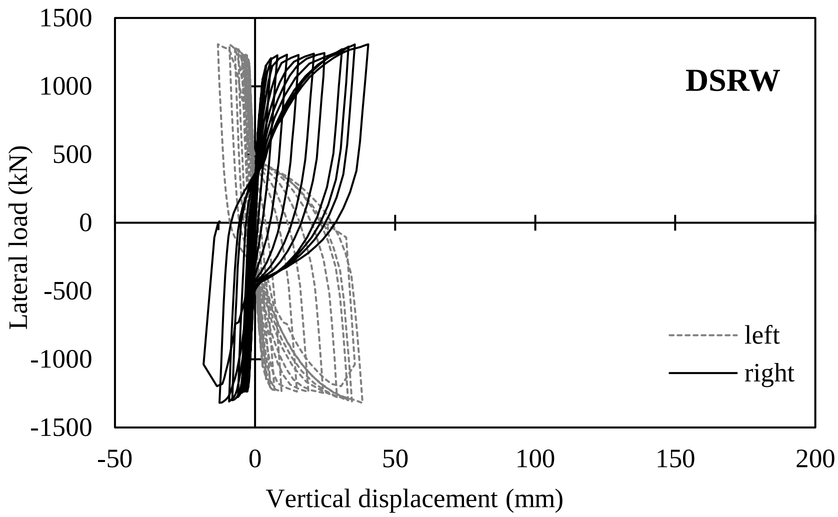

(b)

Figure 6-7 - Lateral load-vertical displacement response of Wall DSRW: (a) at the top and (b) at the lower portion of the wall

Wall DHW experienced a maximum Δ_v of 150 mm, on average, at the top of the wall (Figure 6-8 (a)). The wall developed larger vertical displacements in one side at late stages of loading, as shown in Figure 6-8 (b), which is due to a large localized crack that opens up primarily at the right side of the critical section of this wall. Maximum Δ_v at the lower portion of the wall is equal to 141 mm on the right side, whereas Δ_v is limited to 83 mm on the left side. Residual vertical displacements are negligible in Wall DHW, which is indicated by the substantial pinching of the hysteretic loops depicted in Figure 6-8.

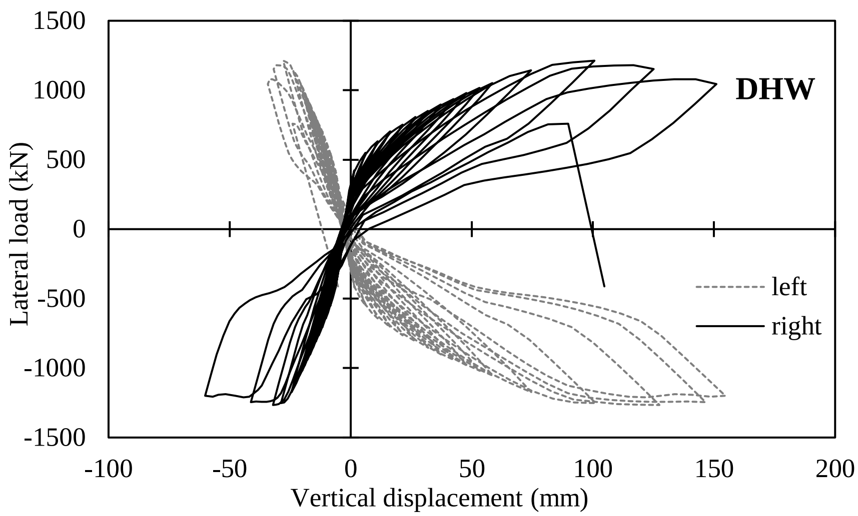

(a)

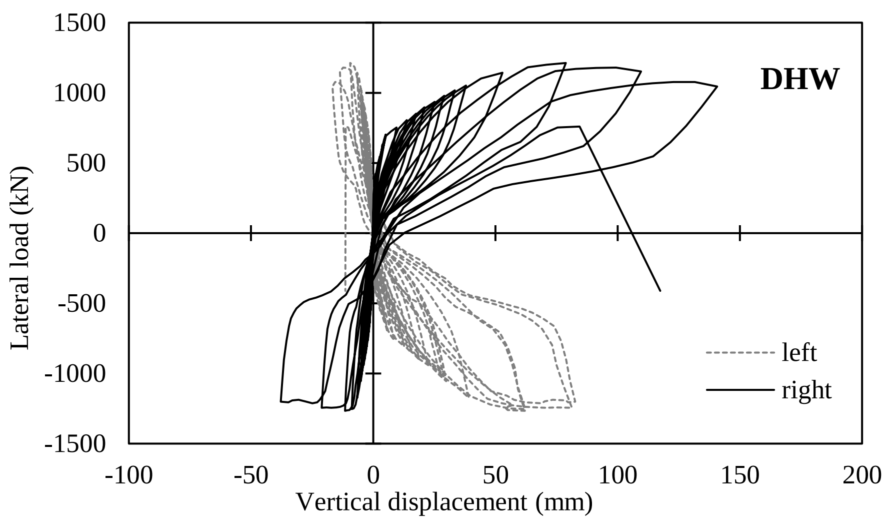

(b)

Figure 6-8 - Lateral load-vertical displacement response of Wall DHW: (a) at the top and (b) at the lower portion of the wall

Figure 6-9 provides the displaced shape of the lower portion of the ductile Walls DSRW and DHW combined with the predicted crack pattern. Figure 6-9 (a) and (c) illustrate the state of the walls at the peak of the cycle corresponding to 2.5% drift. Figure 6-9 (b) and (d) display the walls at the zero load beyond 2.5% drift. The drifts were calculated as the top displacements divided by the height of the wall, which corresponds to the point where displacements were applied in the models. The drift of 2.5% is used herein to reference the limit imposed by the NBC 2015 (NRC, 2015) to the lateral deflection of normal importance buildings. The longitudinal steel reinforcement in the web and boundary zones yielded at early stages of loading in both walls. In Wall DSRW, significant local shear distortion of the concrete elements was observed at the interface between the boundary and web regions, which is attributed to the large difference in reinforcement ratio between the two regions. Yielding of the horizontal reinforcement in the web zone was observed at late stages of loading, culminating in fracture of several bars at drifts of 3.0-3.5% at a height of 1700-1900 mm. Global failure occurred at 3.5% drift when the concentrated longitudinal steel bars in the boundary zone ruptured.

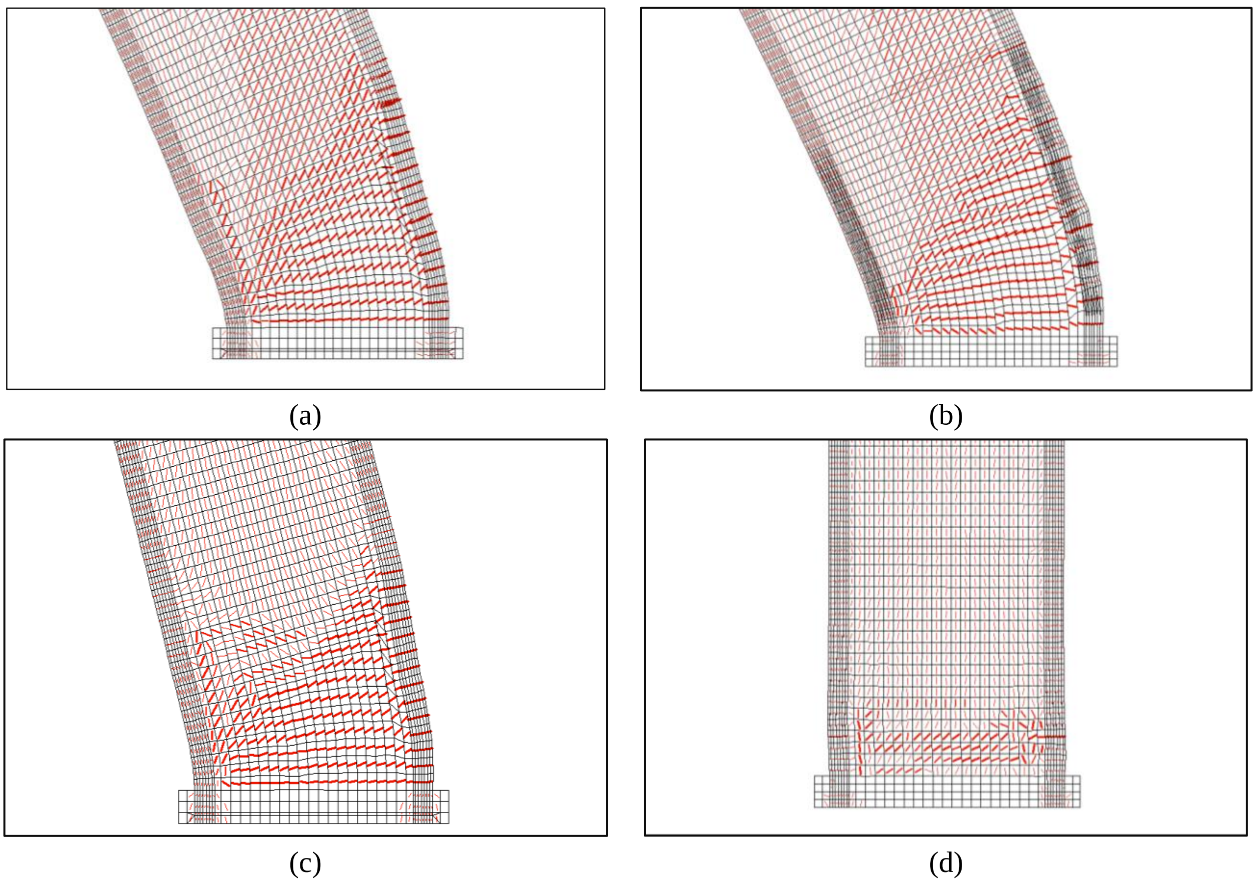

Figure 6-9 - Displaced shape and crack pattern of: Wall DSRW (a) at peak drift of 2.5% and (b) at zero load, and Wall DHW (c) at peak drift of 2.5% and (d) at zero load

In Wall DHW, the presence of SMA bars shifted the critical section slightly above the base of the wall. At the critical section, large horizontal cracking surfaced, and fracture of the longitudinal steel bars in the web zone was captured at 3.5% drift. The critical section corresponded to a height of 1200 mm. The lateral capacity of Wall DHW was reduced by rupture of the steel reinforcement in the web zone. The smooth surface of the SMA bars led to concentration of damage at localized cracks in the concrete. The SMA bars experienced pseudo-yielding at approximately 0.5% drift and remained within the superelastic range during the entire analysis without fracturing.

6.2.2 Hysteretic response of moderately ductile walls

Figure 6-10 and Figure 6-11 present the hysteretic response of the moderately ductile walls MDSRW and MDHW, respectively. Wall MDSRW sustained peak strength (F_{max}) of 973 kN and experienced a displacement ductility (μ) of 7.7, which is associated to a yield displacement (Δ_y) of 156 mm and an ultimate displacement (Δ_u) of 1201 mm. The calculated effective stiffness (k_{eff}) is equal to 5.3 kN/mm.

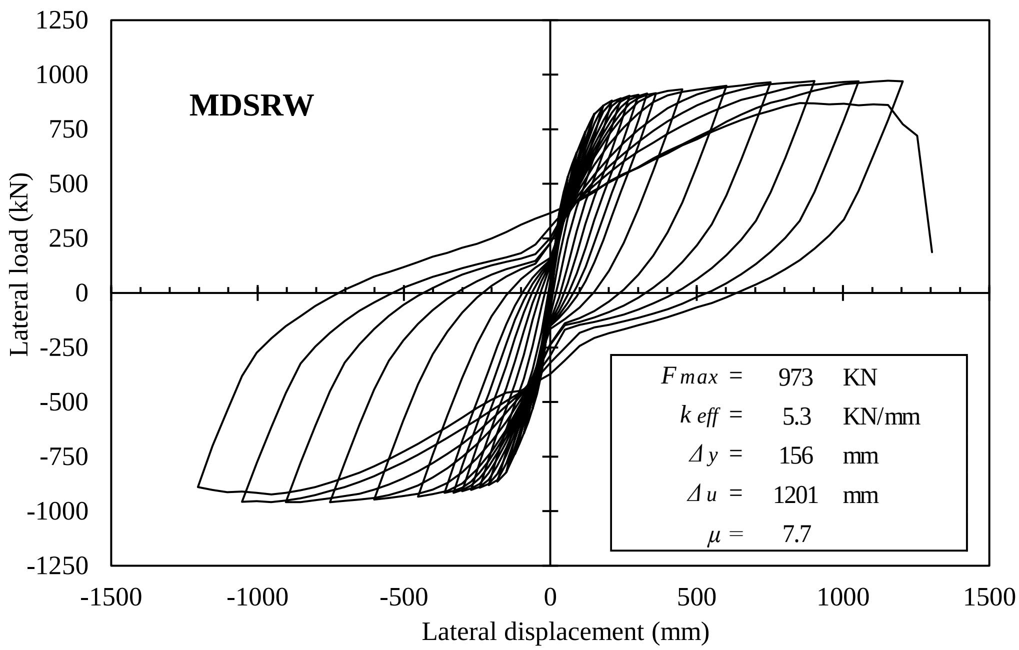

Figure 6-10 - Lateral load-displacement hysteretic response of Wall MDSRW

Wall MDHW sustained F_{max} of 926 kN and Δ_u of 1174 mm. The pseudo-yield point was determined at Δ_y of 333 mm, resulting in an effective stiffness of 2.3 kN/mm and a displacement ductility of 3.5.

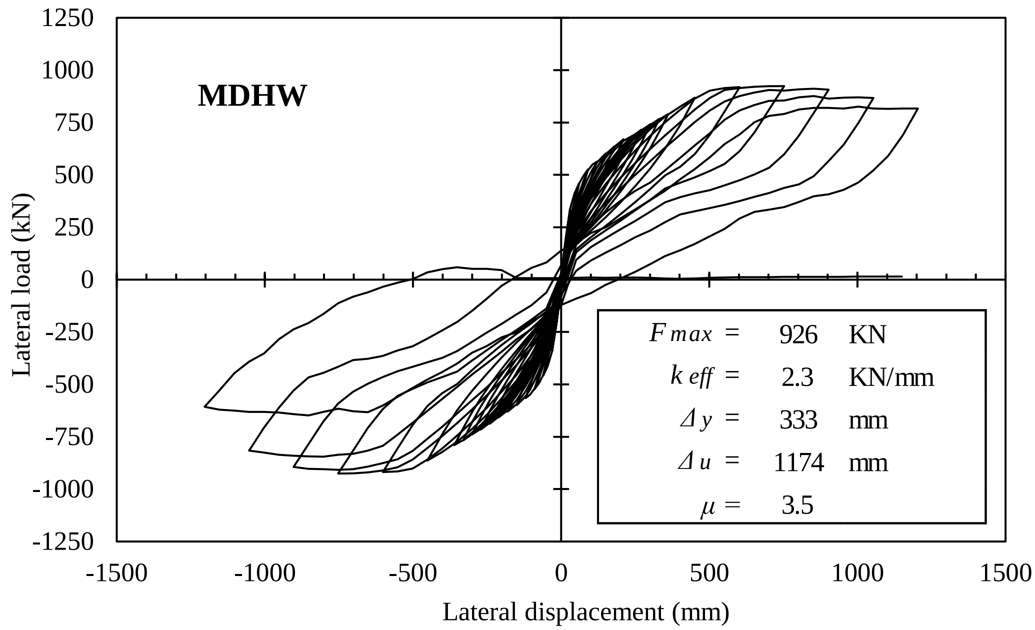

Figure 6-11 - Lateral load-displacement hysteretic response of Wall MDHW

The lateral load-vertical displacement response of the moderately ductile walls is illustrated in Figure 6-12 and Figure 6-13. The responses illustrate vertical displacements recorded at the top of the walls and at the lower portion of the walls, as previously explained. Similar vertical displacements were experienced by the left and right sides of Wall MDSRW, as depicted in Figure 6-12, with the exception of late stages of loading. The larger vertical displacements in the positive side of Figure 6-12, compared to the negative side, are due to the elongation of the reinforcement in tension. Maximum Δ_v observed in Figure 6-12 (a) is, on average, 173 mm. From this total vertical displacement, 41 mm is concentrated at the lower portion of Wall MDSRW, which is shown in Figure 6-12 (b).

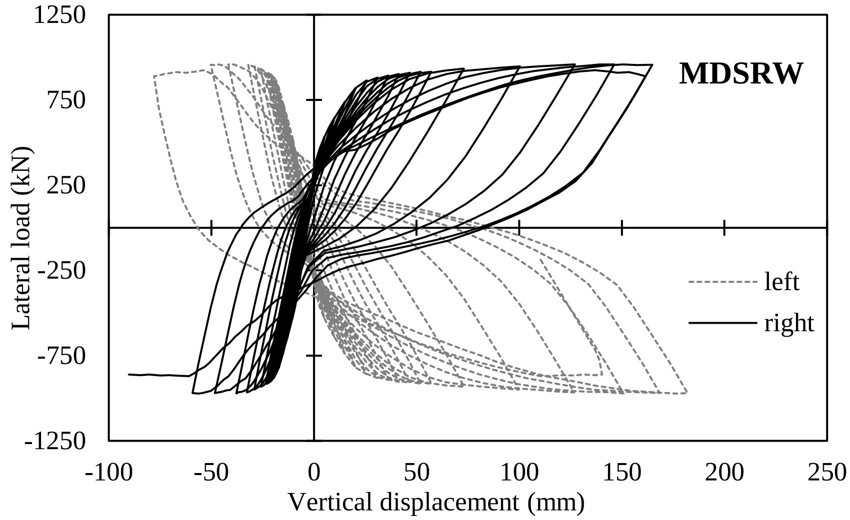

(a)

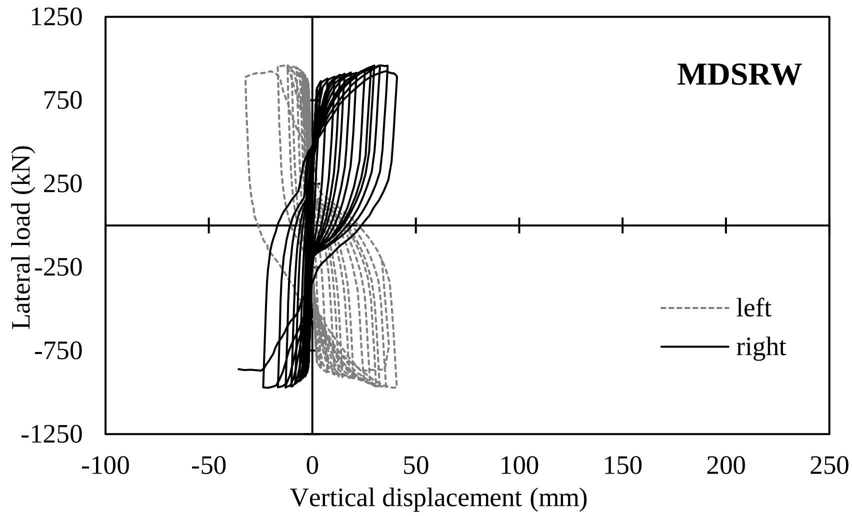

(b)

Figure 6-12 - Lateral load-vertical displacement response of Wall MDSRW: (a) at the top and (b) at the lower portion of the wall

The vertical displacements experienced by Wall MDHW, as illustrated in Figure 6-13, are fairly similar between the two sides of the wall, with variation only at late stages of loading. The average maximum Δ_v at the top of the wall is 149 mm (Figure 6-13 (a)), while average Δ_v at the lower portion of the wall is 73 mm (Figure 6-13 (b)).

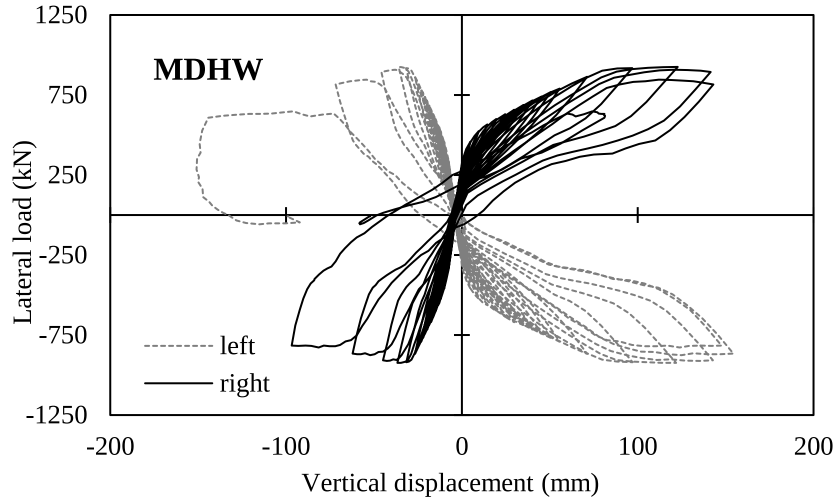

(a)

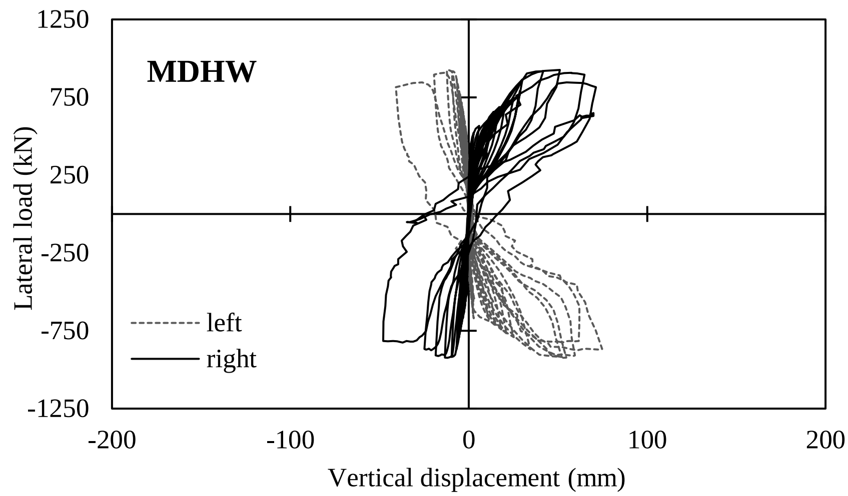

(b)

Figure 6-13- Lateral load-vertical displacement response of Wall MDHW: (a) at the top and (b) at the lower portion of the wall

Figure 6-14 provides the displaced shape of the lower portion of the moderately ductile Walls MDSRW and MDHW combined with the predicted crack pattern. Figure 6-14 (a) and (c) illustrate the state of the walls at the peak of the cycle corresponding to 2.5% drift. Figure 6-14 (b) and (d) display the walls at the zero load beyond 2.5% drift. In Wall MDSRW, the longitudinal reinforcement in the web and boundary zones yielded at early stages of loading, whereas yielding of the horizontal reinforcement in the same zones was captured at approximately 2.0% drift. A large shear distortion of the concrete elements was observed at the interface between the boundary and web regions, which is attributed to the large difference in reinforcement ratio between the two regions. Fracture occurred in multiple horizontal bars of the web zone starting at a drift of 3.5%, resulting in large crack opening in the concrete. These cracks resulted in fracture of a number longitudinal bars in the web zone at one cycle prior to failure of the bars in the edges. Global failure occurred when the concentrated longitudinal steel bars in the boundary zone ruptured at 4% drift.

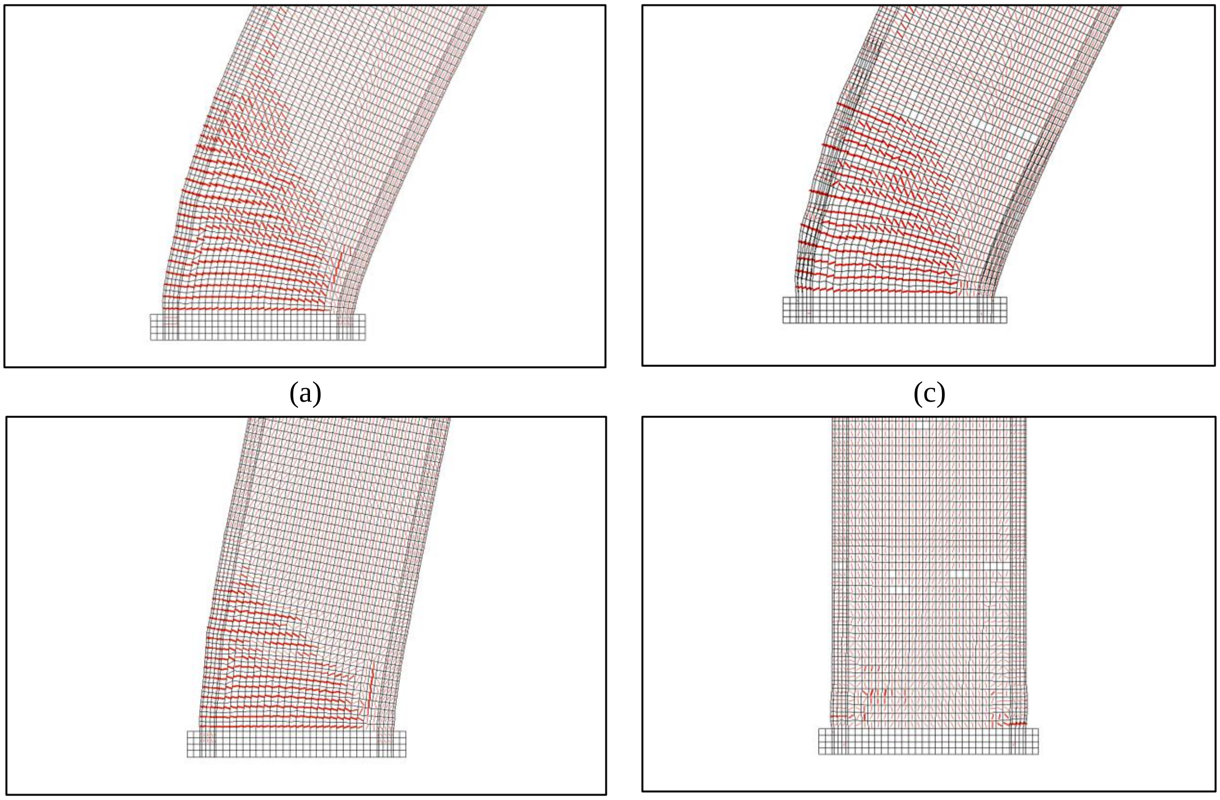

(a) (c) (b) (d)

Figure 6-14 - Displaced shape and crack pattern of: Wall MDSRW (a) at peak drift of 2.5% and (b) at zero load, and Wall MDHW (c) at peak drift of 2.5% and (d) at zero load

In Wall MDHW, the presence of SMA bars shifted the critical section slightly above the base of the wall, to a height of approximately 1000 mm. Yielding of the horizontal bars in the web zone occurred approximately at 3% drift, and fracture was observed in these bars at the critical section at 4% drift. As a result, large horizontal cracking surfaced, and fracture of multiple longitudinal steel bars in the web zone was observed at 4% drift during the positive and negative cycles. Significant bulging appeared at the critical section of the wall at 3.5%, which was not observed in any other wall. Reduced recentering, yet substantial, was evident upon unloading following the cycles to 3.5% and 4% drift. The lateral capacity of Wall MDHW was reduced by failure of the steel reinforcement in the web zone. Concentration of damage at localized cracks in the concrete was evident in Wall MDHW, which is explained by the smooth surface of SMA bars. Strains in the SMA bars remained within the superelastic range during the entire analysis, not showing signs of fracturing.

6.3 Dynamic response

The dynamic response of the walls is presented in this section, where natural and simulated ground motion records were employed to perform nonlinear time history analyses of the walls, as detailed in Section 4.4. Analyses were run for a duration that would allow the complete decay of the response of the walls in free vibration after the base excitation had ceased, permitting an accurate calculation of the final residual drifts. In general, analyses continued for 20 s following the duration of the ground motion. In the case of the simulated records from the M9 Cascadia earthquakes in Vancouver, which have a duration of 260 s, analyses were conducted for a total of 150 s due to computational time constraints. The results from dynamic analysis will be presented in terms of transient and permanent roof drifts, as well as interstorey drifts, and cracking pattern. Additionally, one record from the Vancouver seismic zone, amplified by 150% and 200%, will be used to further investigate the nuances in the behaviour of the ductile walls under seismic excitation. In addition to the evaluation of lateral drifts, the results from the analyses with the amplified record will include assessment of progress of damage and failure mechanisms.

Prior to the application of the ground motion records, the modal periods of vibration of the walls were obtained from eigenvalue analysis using VecTor2 (Vecchio et al., 2013), considering cracked sections with stiffness reduction factors calculated according to Equation 2-6. Table 6-1 lists the modal periods of vibration of each wall. The modes of vibration correspond to the storey levels of the walls.

Table 6-1 - Modal periods of vibration from eigenvalue analysis of walls

Mode of vibration	Wall MDSRW T (s)	Wall MDHW T (s)	Wall DSRW T (s)	Wall DHW T (s)
1	1.81	1.88	1.73	1.86
2	0.32	0.32	0.31	0.31
3	0.13	0.13	0.13	0.13
4	0.08	0.08	0.08	0.08
5	0.06	0.06	0.06	0.06
6	0.05	0.05	0.05	0.05
7	0.04	0.04	0.04	0.04
8	0.04	0.04	0.04	0.04
9	0.04	0.04	0.04	0.04
10	0.04	0.04	0.04	0.04

6.3.1 Dynamic response of ductile walls

Figure 6-15 illustrates the lateral roof displacement time history of Wall DSRW when subjected to one representative record of each seismic hazard scenario: earthquake Record 150 - Coyote Lake, 1979, representing Scenario 1 Figure 6-15 (a), earthquake Record 359 - Coalinga, 1983, representing Scenario 2 Figure 6-15 (b), and simulated Record M9 Cascadia 14, representing Scenario 3 Figure 6-15 (c). The dashed lines in Figure 6-15 mark the yield and ultimate displacements of Wall DSRW, respectively in grey and red. Yielding corresponded to 179 mm in the hysteretic response of the wall, while ultimate displacement was equal to 847 mm. The lateral roof displacement time histories corresponding to each of the eleven ground motion records chosen for the three different seismic hazard scenarios in Vancouver are available in Table C-1 in Appendix C.

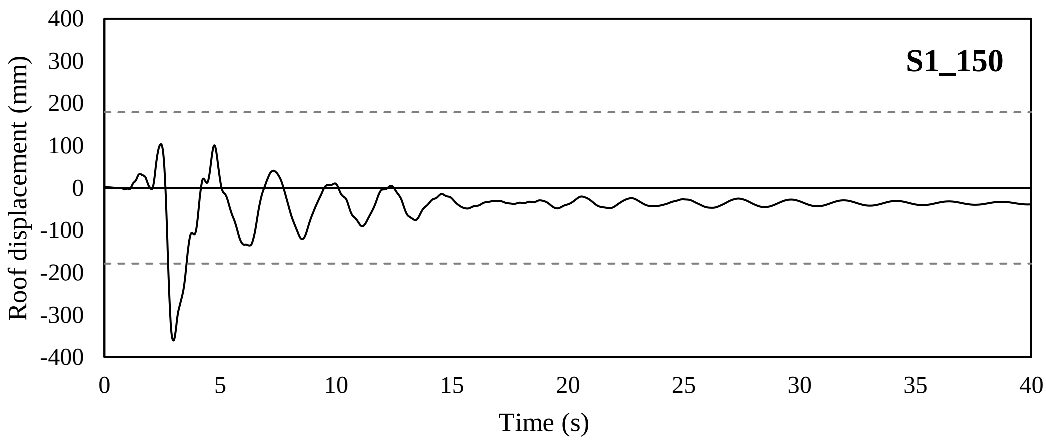

(a)

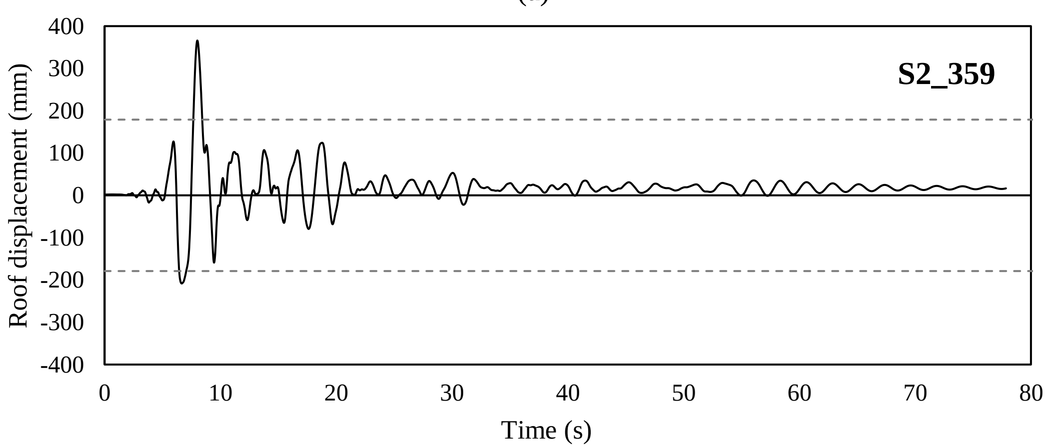

(b)

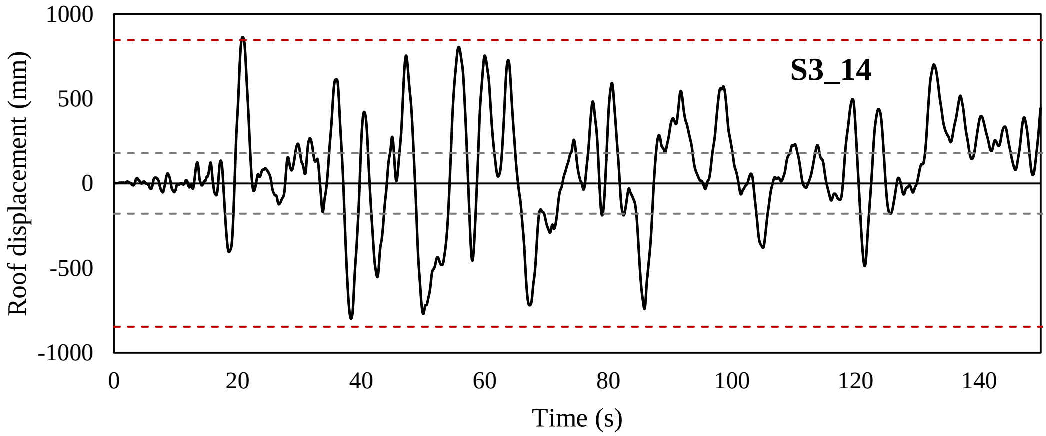

(c)

Figure 6-15 - Lateral roof displacement time histories of Wall DSRW when subjected to ground motion records from: (a) Scenario 1, (b) Scenario 2 and (c) Scenario 3

The seismic demand induced by most of the earthquake records from Scenarios 1 and 2 was sufficient to trigger yielding in the wall, resulting in plastic deformations. The ground motion records from Scenario 3 induced displacements in the wall that approached the ultimate displacement, exceeding it in some cases, leading to failure of the wall. Failure induced by Records 15 and 23 caused a limitless increase of the lateral displacements in the models at the end of the analyses. For this reason, permanent deformations in Wall DSRW when subjected to Records 15 and 23 could not be recorded, and these records were disregarded from the mean responses in terms of permanent deformation. In turn, transient deformations were recorded when the roof displacement reached the capacity of the wall. In the case of Record 14, failure did not cause instability and the analysis continued. However, the analysis was interrupted after 150 s as failure of the wall had already occurred. Failure in Wall DSRW when subjected to the three records from Scenario 3 occurred due to fracture of the longitudinal reinforcement in the boundary zone at the base of the wall, along with several adjacent bars in the web zone. Fracturing of the bars was identified by the developed stress of 600 MPa, which corresponded to f_u of steel adopted in the models.

Ratcheting can be identified in the responses of Wall DSRW as the accumulation of damage in one direction, which hindered recentering in the wall after a certain point of the responses. As a result, the wall exhibited permanent deformations at the end of the analyses, as observed in Figure 6-15. Figure 6-16 illustrates the displaced shape of Wall DSRW, along with the cracking pattern, at the end of the dynamic analyses for the three seismic hazard scenarios. Residual deformation is evident in the displaced shapes of the wall, and the presence of stiff slabs in the model noticeably influenced the cracking pattern.

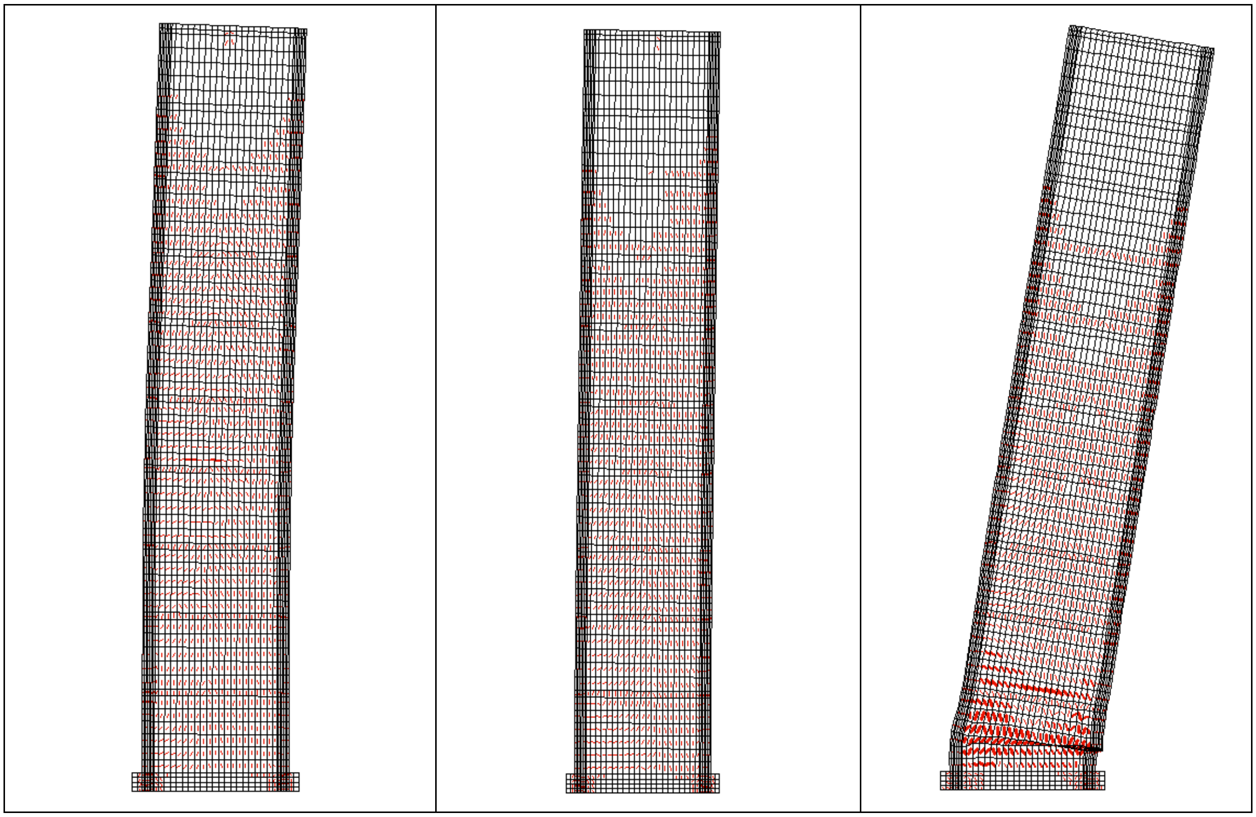

(a) (b) (c)

Figure 6-16 - Displaced shape and cracking pattern of Wall DSRW at the end of analysis when subjected to ground motion records from: (a) Scenario 1, (b) Scenario 2 and (c) Scenario 3

Due to the great variability existing among earthquake records, the NBC 2015 (NRC, 2015) requires that the mean response be determined from the dynamic analyses. Figure 6-17 (a) contains the peak lateral displacements along the height of Wall DSRW from the eleven analyses performed, which correspond to the peak displacement experienced by each storey during the analyses. The mean response is also presented. The maximum transient roof displacement experienced by Wall DSRW was equal to 946 mm (when subjected to Record M9 Cascadia 23), which corresponds to a drift of 3.4%. Maximum interstorey drift occurred at storey 10 for Scenarios 1 and 2, and at storeys 8 and 10 for Scenario 3. The mean response from the profiles shown in Figure 6-17 (a) corresponds to a transient roof displacement of 443 mm (drift of 1.45%) and a maximum transient interstorey drift of 2% at storey 10. The displacement profiles of the wall at the end of the analyses are illustrated in Figure 6-17 (b). In terms of permanent deformations, Wall DSRW exhibited average roof displacement of 40 mm (0.13% drift) and maximum interstorey drift of 0.17% at storey 10. On average, the wall was able to recover 75% of the experienced roof displacement. Note that the average considered all eleven records; the average between the analyses that did not fail indicates a recovery of 92%. The results obtained from the eleven time history analyses of Wall DSRW, along with the mean of the results, are listed in Table 6-2, where the roof displacements exceeding Δ_y are highlighted.

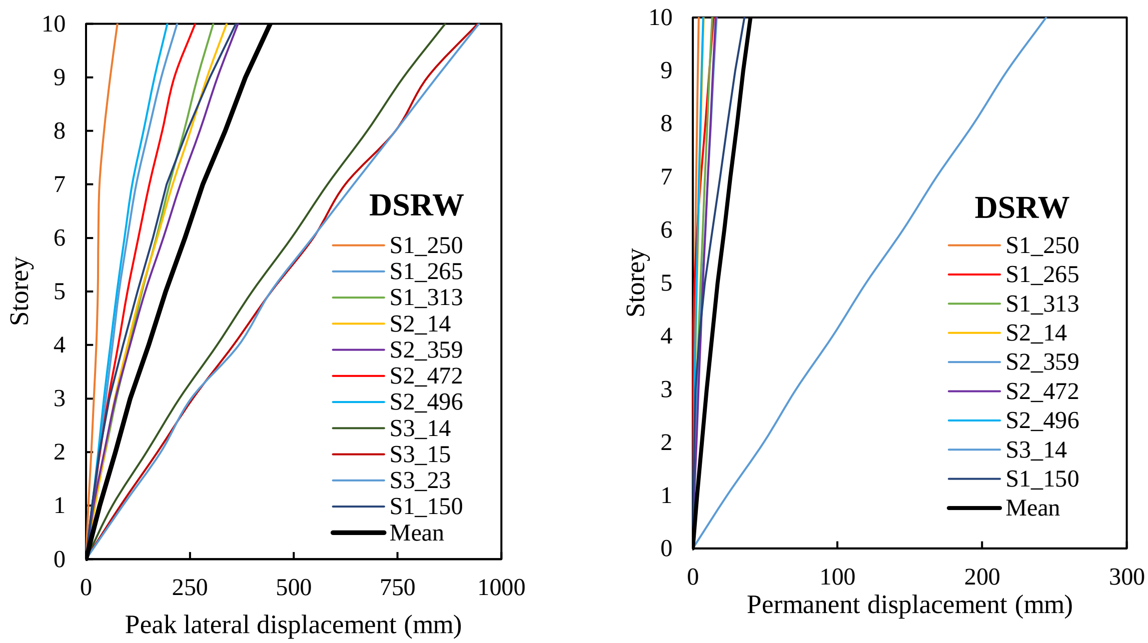

(a) (b)

Figure 6-17 - Lateral displacement profiles of Wall DSRW: (a) peak lateral displacements and (b) displacements at the end of analysis

Table 6-2 - Summary of results from time history analyses of Wall DSRW

Record	Transient deformation			Permanent deformation			Recovery of roof drift (%)
	Roof displacement (mm)	Roof drift (%)	Interstorey drift (%) - associated storey	Roof displacement (mm)	Roof drift (%)	Interstorey drift (%) - associated storey	
S1_150	361	1.18	2.1 - 10	36	0.12	0.21 - 10	90.1
S1_250	76	0.25	0.6 - 10	4	0.01	0.02 - 10	94.6
S1_265	219	0.72	1.3 - 10	14	0.05	0.10 - 10	93.4
S1_313	306	1.00	1.3 - 10	13	0.04	0.06 - 10	95.6
S2_14	338	1.11	1.6 - 10	7	0.02	0.04 - 10	97.8
S2_359	366	1.20	1.6 - 10	16	0.05	0.07 - 10	95.5
S2_472	263	0.86	1.7 - 10	16	0.05	0.06 - 10	94.0
S2_496	196	0.64	1.0 - 10	7	0.02	0.04 - 10	96.3
S3_14	865	2.83	3.4 - 10	244	0.80	0.89 - 10	71.8
S3_15	943	3.09	4.0 - 8 & 10	-	-	-	0
S3_23	946	3.10	3.4 - 8 & 10	-	-	-	0
Mean	443	1.45	2.0 - 10	40	0.13	0.17 - 10	75.4

The lateral roof displacement time histories from the eleven dynamic analyses of Wall DHW are available in Table C-2 in Appendix C. Figure 6-18 illustrates the results from one ground motion record representative of each seismic hazard scenario, including dashed lines representing calculated Δ_y of 375 mm (grey dashed lines) and Δ_u of 991 mm (red dashed lines), respectively.

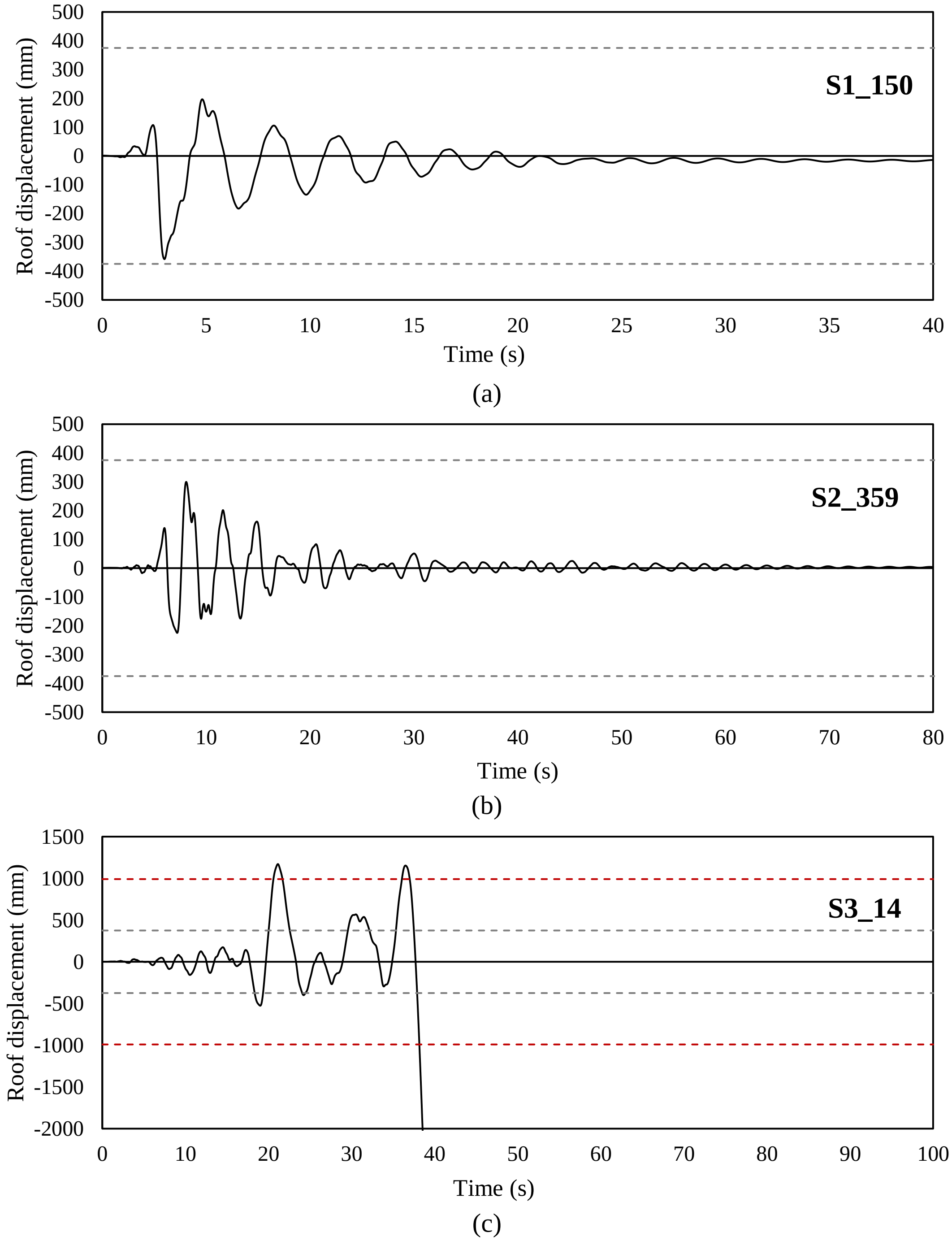

Figure 6-18 - Lateral roof displacement time histories of Wall DHW when subjected to ground motion records from: (a) Scenario 1, (b) Scenario 2 and (c) Scenario 3

The seismic demand from most of the earthquake records representing Scenarios 1 and 2 was not sufficient to exceed pseudo-yielding displacement of the hybrid wall, preventing the accumulation of inelastic deformation in Wall DHW, which resulted in recentering of Wall DHW. At the end of the analyses, the wall exhibited negligible permanent deformation when subjected to records from Scenarios 1 and 2. The analyses employing the three records from Scenario 3, such as the analysis using Record M9 Cascadia 14 that is shown in Figure 6-18 (c), exceeded the capacity of the wall and led to failure, which occurred with fracture of the longitudinal steel bars in the web zone of Wall DHW. The failure caused instability of the analyses, resulting in an abrupt increase of displacements, as evident in Figure 6-18 (c). Figure 6-19 illustrates the displaced shape of Wall DHW at the end of the three presented analyses, along with the cracking pattern. The displaced shape of Wall DHW in Figure 6-19 (c) represents the wall at failure rather than the permanent deformation.

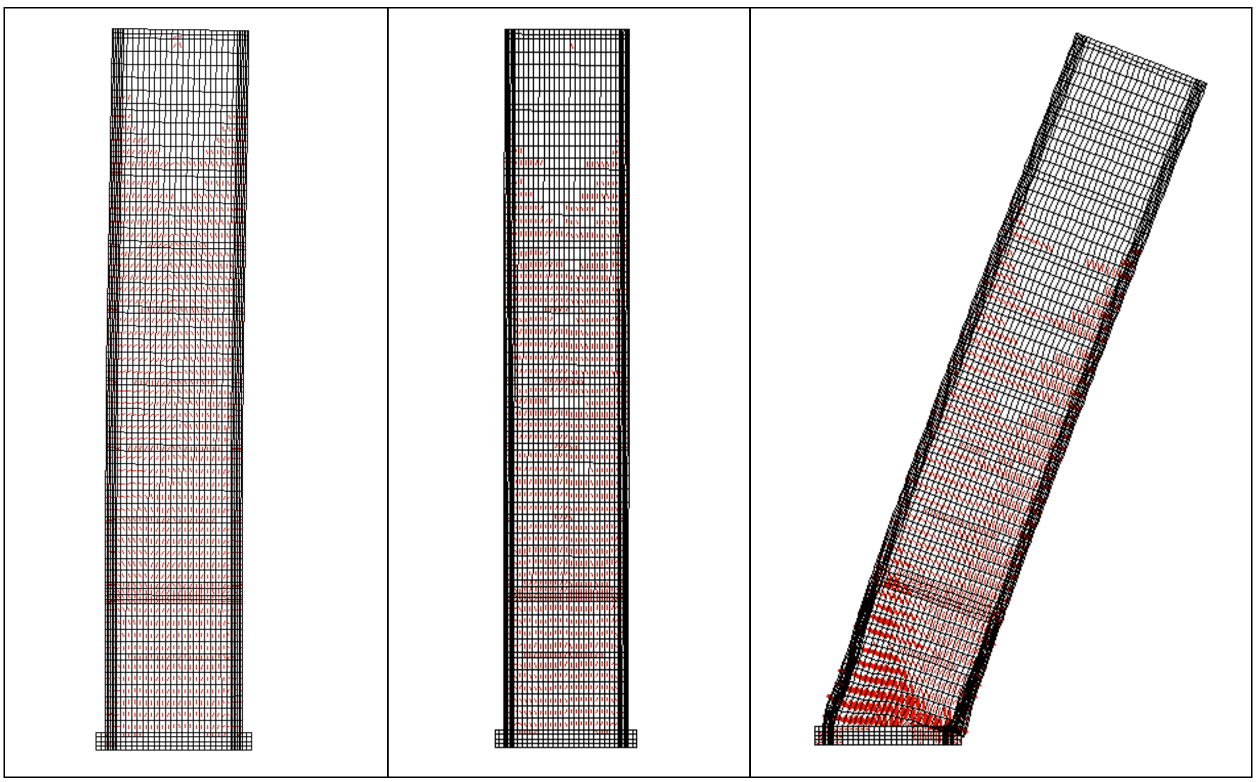

(a) (b) (c)

Figure 6-19 - Displaced shape and cracking pattern of Wall DHW at the end of analysis when subjected to the ground motion record corresponding to: (a) Scenario 1 (permanent deformation), (b) Scenario 2 (permanent deformation), and (c) Scenario 3 (failure)

Lateral displacement profiles of Wall DHW are provided in Figure 6-20, corresponding to the peak lateral displacements (Figure 6-20 (a)) and the permanent displacements recorded at the end of the analyses (Figure

6-20 (b)). The response from each of the eleven analyses and the mean response are provided. Due to failure of the wall when subjected to records from Scenario 3, the peak displacements of Wall DHW were recorded at the point when the lateral capacity was reached. In those cases, permanent defamations were ignored and removed from the averaging process, given that the records caused failure of the wall. Wall DHW experienced maximum transient roof displacement of 997 mm (3.27% drift), as shown in Figure 6-20 (a), when subjected to Record M9 Cascadia 15. The maximum transient interstorey drift in this analysis was equal to 3.78% at storeys 6, 8 and 10. On average, the transient roof displacement of the wall was equal to 489 mm (1.6% drift), while the maximum interstorey drift was equal to 2.07% at storeys 6, 8 and 10. From Figure 6-20 (b), the permanent roof displacement was, on average, equal to 6 mm (0.02% drift), and the maximum sustained permanent interstorey drift was equal to 0.03% at storey 10. On average, the wall was able to recover 71% of the experienced roof displacement. Note that the average considered all eleven records; the average between the analyses that did not fail indicates a recovery of 98%. Results from each of the eleven analyses, as well as the mean of the results, are summarized in Table 6-3, where the roof displacements that exceeded Δ_y are highlighted.

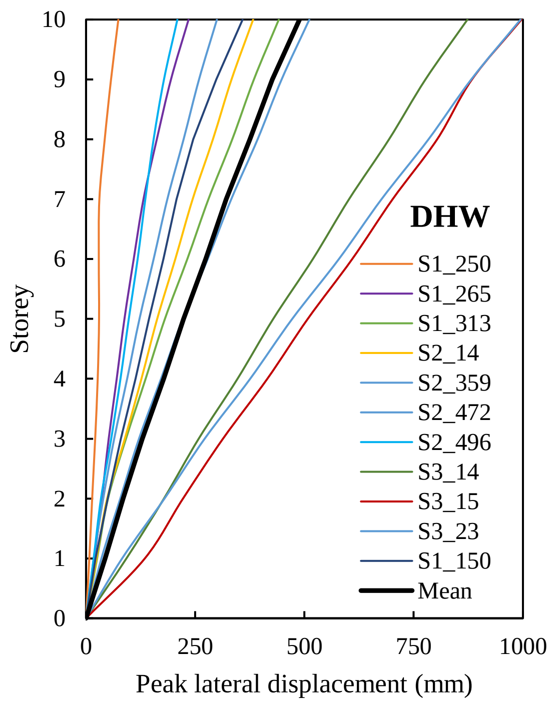

(a)

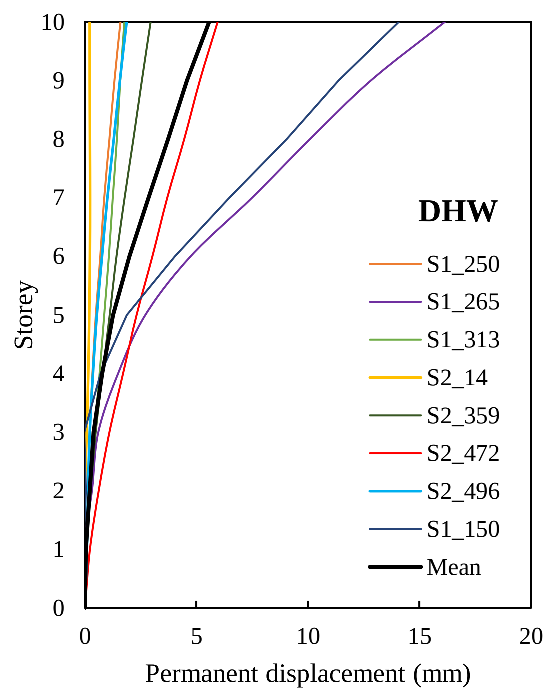

(b)

Figure 6-20 - Lateral displacement profile of Wall DHW: (a) peak lateral displacements and (b) permanent displacements at the end of the analyses

Table 6-3 - Summary of results from time history analyses of Wall DHW

Record	Transient deformation			Permanent deformation			Recovery of roof drift (%)
	Roof displacement (mm)	Roof drift (%)	Interstorey drift (%) - associated storey	Roof displacement (mm)	Roof drift (%)	Interstorey drift (%) - associated storey	
S1_150	358	1.18	2.0 - 10	14	0.05	0.09 - 10	96
S1_250	74	0.24	0.6 - 10	2	0.01	0.01 - 10	98
S1_265	235	0.64	1.3 - 10	16	0.05	0.11 - 10	93
S1_313	441	1.45	1.9 - 10	2	0.06	0.01 - 10	99.6
S2_14	383	1.25	1.6 - 10	0.2	0.00	0.00	99.9
S2_359	300	0.98	1.4 - 10	3	0.01	0.01 - 10	99
S2_472	511	1.68	2.1 - 10	6	0.02	0.03 - 10	99
S2_496	209	0.69	1.0 - 10	2	0.01	0.01 - 10	99
S3_14	873	2.86	3.2 - 8 & 10	-	-	-	0
S3_15	997	3.27	3.8 - 6, 8 & 10	-	-	-	0
S3_23	995	3.26	3.8 - 6, 8 & 10	-	-	-	0
Mean	489	1.60	2.1 - 6, 8 & 10	6	0.02	0.03 - 10	71

6.3.2 Dynamic response of moderately ductile walls

The response of Wall MDSRW to two ground motion records for Montreal are illustrated in Figure 6-21. Figure 6-21 (a) represents Record 30 (simulated record of M6 at a distance of 14.3 km) for the seismic hazard Scenario 1, and Figure 6-21 (b) represents Record 6 (simulated record of M7 at a distance of 50.3 km) for the seismic hazard Scenario 2. The complete time histories of the roof displacement of Walls MDSRW and MDHW are available in Appendix C, in Table C-3 and Table C-4, respectively. In general, the ground motion records representative of the moderate seismic zone of eastern Canada did not induced large inelastic demands in Walls MDSRW and MDHW. Few records induced displacements that were equal to or slightly above Δ_y of the walls. The yield displacement of the wall is marked by dashed lines. Wall MDSRW had Δ_y determined from the reverse cyclic analysis as equal to 156 mm. As a result, permanent damage exhibited by the walls was very limited.

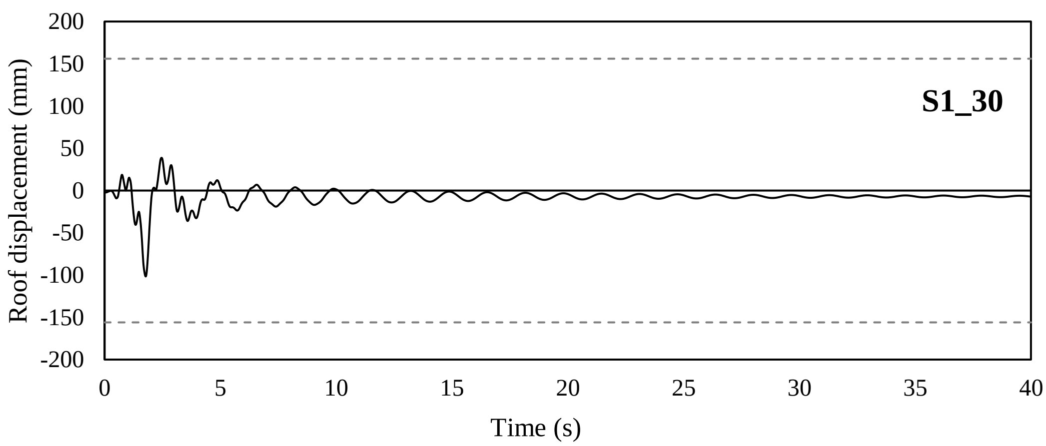

(a)

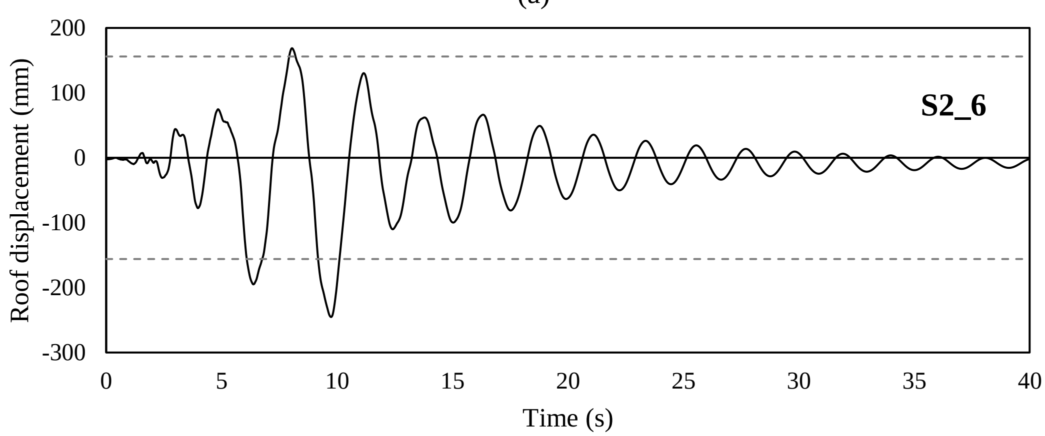

(b)

Figure 6-21 - Lateral roof displacement time histories of Wall MDSRW when subjected to ground motion records from: (a) Scenario 1 and (b) Scenario 2

Figure 6-22 illustrates the displaced shapes and cracking patterns sustained by Wall MDSRW at the end of the selected analyses. Further discussion about the seismic demand experienced by the walls is provided in Section 7.4.1.

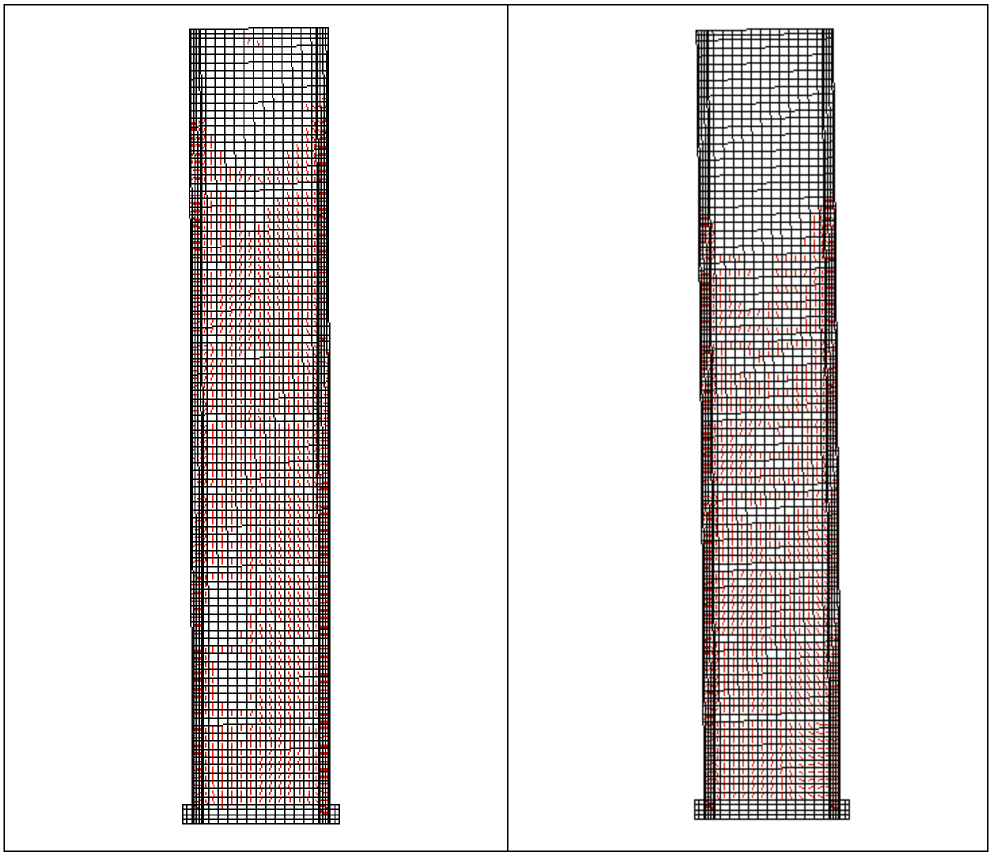
(a) (b)

Figure 6-22 - Displaced shape and cracking pattern of Wall MDSRW at the end of analysis when subjected to the ground motion record from: (a) Scenario 1 and (b) Scenario 2

Figure 6-23 provides the profiles of lateral displacement of Wall MDSRW when subjected to each of the eleven simulated ground motion records. The peak displacements per storey level experienced by the wall throughout the analyses are shown in Figure 6-23 (a), along with the mean displacements determined from the eleven profiles. Wall MDSRW experienced a maximum roof displacement of 245 mm (drift of 0.8%) when subjected to Record 6 (M7 at 50.3 km). The largest interstorey drift, identified at storey 8, was 1%. The average response of Wall MDSRW corresponded to a transient roof displacement of 145 mm (0.48% drift) and a maximum interstorey drift of 1.03% at storey 10. The profile of permanent displacements along the height of Wall MDSRW is illustrated in Figure 6-23 (b). Average permanent roof displacement was determined as equal to 6 mm (0.02% drift), while the maximum interstorey drift was 0.03% at storey 10. On average, Wall MDSRW was able to recover 96% of the experienced roof displacements. When subjected to Record 6, Wall MDSRW sustained the largest permanent displacements, with a roof displacement of 15 mm (0.50% drift), which corresponds to a recovery of 94%. Results from the eleven analyses are listed in Table 6-4, where the roof displacements that exceeded Δ_y are highlighted.

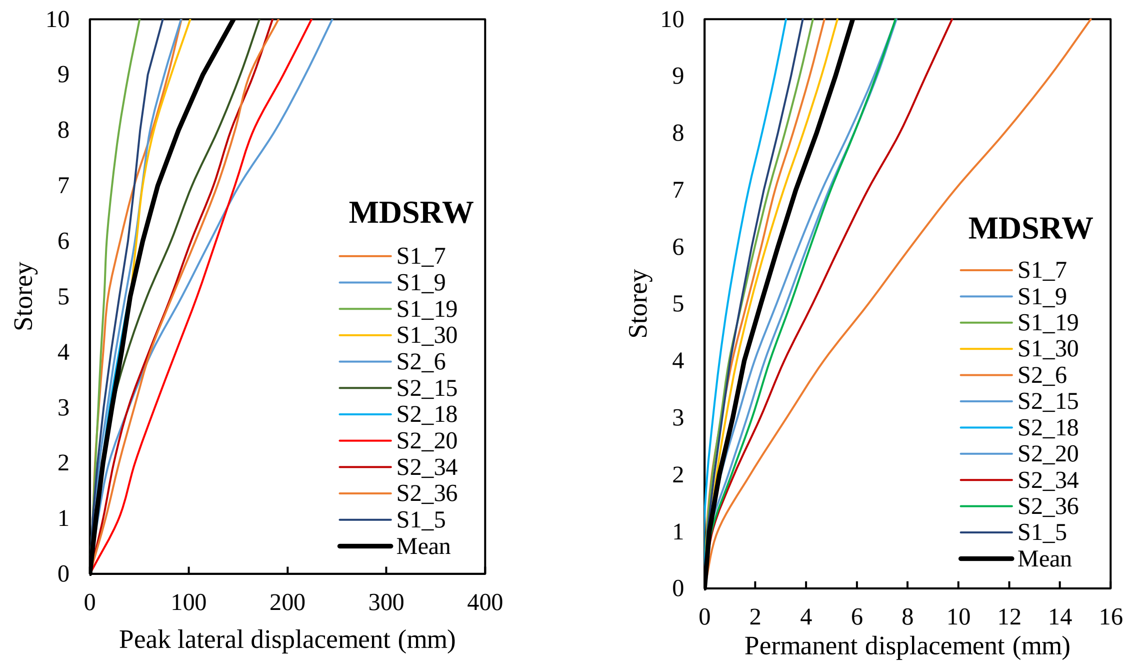

(a) (b)

Figure 6-23 - Lateral displacement profiles of Wall MDSRW: (a) peak lateral displacements and (b) permanent displacements at the end of the analyses

Table 6-4 - Summary of results from time history analyses of Wall MDSRW

Record	Transient deformation			Permanent deformation			Recovery of roof drift (%)
	Roof displacement (mm)	Roof drift (%)	Interstorey drift (%) - associated storey	Roof displacement (mm)	Roof drift (%)	Interstorey drift (%) - associated storey	
S1_5	74	0.24	0.5 - 10	4	0.01	0.03 - 10	94.8
S1_7	93	0.30	0.6 - 8	5	0.02	0.03 - 8	94.9
S1_9	92	0.30	0.6 - 10	6	0.02	0.03 - 10	93.7
S1_19	50	0.16	0.4 - 10	4	0.01	0.03 - 10	91.5
S1_30	102	0.33	0.6 - 10	5	0.02	0.03 - 10	94.8
S2_6	245	0.80	1.0 - 5 & 9	15	0.05	0.07 - 5 & 9	93.8
S2_15	172	0.56	0.9 - 8	8	0.03	0.03 - 8	95.6
S2_18	145	0.48	1.0 - 10	3	0.01	0.03 - 10	97.8
S2_20	224	0.73	1.0 - 9	8	0.03	0.03 - 9	96.6
S2_34	185	0.61	0.6 - 10	10	0.03	0.03 - 10	94.7
S2_36	191	0.63	1.0 - 10	8	0.03	0.03 - 10	96.1
Mean	145	0.48	1.0 - 10	6	0.02	0.03 - 10	96.0

For Wall MDHW, the roof displacement time histories corresponding to two analyses are illustrated in Figure 6-24, the first representing Scenario 1 (Figure 6-24 (a)) and the second representing Scenario 2 (Figure 6-24 (b)). From the hysteretic response of the wall, Δ_y (dashed lines in Figure 6-24) was found to be equal to 333 mm in the hysteretic response of the wall. The seismic demand imposed by the employed ground motion records did not induce displacements larger than Δ_y in Wall MDHW. Consequently, the superelastic capacity of the SMA reinforcement was not achieved. At the end of the analyses, Wall MDHW exhibited recentered shapes with negligible residual displacements, as illustrated in Figure 6-25 for the analyses using Record 30, from Scenario 1 (Figure 6-25 (a)), and Record 6, from Scenario 2 (Figure 6-25 (b)).

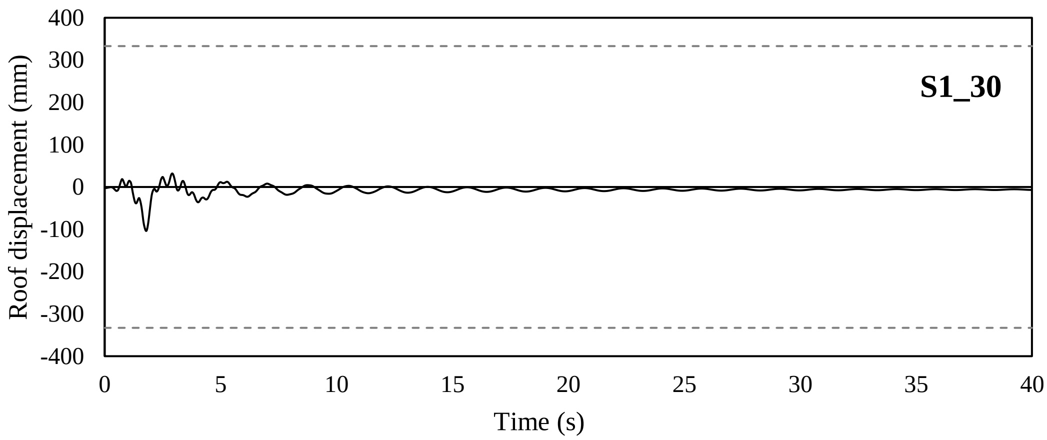

(a)

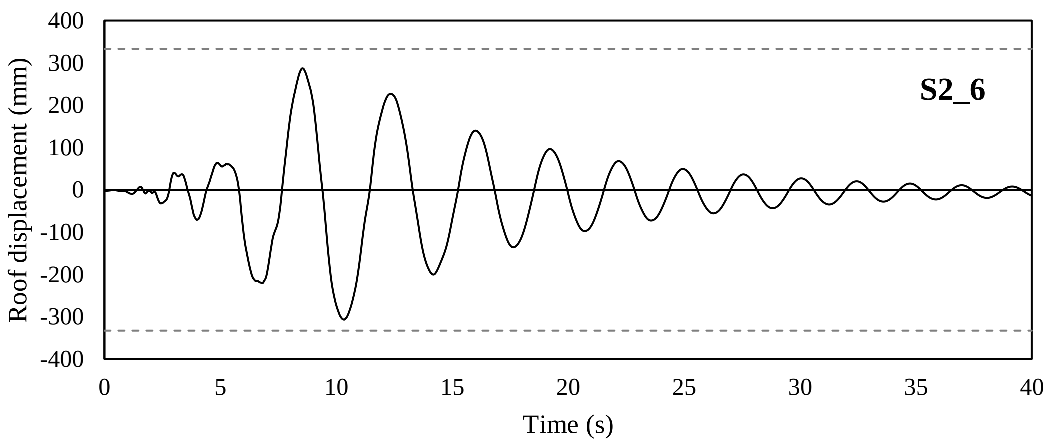

(b)

Figure 6-24 - Lateral roof displacement time histories of Wall MDHW when subjected to ground motion records from: (a) Scenario 1 and (b) Scenario 2

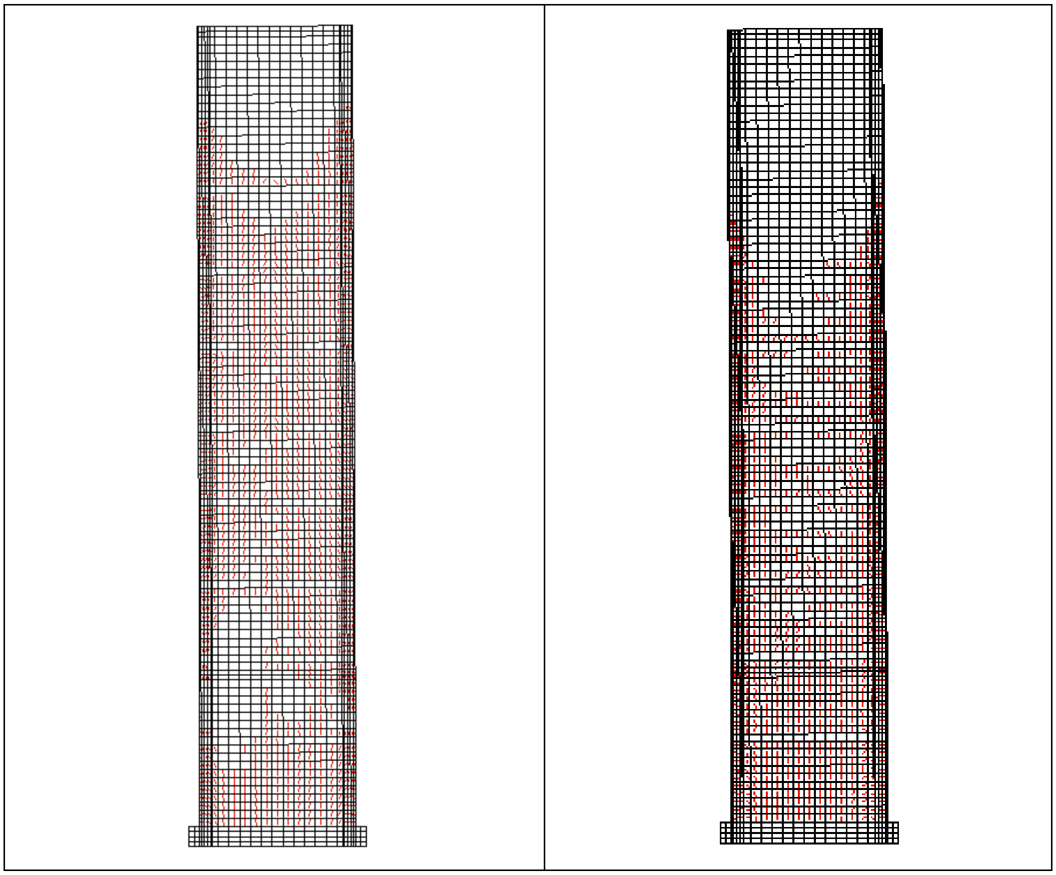

Figure 6-25- Displaced shape and cracking pattern of Wall MDHW at the end of analysis when subjected to the ground motion record from: (a) Scenario 1 and (b) Scenario 2

Figure 6-26 (a) provides the peak lateral displacements experienced by Wall MDHW during each of the eleven analyses, as well as the mean response. Maximum roof displacement was found to be equal to 307 mm (1% drift), corresponding to Record 6 (M7 at 50.3 km), while the average transient roof displacement was equal to 149 mm (0.49% drift). The maximum interstorey drift, induced by Record 6, occurred at storey 9 and was equal to 1.33%, while the average response indicated maximum interstorey drift of 0.67% at storey 8. Figure 6-26 (b) illustrates the permanent displacements along the height of Wall MDHW at the end of the analyses, as well as the mean permanent displacements. The average permanent displacement sustained by the wall was equal to 5 mm (0.17% drift), resulting in 97% recovery of roof displacement in Wall MDHW. The maximum permanent interstorey drift in the average response was negligible, computed as equal to 0.03% at storey 8. In the case of Record 6, Wall MDHW sustained a roof displacement of 9 mm (0.3% drift), resulting in a recovery of 97%. Table 6-5 summarizes the results of each of the eleven analyses performed on Wall MDHW, with the roof displacements that reached the value of Δ_y highlighted.

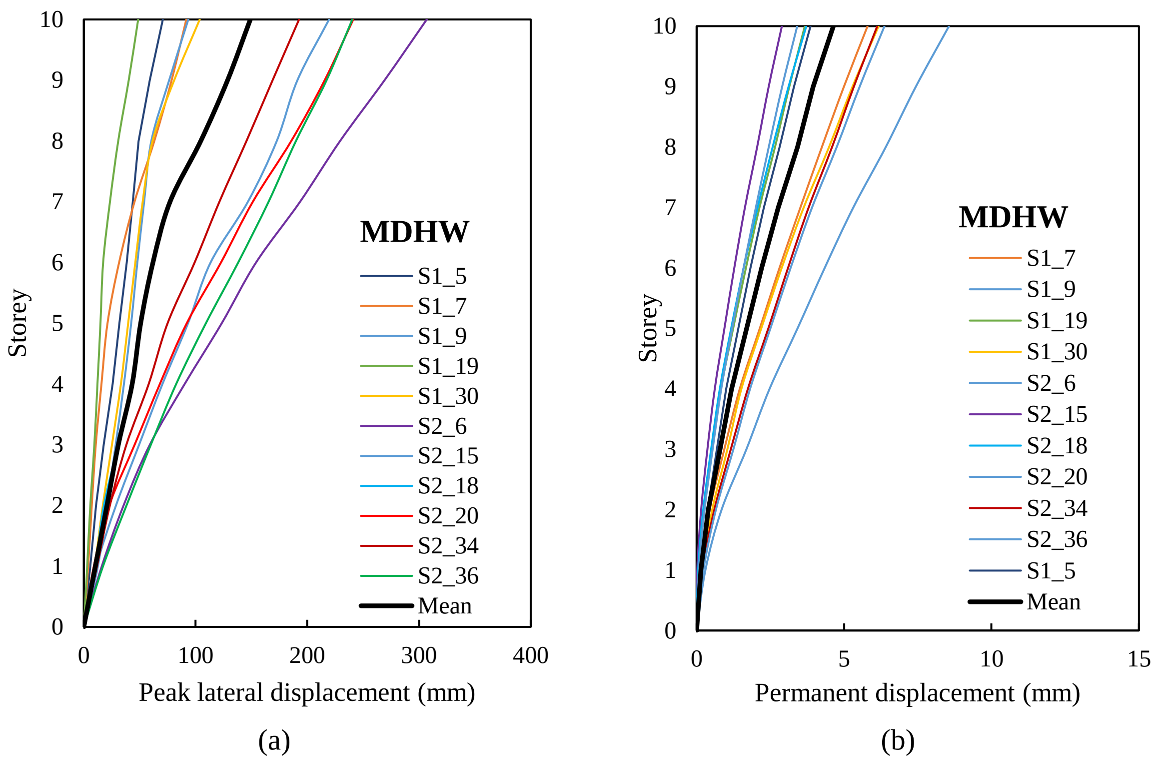

Figure 6-26 - Lateral displacement profiles of Wall MDHW: (a) peak lateral displacements and (b) permanent displacements at the end of the analyses

Table 6-5 - Summary of results from time history analyses of Wall MDHW

Record	Transient deformation			Permanent deformation			Recovery of roof drift (%)
	Roof displacement (mm)	Roof drift (%)	Interstorey drift (%) - associated storey	Roof displacement (mm)	Roof drift (%)	Interstorey drift (%) - associated storey	
S1_5	71	0.23	0.40 - 10	4	0.01	0.03 - 10	94.5
S1_7	92	0.30	0.53 - 8	6	0.02	0.03 - 8	94
S1_9	94	0.31	0.56 - 10	5	0.02	0.03 - 10	95
S1_19	49	0.16	0.30 - 9	4	0.01	0.03 - 9	92
S1_30	104	0.34	0.77 - 10	6	0.02	0.03 - 10	94
S2_6	307	1.01	1.33 - 9	9	0.03	0.03 - 9	97
S2_15	220	0.72	1.10 - 7	3	0.01	0.01 - 7	99
S2_18	149	0.49	0.93 - 8	4	0.01	0.03 - 8	97.5
S2_20	241	0.79	1.13 - 8	3	0.01	0.03 - 8	99
S2_34	193	0.63	0.80 - 6, 8 & 10	6	0.02	0.03 - 6, 8 & 0	97
S2_36	240	0.79	0.97 - 6	6	0.02	0.03 - 6	96
Mean	149	0.49	0.67 - 8	5	0.016	0.03 - 8	97

6.3.3 Dynamic response to amplified earthquake records

In order to further investigate the behaviour of the ductile walls under seismic excitation, additional analyses were run with amplified ground motion records. Two potential records were identified for the analysis: the scaled Record 150 - Coyote Lake, 1979, representative of Scenario 1, and the Record M9 Cascadia 14. The scaled Record 150 - Coyote Lake, 1979, representative of Scenario 1, was chosen and further amplified to 150% and 200%. This record was preferred given the less time-consuming analysis compared to that using records from Scenario 3. Figure 6-27 illustrates the roof displacement time history of Wall DSRW when subjected to 150% and 200% of Record 150. The yielding (grey dashed lines) and ultimate displacements (red dashed line) determined from the hysteretic response of the wall are indicated in Figure 6-27.

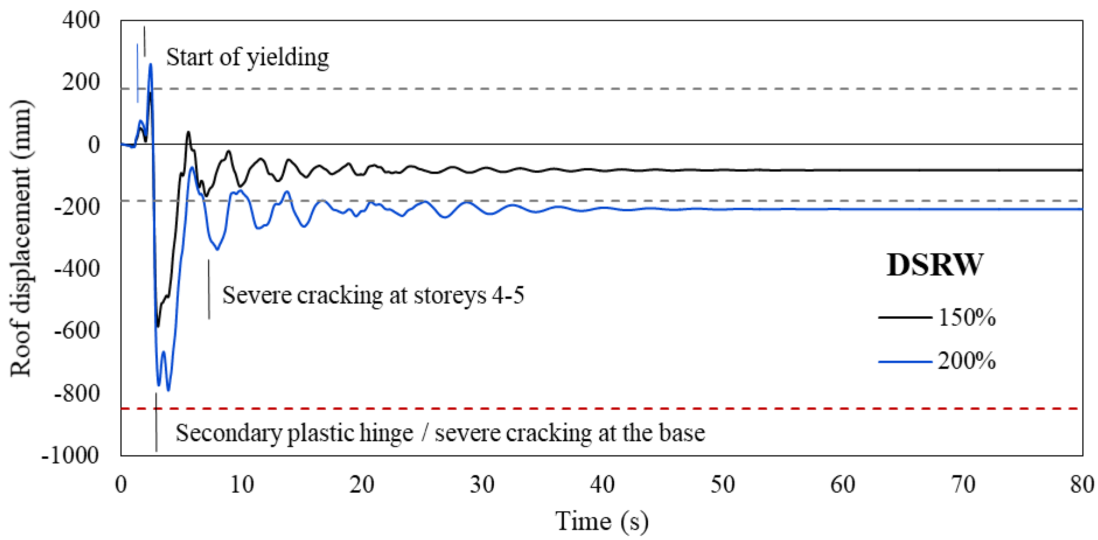

Figure 6-27- Lateral roof displacement time histories of Wall DSRW subjected to 150% and 200% of Record 150

Response of Wall DSRW, when subjected to the amplified record to 150%, remained elastic up to 2.4 s of analysis, when the roof displacement reached 167 mm, and the concentrated steel reinforcement in the boundaries yielded, causing the initiation of accumulation of inelastic deformation. When subjected to the amplified record to 200%, yielding initiated at 2 s (approximately 75 mm roof displacement). After 2.7 s in both analyses, all the longitudinal reinforcement in the cross-section of the wall had yielded. Figure 6-28 illustrates the stress in the longitudinal reinforcement of Wall DSRW at 3 s, where the bright green and the dark blue colours represent the elements that experienced stresses of 400 MPa, i.e. the yielding stress of steel, in tension and in compression, respectively. Yielding of the longitudinal steel indicates that 3 s corresponds to the time in the analysis when a secondary plastic hinge formed at storey 5, extending up to storey 6. Cracking surfaced as distributed cracks throughout the cross-section of the wall, with larger cracks developing at the base of the wall (fully developed at 3 s) and at storeys 4, 5, and 6 (fully developed at 7.5 s).

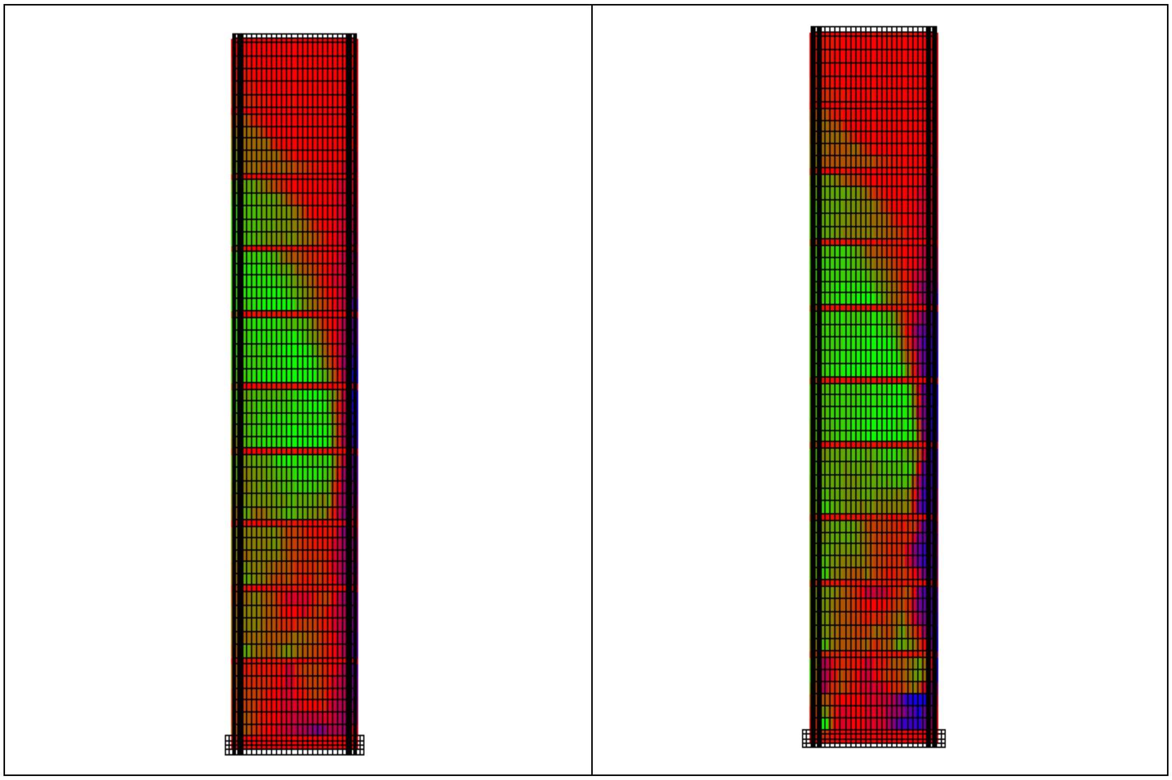

(a) (b)

Figure 6-28 - Stress in the longitudinal reinforcement of Wall DSRW at 3 s of analysis, when subjected to Record 150 scaled (a) to 150% and (b) to 200%

Figure 6-29 depicts the displaced shape of Wall DSRW at the end of the analyses using 150% and 200% of Record 150. Contrary to that observed in the analyses using ground motion records from Scenario 3, the steel reinforcement in the wall did not rupture when subjected to 150% and 200% of Record 150. The peak displacements experienced by Wall DSRW did not exceed Δ_u (847 mm). At the end of both analyses, the sustained inelastic damage inhibited recentering of the wall, and significant permanent damage was present.

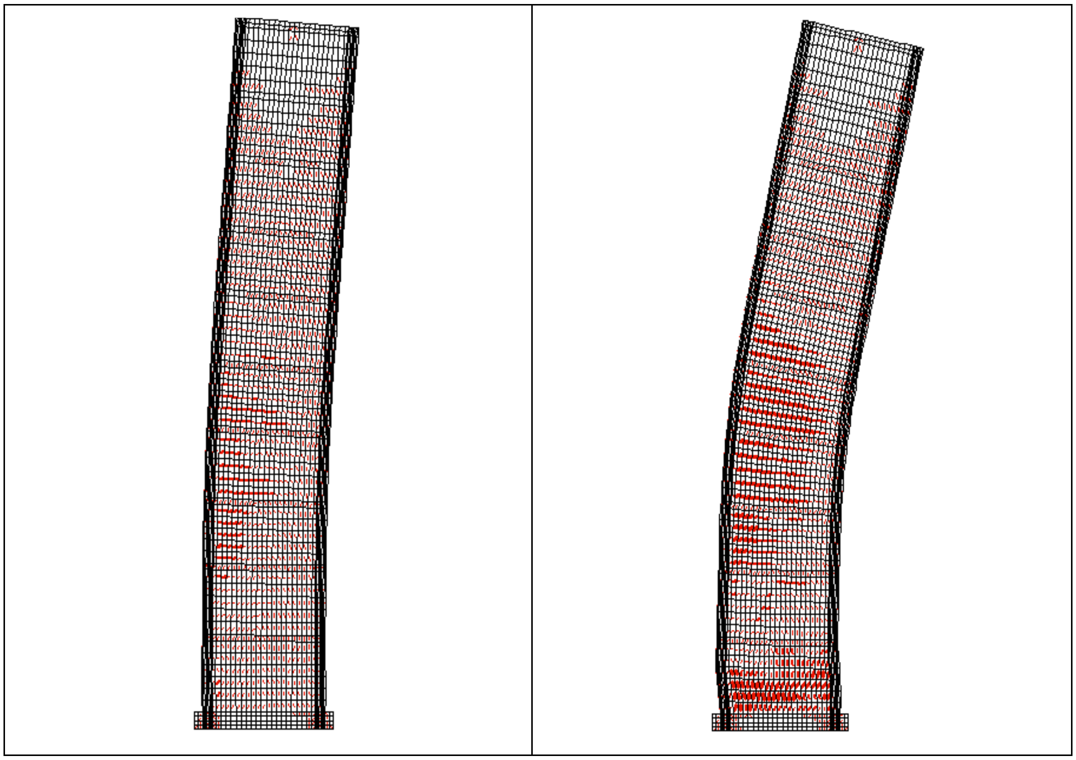

(a) (b)

Figure 6-29- Displaced shape and cracking pattern of Wall DSRW at the end of analysis when subjected to Record 150 scaled: (a) to 150% and (c) to 200%

Figure 6-30 contains the profile of lateral displacements of Wall DSRW when subjected to different intensities of Record 150, in terms of peak transient displacements (Figure 6-30 (a)), permanent displacements at the end of analysis (Figure 6-30 (b)), peak transient interstorey drifts (Figure 6-30 (c)), and permanent interstorey drifts (Figure 6-30 (d)). Wall DSRW experienced a peak roof displacement of 585 mm (1.92% drift) when subjected to 150% of Earthquake 150, and 790 mm (2.6% drift) when subjected to 200%. The maximum interstorey drift was recorded at storey 10 in both analyses, corresponding to 3.4% for 150% amplification and to 3.8% for 200% amplification. Significant interstorey drifts can also be observed in Figure 6-30 (c) in storey 6, for 150% amplification, and in storeys 6 and 8, for 200% amplification, which is explained by the formation of a secondary plastic hinge at upper levels during the analyses. At the end of analyses, permanent roof displacements in Wall DSRW were equal to 82 mm (0.3% drift) and to 207 mm (0.68% drift) for the 150% and 200% amplifications, respectively. The maximum permanent interstorey drift occurred at storey 8 under 150% excitation, corresponding to 0.43%, and at storey 10 under 200% excitation, corresponding to 1.2%. Both analyses also resulted in significant interstorey drifts at storey 6. Wall DSRW was able to recover 86% of the roof displacement experienced when subjected to the 150% earthquake, and 74% when subjected to the 200% earthquake.

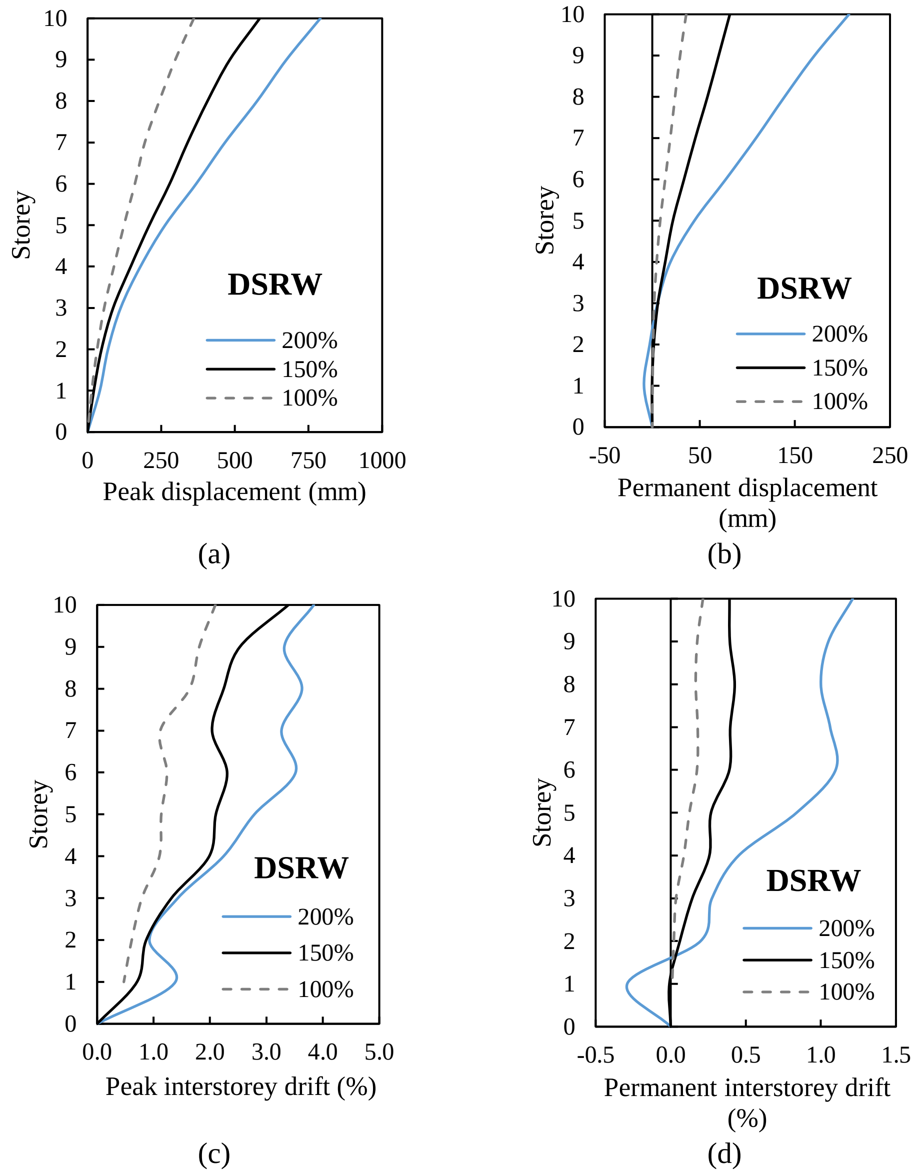

Figure 6-30- Lateral displacement profile of Wall DSRW corresponding to different intensities of Record 150: (a) peak lateral displacements, (b) permanent displacements at the end of analysis, (c) peak interstorey drifts and (d) permanent interstorey drifts at the end of analysis

Figure 6-31 provides the roof displacement time history of Wall DHW when subjected to 150% and 200% of Record 150. The values of Δ_y and Δ_u are also plotted, corresponding to 375 mm and 991 mm, respectively. Yielding of the steel reinforcement in the web zone of Wall DHW initiated at 1.8 s of analysis, when the roof displacement was approximately 51 mm under 150% excitation. Under 200% excitation, yielding was captured at 1.4 s, at 41 mm roof displacement. At approximately 3.1 s, the roof displacement reached 546 mm at 150% and 684 mm at 200%, and all longitudinal bars in the web zone of the wall had yielded. Large, localized cracks surfaced in the lower portion of Wall DHW, specifically at a critical section located approximately 1350 mm from the base, which were fully developed at 3.1 s. Storeys 5 and 6 also exhibited substantial levels of cracking, which was fully developed at approximately 7 s of analysis at 150%, and 8.5 s at 200% excitation. The SMA bars experienced pseudo-yielding but did not reach the superelastic strain limit of the material during analysis.

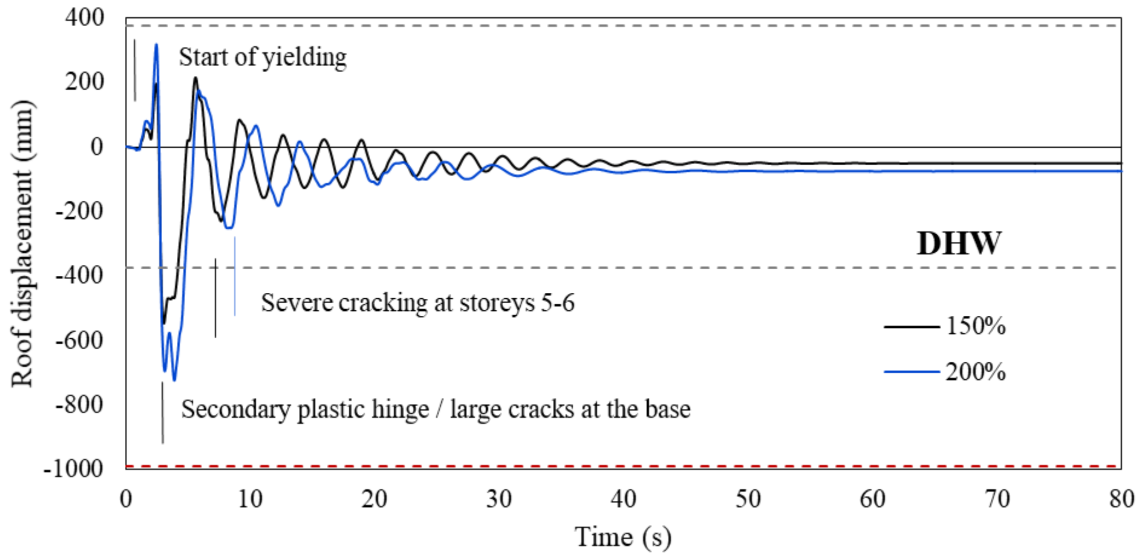

Figure 6-31 - Lateral roof displacement time histories of Wall DHW subjected to 150% and 200% of Record 150

Storeys 5 and 6 corresponded to the location where a secondary plastic hinge was formed, which was identified by the stress developed in the longitudinal steel reinforcement corresponding to f_y of 400 MPa. Figure 6-32 illustrates the stress of the truss bar elements in the finite element model of Wall DHW at 3.1 s, when subjected to 150% (a) and 200% (b) of Record 150. The bright green and the dark blue colours represent the elements where f_y is reached, in tension and compression, respectively. Figure 6-33 depicts the displaced shape of Wall DHW, along with the cracking patterns, at the end of analysis using Record 150 with 150% (a) and 200% (b) amplification.

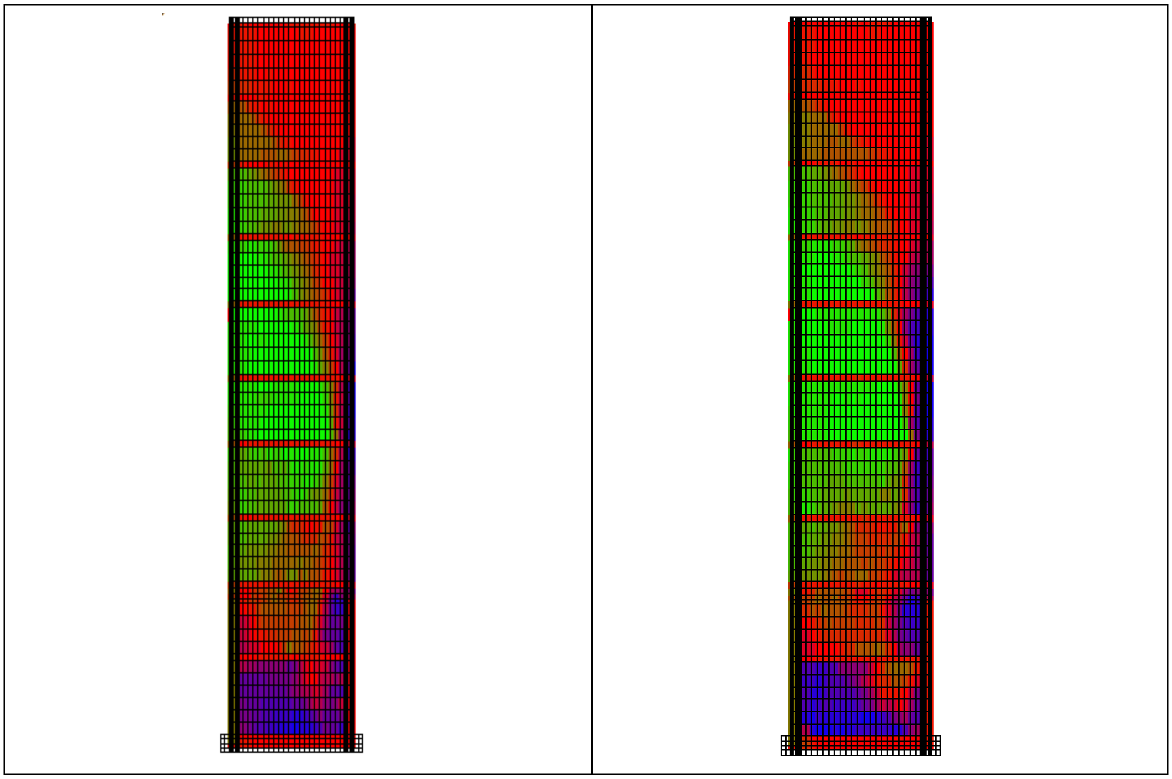

(a) (b)

Figure 6-32 - Stress in the longitudinal reinforcement of Wall DHW at 3.1 s of analysis when subjected to Record 150: (a) at 150% and (b) at 200%

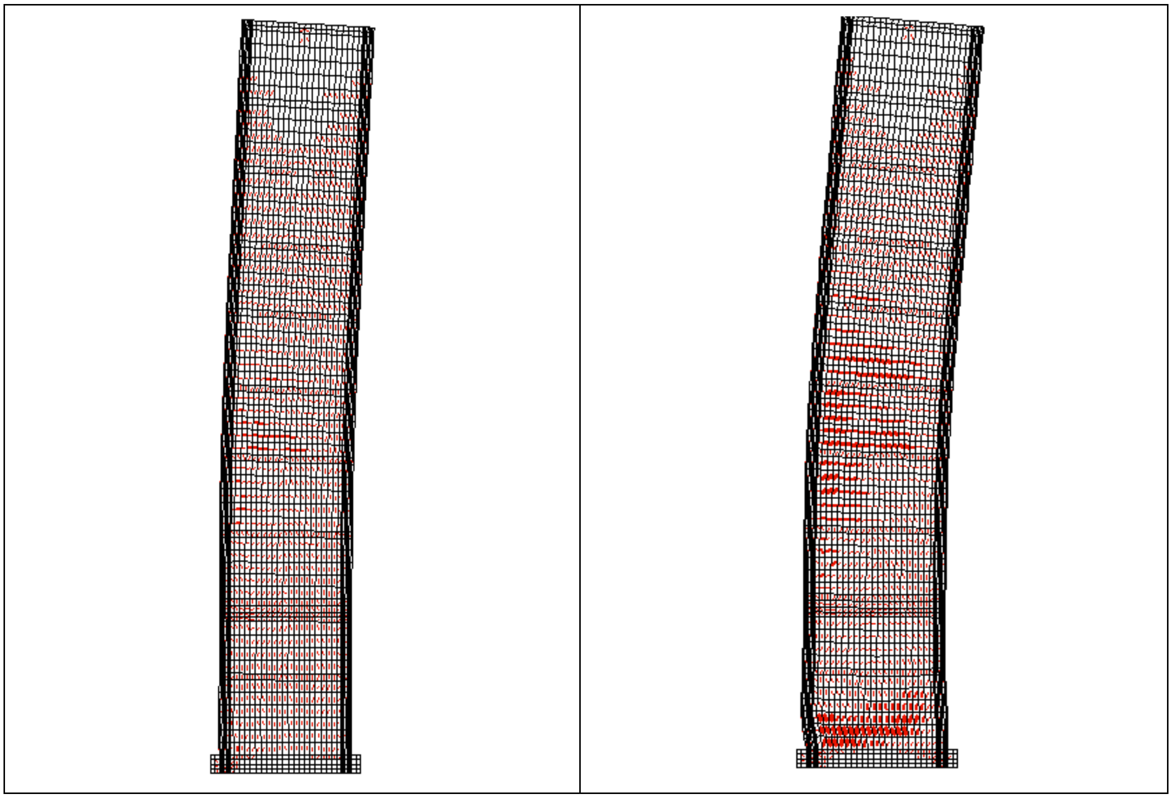
(a) (b)

Figure 6-33 - Displaced shape and cracking pattern of Wall DHW at the end of analysis when subjected to Record 150: (a) at 150% and (c) at 200%

From Figure 6-34 (a), the transient roof displacement in Wall DHW reached 547 mm (1.79% drift) when the 150% Earthquake was applied, and 724 mm (2.38% drift) when subjected to the 200% Earthquake. From Figure 6-34 (c), maximum interstorey drift was exhibited by storey 10, and corresponded to 3.23% at 150%, and to 3.8% at 200%. Substantial interstorey drifts were also experienced by storeys 6 and 8. At the end of analysis, Wall DHW sustained permanent roof displacement of 49 mm (0.16% drift) and 74 mm (0.24% drift), respective to the 150% and 200% excitations, as is evident in Figure 6-34 (b). The maximum permanent interstorey drift of 0.3% occurred at storey 10 for 150% amplification, as shown in Figure 6-34 (d). For 200% amplification, the maximum permanent interstorey drift of 0.47% occurred at storeys 8 and 10. Wall DHW recovered 91% of the roof displacements induced by the 150% Earthquake, and 90% of that induced by the 200% Earthquake.

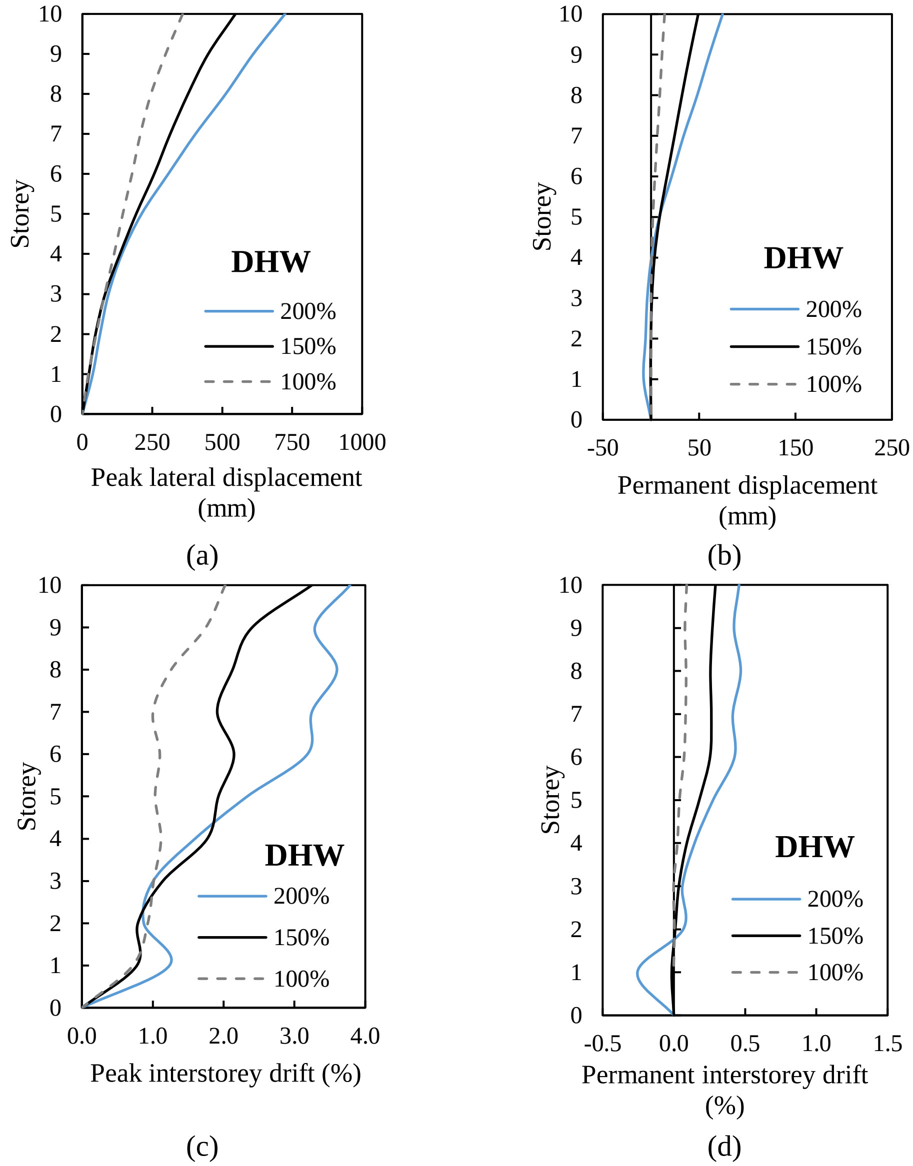

Figure 6-34 - Lateral displacement profile of Wall DHW corresponding to different intensities of Record 150: (a) peak lateral displacements, (b) permanent displacements at the end of analysis, (c) peak interstorey drifts and (d) permanent interstorey drifts at the end of analysis

7. DISCUSSION OF NUMERICAL RESULTS

This chapter discusses the numerical results presented in Chapter 6 with respect to the contribution of superelastic Ni-Ti SMA to the seismic response of ductile and moderately ductile shear walls investigated in this research study. Parameters of the response of the hybrid walls are assessed against those of the conventional steel-reinforced walls. From the monotonic and hysteretic responses, the comparison includes the lateral capacity (equivalent stiffness, strength, and displacement ductility), the self-centering capacity (residual drifts and recovery), and energy dissipation capacity, as well as the calculated wall rotation. Monotonic and hysteretic responses of each wall are also assessed against each other. From the time history analyses, the discussion will address the profiles of transient peak displacements and permanent displacements. Initially, the static response of the walls is assessed against benchmark studies in order to validate the analyses conducted herein.

7.1 Analysis validation

Results from a numerical study (Maciel et al., 2016) that investigated the effect of varying axial load ratios on slender, hybrid SMA-steel and conventional steel RC shear walls, previously tested and modelled by Abdulridha and Palermo (2017), were used to validate the results from the static analyses in this thesis. The walls are comparable given the SMA arrangement (Ni-Ti bars replacing the reinforcing steel in the boundary zones within the plastic hinge region) and aspect ratio (slender walls with aspect ratio greater than 2.0). Figure 7-1 illustrates the hysteretic response at 7.5% axial load of the hybrid wall analyzed by Maciel et al. (2016) (Figure 7-1 (a)) and from reverse cyclic analysis of Wall DHW investigated in this thesis, which was subjected to an axial load ratio of 6.9% (Figure 7-1 (b)). Similar behaviour between the two hysteretic responses can be observed in terms of pinching, shape of the hysteretic loops, and residual drifts up to 3.5% drift, given the slightly lower lateral displacement capacity of Wall DHW.

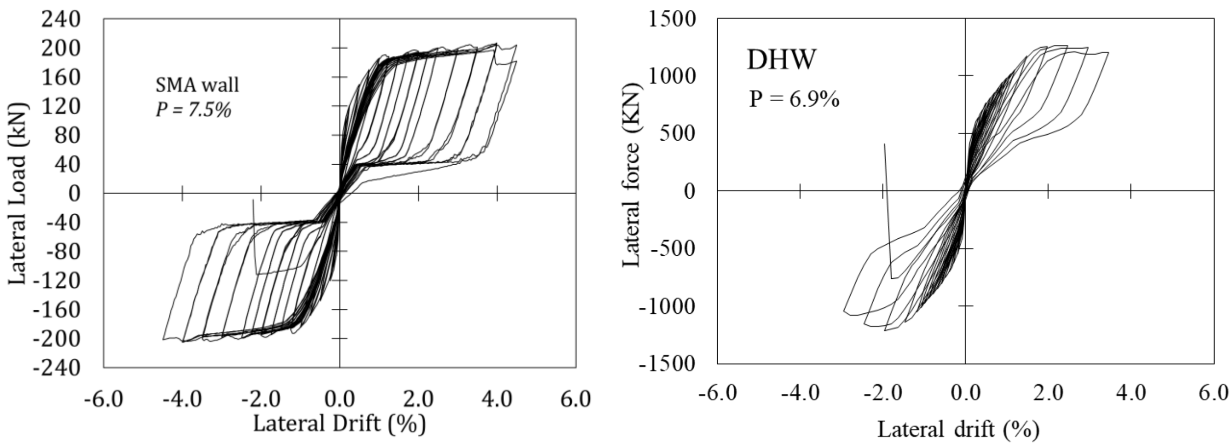

(a) (b)

Figure 7-1 - Hysteretic response from reverse cyclic analysis: (a) hybrid SMA-steel wall (Maciel et al., 2016) and (b) Wall DHW

Figure 7-2 contains the envelope of the lateral load-drift response obtained from experimental testing of the conventional steel-reinforced wall and the hybrid SMA-steel reinforced wall by Abdulridha and Palermo (2017) (Figure 7-2 (a)), and the envelope of lateral load-drift response of the conventional and hybrid ductile walls investigated in this thesis (Figure 7-2 (b)). The shape of the curves in Figure 7-2 (a), up to drift levels of 3.5%, is clearly very similar to that in (Figure 7-2 (b)) for both the conventional and the hybrid wall. This is an indication that the reverse cyclic analyses conducted herein could adequately predict the evolution of stiffness and lateral capacity of the walls, as well as capture the variation of these response parameters between conventional and hybrid walls.

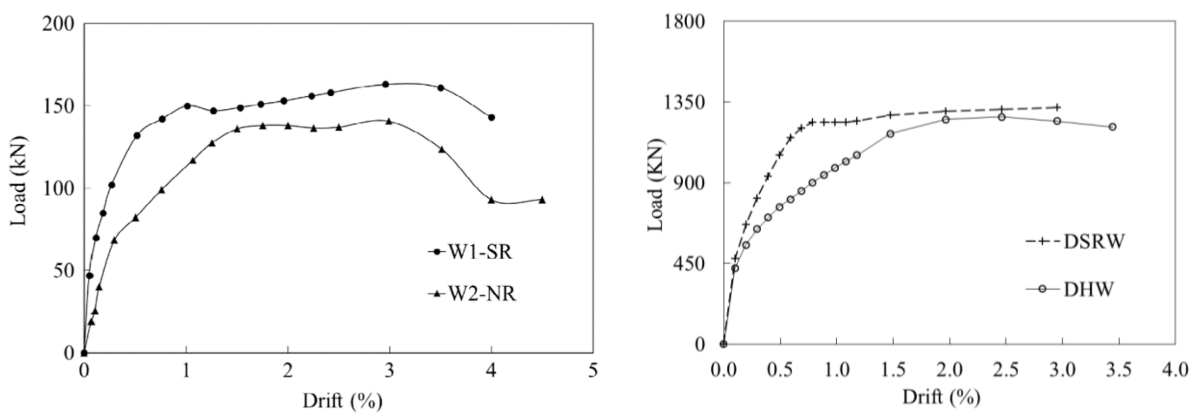

(a) (b)

Figure 7-2 - Envelope of lateral load-drift response of conventional and hybrid SMA-steel reinforced walls: (a) experimental response from Abdulridha and Palermo (2017) and (b) prediction of ductile walls DSRW and DHW

7.2 Assessment of monotonic response

Figure 7-3 illustrates the monotonic response of Wall DHW along with that of Wall DSRW. The effective stiffness of Wall DHW corresponds to 45% of Wall DSRW, which is explained by the lower modulus of elasticity of SMA compared to that of steel reinforcing bars. However, the hybrid wall exhibits comparable lateral strength to the steel-reinforced wall, with a difference of only 5%. The lower displacement ductility of Wall DHW is partially due to the much higher pseudo-yield displacement of this wall. The displacement capacity of Wall DHW is 15% lower than Wall DSRW. This lower capacity is attributed to the fracture of the longitudinal reinforcing steel identified in the web zone of the hybrid wall during the pushover analysis. Fracturing of the reinforcement in the web was the result of larger crack openings in Wall DHW, which led to localized strain accumulation in the reinforcing bars.

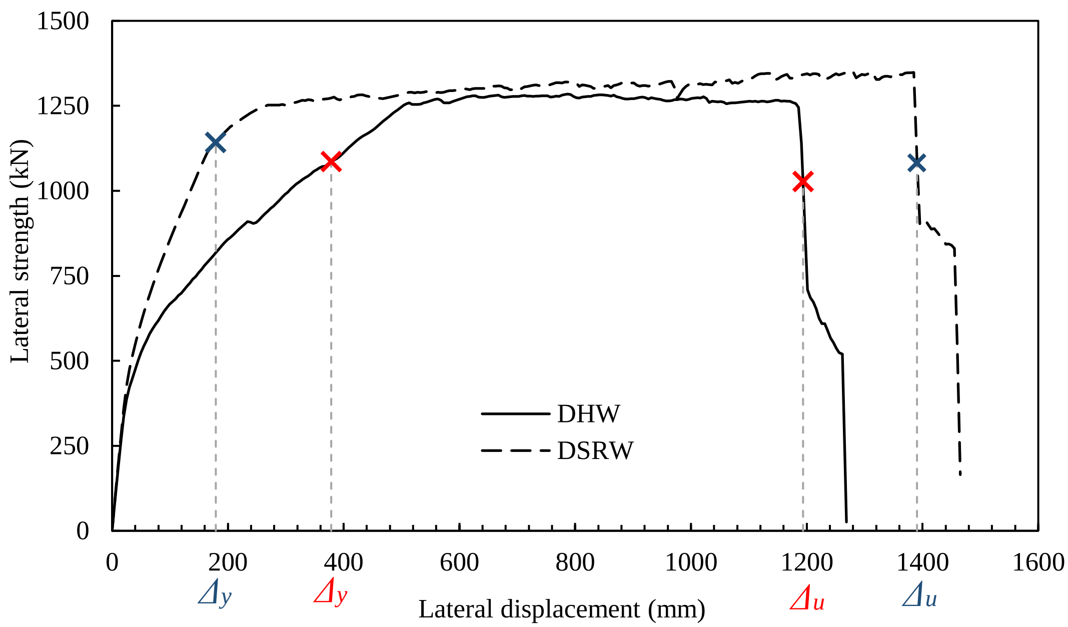

Figure 7-3 - Monotonic response of ductile walls DSRW and DHW

Figure 7-4 presents the monotonic response of the moderately ductile Walls MDSRW and MDHW. Analogous behaviour to that between the ductile walls was observed in Wall MDHW and Wall MDSRW in terms of comparable strength (5% drop), lower effective stiffness, and slightly lower displacement ductility. k_{eff} of Wall MDHW corresponds to 44% of Wall MDSRW. Higher Δ_y, more than two times greater than Δ_y of the steel-reinforced wall, resulted in a smaller displacement ductility of Wall MDHW when compared to Wall MDSRW. However, the moderately ductile hybrid wall experienced similar ultimate displacement as the steel-reinforced wall, with a difference of only 3.6%.

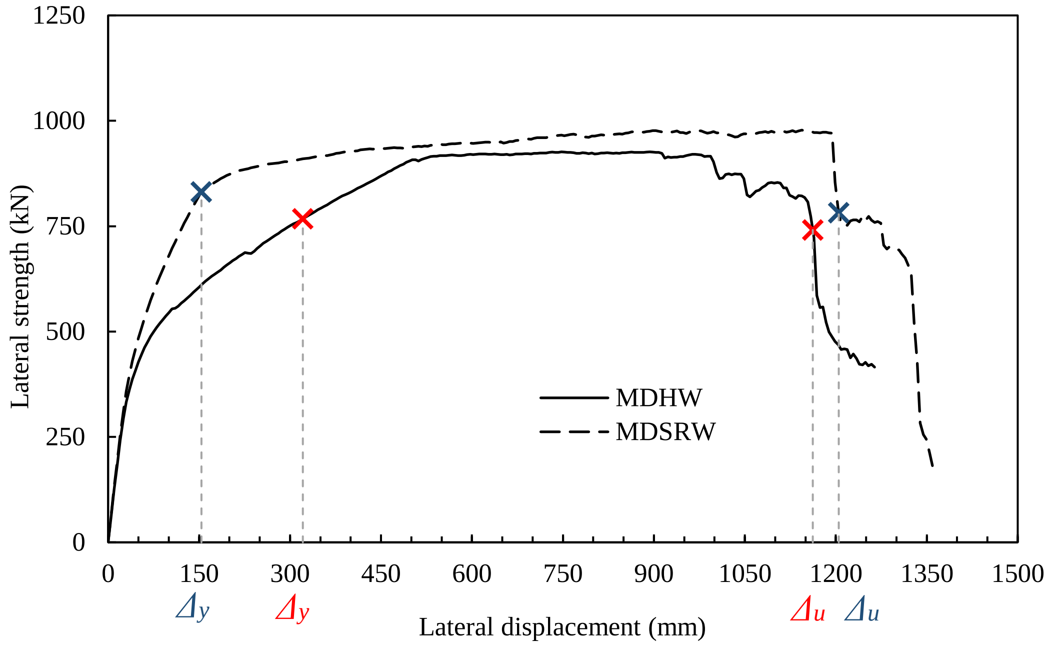

Figure 7-4 - Monotonic response of moderately ductile Walls MDSRW and MDHW

7.3 Assessment of hysteretic response

Figure 7-5 illustrates the lateral load-lateral displacement and drift responses of the ductile walls. The drifts were calculated as the top displacement divided by the height of the wall, which corresponds to the point where displacements were applied in the models. Walls DSRW and DHW sustained peak strengths (F_{max}) of 1319 kN and 1266 kN, respectively. The strength of Wall DHW was only 4% lower than that of Wall DSRW. The calculated effective stiffness (k_{eff}) was 6.4 kN/mm for Wall DSRW and 2.8 kN/mm for Wall DHW. The lower k_{eff} of Wall DHW, 44% of k_{eff} of Wall DSRW, was expected given the lower modulus of elasticity of the Ni-Ti SMA bars. This reduction in stiffness, however, does not infer an inferior seismic response. A lower stiffness elongates the fundamental period of the structure, which, in turn, would result in lower seismic forces if the walls were to be redesigned. Walls DSRW and DHW experienced displacement ductilities (μ) of 4.7 and 2.6, respectively. These ductilities correspond to ultimate displacements (Δ_u) of 847 mm and 991 mm, respectively. Wall DSRW exceeded the ductility capacity of 3.5 specified in the Canadian concrete design code for ductile shear walls. It was observed that rupture of the reinforcing steel in the web zone reduced the ductility of the SMA-reinforced wall. The lower displacement ductility of Wall DHW can also be attributed to the much higher pseudo-yield displacement (onset of reorientation) of this wall. Note; however, that a more appropriate comparison between the walls is the drift capacity.

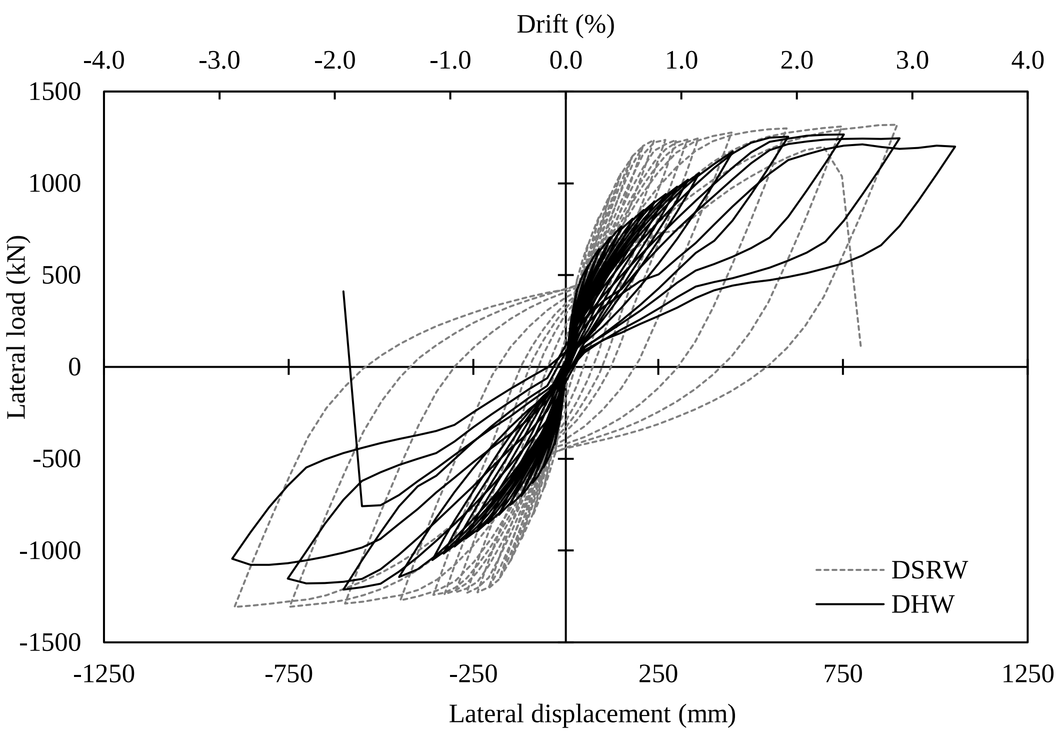

Figure 7-5 - Lateral load-displacement hysteretic response of ductile walls

In Figure 7-6, the monotonic and reverse cyclic responses of the ductile walls are superimposed. It can be observed that the monotonic responses form the envelope of the cyclic responses, but lower displacement capacities are exhibited by the cyclic responses compared to that anticipated by the monotonic responses of both walls. The lateral displacement capacity of Walls DSRW and DHW under reverse cyclic loading represents 61% and 83% of that exhibited under monotonic loading, respectively. Under cyclic loading, the longitudinal steel yields at both ends of the walls, resulting in large flexural cracking extending the full length of the walls. The repetition of cycles results in an accumulation of damage that does not occur under monotonic loading. The incidence of cracking only in one direction from monotonic loading delayed the progress of failure mechanisms.

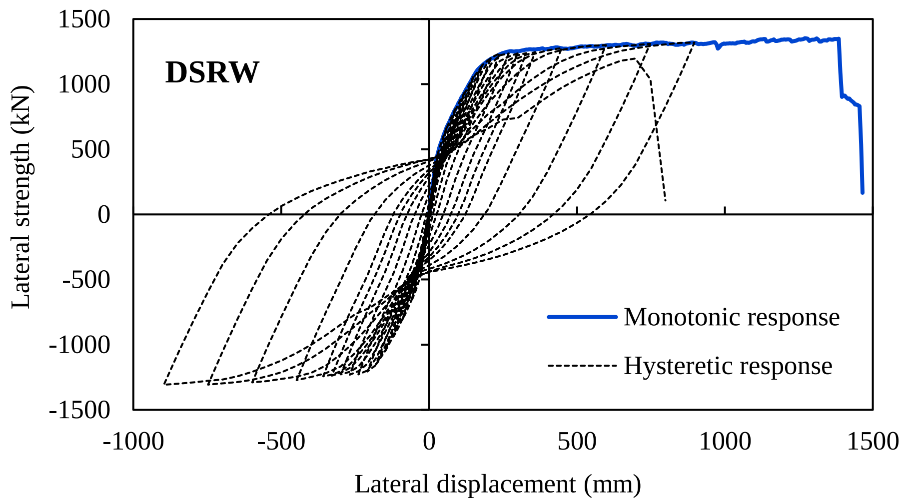

(a)

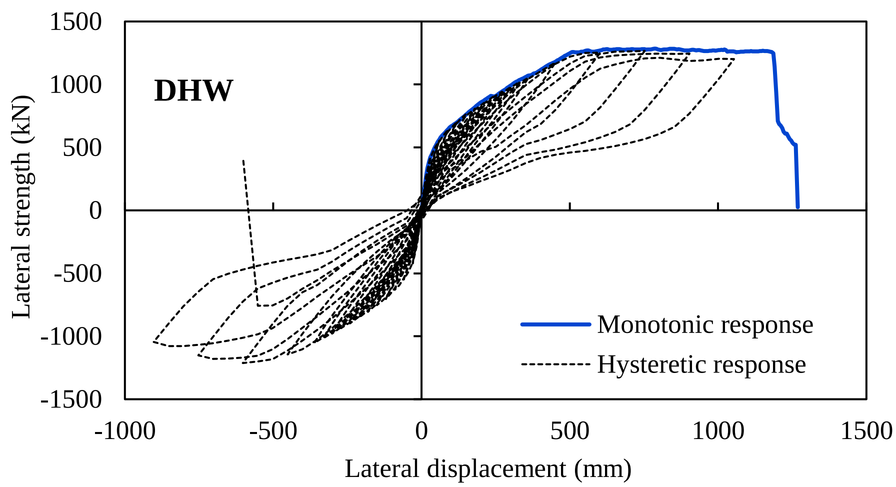

(b)

Figure 7-6 - Monotonic and hysteretic responses of the ductile walls: (a) Wall DSRW and (b) Wall DHW

Figure 7-7 shows the hysteretic response of the moderately ductile walls. Similar lateral strength was demonstrated by both walls, with F_{max} of 973 kN and 926 kN for Walls MDSRW and MDHW, respectively. Strength of Wall MDSRW was only 5% greater than that of Wall MDHW. In terms of stiffness, k_{eff} of Wall MDHW was found to be approximately 44% of that of Wall MDSRW. The smaller yield displacement of Wall MDSRW (156 mm) compared to Wall MDHW (333 mm) contributed to the greater displacement ductility of this wall (μ = 7.7) compared to that of the hybrid wall (μ = 3.5). The response of Wall MDSRW significantly exceeded the ductility capacity of 2.5 specified by the Canadian design code for moderately ductile shear walls. Both walls experienced similar lateral displacement capacity, sustaining Δ_u of 1201 mm (Wall MDSRW) and 1174 mm (Wall MDHW).

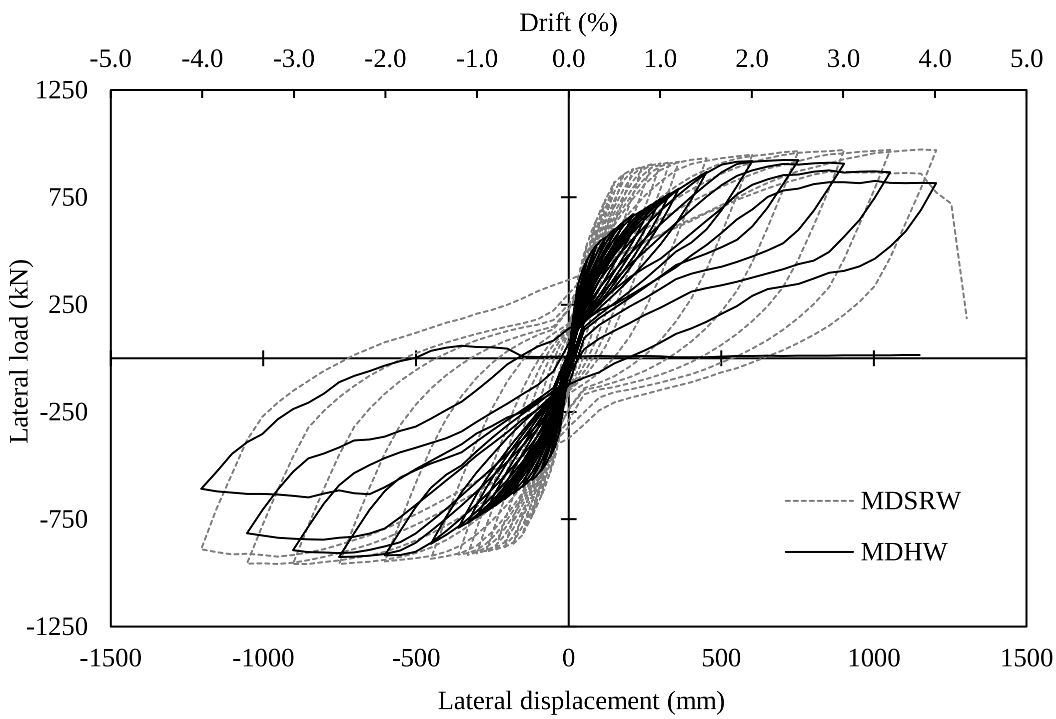

Figure 7-7 - Lateral load-displacement hysteretic response of moderately ductile walls

In Figure 7-8, the monotonic responses of the moderately ductile walls is superimposed on their respective hysteretic responses. The monotonic responses follow the envelope of the hysteretic responses for both walls. In contrast to that observed in the ductile walls, the lateral displacement capacity of the moderately ductile walls predicted under monotonic loading is an excellent match to that exhibited under reverse cyclic loading, with variations of only 0.3% in Wall MDSRW and 1% in Wall MDHW in terms of ultimate displacement.

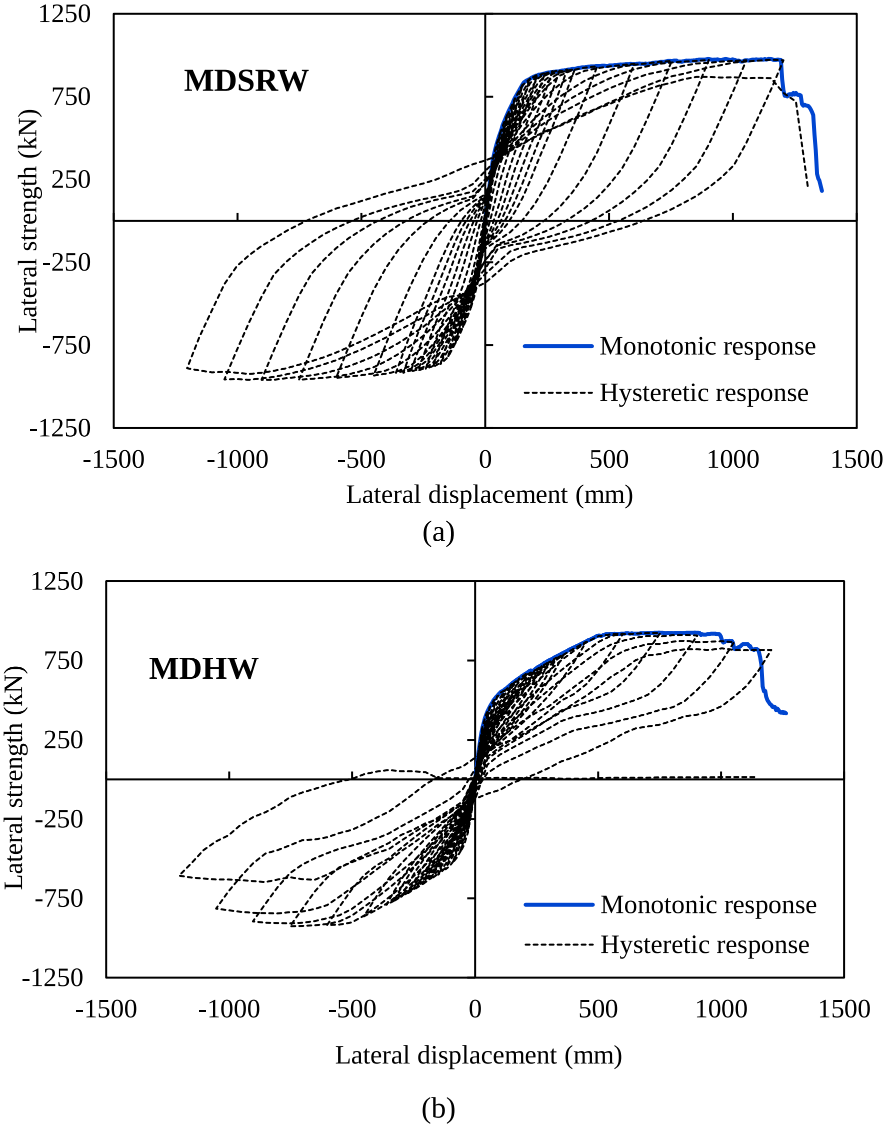

Figure 7-8 - Monotonic and hysteretic responses of the moderately ductile walls: (a) Wall MDSRW and (b) Wall MDHW

7.3.1 Energy dissipation

Figure 7-9 (a) provides the hysteresis loop of the ductile walls at the drift ratio of 2.5%. The response of Wall DHW exhibits more pronounced pinching than Wall DSRW. Pinching in Wall DHW is primarily due to the superelastic feature of the SMA bars. Conversely, wider hysteretic loops in Wall DSRW are the result of yielding of the reinforcing steel. The energy dissipated by the walls during each cycle was calculated based on the area of the force-displacement loop. The cumulative dissipated energy versus drift for the ductile walls is shown in Figure 7-9 (b). The energy dissipation capacity of Wall DSRW shows a more pronounced increase than that of Wall DHW. There is a noticeable increase in the energy dissipated by the steel-reinforced wall at higher drifts. At a drift of 2.5%, Wall DSRW dissipated 4179 kNm of energy, while Wall DHW dissipated 1570 kNm. The energy dissipated by Wall DHW is approximately 38% of Wall DSRW at 2.5% drift, and 47% in total. As mentioned, the lower energy dissipation capacity in Wall DHW relates to the flag-shaped hysteretic behaviour with significant pinching and does not necessarily implicate in inferior seismic performance, which will be further addressed in the discussion of the results from the time-history analysis of the walls.

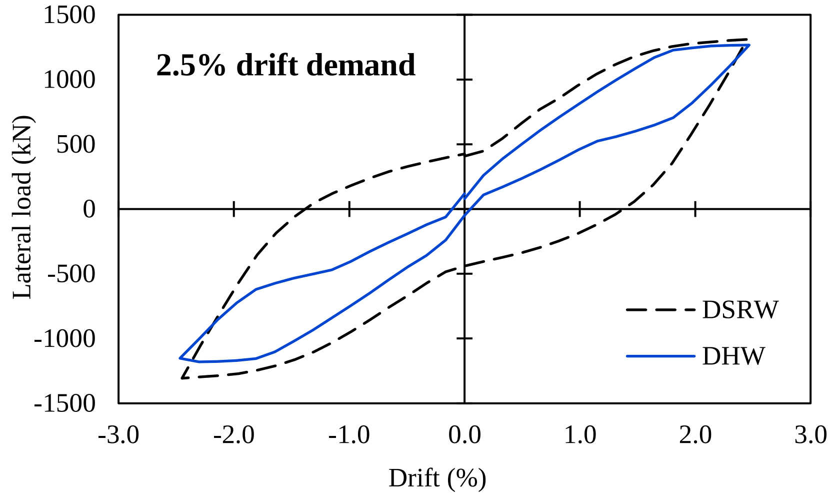

(a)

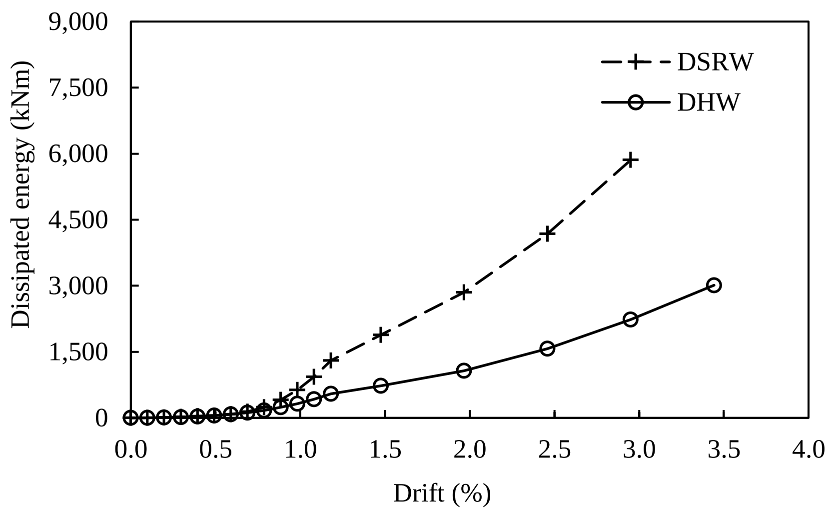

(b)

Figure 7-9 - Energy dissipation of Walls DSRW and DHW: (a) hysteresis cycle at 2.5% drift, and (b) cumulative dissipated energy

The hysteresis loop at the drift ratio of 2.5% of the moderately ductile walls is depicted in Figure 7-10 (a). The response of the moderately ductile walls is analogous to that of the ductile walls. More pronounced pinching is present in the response of the hybrid wall, due to the superelastic response of the SMA bars, in contrast with the wider hysteretic loops of the steel-reinforced wall. The cumulative dissipated energy versus drift of the moderately ductile walls is shown in Figure 7-10 (b). The energy dissipation of the moderately ductile walls followed the same trend as that of the ductile walls, with higher levels of energy dissipation in the steel-reinforced wall, specifically at higher drifts, compared to Wall MDHW. At a drift of 2.5%, Wall MDHW dissipated 1114 kNm of energy, while Wall MDSRW dissipated 2995 kNm. At 2.5% drift, the energy dissipated by Wall MDHW is approximately 37% of Wall MDSRW.

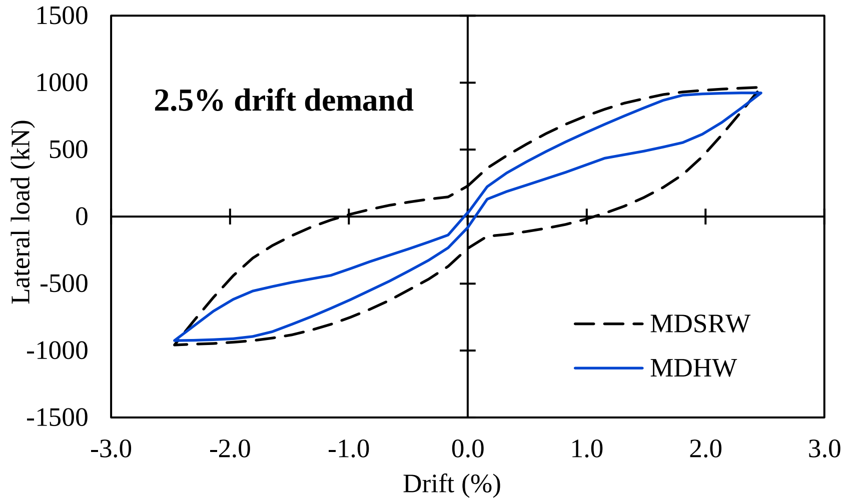

(a)

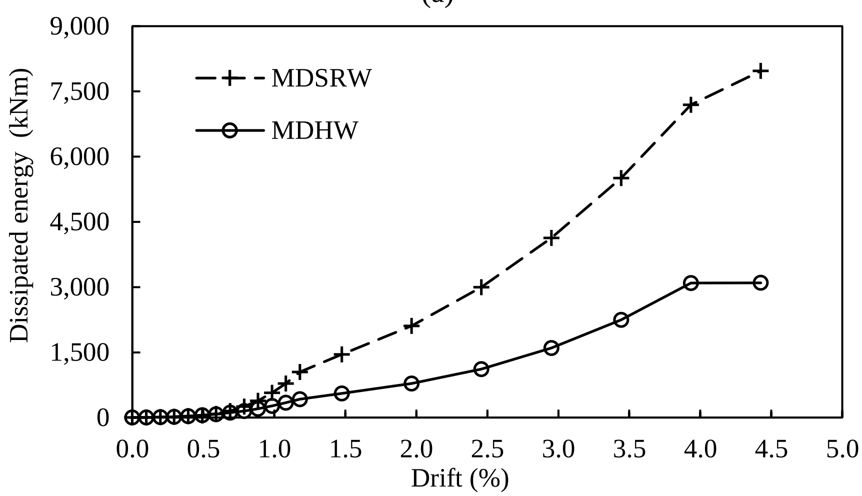

(b)

Figure 7-10 - Energy dissipation of Walls MDSRW and MDHW: (a) hysteresis cycle at 2.5% drift, and (b) cumulative dissipated energy

7.3.2 Self-centering capacity

Figure 7-11 (a) illustrates the lateral load versus drift envelope from the hysteretic response of the ductile walls. Wall DHW sustained drifts up to 3.5%, whereas maximum drift in Wall DSRW was 3%. Therefore, both walls provided lateral drift capacities in excess of the code limit of 2.5% for normal importance buildings. Figure 7-11 (b) presents the residual drift versus peak drift of the ductile walls. The residual drift of the walls corresponded to the drift at the completion of unloading. Residual drifts in Wall DSRW become evident at a drift of 0.7% and increase almost linearly thereafter. At a peak drift of 3%, a residual drift of 1.78% is exhibited in Wall DSRW. Wall DHW initially experienced residual drifts similar to those of Wall DSRW. However, beyond 0.6% drift, Wall DHW maintained significantly smaller residual drifts for all peak drifts in comparison to Wall DSRW, showing a residual drift of 0.16% at 3% peak drift, which represents a reduction in residual drift of 89% from the steel-reinforced wall to the hybrid wall.

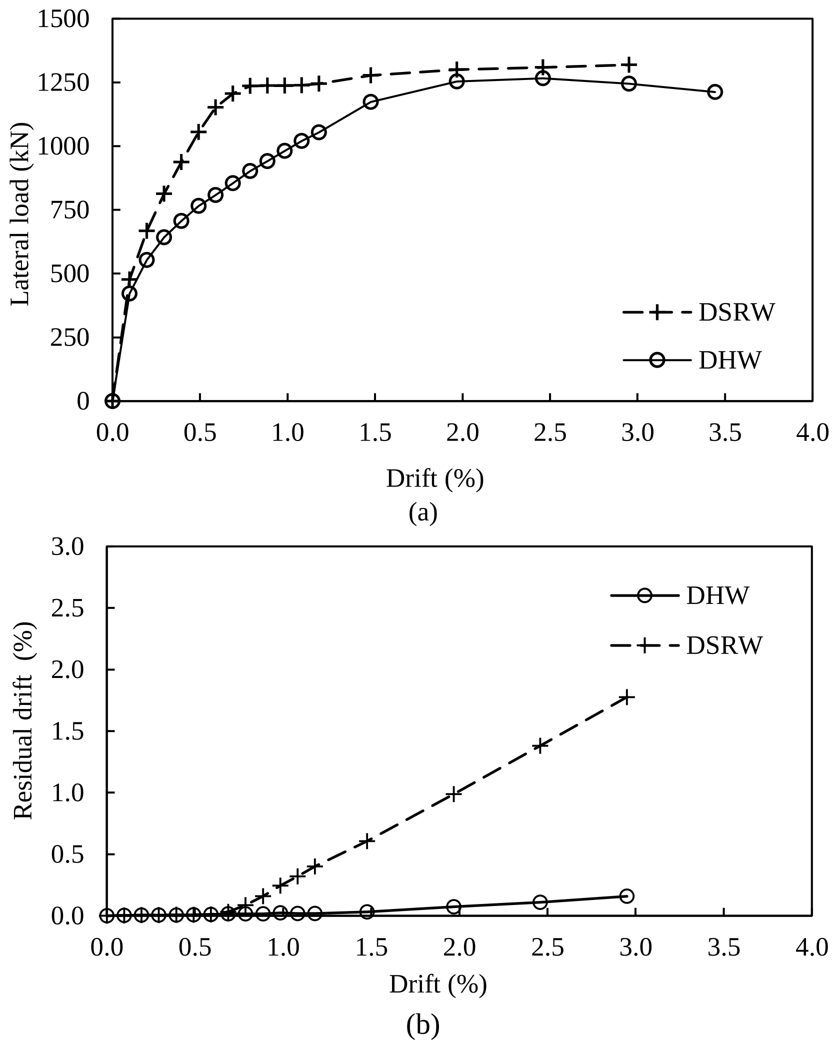

Figure 7-11 - Self-centering capacity of ductile walls: (a) envelope of lateral load-drift response and (b) residual drift-peak drift response

Figure 7-12 illustrates the recovery capacity of the ductile walls. In self-centering systems, the recovery capacity has the purpose of permitting post-earthquake repairs (Abdulridha and Palermo, 2017). The recovery was calculated as the ratio of the difference between the peak and the residual drift to the peak drift at each drift. At a drift of 2.5%, Wall DHW provides a recovery capacity of 96%, compared to the approximate recovery capacity of 44% of Wall DSRW. Wall DHW sustained significantly smaller residual drifts than Wall DSRW, demonstrating higher self-centering capacity. The self-centering effect of SMA is further confirmed by the realigned position of Wall DHW upon unloading (Figure 6-9 (d)) compared to the significant permanent deformation of Wall DSRW (Figure 6-9 (b)).

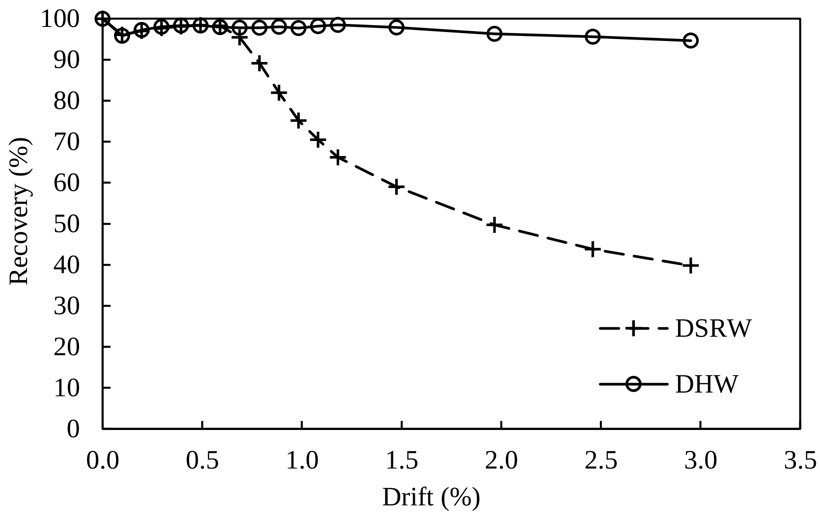

Figure 7-12 - Recovery-drift response of ductile walls

Figure 7-13 (a) illustrates the lateral load versus drift envelope from the hysteretic response of the moderately ductile walls. Both walls sustained drifts up to 4.5%, satisfying the code limit of 2.5% maximum lateral drift. Figure 7-13 (b) presents the residual drift versus peak drift of the moderately ductile walls. Similar to that observed in Wall DSRW, residual drifts in Wall MDSRW become noticeable at a drift of 0.7% and increase almost linearly thereafter. At a peak drift of 3%, a residual drift of 1.42% is exhibited in Wall MDSRW. Wall MDHW initially experienced residual drifts similar to those of Wall MDSRW. Beyond 0.7% drift, Wall MDHW maintained substantially smaller residual drifts for all peak drifts in comparison to Wall MDSRW. Residual drift in Wall MDHW is equal to 0.09% at 3% peak drift, which represents a reduction of 94% from the residual drift of the steel-reinforced wall to that of the hybrid wall. Wall MDHW sustained significantly smaller residual drifts than Wall MDSRW, demonstrating higher self-centering capacity. Wall MDHW suffered significant strength degradation beyond 3% drift caused by the fracture of multiple steel reinforcing bars from the vertical reinforcement of the web zone of the wall, and from the horizontal reinforcement at late stages of drift. As a result, residual drifts in Wall MDHW increased at the end of the analysis but remain approximately equal to 70% of that in Wall MDSRW.

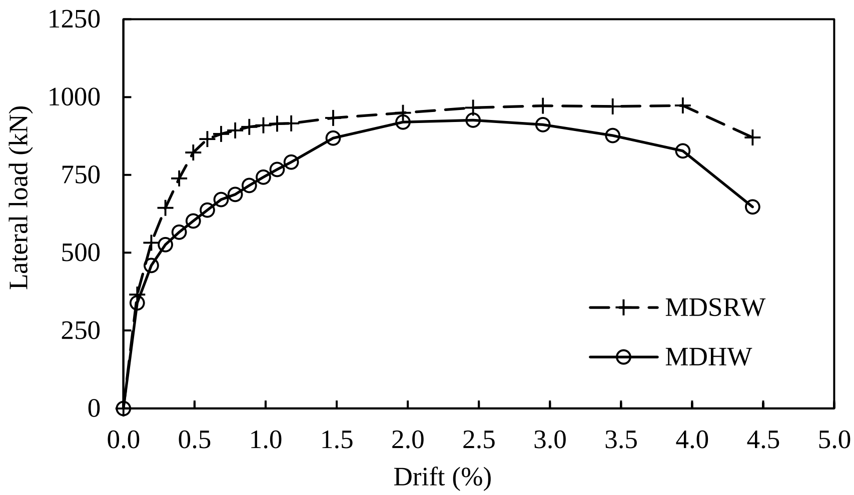

(a)

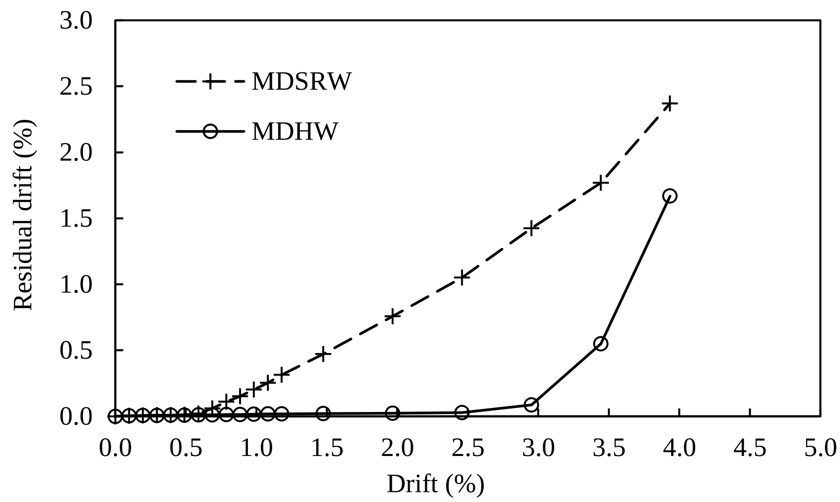

(b)

Figure 7-13 - Self-centering capacity of moderately ductile walls: (a) envelope of lateral load-drift response and (b) residual drift-peak drift response

The recovery capacity of the moderately ductile walls is presented in Figure 7-14. At a drift of 2.5%, Wall MDHW provides a recovery capacity of approximately 99%, compared to the approximate recovery capacity of 57% of Wall MDSRW. Due to the fracture of multiple steel reinforcing bars in the web zone, recovery of Wall MDHW is reduced at the end of the analysis but remains approximately 1.5 times that of Wall MDSRW at 4% drift. The self-centering effect of SMA is evident in the hybrid moderately ductile wall, which can be further observed in the realigned position of Wall MDHW upon unloading (Figure 6-14 (d)) compared to the significant permanent deformation of Wall MDSRW (Figure 6-14 (b)).

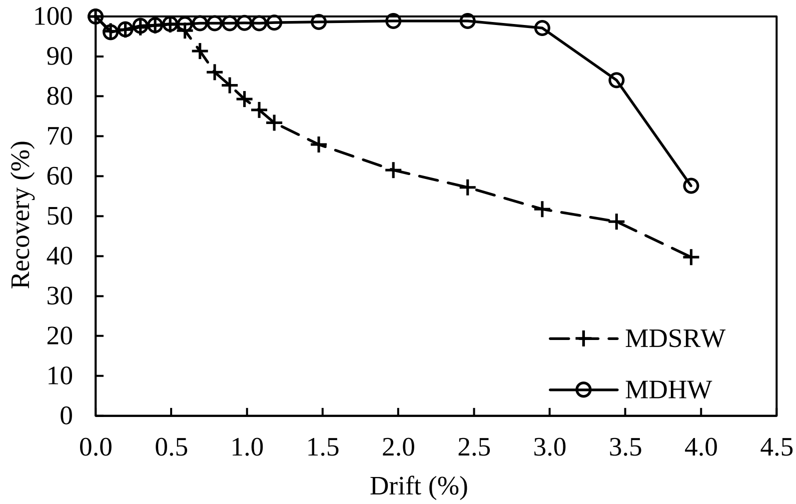

Figure 7-14 - Recovery-drift response of moderately ductile walls

7.3.3 Wall rotation

The rotation of the ductile walls is illustrated in Figure 7-15, where the total rotation is presented along with the rotation corresponding to the lower portion of the wall. Wall rotation was calculated based on the variation of vertical displacements between the left and right sides of the walls and the length of the walls. For the hybrid SMA-steel reinforced walls, the rotation recorded at the lower portion of the walls represents rocking above the cracked critical section, while the remaining rotation in the hybrid walls, and the total rotation in the steel-reinforced walls, are the result of flexure along the wall height.

Wall DSRW (Figure 7-15 (a)) experienced a maximum rotation of 0.009 in the lower portion of the wall (height of 1200 mm). This rotation corresponds to 29% of the maximum total rotation of 0.031. In contrast, a much greater percentage of wall rotation is concentrated in the lower portion of Wall DHW. On the positive side of Figure 7-15 (b), 85% of the maximum wall rotation (0.031) of Wall DHW is concentrated at the lower portion of the wall (0.026). Walls DSRW and DHW experience similar levels of total wall rotation. However, significant variation exists between the rotations in the lower portion of the walls. At the positive side, the maximum rotation sustained by the lower portion of Wall DHW is nearly three times greater than that in Wall DSRW. This concentration of the rotation is explained by the large crack that formed at the critical section of the hybrid wall due to the smoothness of the SMA bars, on top of which the wall rotates as a rigid body. In contrast, cracking in the steel-reinforced wall is more evenly distributed, and the rotation is associated with flexure rather than rocking. The fact that most of the wall rotation is concentrated within a height of 1200 mm in the hybrid wall, which is shorter than the anticipated plastic hinge of the walls (6050 mm), indicated that the length of the SMA bars employed in the hybrid walls could be reduced, resulting in a more efficient and less costly design. Reduced lengths of SMA bars in hybrid SMA-steel reinforced concrete shear walls were briefly investigated and were discussed in Section 5.1.2.

When comparing the shape of the hysteretic loops in Figure 7-15 (a) and (b), it is evident that the response of Wall DHW presents substantially greater level of pinching, which is a consequence of the superior self-centering capacity demonstrated by the hybrid SMA-Steel reinforced concrete system.

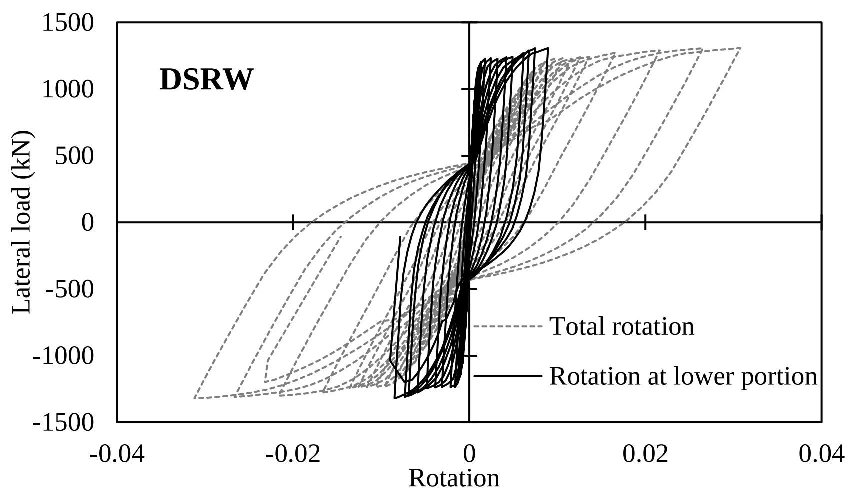

(a)

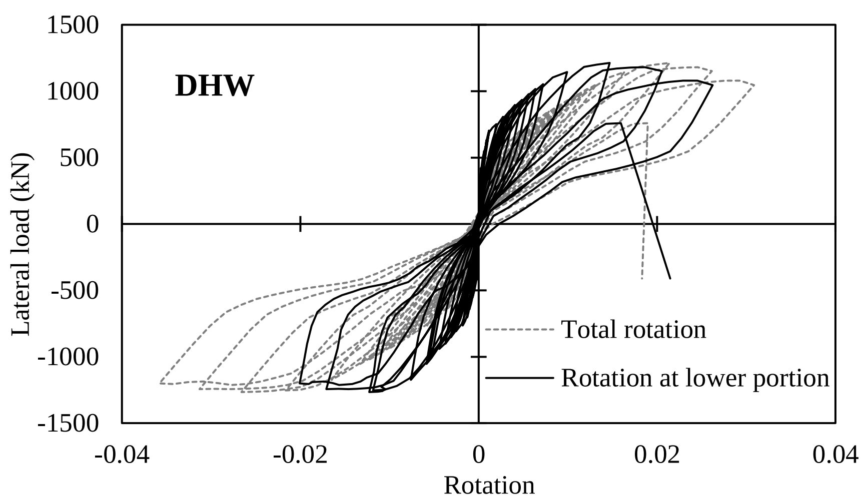

(b)

Figure 7-15 - Wall rotation of ductile walls: (a) Wall DSRW and (b) Wall DHW

Figure 7-16 illustrates the rotation of Walls MDSRW (a) and MDHW (b) in terms of total wall rotation and rotation at the lower portion of the walls. Figure 7-16 (a) demonstrates that the maximum wall rotation of Wall MDSRW is 0.040, while the maximum rotation sustained in the lower portion of the wall is equal to 0.012. Thus, the lower portion of Wall MDSRW contributes approximately 30% of the total wall rotation at the end of loading. The maximum wall rotation recorded in Wall MDHW, as shown in Figure 7-16 (b), is equal to 0.041. In the positive direction, the maximum wall rotation is 0.038, from which 78% is concentrated in the lower portion of the wall (0.029). Both walls experience equivalent levels of total wall rotation, but a significant deviation in behaviour is observed in the lower portion of the walls. In the positive direction, the lower portion of Wall MDHW sustains a rotation at the end of loading that is 2.4 times greater than the lower portion of Wall MDSRW. Similar to that observed for the ductile walls, the localized crack that surfaced at the critical section of Wall MDHW allowed the wall to rotate as a rigid body, resulting in concentration of wall rotation at the lower portion of the wall, while the distributed damage on Wall MDSRW led to larger values of rotation due to flexure. The reduced residual rotations at zero load exhibited by the response of Wall MDHW (Figure 7-16 (b)), compared to the response of Wall MDSRW (Figure 7-16 (a)), further demonstrates the higher level of self-centering achieved by the hybrid wall.

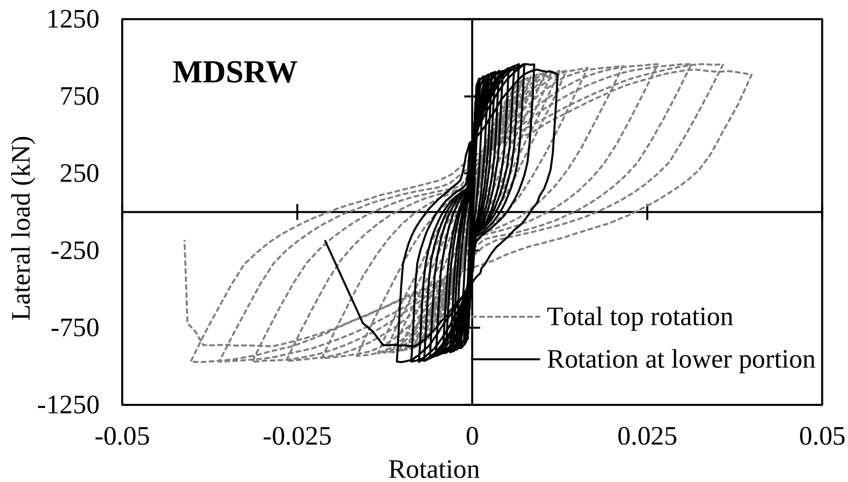

(a)

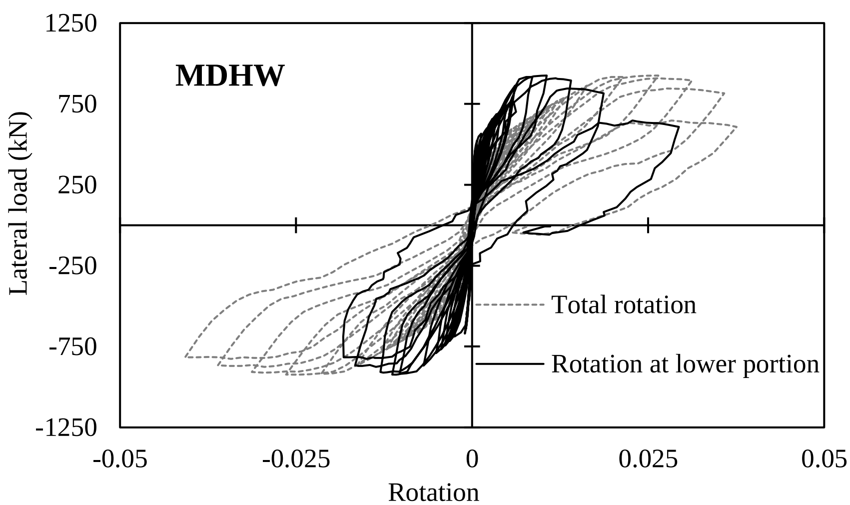

(b)

Figure 7-16 - Wall rotation of moderately ductile walls: (a) Wall MDSRW and (b) Wall MDHW

7.4 Assessment of seismic performance

A discussion around the observed response of the walls to the seismic demand imposed by the ground motion records employed in the dynamic analyses is first presented. The seismic performance of the walls will be assessed in terms of the average drifts presented in Section 6.3, which were computed based on the response of the walls to the eleven ground motion records employed in each seismic hazard scenario. The performance of the ductile steel-reinforced concrete wall and the hybrid SMA-steel reinforced concrete wall under the same earthquake records will also be compared. Lastly, the response of the walls to the amplified ground motion records will be discussed.

7.4.1 Seismic demands

The fundamental periods of vibration obtained from eigenvalue analysis of the walls in VecTor2 (Vecchio et al., 2013) were in good agreement with the periods of the building obtained from modal analysis. The fundamental period of the building in Vancouver and Montreal was equal to 1.95 s and to 1.96 s, respectively. The periods corresponding to the first mode of vibration of Walls MDSRW, MDHW, DSRW and DHW, determined in VecTor2 and listed in Table 6-1, were found to be 9.3% shorter than the period of the building in the corresponding design location, determined in SAP2000® (CSI, 2016), on average. The difference in period is attributed to the difference in stiffness that arises from the simplicity of the input model in SAP2000®, where the reinforcement in the cross-section of the walls was not fully detailed given the limitations of the membrane element available in the program's library.

For the building in Vancouver, the ground motion records representative of Scenario 3 induced larger displacement demands on the ductile walls compared to Scenarios 1 and 2 given the fundamental period of the walls between 1.73 s and 1.88 s. Hazard deaggregations in Vancouver indicated that Scenario 3 has a stronger influence in structures with periods within 1.0-2.6 s. For the building in Montreal, the response of the moderately ductile walls was more strongly influenced by records from Scenario 2 compared to Scenario 1, as the main period range affected by this scenario corresponds to 1.0-2.6 s.

In terms of ultimate displacements, the response spectrum analysis in SAP2000® resulted in maximum total top displacement of 503 mm for the building in Vancouver, and 201 mm for the building in Montreal. The mean peak transient displacement, determined from the eleven time history analyses performed for each wall, corresponded to 443 mm in Wall DSRW, and 149 mm in Wall MDSRW. The displacement demand of the walls was therefore 12% and 26% lower than predicted for the buildings in Vancouver and Montreal, respectively.

For the building in Montreal, the performance anticipated when defining the seismic demand according to the NBC 2015 (NRC, 2015) and designing the walls according to the seismic design procedure in the CSA-A23.3-2014 (CSA, 2013) did not match the observed seismic response of the walls when subjected to the dynamic analyses. The selected ground motion records for eastern Canada induced lower than expected demands on the walls. This behaviour was an indication that the assumptions and restrictions from the seismic codes led to an over-conservative design of the shear walls in this design location.

The initial modal analyses using the 3-D model of the buildings indicated fundamental periods that were longer than the upper limit specified by the NBC 2015 for structures containing RC shear walls as the main seismic force-resisting system. The reduced base shear resulting from analysis of the building in Vancouver had to be amplified to meet 80% of the base shear calculated using the code upper limit for the period. Therefore, the ductile walls were designed to resist higher forces than that potentially induced by earthquakes characteristic of western Canada in a building such as the one under study. The strength of both the ductile and the moderately ductile walls was further increased by adopting a larger reinforcement ratio for the vertical reinforcement in the web zone of the walls, due to the early fracture of the steel bars in the web zone of the hybrid walls identified during static analysis.

The attenuated response of the walls to the seismic excitations can be further discussed in terms of the ductility and overstrength of the steel-reinforced walls. The displacement ductility (μ) computed from the hysteretic response of the walls, presented in Section 6.2, was significantly larger than that defined in the NBC 2015. For reinforced concrete shear walls, the NBC 2015 specifies the ductility-related force modification factor R_d as 3.5 for ductile walls, while Wall DSRW experienced μ of 4.7. A greater variation was found in the moderately ductile wall, where R_d is prescribed as equal to 2.0 in the NBC 2015, and the hysteretic response of Wall MDSRW exhibited μ equal to 7.7. In terms of overstrength, it was verified that the final design of the walls did not lead to the level of overstrength prescribed by the NBC 2015 in the form of the overstrength force-modification factor R_o. The NBC 2015 prescribes values for R_o equal to 1.6 and to 1.4 for ductile and moderately ductile shear walls, respectively. Conversely, Walls DSRW and MDSRW exhibited overstrength, measured as the ratio of F_{max} to F_y in the hysteretic response of the walls, equal to 1.15 and 1.18, respectively. As a result, the base shear reduction factor R_dR_o that was anticipated to be equal to 5.6 and to 2.8 in the ductile and the moderately ductile shear walls, respectively, was determined to be equal to 5.4 and 9.09 in the designed walls. The variation is not significant for the ductile wall, but the large discrepancy between the values in the moderately ductile wall indicates that this wall could have been designed to sustain a substantially lower base shear. In turn, the level of seismic excitation contained in the UHS of Montreal would induce a larger demand on the wall.

Following the equal displacement principle, the building under study was expected to experience yielding at a lateral top displacement of 105 mm when the values of R_d and R_o provided by the NBC 2015 for ductile shear walls are used to reduce the base shear. The building with moderately ductile shear walls was expected to yield at 72 mm. However, the hysteretic response of the designed steel-reinforced walls indicated Δ_y of 179 mm in the ductile wall, Wall DSRW, and 156 mm in the moderately ductile wall, Wall MDSRW. With that, yielding was delayed, and the improvement in the seismic performance of the SMA-reinforced walls was less evident in the dynamic analyses, provided that the response of the walls to several of the ground motion records employed was mainly in the elastic range.

If adequate design provisions were available for SMA-reinforced concrete shear walls, the reduction in the design base shear could be more significant in Walls DHW and MDHW. Eigenvalue analysis of the walls in VecTor2 (Vecchio et al., 2013) indicated that the replacement of steel bars with SMA bars in the boundaries of the walls, within the plastic hinge region, increased the fundamental period of the walls by an average of 5.3%. Based on the UHS, longer periods result in reduced design shear forces of the walls. However, the fundamental period of the SMA-wall system was bounded by the limits in the NBC 2015, which were developed based on the response of conventional reinforced concrete shear wall systems. Appropriate seismic design provisions would therefore allow designers to take less restrictive limits and more advantage of the flexibility characteristic of concrete walls containing SMA as alternative reinforcement when determining the design base shear.

7.4.2 Lateral drift

Figure 7-17 presents the mean responses of the ductile walls, with the response of Wall DSRW superimposed on that of Wall DHW in terms of maximum transient lateral displacements (Figure 7-17 (a)) and permanent lateral displacements (Figure 7-17 (b)). On average, both walls experienced similar transient displacements at the top, with transient roof drift in Wall DSRW corresponding to 1.45%, while Wall DHW experienced drift of 1.60%. Wall DSRW was able to recover 75% of the average peak displacement experienced during analysis, while recovery in Wall DHW was equal to 71%, on average. Wall DHW experienced peak drifts that were only 10.2% larger than Wall DSRW. In terms of interstorey drifts, maximum transient interstorey drift occurred at the 10th storey for both walls. From that, Wall DSRW recovered 93.5% on average, sustaining 0.13% permanent interstorey drift. Permanent interstorey drift in Wall DHW was 0.02%, representing 99% recovery of interstorey drifts, on average.

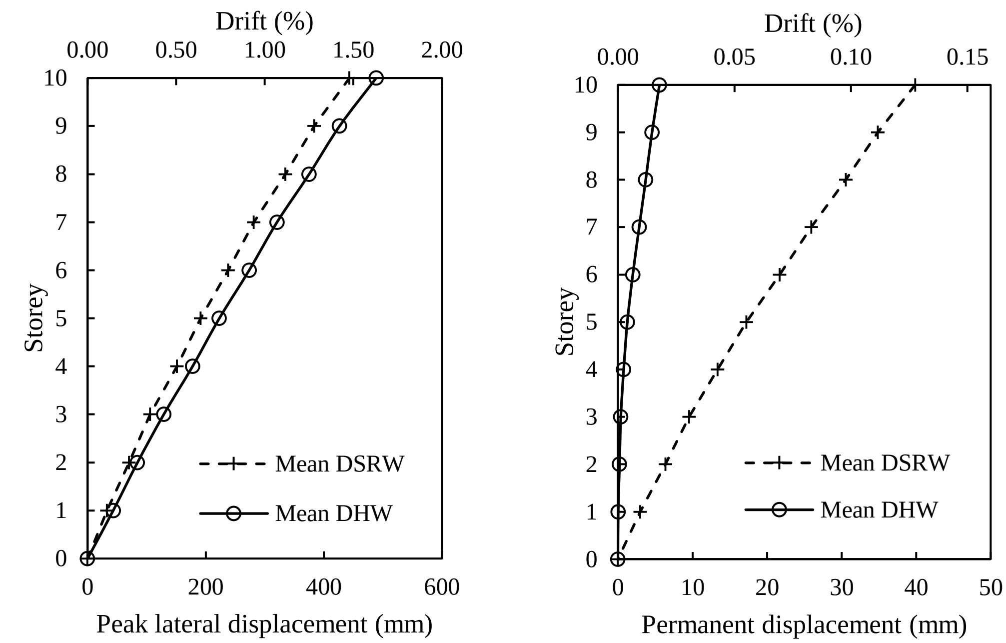

(a) (b)

Figure 7-17 - Mean response of ductile walls: (a) peak lateral displacements and (b) permanent displacements at the end of analysis

Employing the seismic performance assessment limits discussed in Sections 2.4.3 and 2.4.4, it is possible to categorize the performance of the ductile walls given the maximum transient and permanent interstorey drifts recorded during analysis. The ASCE/SEI 41-17 (ASCE, 2017) classifies the seismic performance of buildings, and the FEMA P-58-1 (FEMA, 2012) provides limits for the performance states in terms of peak storey drifts in reinforced concrete wall buildings: if the transient storey drift exceeds 3.6%, the structure is in the Collapse Prevention performance level; drifts of 2.6% indicate Life Safety performance; drifts of 2.2% are the limit for the Operational performance level; and the Immediate Occupancy performance level can only be assigned if transient drifts are limited to 1.0%. In terms of permanent drifts, storey drifts of 2%, for moderately ductile shear walls, and 4%, for ductile shear walls, limit the Collapse Prevention state; drifts of 1% are required for the Life Safety performance level; the Operational level limits storey drifts to 0.5%; and Immediate Occupancy can only be expected when the structure sustains storey drifts smaller than 0.2%. The response of the ductile Walls DSRW and DHW fall into the Immediate Occupancy performance level considering the maximum permanent interstorey drifts exhibited by both walls, which were smaller than 0.2% (0.17% in Wall DSRW and 0.03% in Wall DHW). However, the limit for the transient storey drifts governed, categorizing the walls in the Operational performance level given the peak interstorey drifts of 2.00% and 2.07% experienced respectively by walls DSRW and DHW.

The lower displacement recovery capacity of Wall DHW in terms of roof drifts indicated by the mean response should be carefully considered. Due to failure of both ductile walls under the records from Scenario 3, the adoption of peak roof displacements equal to Δ_u incurred in larger displacements in Wall DHW compared to Wall DSRW, as the hybrid wall had greater Δ_u. Both walls were unable to recover from the displacement demand imposed by Records 15 and 23, and therefore the recovery in these analyses was considered to be 0%. However, the analysis of Wall DSRW under Record 14 permitted determining permanent displacements, and a non-zero recovery was considered for this analysis. In fact, the steel-reinforced wall did not resist the excitation of Record 14 as much as the SMA-reinforced wall, but the permanent deformation in the latter could not be determined due to instability of the analysis beyond the capacity of the wall. Fracture of the longitudinal bars in the edge zone and in several bars in the web zone at the base of Wall DSRW indicated failure of the wall. The difference in the behaviour of the walls beyond failure is attributed to the numerical analysis rather than the capacity of the walls. Furthermore, the predicted fracture of the longitudinal steel reinforcement in the web zone of Wall DHW when subjected to the records from Scenario 3 confirms the assumption from static analysis that the lateral capacity of the hybrid SMA-steel reinforced concrete walls was capped off by the capacity of the steel bars. A design alternative should be investigated to prevent the steel in the web zone from controlling the capacity of the hybrid walls so that the superelasticity of SMA can be better exploited.

A better comparison of the seismic response of the ductile walls is provided when assessing the responses to individual records from different scenarios. Figure 7-18 compares the roof displacement time history of Walls DHW and DSRW resulting from Records 150 - Coyote Lake, 1979 (Scenario 1) and Record 359 - Coalinga, 1983 (Scenario 2).

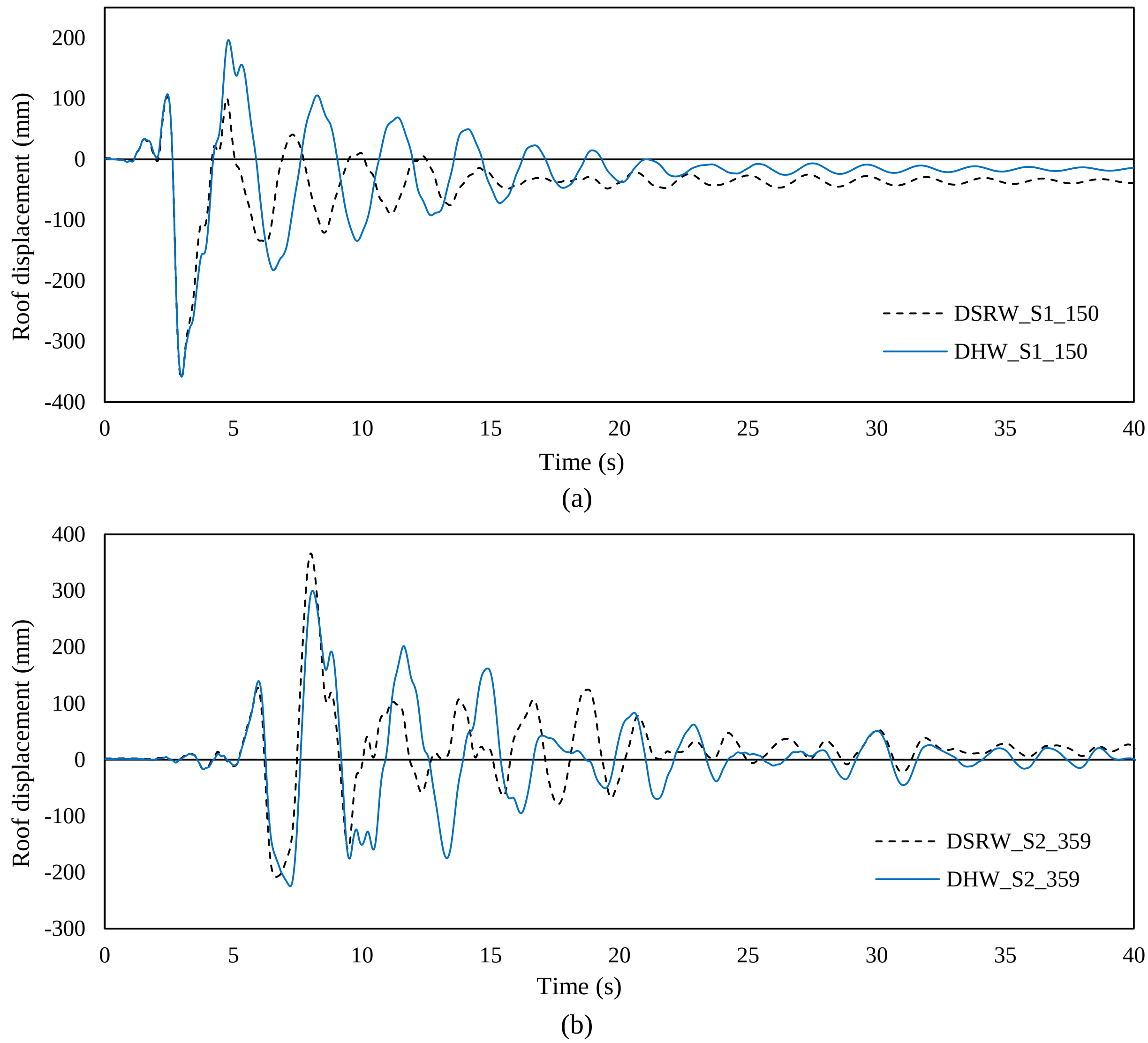

Figure 7-18 - Roof displacement time histories of Walls DSRW and DHW under: (a) Record 150 and (b) Record 359

When subjected to record 150, the walls experienced the same level of peak roof drift (1.18% in both walls). Despite the large pulse in one direction caused by Record 150, as shown in Figure 7-18 (a), subsequent smaller load cycles were sufficient for Wall DHW to recover 96% of the lateral drift, whereas recovery in Wall DSRW was equal to 90%. The permanent roof drift exhibited by Wall DHW was 61% smaller than Wall DSRW. The excitation of Record 359, as illustrated in Figure 7-18 (b), induced larger drifts in Wall DSRW, which reached a roof drift of 1.2%, while Wall DHW experienced peak roof drift of 0.98%. Permanent drifts at the end of analysis predicted for Wall DHW were 80% smaller than those predicted for Wall DSRW. Recovery was equal to 95.5% in Wall DSRW and 99% in Wall DHW. Considering that the selected earthquake records induced smaller than expected demands in the walls, as discussed in Section 7.4.1, Wall DHW exhibited an improved performance compared to Wall DSRW. Wall DHW experienced comparable levels of peak drifts and reduced permanent drifts.

It has been observed that the advantages of using SMA as alternative reinforcement in concrete are more evident when structural elements are subjected to higher seismic loads (Alam et al., 2009). Records from Scenarios 1 and 2 barely induced Δ_y in the walls, while the specific characteristics of the simulated ground motion records of Scenario 3 caused failure of the walls and instability of the analyses. In the first case, only a minor portion of the inelastic capacity of the walls was achieved; in the second case, it was not possible to look at the deformed shape of the walls at the end of the analyses. For these reasons, an earthquake record from Scenario 1 was chosen and employed in the analysis with magnified acceleration time histories. The objective was to investigate the behaviour of the ductile walls when the seismic demand was approaching the lateral resistance, and the ductility of the walls was requested to a larger extent. Figure 7-19 illustrates the response of Wall DHW along with that of Wall DSRW when subjected to Record 150 - Coyote Lake, 1979 amplified by 150% (a) and 200% (b). Although both walls experience comparable levels of peak roof displacement, Wall DHW is significantly more effective in minimizing the permanent displacements at the end of the excitation, particularly under the 200% earthquake.

In Figure 7-20, the lateral displacement profiles of Walls DSRW and DHW when subjected to 150% and 200% of Record 150 are compared in terms of peak lateral drifts (Figure 7-20 (a)) and permanent drifts (Figure 7-20 (b)). Wall DHW experienced smaller peak roof drifts compared to Wall DSRW in both analyses, corresponding to a reduction of 25% on average. The roof drift sustained by Wall DHW at the end of analysis was 59.7% of that sustained by Wall DSRW at 150% excitation, and 35.7% of that corresponding to the excitation of 200%. Similar recovery capacity was exhibited by Wall DHW under the two levels of excitation (91% at 150% and 90% at 200%). Wall DSRW exhibited lower recovery under the amplified record to 150% (86%), which was further reduced to 74% when the earthquake was amplified to 200%. Therefore, Wall DHW experienced recovery capacity that was 6.5% greater at 150% amplification, but 22% greater at 200% amplification, compared to Wall DSRW. The peak and the permanent interstorey drifts experienced by the walls under the amplified Record 150 can be compared in Figure 7-20 (c) and Figure 7-20 (d), respectively. Wall DHW exhibited minimized top storey interstorey drifts, and the reduction was even more significant at storey 6, where a secondary plastic hinge was identified in both walls. At storey 6, the interstorey drift in Wall DHW was 64% of that exhibited by Wall DSRW at 150% amplification, and 42% at 200% amplification. The SMA-reinforced wall performed better than the steel-reinforced wall in limiting the permanent drifts by utilizing the recentering capability of superelastic Ni-Ti SMA.

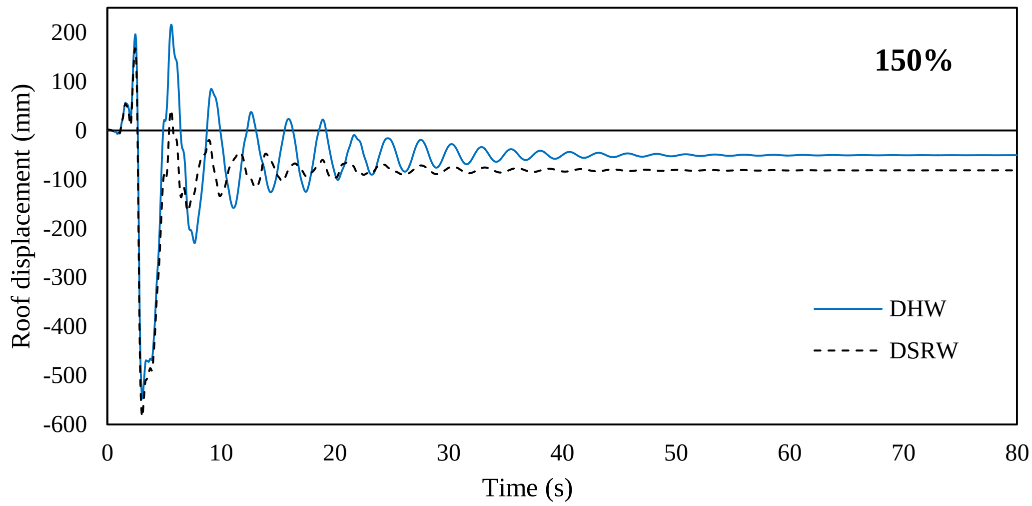

(a)

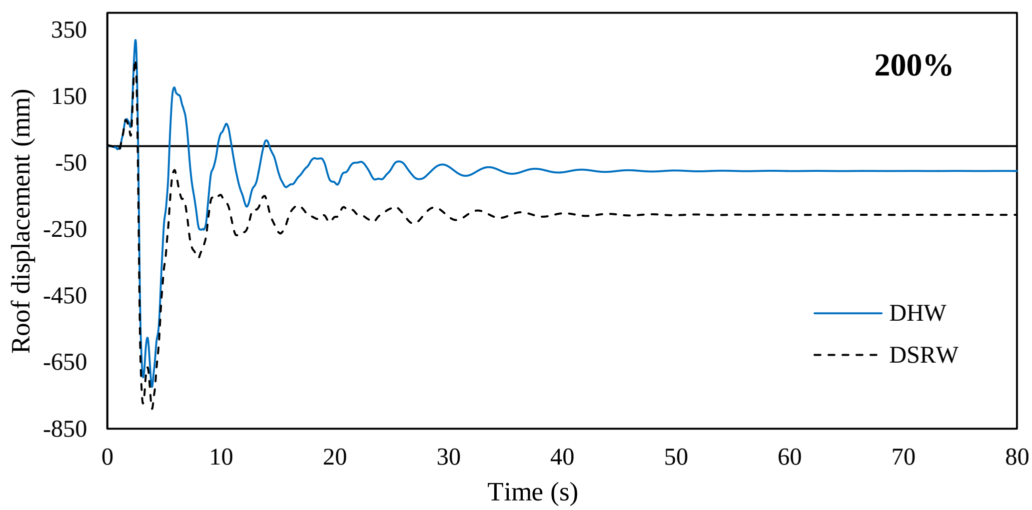

(b)

Figure 7-19 - Roof displacement time histories of Walls DSRW and DHW under: (a) Record 150 scaled to 150% and (b) Record 150 scaled to 200%

According to the seismic performance assessment limits from the ASCE/SEI 41-17 (ASCE, 2017) and the storey drifts from the FEMA P-58-1 (FEMA, 2012), both walls exhibited peak transient storey drifts compatible with the Collapse Prevention performance level at 150%. At 200%, the limit state was exceeded by both walls, which is reasonable given the intensity of the amplified ground motions. The sustained permanent storey drifts would classify the structure in the Operation level when subjected to 150% of the earthquake. At 200%, the maximum interstorey drift sustained by Wall DHW remained below the limit for the Operational performance level, while Wall DSRW progressed to the Collapse Prevention state. The interstorey drifts along the height of the walls indicate that the hybrid wall is less vulnerable to the negative effects of the secondary plastic hinge formed at upper levels compared to the conventional steel-reinforced wall, which is further stressed by the improved performance of Wall DHW at 200% in terms of interstorey drifts.

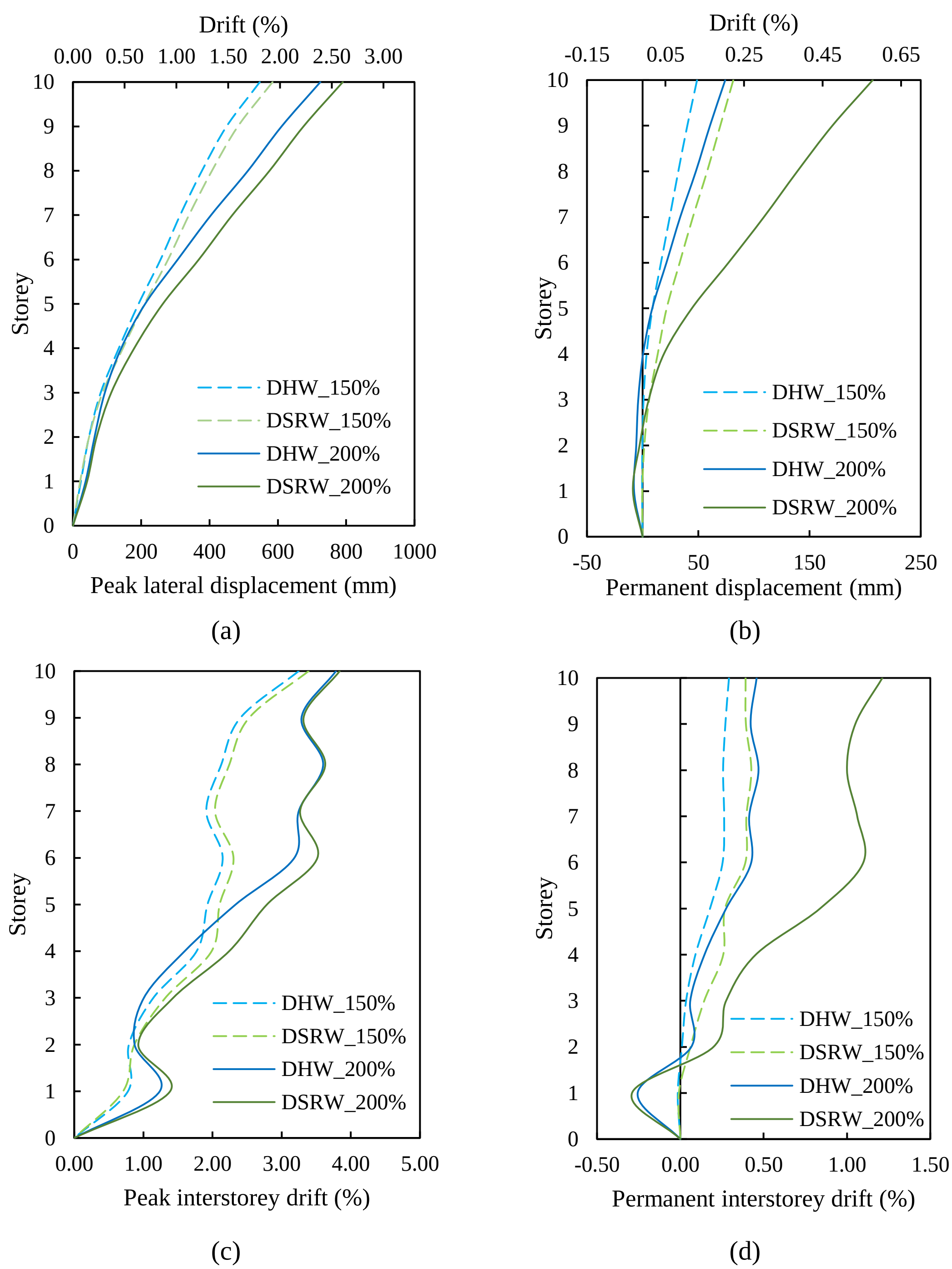

Figure 7-20 - Response of the ductile walls when subjected to magnified earthquake record: (a) peak lateral displacements, (b) permanent displacements at the end of analysis, (c) peak interstorey drifts and (d) permanent interstorey drifts at the end of analysis

Figure 7-21 provides a comparison of the mean responses of the moderately ductile Walls MDSRW and MDHW. The mean responses were determined by considering the response to the selected eleven ground motion records. In terms of maximum lateral drifts (Figure 7-21 (a)), Wall MDHW experienced a roof drift of only 2.5% larger than that of Wall MDSRW. Average transient roof drifts were equal to 0.49% in Wall MDHW and 0.48% in Wall MDSRW. Maximum transient interstorey drifts were, on average, equal to 0.67% and 1.03 % in Walls MDHW and MDSRW, respectively. Regarding permanent drifts, according to the profiles in Figure 7-21 (b), there is a negligible improvement in the permanent roof drift exhibited by Wall MDHW (0.017%) compared to that exhibited by Wall MDSRW (0.02%). The recovery of Wall MDHW was 0.9% greater than that of Wall MDSRW. Permanent drifts were very small in both walls as a result of negligible interstorey. Both walls would be categorized in the Immediate Occupancy performance level according to ASCE/SEI 41-17 (ASCE, 2017) and the storey drift limits in the FEMA P-58-1 (FEMA, 2012).

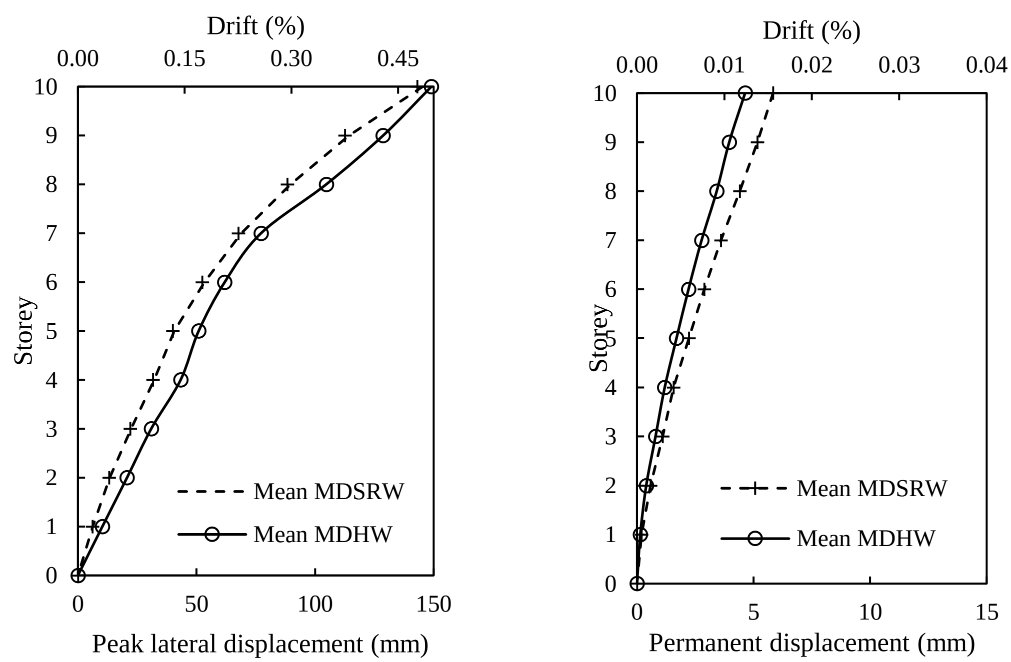

(a) (b)

Figure 7-21 - Mean response of moderately ductile walls: (a) peak lateral displacements and (b) permanent lateral displacements

The response of the moderately ductile walls to amplified ground motion records was not investigated given that none of the employed ground motion records incurred in inelastic response of these walls. Figure 7-22 illustrates the roof displacement time histories of Walls MDSRW and MDHW when subjected to the ground motion Records 30 (Scenario 1) (Figure 7-22 (a)) and Record 36 (Scenario 2) (Figure 7-22 (b)). When comparing the response of the walls to individual records, a few differences in the behaviour of the moderately ductile walls became evident. Both walls experienced the same level of peak roof drifts under Record 30, and exhibited comparable levels of residual drifts, which are due to the elastic behaviour of both walls during the analysis. In the elastic range, the beneficial effects of the superelastic SMA in Wall MDHW cannot be observed. Wall MDHW experienced 25.6% larger roof drift compared to Wall MDSRW when subjected to Record 36. The hybrid wall was able to recover 98% of the lateral drift, exhibiting a permanent roof drift that was 25% smaller than Wall MDSRW. The displacement demand imposed by Record 36 triggered yielding in Wall MDSRW, thus an improvement in the response of the hybrid wall was evident, although permanent deformations were small in both walls. The results from dynamic analysis indicate that eastern Canada might not be the best scenario for the implementation of self-centering, SMA-reinforced concrete shear walls, provided the level of seismic demand associated with this moderate seismic zone.

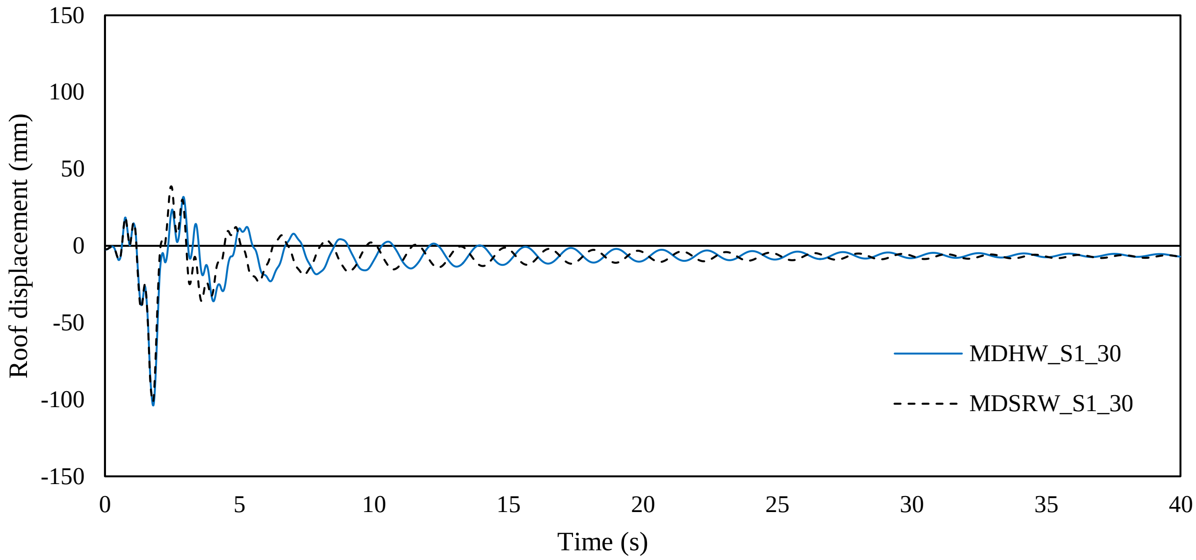

(a)

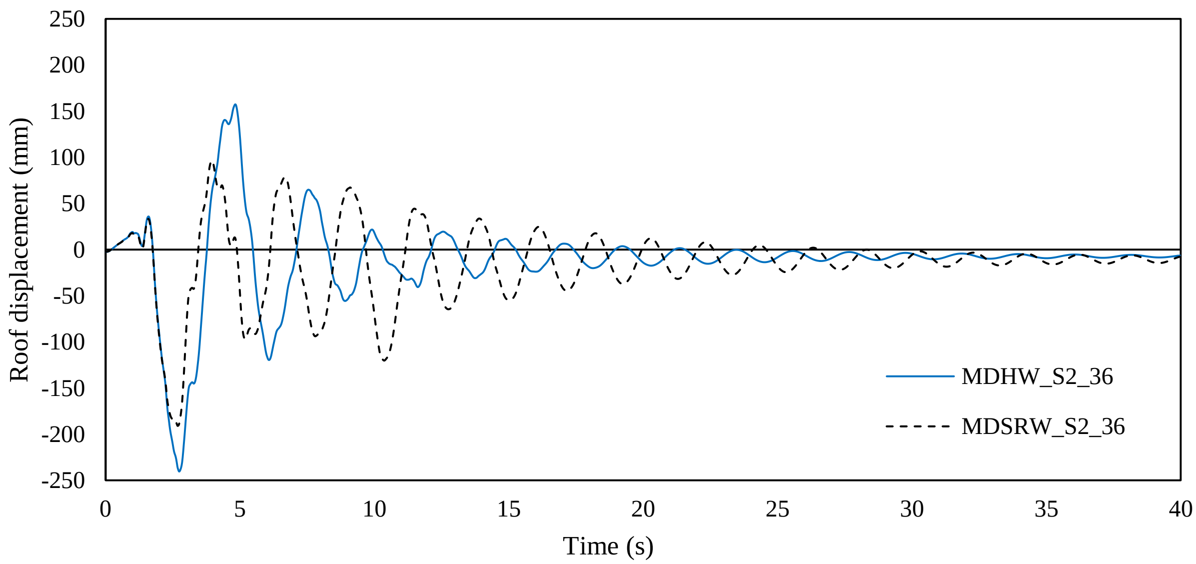

(b)

Figure 7-22 - Roof displacement time histories of Walls MDSRW and MDHW under: (a) Record 30 and (b) Record 36

8. CONCLUSIONS AND RECOMMENDATIONS

8.1 Conclusions

The seismic performance and the potential benefits of implementing a hybrid SMA-steel reinforcing system in a mid-rise reinforced concrete shear wall structure were investigated by comparing the response of alternative SMA-reinforced walls with the response of companion conventional steel-reinforced walls. Static and dynamic numerical simulations using finite element modelling were performed. Reverse cyclic analysis of the proposed hybrid reinforcing system resulted in wall strengths comparable to that of steel-reinforced walls. The SMA reinforcement was effective in controlling permanent deformations and demonstrated superior self-centering capabilities with significant energy dissipation. The dynamic analyses confirmed the potential benefits of using superelastic Ni-Ti SMA as alternative reinforcement in concrete walls, specifically in higher seismic zones. The SMA-reinforced walls performed better than the steel-reinforced walls in limiting the permanent drifts by utilizing the recentering capability of superelastic Ni-Ti SMA, which was more evident under amplified ground motions. Amplification of the seismic demand permitted to capture the inelastic response of the walls for large seismic demands.

The following conclusions are based on the analyses conducted in this study:

Static behaviour of walls

1. The monotonic response of the walls indicated similar lateral strength of the hybrid SMA-steel-reinforced concrete walls compared to the conventional steel-reinforced concrete walls. The lateral strength of the SMA-reinforced walls was, on average, only 5% lower than the lateral strength the steel-reinforced walls;

2. Given the smaller modulus of elasticity of SMA, the SMA-reinforced walls demonstrated lower effective stiffness, corresponding to approximately 45% on average of the stiffness of the conventional walls;

3. The displacement ductility experienced by the conventional steel-reinforced walls exceeded the ductility prescribed by the NBC 2015 for both the ductile and the moderately ductile shear walls;

4. The monotonic response formed the envelope of the hysteretic response of the walls. However, the displacement capacity experienced by the walls under reverse cyclic loading was lower than the

displacement capacity of the walls under monotonic loading, which is attributed to the accumulation of damage characteristic of reverse cyclic loading;

5. When compared to the numerical results from the benchmark studies by Abdulridha and Palermo (2017) and Maciel et al. (2016), the monotonic and hysteretic responses of the walls exhibited comparable responses, pinching of the hysteretic loops, and the level of residual drifts, up to drift demands that exceed the code limit of 2.5%. However, the simulation of the behaviour at late stages of loading and near failure is very sensitive to the modelling decisions, which was difficult to evaluate given the lack of experimental testing of full-scale hybrid walls with the characteristics of the walls investigated in this thesis;

6. The SMA-reinforced walls experienced lower displacement ductility compared to the steel-reinforced walls. However, the SMA-reinforced walls exhibited comparable or larger ultimate displacements and significantly larger pseudo-yield displacements, which led to a reduced displacement ductility. In addition, it is believed that rupture of the reinforcing steel in the web zone limited the displacement ductility of the SMA-reinforced walls;

7. Larger cracks surfaced on the SMA-reinforced walls. The smooth surface of Ni-Ti SMA bars led to concentration of damage at more spaced cracks, which widen with the increase in localized stress. The occurrence of larger cracks might be connected to the more sensitive response of SMA-reinforced walls to the reinforcement ratio employed in the web zone of the walls observed in analysis;

8. Under reverse cyclic loading, both the SMA-reinforced and the steel-reinforced concrete walls maintained a stable response beyond the code limit of 2.5% for lateral drift, without suffering significant loss in load carrying capacity, and ensuring a satisfactory response. The SMA-reinforced wall sustained high levels of drift without exhibiting significant permanent deformation;

9. The SMA-reinforced walls demonstrated substantially higher recovery capacity than the steel-reinforced walls. At 2.5% drift, recovery of the SMA-reinforced walls was 98% on average, while the average recovery of the steel-reinforced walls was 51%. At the end of analysis, the reduction in residual drifts provided by the replacement of steel reinforcing bars by Ni-Ti SMA bars reached 92% on average;

10. The lateral load-vertical displacement response of the SMA-reinforced walls exhibited significant pinching, while the steel-reinforced walls sustained substantial residual vertical displacements.

Asymmetry was observed in the response of the SMA-reinforced walls, which is attributed to the large cracks that opened at the base of the walls primarily to one side;

11. The majority of the wall rotation experienced by the SMA-reinforced walls was concentrated at the lower portion of the walls (up to a height of 1200 mm), corresponding to 82% on average. The large, localized cracks characteristic of concrete reinforced with smooth bars permitted the hybrid walls to rock on top of the critical section. In the steel-reinforced walls, rotation was more uniformly distributed along the height of the walls. The evidence that most of the wall rotation is concentrated within a height of 1200 mm in the hybrid walls, which is shorter than the anticipated plastic hinge region of 6050 mm, indicates that the length of the SMA bars employed in the hybrid walls could be reduced, resulting in a more efficient and economic use of the superelasticity of the; and

12. The steel-reinforced walls dissipated more energy than the SMA-reinforced walls. The lower energy dissipation capacity, however, does not necessarily imply deficient seismic performance, as flag-shaped hysteretic behaviour, such as that of SMA, can provide stable seismic responses due to the combined effect of adequate energy dissipation and significant self-centering capacity.

Dynamic behaviour of walls

1. Eigenvalue analysis of the walls indicated fundamental periods in agreement with that determined by modal analysis of the building. The fundamental period of the SMA-reinforced walls was 5% longer than the fundamental period of the equivalent steel-reinforced walls, on average;

2. The displacements corresponding to yielding in the steel-reinforced walls and pseudo-yielding in the SMA-reinforced walls were found to be larger than those determined following the equal displacement principle. As a result, yielding was delayed, and the improvement in the seismic performance of the SMA-reinforced walls was less evident in the dynamic analyses, specifically for those records that did not impose displacement demands beyond the yield displacement of the walls;

3. The maximum inelastic top displacements predicted by response spectrum analysis were not achieved by the mean peak transient displacement determined from the eleven time history analyses performed with each wall. The roof displacement in the walls was 12% lower than predicted in Vancouver, and 26% lower in Montreal;

4. In general, and with the exception of the Cascadia-generated ground motions, the response of the walls to dynamic analyses using ground motion records selected and scaled to match the UHS of

each seismic zone was lower than expected, which indicated overdesign of the walls. Design of the ductile shear walls in Vancouver was governed by the code restriction to the base shear reduction corresponding to 80% of the static base shear. The strength of the ductile and the moderately ductile walls was further increased by the adoption of a higher ratio of steel reinforcement in the web zone of the walls to prevent premature failure of the bars in the SMA-reinforced walls;

5. For western Canada, ground motion records representative of Scenario 3 (Cascadia) dominated the response of the ductile walls, exceeding the capacity of the walls and leading to failure. The seismic demand induced by most of the earthquake records from Scenarios 1 and 2 was sufficient to trigger yielding in the steel-reinforced wall, resulting in plastic deformations. Conversely, the larger pseudo-yielding displacement of the SMA-reinforced wall was not exceeded by most of the earthquake records from Scenarios 1 and 2, inhibiting the accumulation of inelastic deformation in Wall DHW. As a result, recentering was exhibited in the dynamic responses of Wall DHW;

6. Although the selected earthquake records induced smaller than expected demands in the walls, Wall DHW exhibited an improved performance to individual records compared to Wall DSRW, experiencing comparable levels of peak drifts and reduced permanent drifts;

7. On average, Wall DSRW was able to recover 75% of the experienced roof displacement, while Wall DHW recovered 71%. The lower recovery capacity of the SMA-reinforced wall indicated by the mean response should be carefully considered. The specific characteristics of the simulated ground motion records from Scenario 3 caused failure of the ductile walls and instability of the analyses. The difference in the behaviour of the models beyond failure is therefore attributed to the numerical analysis rather than the capacity of the walls;

8. For western Canada, failure of the SMA-reinforced wall under records from Scenario 3 occurred in the form of fracture of the longitudinal steel bars in the web zone of the wall. A design alternative should be investigated to prevent the steel in the web zone from controlling the capacity of the SMA-reinforced walls so that the superelasticity of SMA can be better exploited;

9. According to the seismic performance limits in the ASCE/SEI 41-17 (ASCE, 2017) and the storey drift limits in the FEMA P-58-1 (FEMA, 2012), the response of the ductile walls DHW and DSRW was categorized in the Operational performance level given the predicted peak interstorey drifts;

10. When employing 150% and 200% amplified earthquake records, the sustained inelastic damage inhibited recentering in Wall DSRW, and significant permanent damage was present. Both ductile

walls experienced comparable levels of peak roof displacement, but Wall DHW exhibited substantially larger recovery capacity, particularly under the 200% earthquake. The roof drift sustained by Wall DHW at the end of analysis was 60% of that sustained by Wall DSRW at 150% excitation, and 36% of that corresponding to the amplified excitation to 200%. The SMA bars experienced pseudo-yielding but did not reach the superelastic strain limit of the material during analysis;

11. Both ductile walls exhibited similar behaviour in terms of the secondary plastic hinge that formed between storeys 5-7, where the longitudinal steel reinforcement yielded and substantial interstorey drifts were recorded. Wall DHW exhibited minimized top storey interstorey drifts, and the reduction was even more significant at storey 6, where the interstorey drift in Wall DHW was 64% of that exhibited by Wall DSRW at 150%, and 42% at 200%;

12. The interstorey drifts along the height of the ductile walls indicated that the SMA-reinforced wall was less vulnerable to the negative effects of the secondary plastic hinge that formed at upper levels compared to the conventional steel-reinforced wall, which is further stressed by the improved performance of Wall DHW at 200% in terms of interstorey drifts;

13. For eastern Canada, the response of the moderately ductile walls was more strongly influenced by records from Scenario 2. Few records induced displacements that were above the Δ_y of each wall, and by a negligible extent. Consequently, permanent damage exhibited by the walls was very limited;

14. A large variation was found between the anticipated base shear reduction factor R_dR_o and that determined from the response of Wall MDSRW, indicating that the moderately ductile walls could have been designed to sustain a substantially lower base shear. In turn, the level of seismic excitation contained in the UHS of Montreal would induce a larger demand on the walls;

15. The seismic demand imposed by the employed ground motion records did not induce displacements larger than Δ_y in Wall MDHW. As a result, the superelastic capacity of the SMA reinforcement was not achieved. At the end of the analyses, Wall MDHW recentered and experienced negligible residual displacements. Wall MDHW experienced roof drift only 2.5% larger than Wall MDSRW. On average, Wall DSRW was able to recover 96% of the experienced roof displacement, while 97% recovery of roof displacement was present in Wall MDHW; and

16. Regarding permanent drifts, the permanent roof drift exhibited by Wall MDHW (0.17%) was virtually the same as that observed in Wall MDSRW (0.2%). Both walls were categorized in the Immediate Occupancy performance level according to the ASCE/SEI 41-17.

General conclusions

1. The static analyses indicated similar lateral capacity, in terms of strength and displacement, between the steel-reinforced and the SMA-reinforced concrete shear walls. Lower, but still substantial energy dissipation was associated to the response of the SMA-reinforced walls. The SMA-reinforced walls also exhibited reduced stiffness and significantly increased recovery capacity. Dynamic analysis confirmed that self-centering of SMA-reinforced concrete shear walls results in reduced permanent drifts along the height of the wall. Furthermore, comparable transient peak drifts were experienced by the SMA-reinforced walls despite the reduced stiffness and energy dissipation capacity of the walls compared to steel-reinforced walls;

2. The benefits of superelastic Ni-Ti SMA to the behavioural response of reinforced concrete shear walls demonstrated by static analyses were confirmed by the dynamic analyses. Improved seismic performance was exhibited by the SMA-reinforced walls, specifically at higher seismic demands. The dynamic analyses also indicated the formation of a secondary plastic hinge in the ductile walls corresponding to storeys 5-7. The SMA-reinforced wall was better in reducing the drifts at this location, improving the performance of the wall in terms of interstorey drifts;

3. The dynamic analyses of the shear wall for western Canada revealed improved seismic performance of the mid-rise concrete shear walls when Ni-Ti superelastic SMA was used as alternative reinforcement, particularly when amplified ground motion records were employed. The seismic performance of the moderately ductile shear walls for eastern Canada was not significantly improved by the implementation of SMA bars as alternative reinforcement. Results indicate that the use of self-centering SMA-reinforced concrete shear walls may not be justified for moderate seismic zones; and

4. Appropriate seismic design provisions are required to allow designers to take full advantage of the improved performance of concrete walls containing SMA as alternative reinforcement. Less stringent limits for the fundamental period of the walls would permit exploring the flexibility characteristic of SMA-reinforced concrete walls when determining the design base shear. Attention should be given in design to the early fracture of the steel reinforcement in the web zone of the walls, which limited the ductility of the walls during both static and dynamic analyses. In addition, the results indicate that the

length of the SMA bars in the SMA-reinforced walls could be reduced, leading to a more cost-effective design of this innovative self-centering wall system.

8.2 Recommendations

The following recommendations are based on the findings of this thesis and are suggestions to continue the work presented herein.

1. Experimental testing of the SMA-steel reinforced concrete shear walls investigated herein, conducted in reduced or full-scale, are required to provide information for corroborating the numerical results and for improving the modelling of mid-rise shear walls containing SMA as reinforcement;

2. This thesis investigated a single cross-section and axial load condition for each wall type. Additional numerical analyses are required to evaluate the influence of varying the geometry and layout of the wall cross-section, as well as the sustained axial load ratio, including different wall widths, heights, thicknesses, lengths of the edge zone, arrangement and length of Ni-Ti SMA bars, among other design parameters. Reduced lengths of the SMA bars, in particular, have shown potential to make the use of SMA-reinforced concrete shear walls more cost-effective;

3. The reduced stiffness of SMA-reinforced concrete shear walls, which results in lower seismic forces, could not be exploited fully in this study due to the use of design provisions developed for conventional steel-reinforced concrete elements. Design provisions specifically developed for SMA-reinforced concrete elements are required to optimize the design of the walls in this thesis. The effect of larger deformations resulting from the reduced stiffness of a wall with optimized design must be then investigated;

4. The excellent deformation capacity of superelastic Ni-Ti SMA could be better employed in reinforced concrete shear walls if combined with flexible concrete, which could accommodate the large deformations sustained by highly ductile shear walls. In addition, the use of flexible concrete may delay the surfacing of the localized large cracks characteristic of SMA-reinforced elements, which were critical for the performance of the hybrid walls in this thesis;

5. Although the study presented herein demonstrated the superior self-centering capacity of hybrid SMA-steel reinforced concrete walls, assessing the self-centering of the building requires three-dimensional dynamic analysis of the whole structure to be performed. With that, the possible difficulties imposed by significant deformations in other structural and nonstructural elements to the self-centering of the building could be investigated.

REFERENCES

Abdulridha, A. (2013). Performance of Superelastic Shape Memory Alloy Reinforced Concrete Elements Subjected to Monotonic and Cyclic Loading. PhD thesis, University of Ottawa, Ottawa, ON, Canada.

Abdulridha, A., Palermo, D. (2017). Behaviour and modelling of hybrid SMA-steel reinforced concrete slender shear wall. Engineering Structures, Elsevier, 147:77-89.

Abdulridha, A., Palermo, D., Foo, S., Vecchio, F.J. (2013). Behavior and modeling of superelastic shape memory alloy reinforced concrete beams. Engineering Structures, Elsevier, 49:893-904.

Abraik, E., Youssef, M.A. (2015). Cyclic performance of shape memory alloy reinforced concrete walls. Conference on Response of Structures under Extreme Loading, East Lansing, MI, USA.

Abraik, E., Youssef, M.A. (2016). Performance assessment of three-story shape memory alloy reinforced concrete walls. Resilient Infrastructure, CSCE, London, ON, Canada, 852:1-9.

Abraik, E., Youssef, M.A. (2018). Seismic fragility assessment of superelastic shape memory alloy reinforced concrete shear walls. Journal of Building Engineering, Elsevier, 19:142-153.

Alam, M.S., Moni, M., Tesfamariam, S. (2012). Seismic overstrength and ductility of concrete buildings reinforced with superelastic shape memory alloy rebar. Engineering Structures, Elsevier, 34:8-20.

Alam, M.S., Nehdi, M., Youssef, M.A. (2008). Shape Memory Alloy-based Smart RC Bridges: Overview of State-of-the-art. Smart Structures and Systems, Techno-press, 4(3):367-389.

Alam, M.S., Nehdi, M., Youssef, M.A. (2009). Seismic Performance of Concrete Frame Structures Reinforced with Superelastic Shape Memory Alloys. Smart Structures and Systems, Techno-press, 5(5):565-585.

Alam, M.S., Youssef, M.A., Nehdi, M. (2008). Analytical prediction of the seismic behaviour of superelastic shape memory alloy reinforced concrete elements. Engineering Structures, Elsevier, 30:3399-3411.

Alam, M.S., Youssef, M.A., Nehdi, M. (2007). Utilizing shape memory alloys to enhance the performance and safety of civil infrastructure: a review. Canadian Journal of Civil Engineering, NRC Research Press, 34(9):1075-1086.

Ancheta, T.D., Darragh, R.B., Stewart, J.P., Seyhan, E., Silva, W.J., Chiou, B.S.J., Wooddell, K.E., Graves, R.W., Kottke, A.R., Boore, D.M., Kishida, T., Donahue, J.L. (2013). PEER NGA-West2 Database, PEER Report 2013/03, Pacific Earthquake Engineering Research Center, University of California, Berkeley, CA, USA.

ASCE. (2017). ASCE/SEI 41-17: Seismic Evaluation and Retrofit of Existing Buildings. American Society of Civil Engineers Standard, Reston, Virginia, USA.

ASTM. (2014). ASTM F2516-14: Standard test method for tension testing of nickel-titanium superelastic materials. ASTM International, West Conshohocken, PA, USA.

Atkinson, G.M. (2009). Earthquake time histories compatible with the 2005 National building code of Canada uniform hazard spectrum. Canadian Journal of Civil Engineering, NRC Research Press, 36:991-1000. Retrieved 3 March, 2019, from http://seismotoolbox.ca.

Baker, T., Saiidi, M.S., Nakashoji, B., Bingle, J., Moore, T., Khaleghi, B. (2018). Precast concrete spliced-girder bridge in Washington State using superelastic materials in bridge columns to improve seismic resiliency: From research to practice. PCI Journal, 57-71.

Bentz, E.C., Collins, M.P. (2001). Response2000© User Manual. University of Toronto, Toronto, ON, Canada.

Billah, A.H.M.M., Alam, M.S. (2016). Plastic hinge length of shape memory alloy (SMA) reinforced concrete bridge pier. Engineering Structures, Elsevier, 117:321-331.

Buehler, W.J., Gilfrich, J.V., Wiley, R.C. (1963). Effect of low-temperature phase changes on the mechanical properties of alloys near composition TiNi. Journal of Applied Physics, AIP Publishing, 34:1475-1477.

Chancellor, N.B., Eatherton, M.R., Roke, D.A., Akbaş, T. (2014). Self-centering seismic lateral force resisting systems: high performance structures for the city of tomorrow. Buildings, MDPI, 4(3):520-48.

Christopoulos, C., Filiatrault, A., Folz, B. (2002). Seismic response of self-centering hysteretic SDOF systems. Earthquake Engineering & Structural Dynamics, Wiley, 31(5):1131-1150.

Cortés-Puentes, W.L., Palermo, D. (2015). Tension-Only SMA Bracing for Seismic Retrofitting. The 5th International Conference on Construction Materials: Performance, Innovations and Structural Implications, Whistler, BC, Canada.

Cortés-Puentes, W.L., Zaidi, M., Palermo, D., Dragomirescu, E. (2018). Cyclic loading testing of repaired SMA and steel reinforced concrete shear walls. Engineering Structures, Elsevier, 168:128-141.

Cruz-Noguez, C., Saiidi, M. (2013). Performance of Advanced Materials during Earthquake Loading Tests of a Bridge System. Journal of Structural Engineering, ASCE, 139(1):144-154.

CSA. (2007). CSA-A23.3: Design of Concrete Structures. Canadian Standard Association, Mississauga, ON, Canada.

CSA. (2014). CSA-A23.3: Design of Concrete Structures. Canadian Standard Association, Mississauga, ON, Canada.

CSI. (2016). CSI Analysis Reference Manual: For SAP2000®, ETABS®, SAFE® and CSiBridge®. Computers & Structures, Inc., Berkeley, CA, USA.

Doughton, S. (2017). Shake, rattle - and drive: WSDOT builds flexible bridge to survive earthquakes unscathed. The Seattle Times. Retrieved 10 February, 2019, from http://seattletimes.com/seattle-news/science.

EERI. (n.d.). Concrete Buildings Damaged in Earthquakes. Earthquake Engineering Research Institute. Oakland, CA, USA. Retrieved 15 January, 2019, from http://db.concretecoalition.org.

Elbahy, Y.I., Youssef, M.A., Nehdi, M. (2009). Stress block parameters for concrete flexural members reinforced with superelastic shape memory alloys. Materials and Structures, Springer, 42:1335-1351.

Elbahy, Y.I., Youssef, M.A., Nehdi, M. (2010). Deflection of superelastic shape memory alloy reinforced concrete beams: assessment of existing models. Canadian Journal of Civil Engineering, NRC Research Press, 37:842-854.

FEMA. (1997). FEMA273: NEHRP guidelines for the seismic rehabilitation of buildings. Federal Emergency Management Agency, Washington D.C., USA.

FEMA. (2000). FEMA356: NEHRP guidelines for the seismic rehabilitation of buildings. Federal Emergency Management Agency, Washington D.C., USA.

FEMA. (2012). FEMA P-58-1: Seismic performance assessment of buildings: volume 1 - methodology. Federal Emergency Management Agency, Washington, D.C, USA.

Filiatrault, A., Tremblay, R., Christopoulos, C., Folz, B., Pettinga, D. (2013). Elements of Earthquake Engineering and Structural Dynamics. Presses Internationales Polytechnique, 3rd ed., Quebec, Canada.

Ghassemieh, M., Rezapour, M., Sadeghi, V. (2017). Effectiveness of the shape memory alloy reinforcement in concrete coupled shear walls. Journal of Intelligent Material Systems and Structures, SAGE, 28(5):640-652.

Ghorbani-Renani, I., Velev, N., Tremblay, R., Palermo, D., Massicotte, B., Léger, P. (2009). Modeling and Testing Influence of Scaling Effects on Inelastic Response of Shear Walls. ACI Structural Journal, ACI, 106(3):358-367.

Goulet, C.A., Kishida, T., Ancheta, T.D., Cramer, C.H., Darragh, R.B., Silva, W.J., Hashash, Y.M.A., Harmon, J., Stewart, J.P., Wooddell, K.E., Youngs, R.R. (2014). PEER NGA-East Database, PEER Report 2014/17, Pacific Earthquake Engineering Research Center, University of California, Berkeley, CA, USA.

Henry, R.S., Aaleti, S. Sritharan, S., Ingham, J.M. (2012). Seismic analysis of a low-damage Precast Wall with End Columns (PreWEC) including interaction with floor diaphragms. Journal of the Structural Engineering, Society New Zealand (SESOC), 25(1):69-81.

Henry, R.S., Sritharan, S., Ingham, J.M. (2016). Residual drift analyses of realistic self-centering concrete wall systems. Earthquake and Structures, Techno-press, 10(2):409-428.

Hosseini, M., Beiranvand, P., Dehestani, A., Dehestani, K. (2017). Shape memory alloys and offering superelastic property opportunity in reinforced concrete structures. Archives of Materials Science and Engineering, World Academy of Materials and Manufacturing Engineering, 85(1):5-13.

Kian, M.J.T., Cruz-Noguez, C. (2018). Reinforced Concrete Shear Walls Detailed with Innovative Materials: Seismic Performance. Journal of Composites for Construction, ASCE, 22(6):04018052-1-11.

Kowalsky, M.J. (2000). Deformation limit states for circular reinforced concrete bridge columns. Journal of Structural Engineering, ASCE, 126(8):869-878.

Kwan, W.P., Billington, S.L. (2003). Unbonded post-tensioned concrete bridge piers. I: Monotonic and cyclic analyses. Journal of Bridge Engineering, ASCE, 8(2):92‑101.

Lagoudas, D.C. (2008). Shape Memory Alloys: Modelling and Engineering Applications. Springer, 1st ed., New York, London.

Lamontagne, M., Beauchemin, M., Toutin, T. (2004). Earthquakes of the Charlevoix Seismic Zone, Québec. Recorder, Canadian Society of Exploration Geophysicists, 29:(8).

Luu, H., Ghorbani-Renani, I., Léger, P., Tremblay, R. (2013). Numerical Modeling of Slender Reinforced Concrete Shear Wall Shaking Table Tests Under High-Frequency Ground Motions. Journal of Earthquake Engineering, Taylor & Francis, 17(4):517-542.

Maciel, M., Palermo, D., Abdulridha, A. (2016). Seismic Response of SMA Reinforced Shear Walls. In Special Topics in Structural Dynamics, chapter 9, 185-192. Springer, vol. 6, Bethel, CT, USA.

Marquis, F., Kim, J.J., Elwood, K.J., Chang, S.E. (2017). Understanding post-earthquake decisions on multi-storey concrete buildings in Christchurch, New Zealand. Bull Earthquake Engineering, Springer, 15(2):731-758.

McCormick, J., Aburano, H., Ikenaga, M., and Nakashima, M. (2008). Permissible residual deformation levels for building structures considering both safety and human elements. The 14th World Conference on Earthquake Engineering, Beijing, China.

Nehdi, M., Alam, M.S., Youssef, M.A. (2011). Seismic behavior of repaired superelastic shape memory alloy reinforced concrete beam-column joint. Smart Structures and Systems, Techno-press, 7(5):329-348.

NRC. (2015). Division B, Part4, Structural Design National Building Code of Canada. National Research Council of Canada, Ottawa, ON, Canada.

NRC. (2015b). Structural Commentary J National Building Code of Canada. National Research Council of Canada, Ottawa, ON, Canada.

NRC. (2017). Geological Survey of Canada. Natural Resources Canada, Ottawa, ON, Canada. Retrieved 5 March, 2019, from http://earthquakescanada.nrcan.gc.ca.

Park, R. (1988). Ductility Evaluation from Laboratory and Analytical Testing. Ninth World Conference on Earthquake Engineering, Tokyo-Kyoto, Japan, VIII:605-616.

Saatci, S. (2007). Behaviour and modelling of reinforced concrete structures subjected to impact loads. PhD Thesis, University of Toronto, Toronto, ON, Canada.

Sadeghian, A. (2018). Seismic deformations of taller Reinforced Concrete shear walls located in eastern Canada. PhD Thesis, University of Montreal, Montreal, QC, Canada.

Saiidi, M., Cruz-Noguez, C., Hillis, D. (2010). Multi-Shake Table Seismic Studies of a 33-Meter Railway Concrete Bridge with High-Performance Materials. International Journal of Civil Engineering, Springer, 8(1):13-18.

Schlosser, K. (2016). ‘Flexible’ bridge being built in Seattle is designed to bounce back from big earthquake. GeekWire. Retrieved 10 February, 2019, from http://geekwire.com/2016/flexible-bridge-built-seattle-designed-bounce-back-big-earthquake/.

Smith, B.J., Kurama, Y.C., McGinnis, M.J. (2011). Design and measured behavior of a hybrid precast concrete wall specimen for seismic regions. Journal of Structural Engineering, ASCE, 137(10):1052-1062.

Tarzav, M., Alam, M.S. (2018). Shape memory alloy for bridge columns. Eleventh U.S. National Conference on Earthquake Engineering, Los Angeles, CA, USA.

Tarzav, M., Saiidi, M.S. (2015). Reinforcing NiTi Superelastic SMA for Concrete Structures. Journal of Structural Engineering, ASCE, 141(8):0414197-1-10.

Tremblay, R., Atkinson, G.M., Bouaanani, N., Daneshvar, P., Léger, P., Koboevic, S. (2015). Selection and scaling of ground motion time histories for seismic analysis using NBCC 2015. The 11th Canadian Conference on Earthquake Engineering, Victoria, BC, Canada.

Vecchio, F.J. (2000). Disturbed Stress Field Mode1 for Reinforced Concrete: Formulation. ACI Structural Journal, ACI, 1070-1077.

Vecchio, F.J., Saatci, S. (2007). Dynamic Analysis with VecTor2. University of Toronto, Toronto, ON, Canada.

Vecchio, F.J., Wong, P., Trommels, H. (2013). VecTor2 and Formworks Manual, 2nd ed., University of Toronto, Toronto, ON, Canada.

Vecchio, F.J., Collins, M.P. (1986). The Modified Compression Field Theory for Reinforced Concrete Elements Subject to Shear. ACI Journal, ACI, 83(2):219-231.

Wang, B., Zhu, S. (2018). Seismic behavior of self-centering reinforced concrete wall enabled by superelastic shape memory alloy bars. Bull Earthquake Engineering, Springer, 16:479-502.

Wang, X., Wang, M.L., Zhao, Y., Chen, M., Zhou, L.L. (2004). Smart health monitoring system for a prestressed concrete bridge. SPIE - The International Society for Optical Engineering, Smart Structures and Materials 2004 - Sensors and Smart Structures Technologies for Civil, Mechanical, and Aerospace Systems, 5391:597-608.

Yazgan, U. (2010). The use of post-earthquake residual displacements as a performance indicator in seismic assessment. ETH Zürich, Zurich, Switzerland.

Yin, W., Sczerzenie, F., Long, M., Belden, C., Manjeri, R.M., Lafond, R. (2015). Structure and properties of large diameter hot rolled NiTi bars for seismic applications. Presentation, New Hartford, NY, USA. Retrieved 8 October, 2019, from http://memry.com/sites/default/files/documents.

Youssef, M.A., Alam, M.S., Nehdi, M. (2008). Experimental Investigation on the Seismic Behavior of Beam-Column Joints Reinforced with Superelastic Shape Memory Alloys. Journal of Earthquake Engineering, Taylor & Francis, 12(7):1205-1222.

Youssef, M.A., Elfeki, M.A. (2010). Seismic Performance of Shape Memory Alloy Reinforced Concrete Frames. 10th Canadian Conference on Earthquake Engineering, Toronto, ON, Canada.

APPENDICES

Appendix A: Design process

Table A-1 - Torsional sensitivity check using elastic displacements from unrestrained analysis considering 10% eccentricity

Vancouver								
	X direction				Y direction			
Level	Δ_{max} (mm)	Δ_{min} (mm)	Δ_{avg} (mm)	B_x	Δ_{max} (mm)	Δ_{min} (mm)	Δ_{avg} (mm)	B_x
10	490.0	413.0	451.5	1.09	503.0	399.0	451.0	1.12
9	423.0	357.0	390.0	1.08	434.0	344.0	389.0	1.12
8	357.0	301.0	329.0	1.09	366.0	290.0	328.0	1.12
7	292.0	246.6	269.3	1.08	300.0	238.0	269.0	1.12
6	230.0	194.0	212.0	1.08	236.0	187.0	211.5	1.12
5	172.4	145.5	159.0	1.08	177.0	140.3	158.7	1.12
4	120.0	101.3	110.7	1.08	123.3	97.7	110.5	1.12
3	74.7	63.0	68.9	1.08	76.7	60.8	68.8	1.12
2	38.0	32.0	35.0	1.09	39.2	31.0	35.1	1.12
1	12.8	10.8	11.8	1.08	13.2	10.5	11.9	1.11
Montreal								
	X direction				Y direction			
Level	Δ_{max} (mm)	Δ_{min} (mm)	Δ_{avg} (mm)	B_x	Δ_{max} (mm)	Δ_{min} (mm)	Δ_{avg} (mm)	B_x
10	196.3	165.6	180.96	1.08	201.1	159.5	180.30	1.12
9	169.3	142.8	156.06	1.08	173.4	137.6	155.49	1.12
8	142.6	120.3	131.44	1.08	146.1	115.9	130.97	1.12
7	116.7	98.4	107.55	1.08	119.5	94.8	107.17	1.12
6	92.0	77.6	84.79	1.08	94.3	74.8	84.50	1.12
5	69.0	58.2	63.64	1.08	70.7	56.1	63.43	1.12
4	48.3	40.8	44.55	1.08	49.5	39.3	44.41	1.12
3	30.3	25.6	27.96	1.08	31.1	24.7	27.87	1.12
2	15.7	13.2	14.47	1.08	16.1	12.8	14.43	1.12
1	5.4	4.5	4.94	1.08	5.5	4.4	4.92	1.12

Table A-2 - Interstorey lateral displacements: stability check and drift limits

Vancouver									
		X direction				Y direction			
Level	h_s (m)	Δ_{avg} (mm)	Θ	$(1+\Theta)$	δ_i	Δ_{avg} (mm)	Θ	$(1+\Theta)$	δ_i
10	3.00	62	0.10	1.00	2.06%	62	0.10	1.00	2.05%
9	3.00	61	0.14	1.14	2.05%	61	0.14	1.14	2.04%
8	3.00	60	0.18	1.18	1.99%	60	0.18	1.18	1.99%
7	3.00	57	0.22	1.22	1.91%	57	0.21	1.21	1.90%
6	3.00	53	0.23	1.23	1.78%	53	0.23	1.23	1.78%
5	3.00	48	0.22	1.22	1.61%	48	0.22	1.22	1.61%
4	3.00	42	0.20	1.20	1.39%	42	0.19	1.19	1.39%
3	3.00	34	0.16	1.16	1.12%	34	0.16	1.16	1.12%
2	3.00	23	0.11	1.11	0.78%	23	0.11	1.11	0.78%
1	3.50	12	0.05	1.00	0.34%	12	0.05	1.00	0.34%
		Total δ in X direction:		1.48%		Total δ in Y direction:		1.48%	

Montreal									
		X direction				Y direction			
Level	h_s (m)	Δ_{avg} (mm)	Θ	$(1+\Theta)$	δ_i	Δ_{avg} (mm)	Θ	$(1+\Theta)$	δ_i
10	3.00	25	0.02	1.00	0.83%	25	0.02	1.00	0.83%
9	3.00	25	0.04	1.00	0.82%	25	0.04	1.00	0.82%
8	3.00	24	0.06	1.00	0.80%	24	0.05	1.00	0.79%
7	3.00	23	0.07	1.00	0.76%	23	0.06	1.00	0.76%
6	3.00	21	0.08	1.00	0.71%	21	0.07	1.00	0.70%
5	3.00	19	0.08	1.00	0.64%	19	0.07	1.00	0.63%
4	3.00	17	0.06	1.00	0.55%	17	0.06	1.00	0.55%
3	3.00	13	0.05	1.00	0.45%	13	0.04	1.00	0.45%
2	3.00	10	0.03	1.00	0.32%	10	0.03	1.00	0.32%
1	3.50	5	0.01	1.00	0.14%	5	0.01	1.00	0.14%
		Total δ in X direction:		0.59%		Total δ in Y direction:		0.59%	

Appendix B: Ground motion records employed in dynamic analysis

Table B-1 - Acceleration time history of earthquake records selected for Montreal

Scenario 1

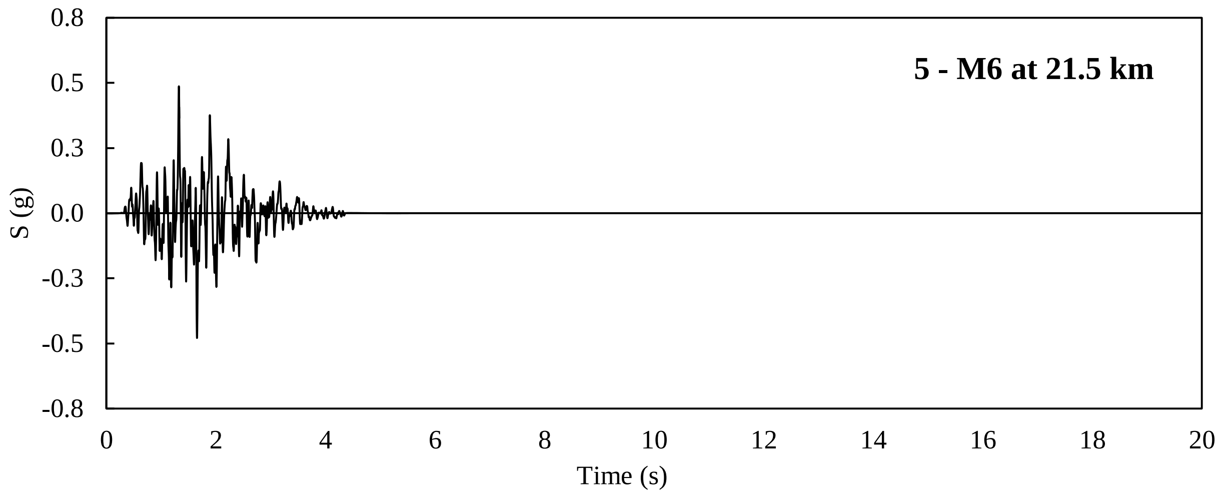

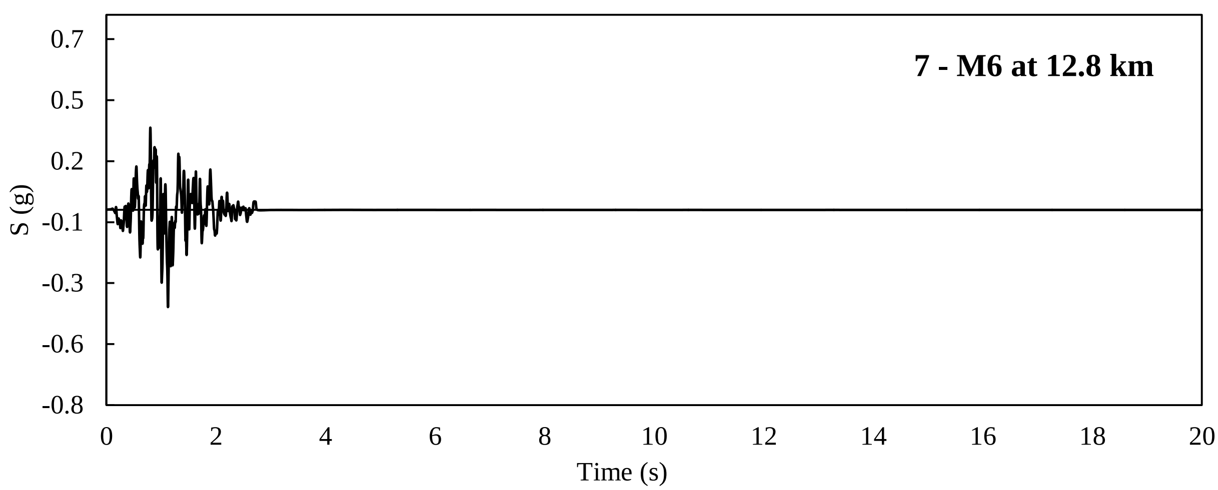

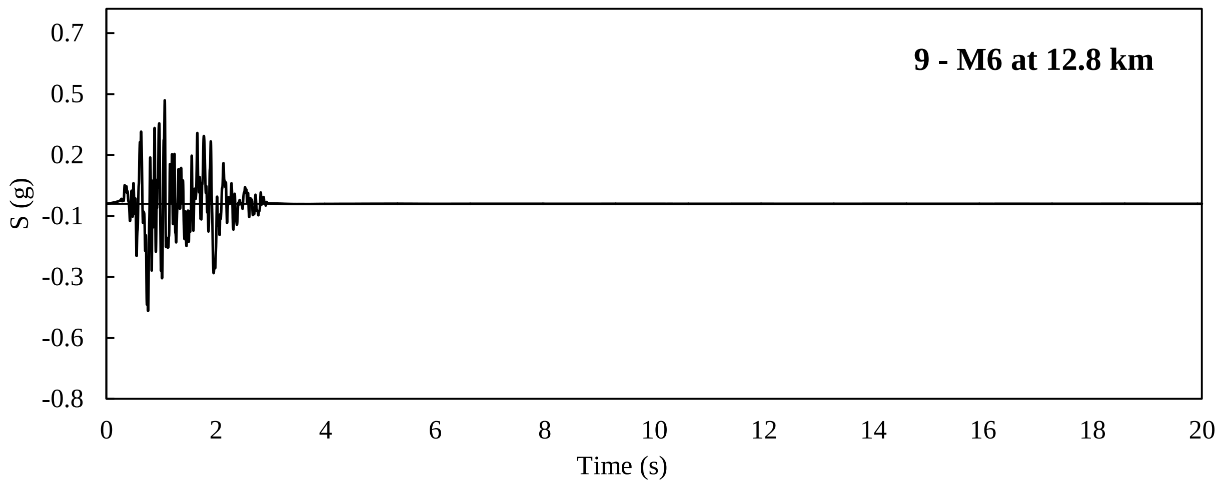
9 - M6 at 12.8 km
S (g)
0.7
0.5
0.2
-0.1
-0.3
-0.6
-0.8
0
2
4
6
8
10
12
14
16
18
20
Time (s)

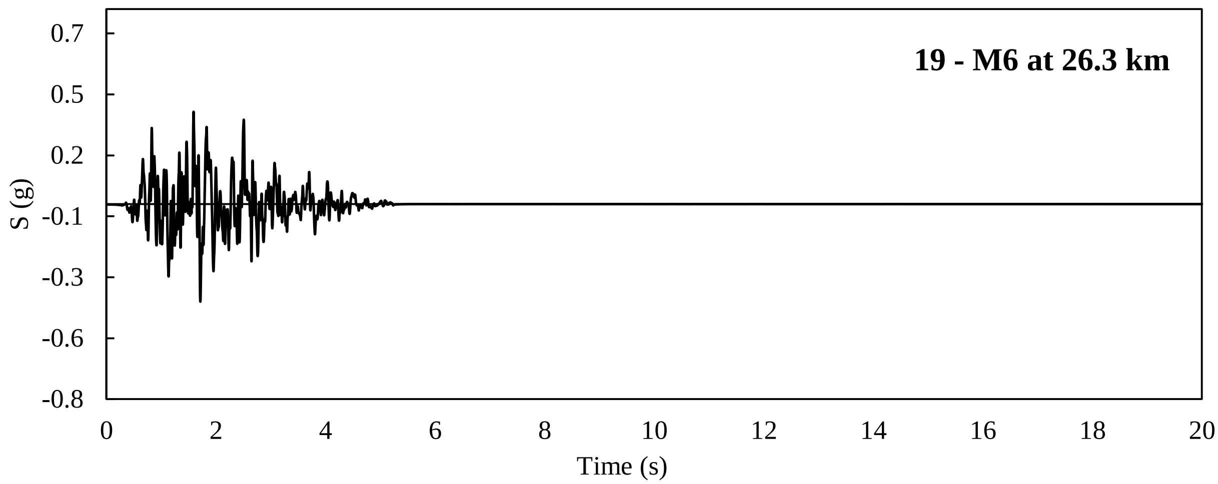
19 - M6 at 26.3 km
S (g)
0.7
0.5
0.2
-0.1
-0.3
-0.6
-0.8
0
2
4
6
8
10
12
14
16
18
20
Time (s)

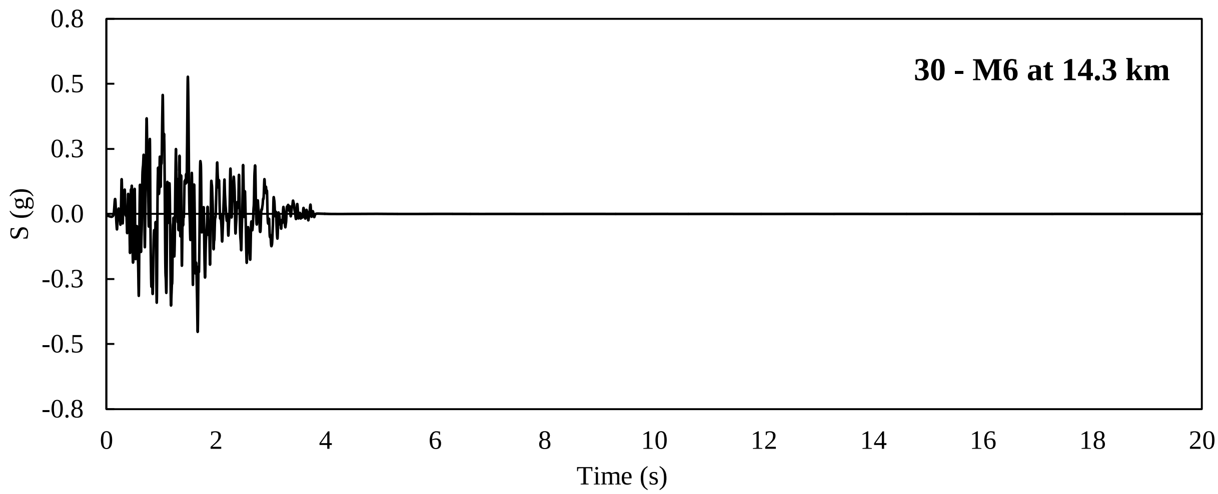
30 - M6 at 14.3 km
S (g)
0.8
0.5
0.3
0.0
-0.3
-0.5
-0.8
0
2
4
6
8
10
12
14
16
18
20
Time (s)

Scenario 2

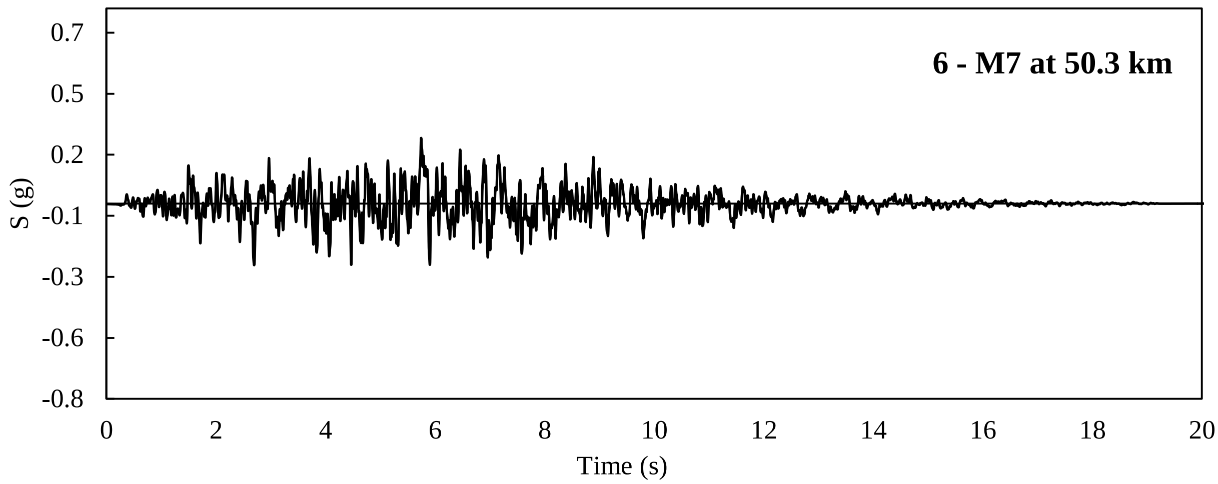
6 - M7 at 50.3 km
S (g)
0.7
0.5
0.2
-0.1
-0.3
-0.6
-0.8
0
2
4
6
8
10
12
14
16
18
20
Time (s)

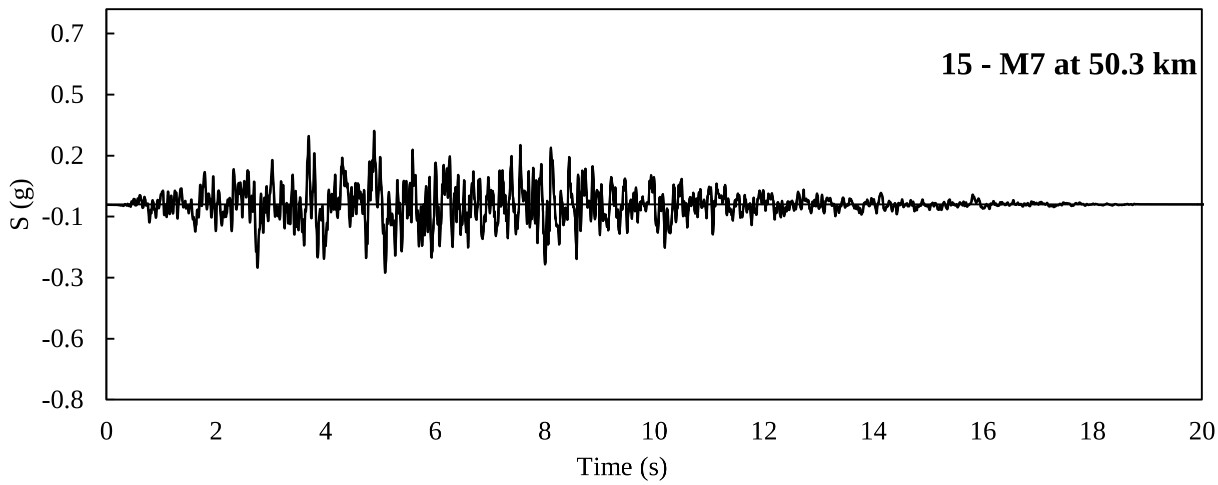
15 - M7 at 50.3 km
S (g)
0.7
0.5
0.2
-0.1
-0.3
-0.6
-0.8
0
2
4
6
8
10
12
14
16
18
20
Time (s)

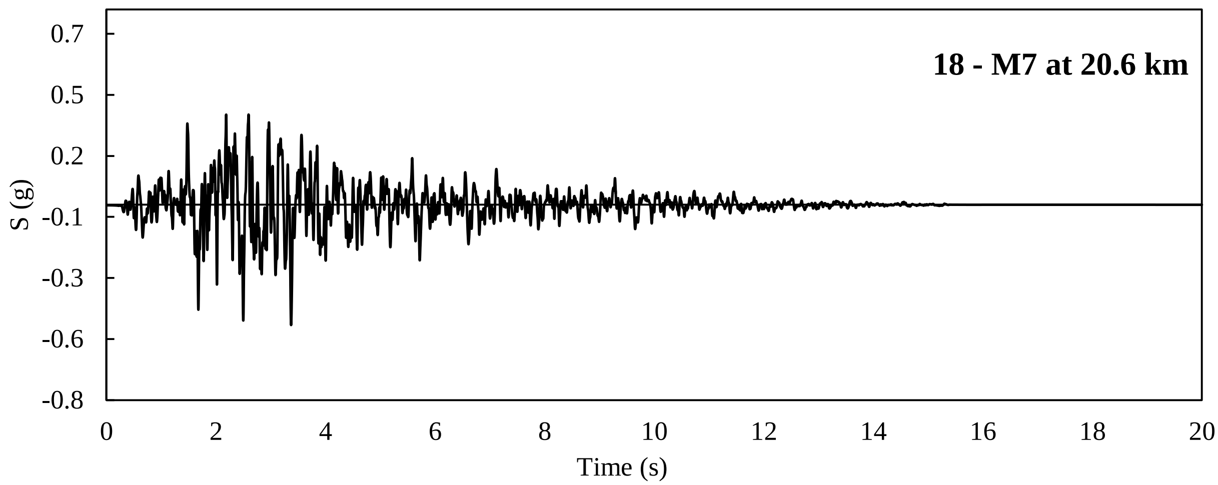
18 - M7 at 20.6 km
S (g)
0.7
0.5
0.2
-0.1
-0.3
-0.6
-0.8
0
2
4
6
8
10
12
14
16
18
20
Time (s)

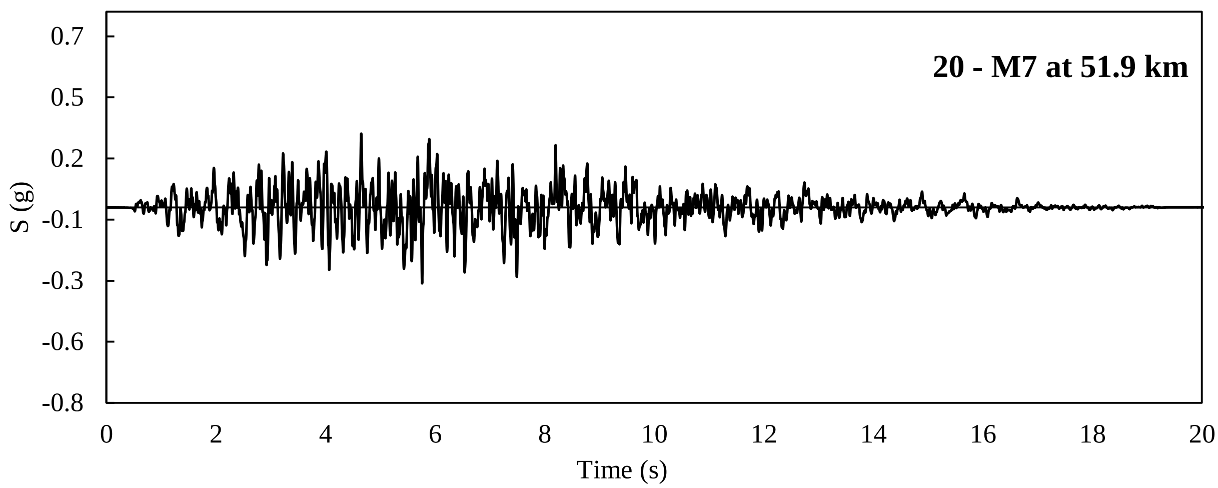
20 - M7 at 51.9 km
S (g)
0.7
0.5
0.2
-0.1
-0.3
-0.6
-0.8
0
2
4
6
8
10
12
14
16
18
20
Time (s)

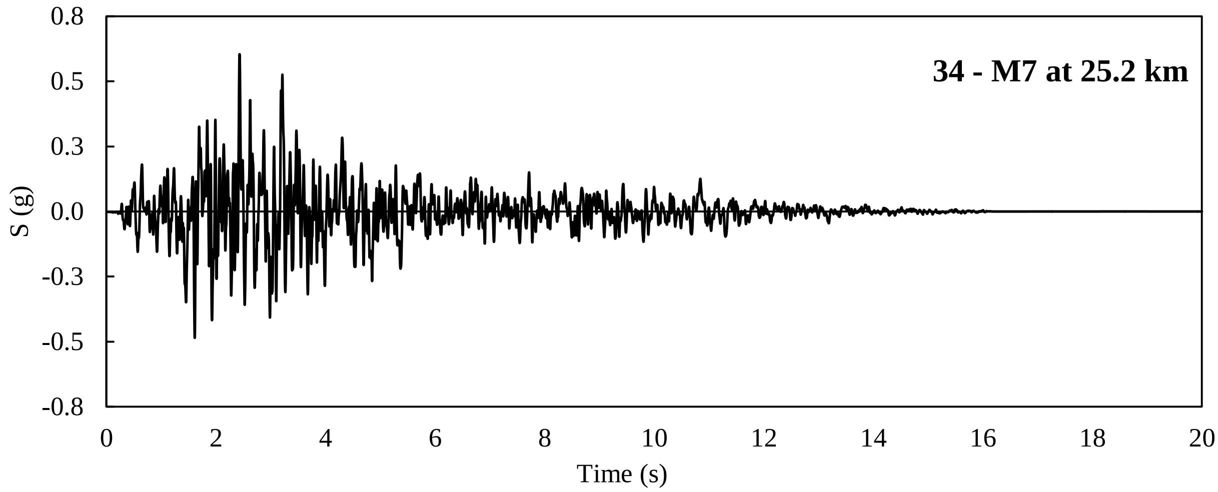
34 - M7 at 25.2 km
S (g)
0.8
0.5
0.3
0.0
-0.3
-0.5
-0.8
0
2
4
6
8
10
12
14
16
18
20
Time (s)

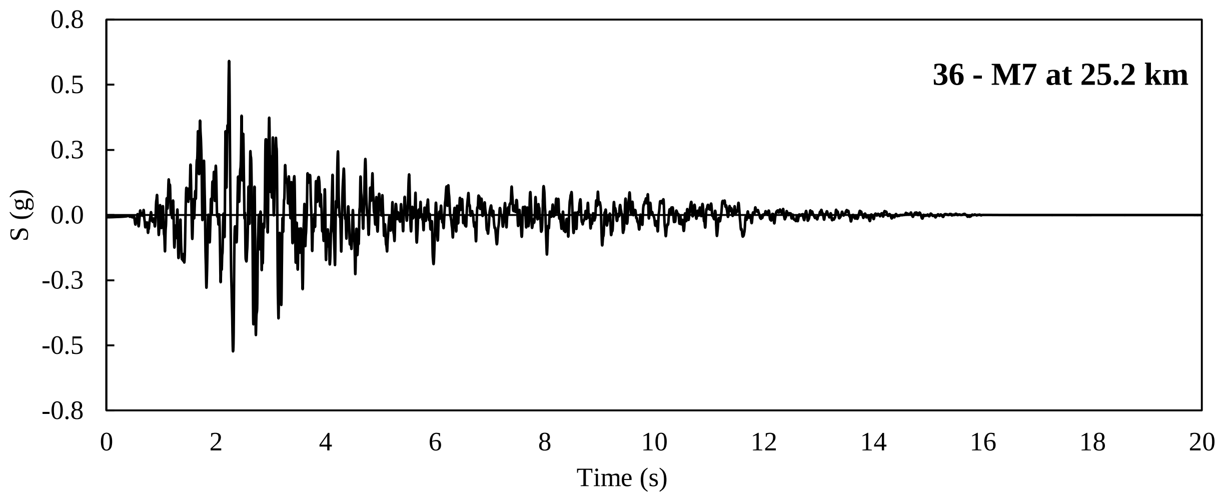
36 - M7 at 25.2 km
S (g)
0.8
0.5
0.3
0.0
-0.3
-0.5
-0.8
0
2
4
6
8
10
12
14
16
18
20
Time (s)

Table B-2 - Acceleration time history of earthquake records selected for Vancouver

Scenario 1

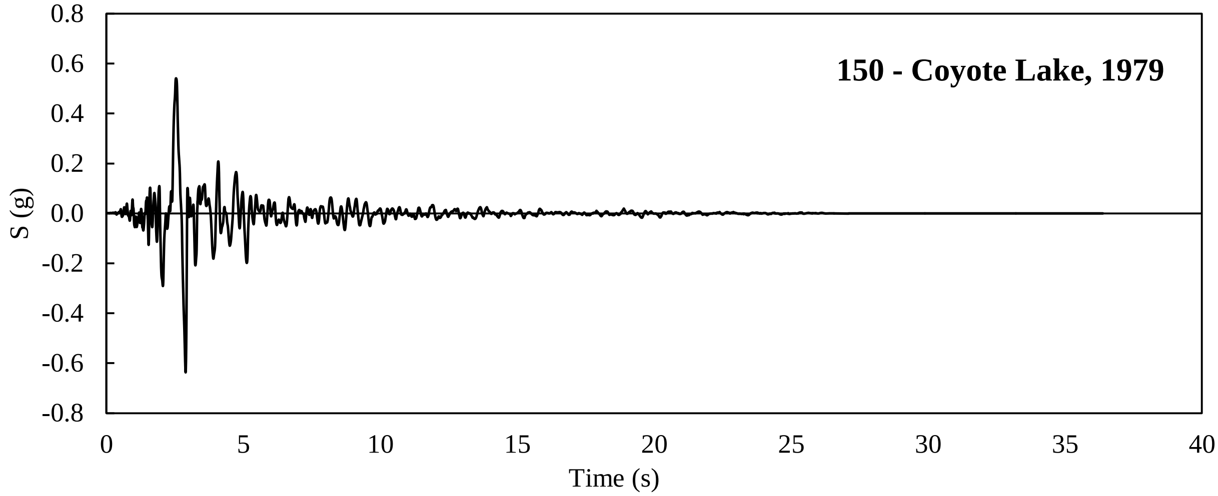

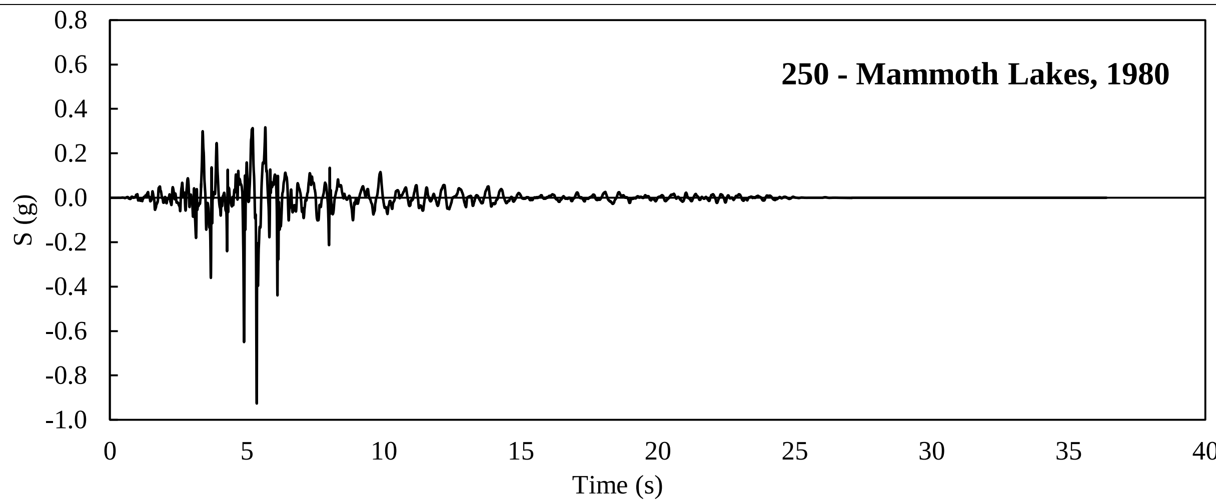

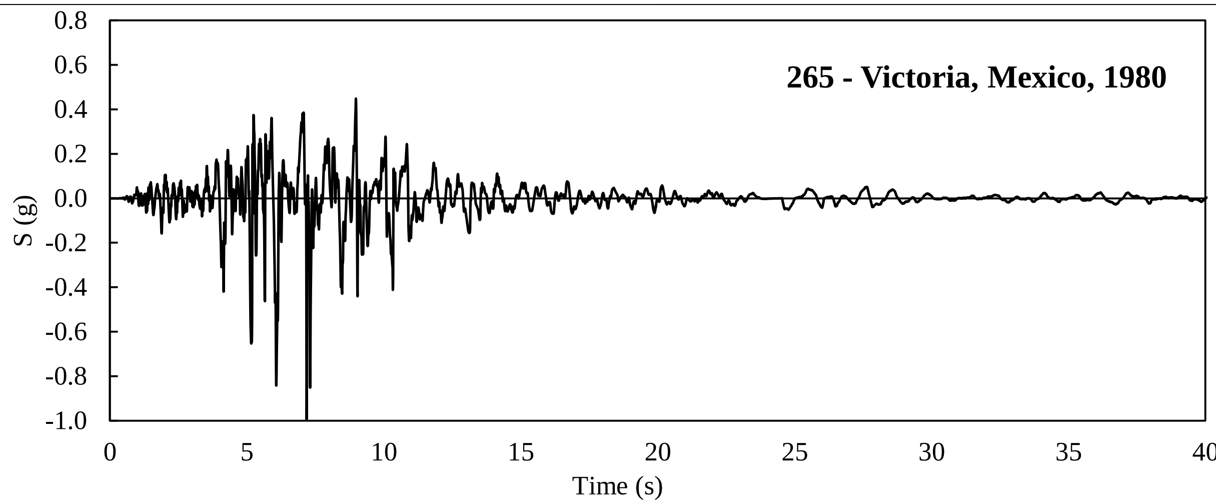

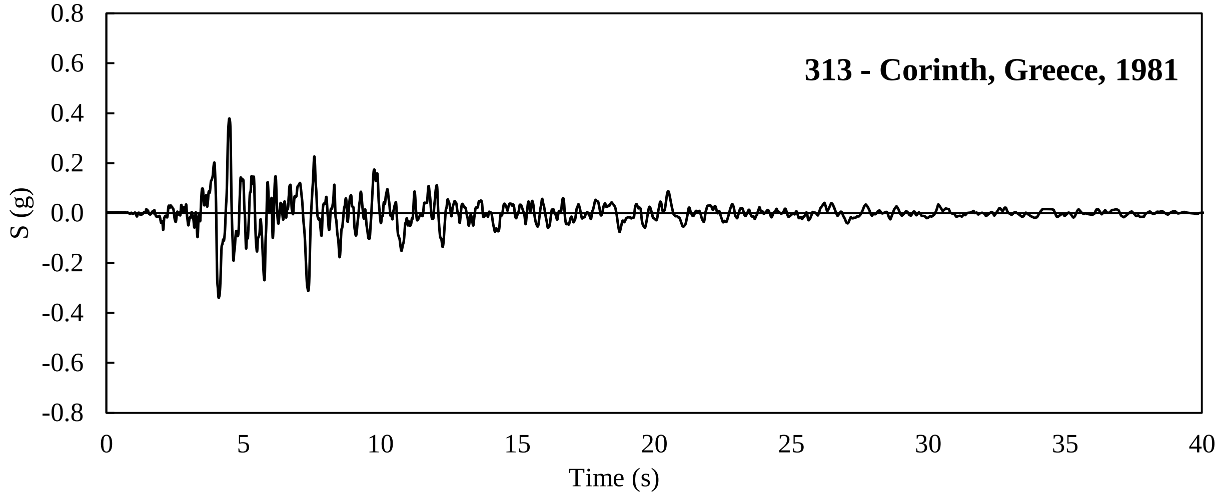
313 - Corinth, Greece, 1981
S (g)
0.8
0.6
0.4
0.2
0.0
-0.2
-0.4
-0.6
-0.8
0
5
10
15
20
25
30
35
40
Time (s)

Scenario 2

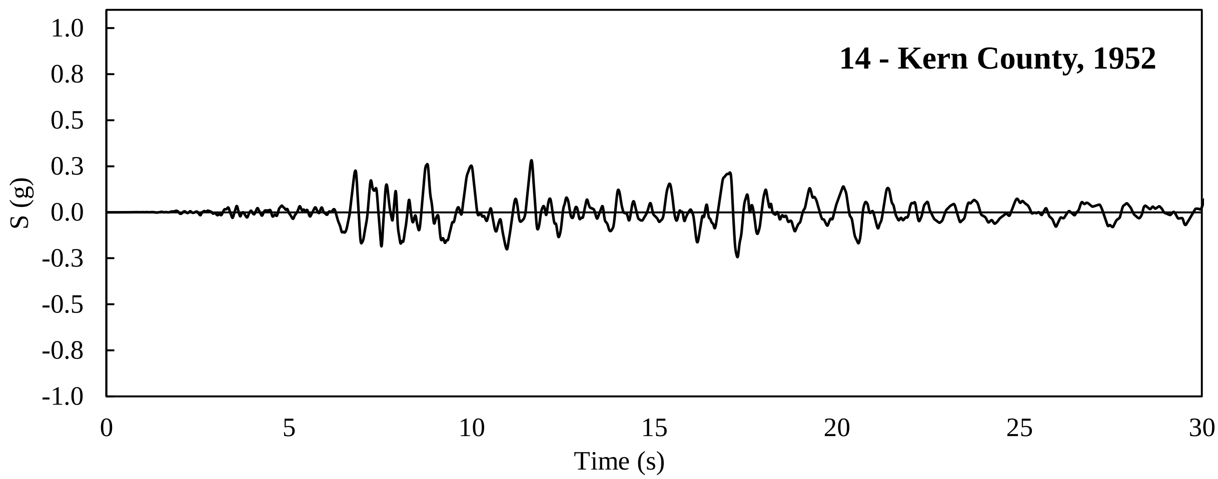
14 - Kern County, 1952
S (g)
1.0
0.8
0.5
0.3
0.0
-0.3
-0.5
-0.8
-1.0
0
5
10
15
20
25
30
Time (s)

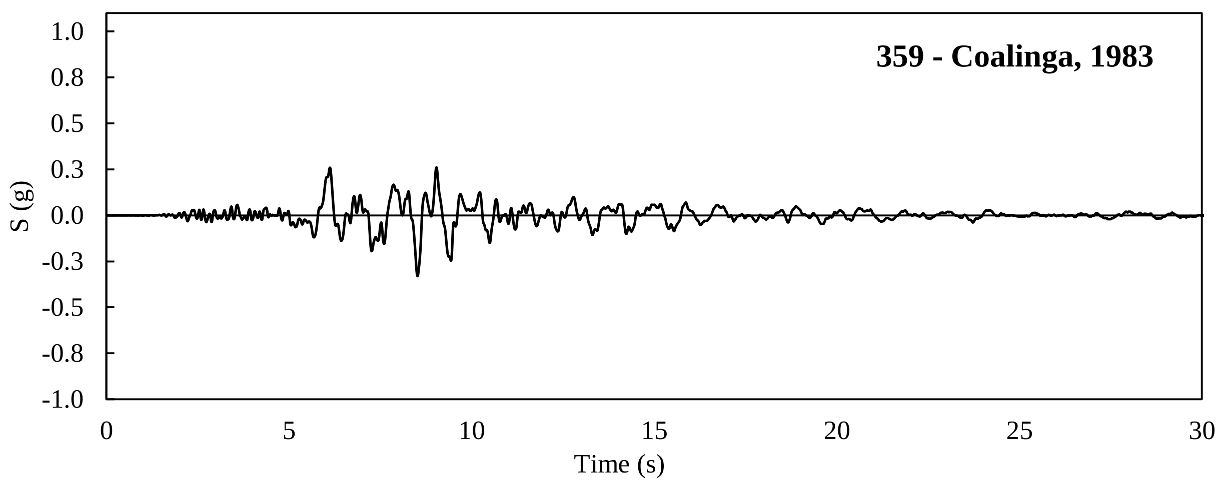
359 - Coalinga, 1983
S (g)
1.0
0.8
0.5
0.3
0.0
-0.3
-0.5
-0.8
-1.0
0
5
10
15
20
25
30
Time (s)

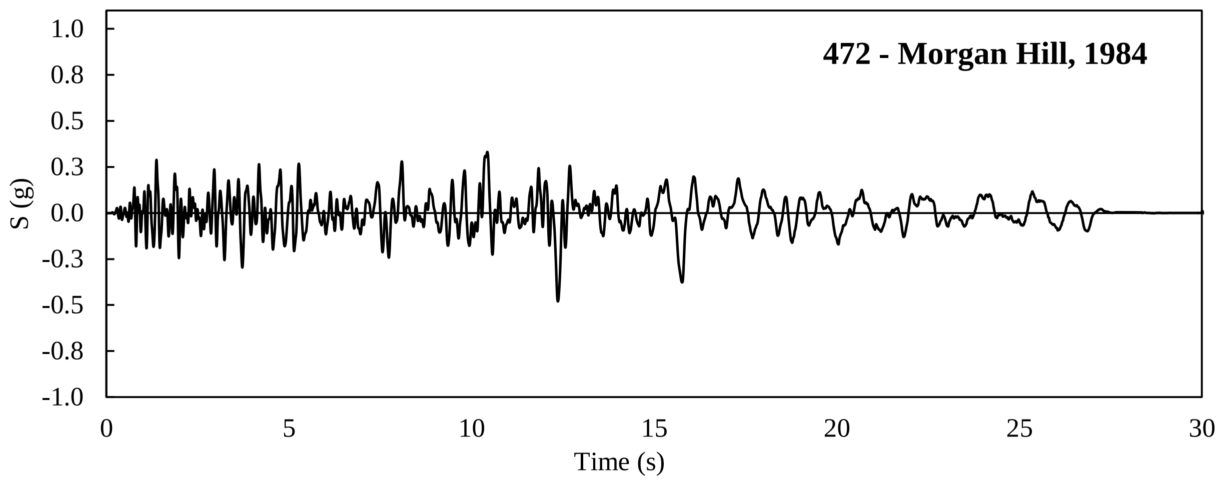
472 - Morgan Hill, 1984
S (g)
1.0
0.8
0.5
0.3
0.0
-0.3
-0.5
-0.8
-1.0
0
5
10
15
20
25
30
Time (s)

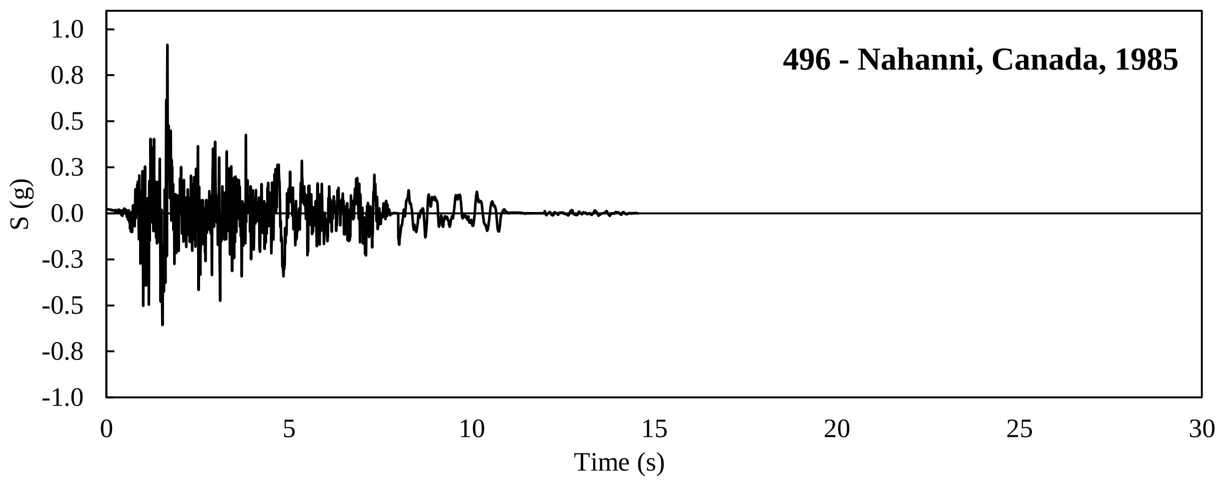
496 - Nahanni, Canada, 1985
S (g)
1.0
0.8
0.5
0.3
0.0
-0.3
-0.5
-0.8
-1.0
0
5
10
15
20
25
30
Time (s)

Scenario 3

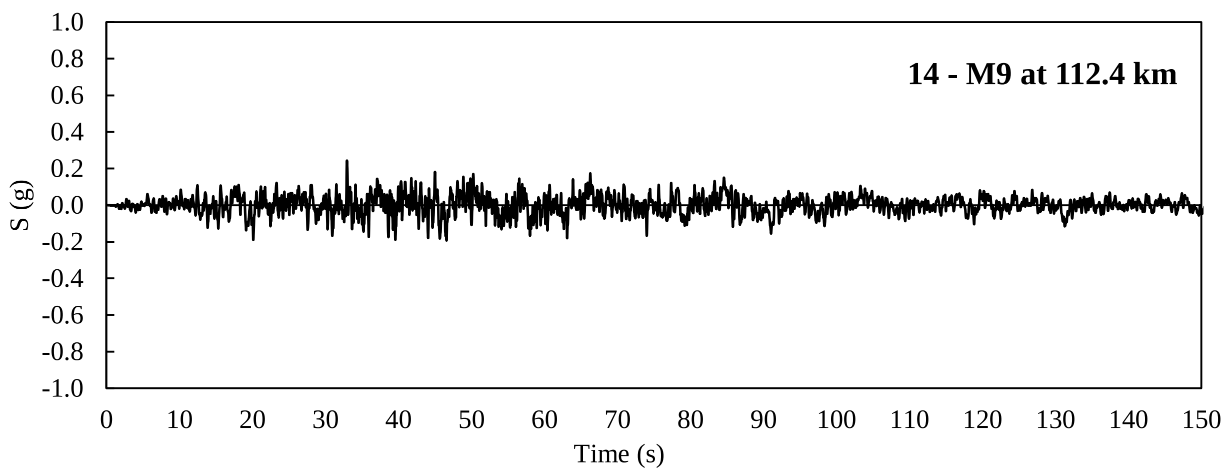
14 - M9 at 112.4 km
S (g)
1.0
0.8
0.6
0.4
0.2
0.0
-0.2
-0.4
-0.6
-0.8
-1.0
0
10
20
30
40
50
60
70
80
90
100
110
120
130
140
150
Time (s)

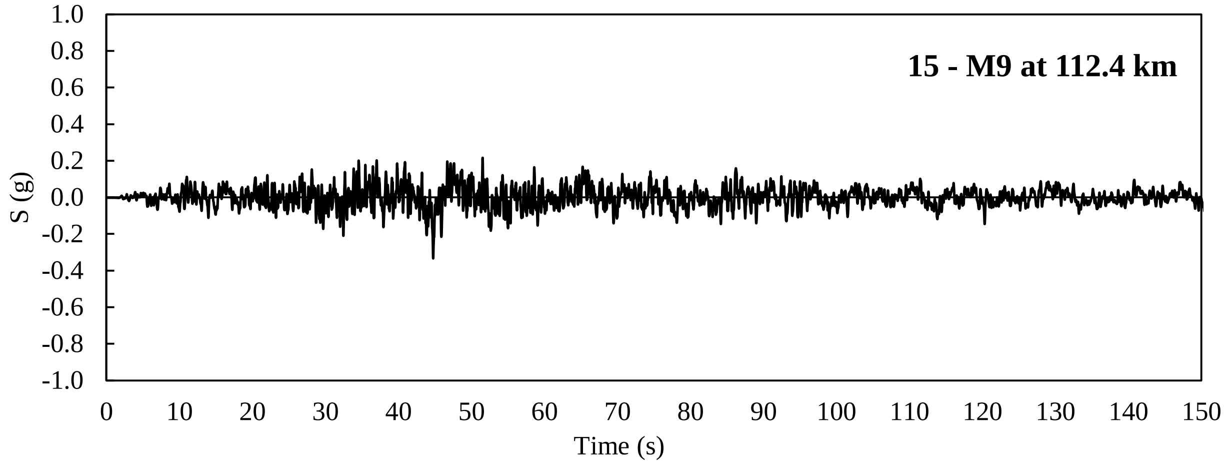
15 - M9 at 112.4 km
S (g)
1.0
0.8
0.6
0.4
0.2
0.0
-0.2
-0.4
-0.6
-0.8
-1.0
0
10
20
30
40
50
60
70
80
90
100
110
120
130
140
150
Time (s)

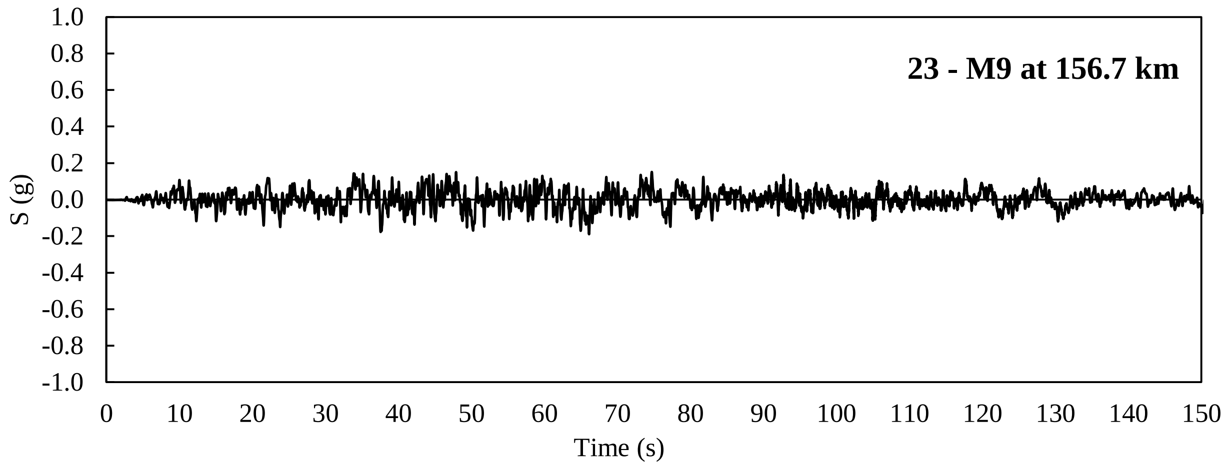
23 - M9 at 156.7 km
S (g)
1.0
0.8
0.6
0.4
0.2
0.0
-0.2
-0.4
-0.6
-0.8
-1.0
0
10
20
30
40
50
60
70
80
90
100
110
120
130
140
150
Time (s)

Table B-3 - Acceleration time history of amplified earthquake records

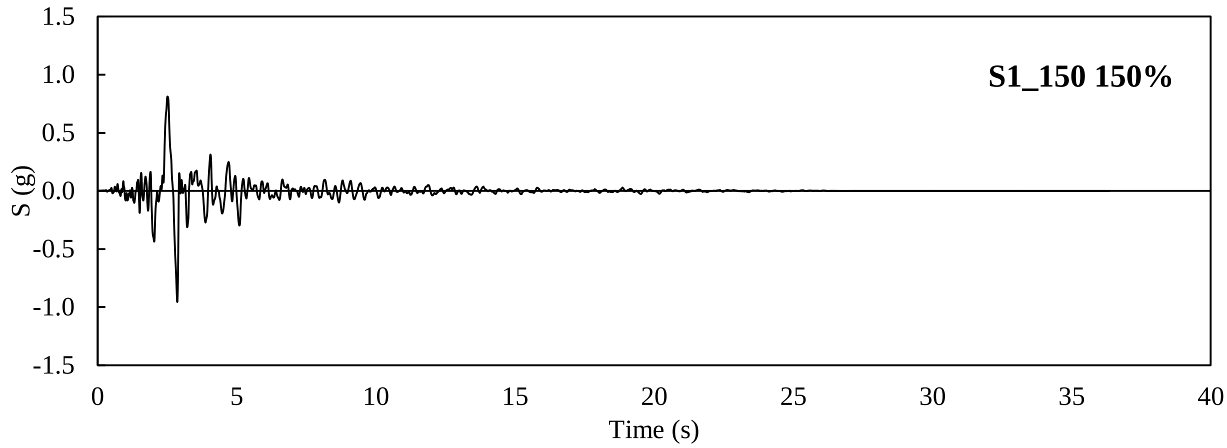

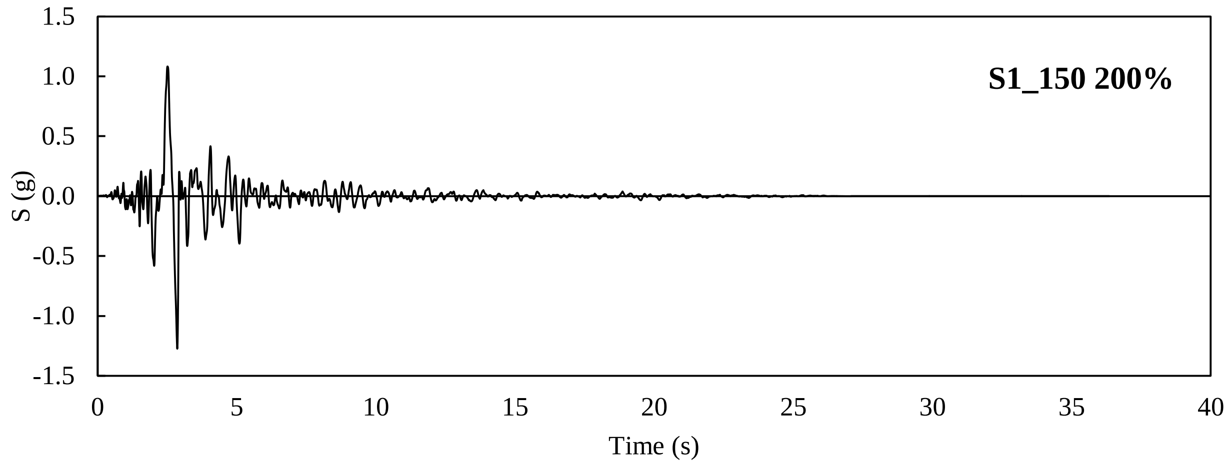

Appendix C: Results from dynamic analysis

Table C-1 - Roof displacement time histories of Wall DSRW

Scenario 1

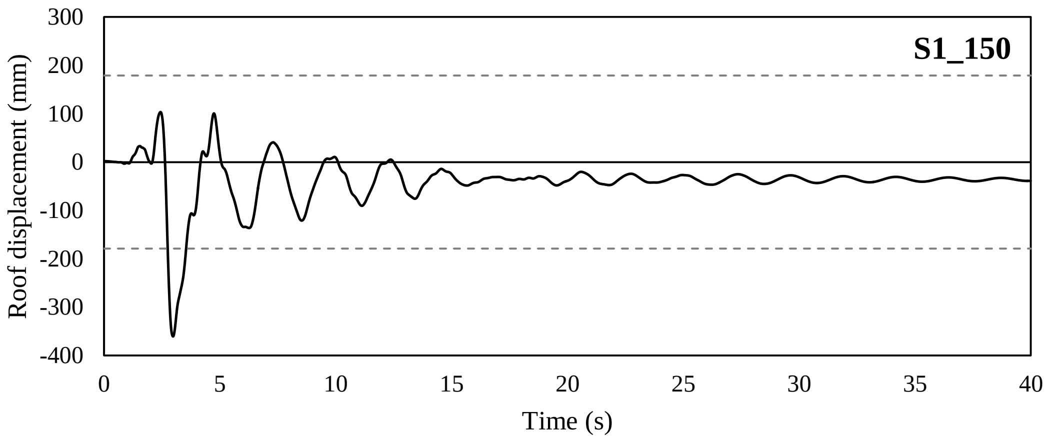

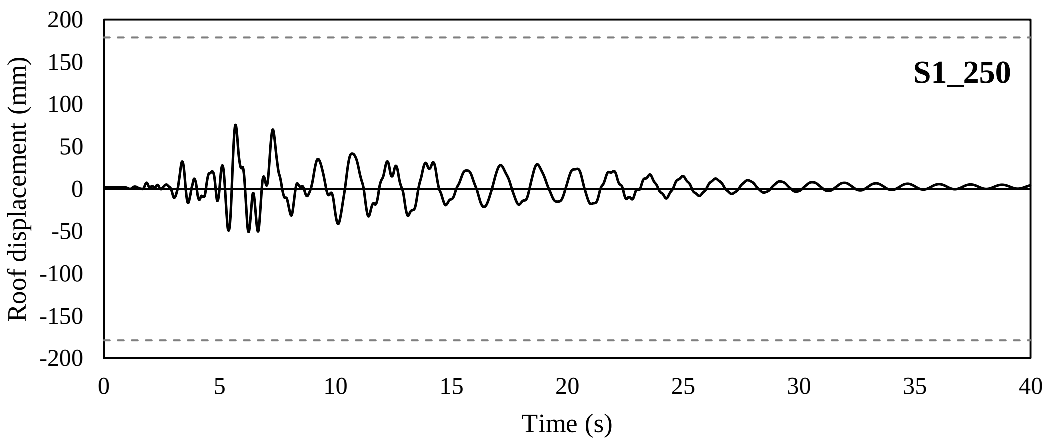

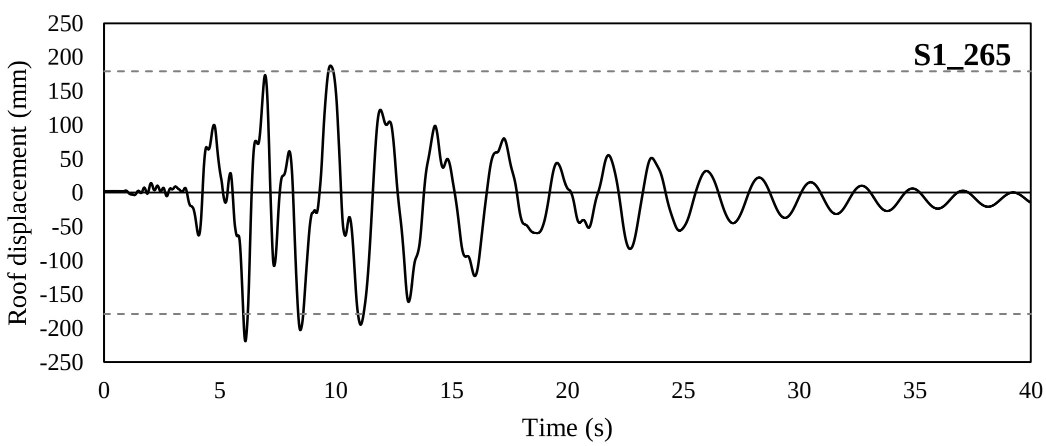

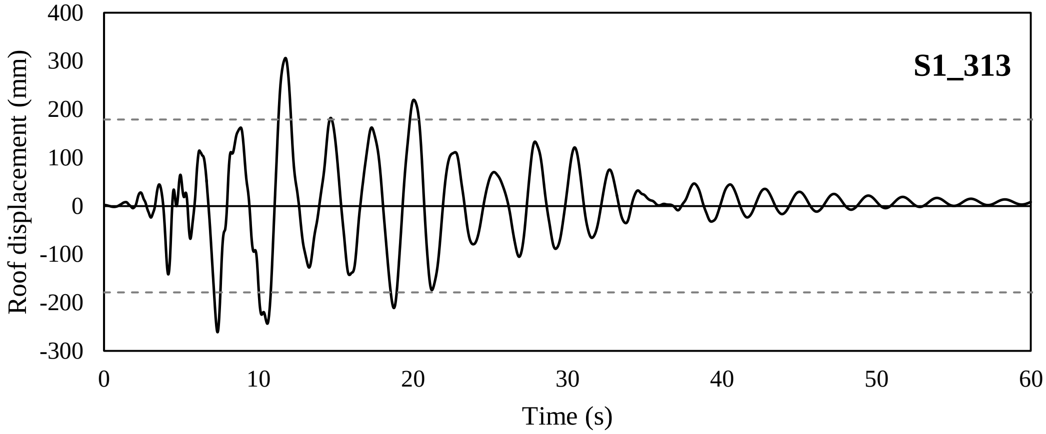
S1_313
Roof displacement (mm)
Time (s)
400
300
200
100
0
-100
-200
-300
0
10
20
30
40
50
60

Scenario 2

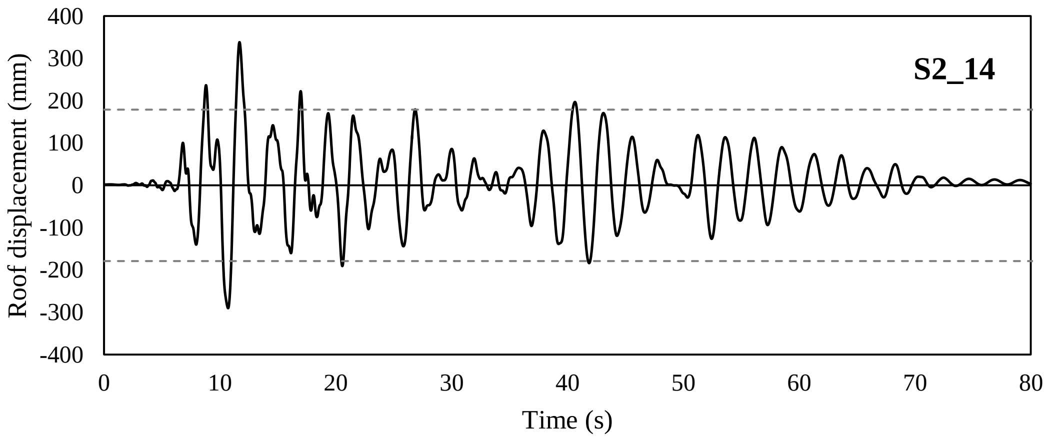
S2_14
Roof displacement (mm)
Time (s)
400
300
200
100
0
-100
-200
-300
-400
0
10
20
30
40
50
60
70
80

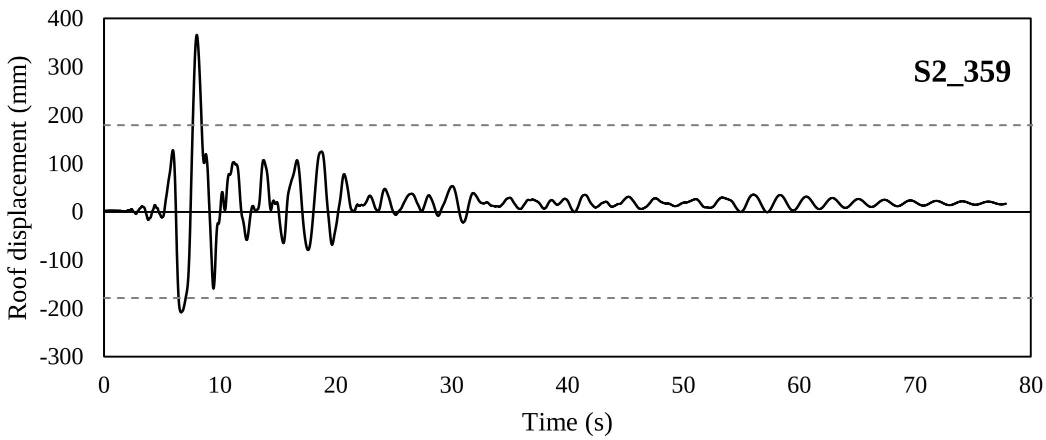
S2_359
Roof displacement (mm)
Time (s)
400
300
200
100
0
-100
-200
-300
0
10
20
30
40
50
60
70
80

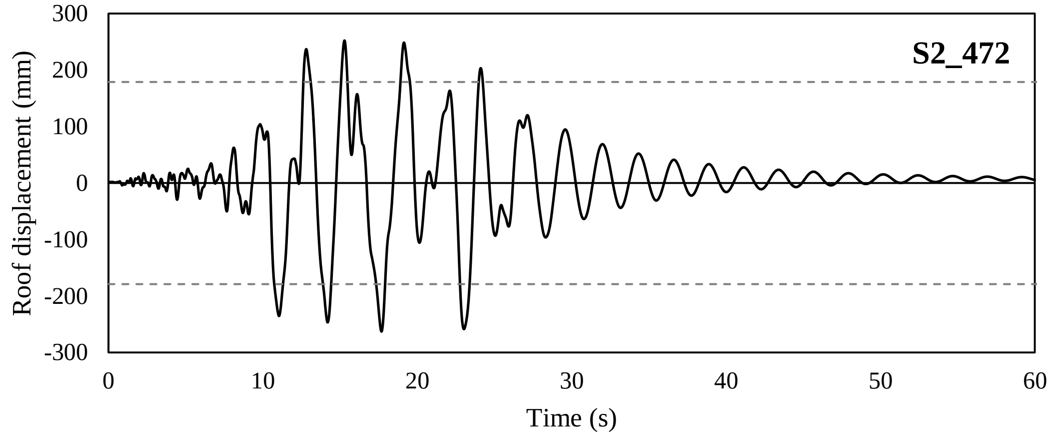
S2_472
Roof displacement (mm)
300
200
100
0
-100
-200
-300
0
10
20
30
40
50
60
Time (s)

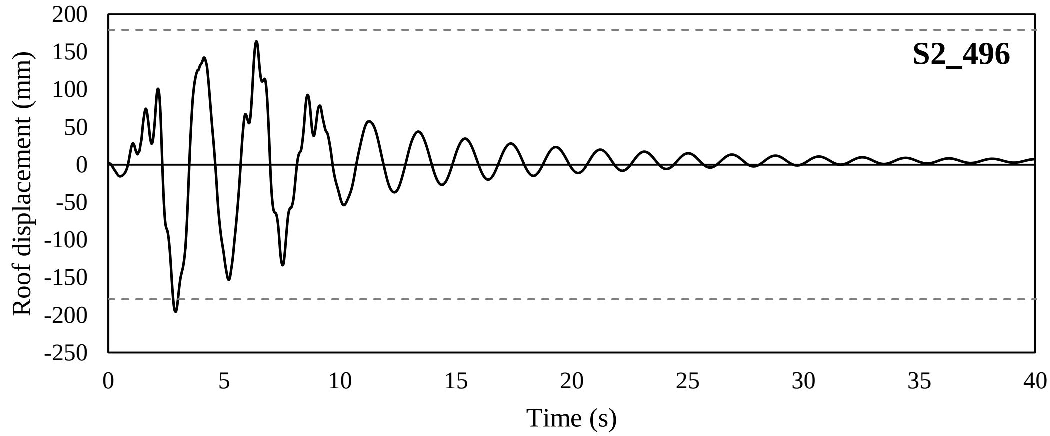
S2_496
Roof displacement (mm)
200
150
100
50
0
-50
-100
-150
-200
-250
0
5
10
15
20
25
30
35
40
Time (s)

Scenario 3

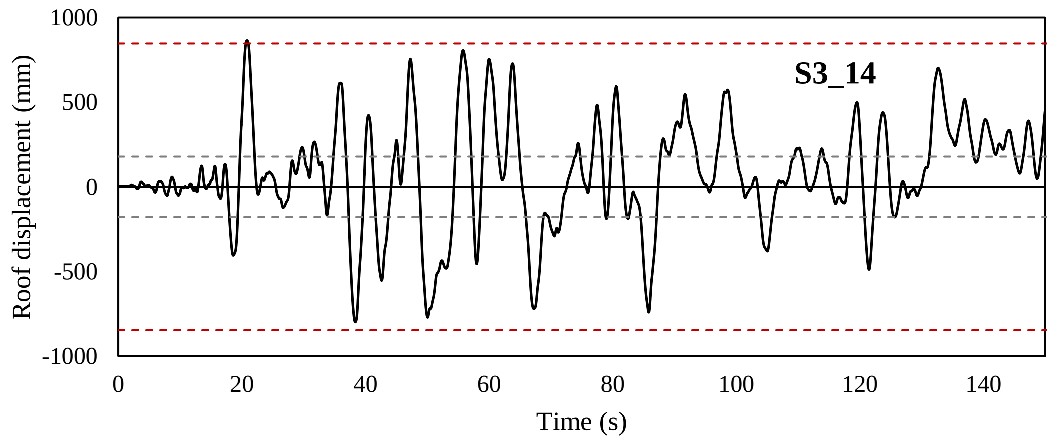
S3_14
Roof displacement (mm)
1000
500
0
-500
-1000
0
20
40
60
80
100
120
140
Time (s)

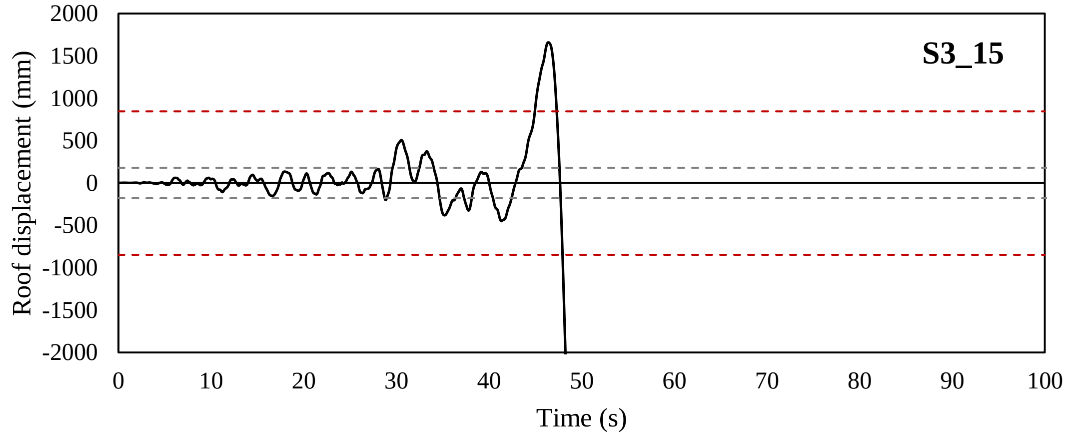
S3_15
Roof displacement (mm)
2000
1500
1000
500
0
-500
-1000
-1500
-2000
0
10
20
30
40
50
60
70
80
90
100
Time (s)

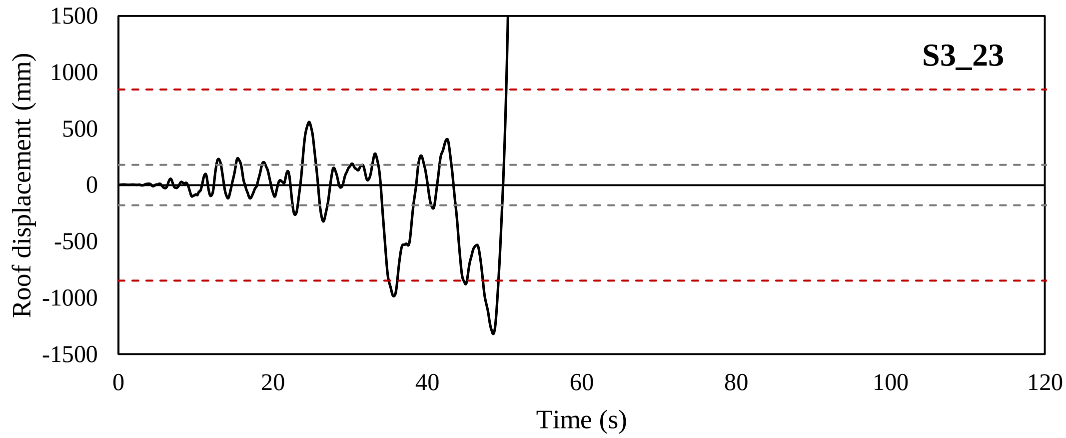
S3_23
Roof displacement (mm)
1500
1000
500
0
-500
-1000
-1500
0
20
40
60
80
100
120
Time (s)

Table C-2 - Roof displacement time histories of Wall DHW

Scenario 1

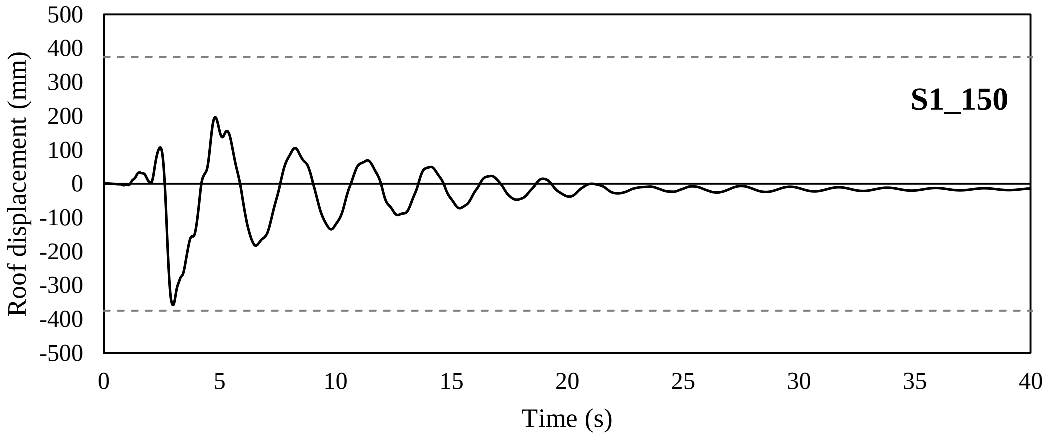

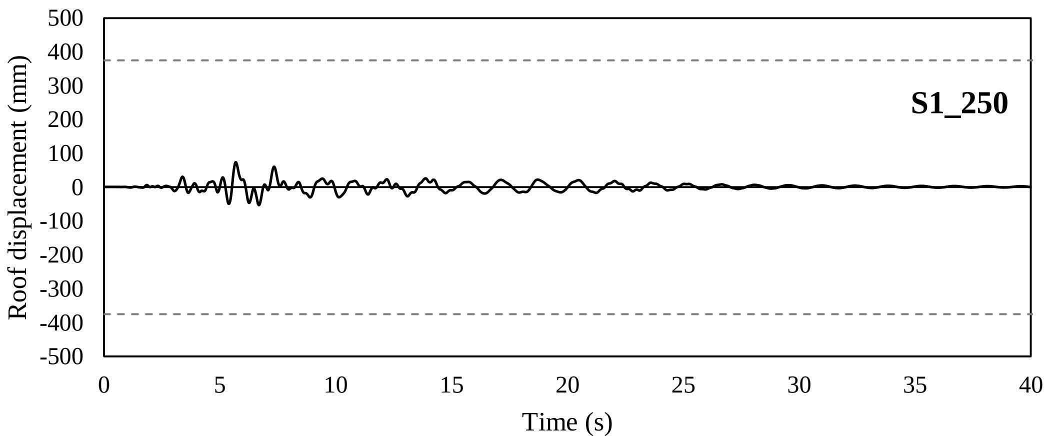

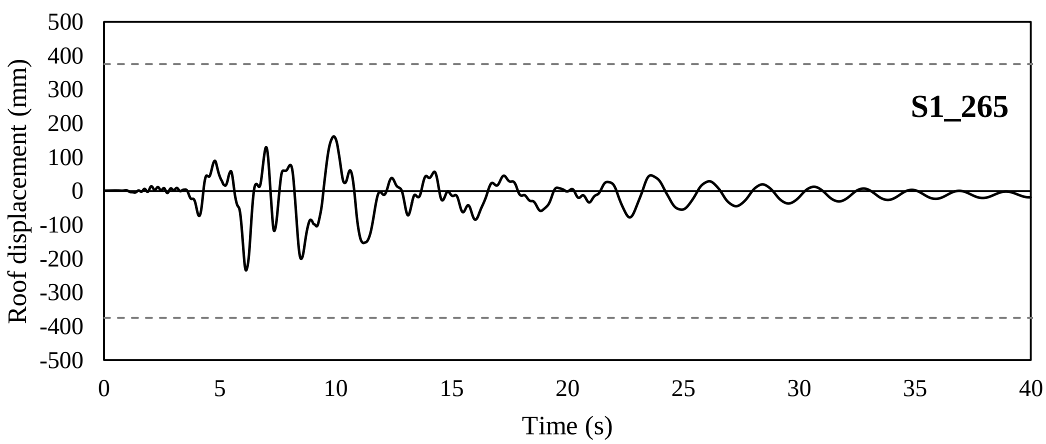

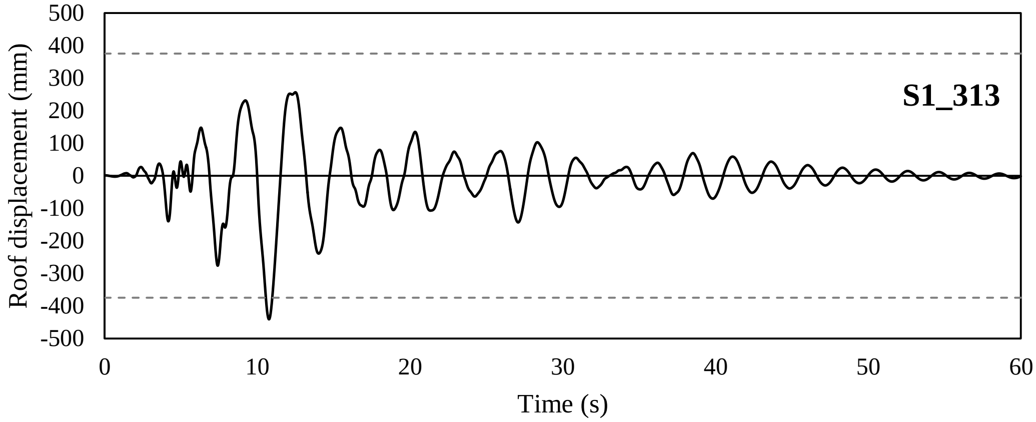
S1_313
Roof displacement (mm)
500
400
300
200
100
0
-100
-200
-300
-400
-500
0
10
20
30
40
50
60
Time (s)

Scenario 2

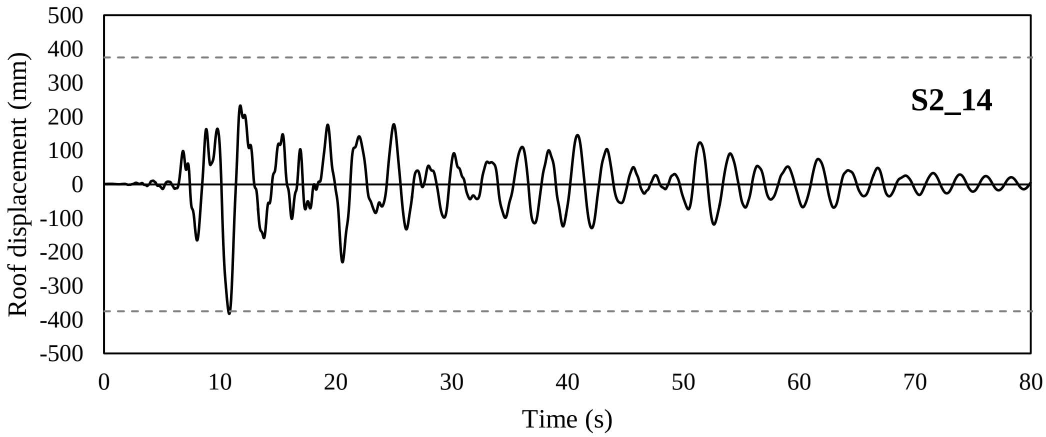
S2_14
Roof displacement (mm)
500
400
300
200
100
0
-100
-200
-300
-400
-500
0
10
20
30
40
50
60
70
80
Time (s)

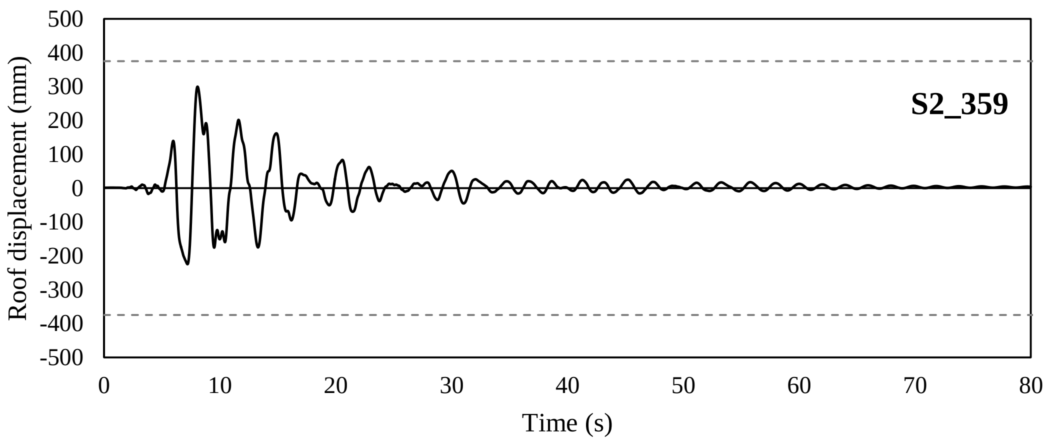
S2_359
Roof displacement (mm)
500
400
300
200
100
0
-100
-200
-300
-400
-500
0
10
20
30
40
50
60
70
80
Time (s)

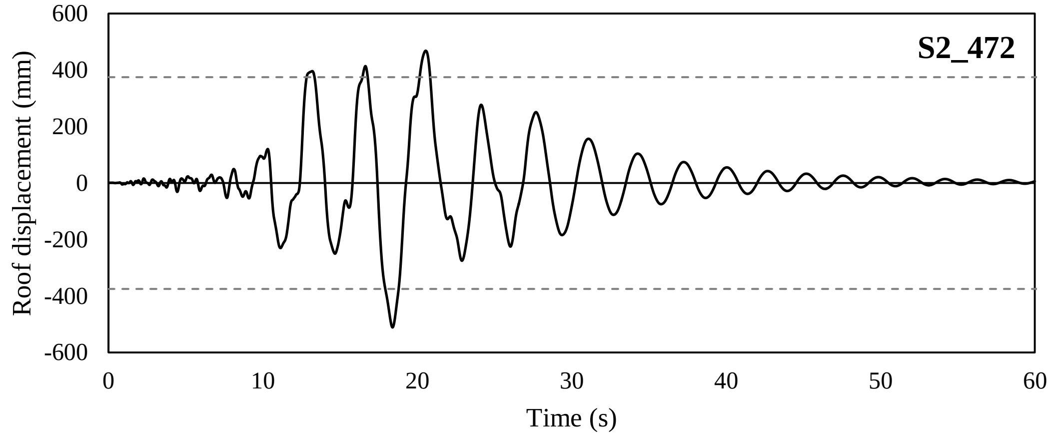
S2_472
Roof displacement (mm)
600
400
200
0
-200
-400
-600
0
10
20
30
40
50
60
Time (s)

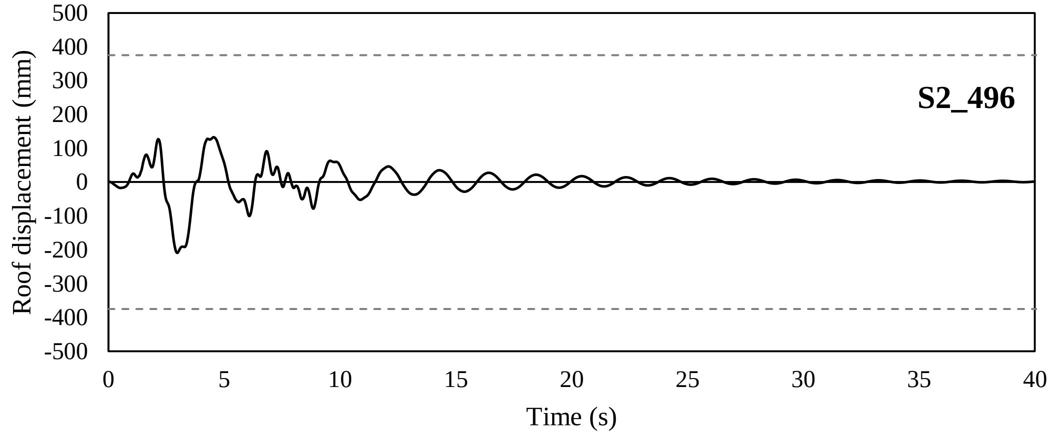
S2_496
Roof displacement (mm)
500
400
300
200
100
0
-100
-200
-300
-400
-500
0
5
10
15
20
25
30
35
40
Time (s)

Scenario 3

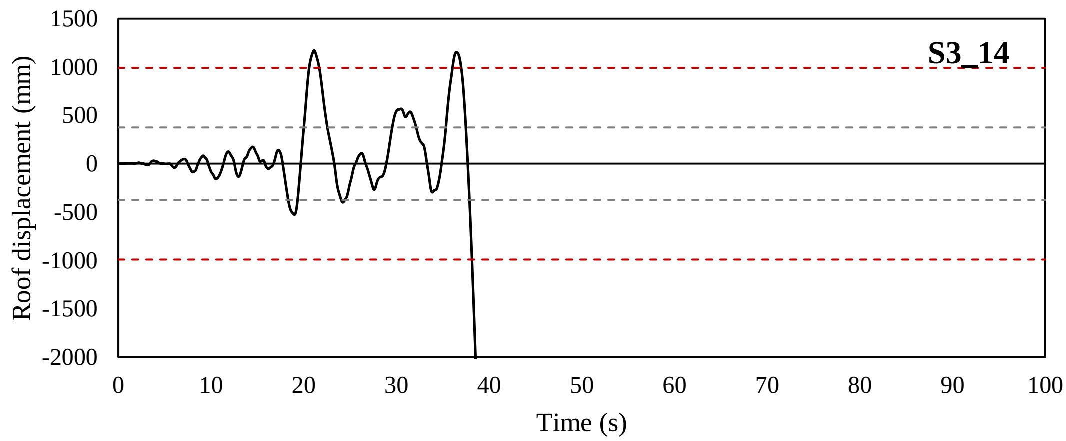
S3_14
Roof displacement (mm)
1500
1000
500
0
-500
-1000
-1500
-2000
0
10
20
30
40
50
60
70
80
90
100
Time (s)

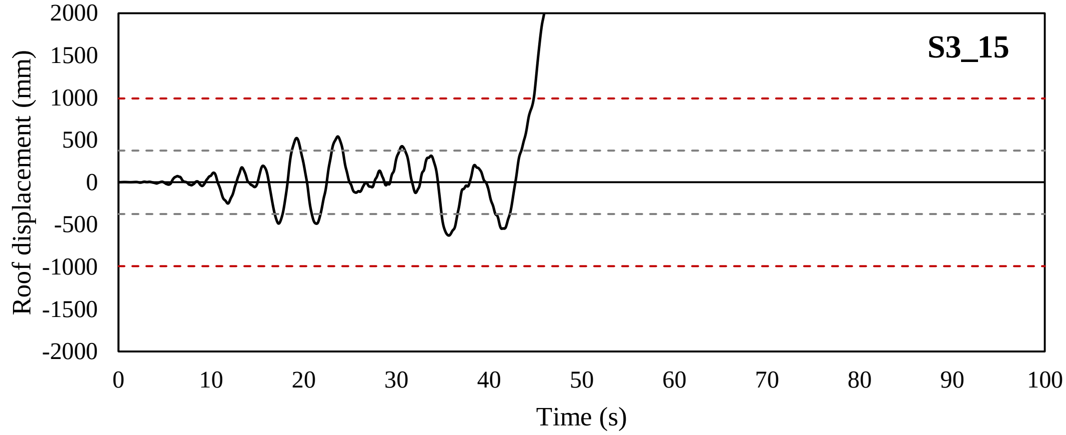
S3_15
Roof displacement (mm)
2000
1500
1000
500
0
-500
-1000
-1500
-2000
0
10
20
30
40
50
60
70
80
90
100
Time (s)

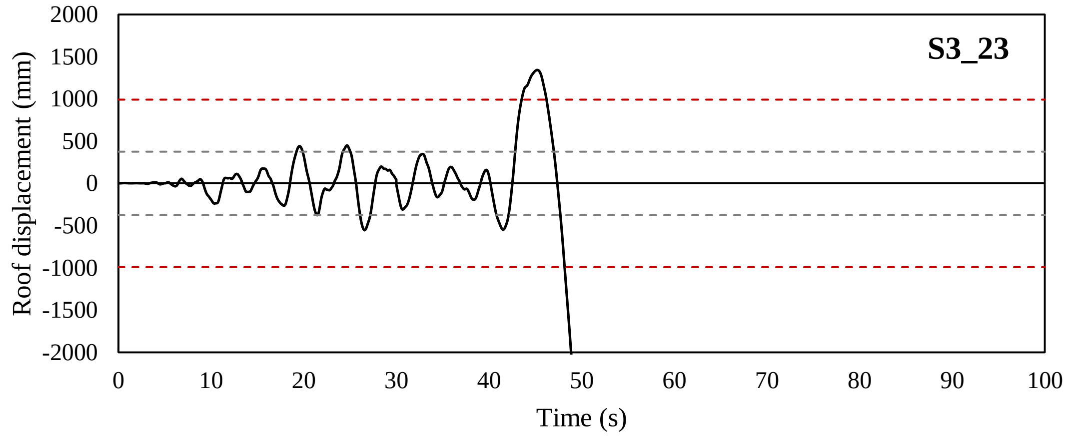
S3_23
Roof displacement (mm)
2000
1500
1000
500
0
-500
-1000
-1500
-2000
0
10
20
30
40
50
60
70
80
90
100
Time (s)

Table C-3 - Roof displacement time histories of Wall MDSRW

Scenario 1

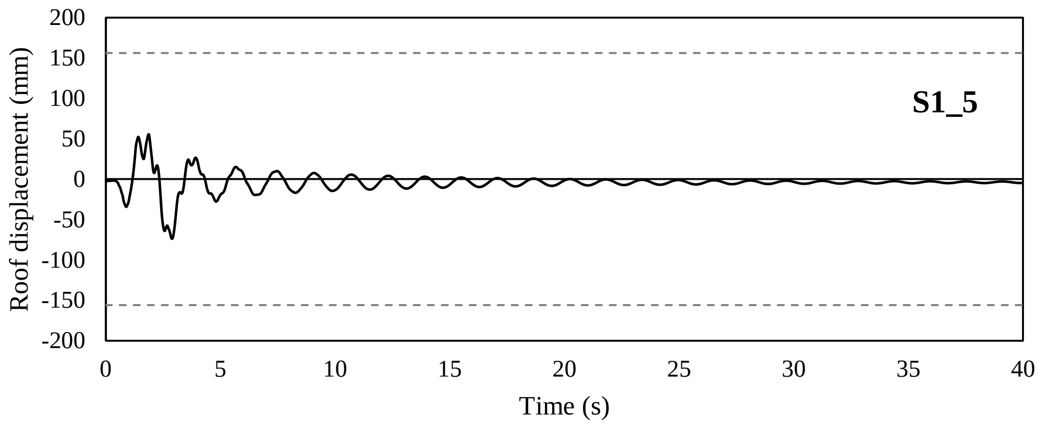

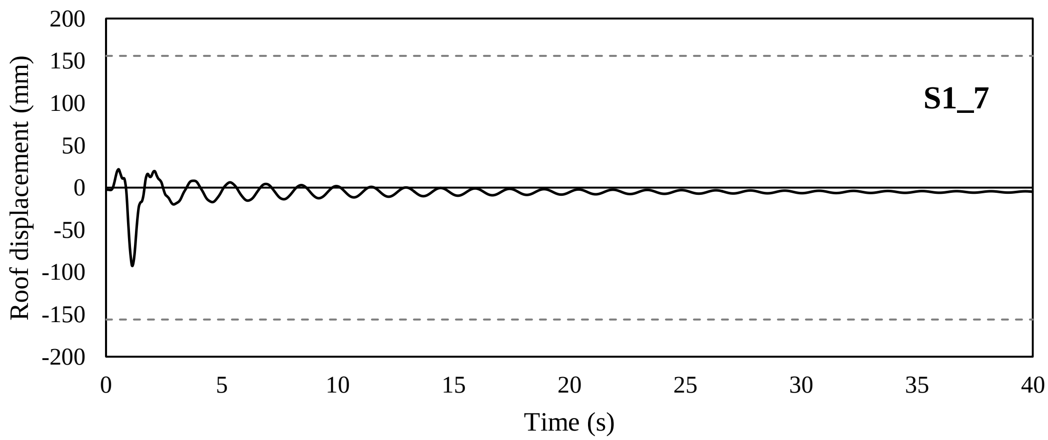

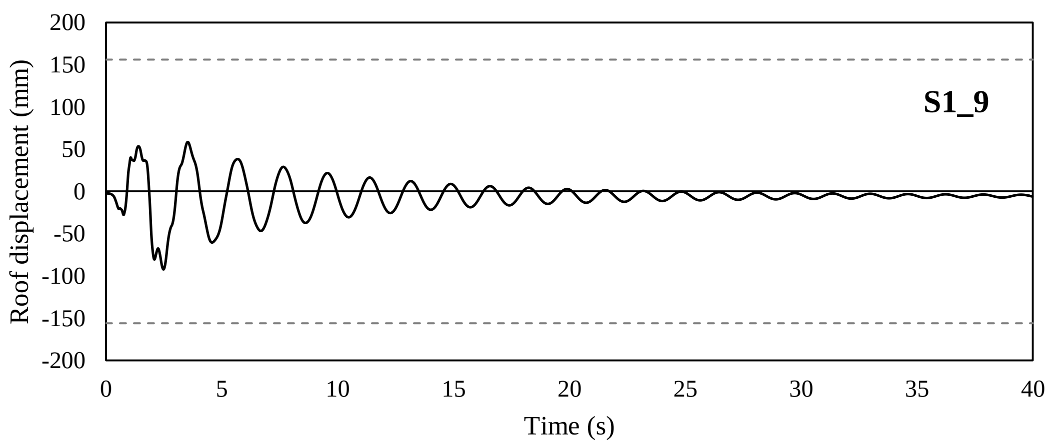

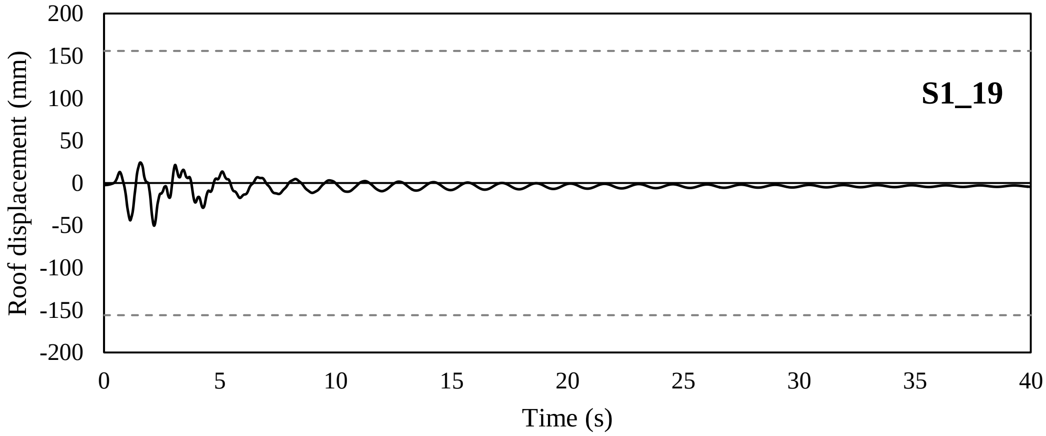
S1_19
Roof displacement (mm)
200
150
100
50
0
-50
-100
-150
-200
0
5
10
15
20
25
30
35
40
Time (s)

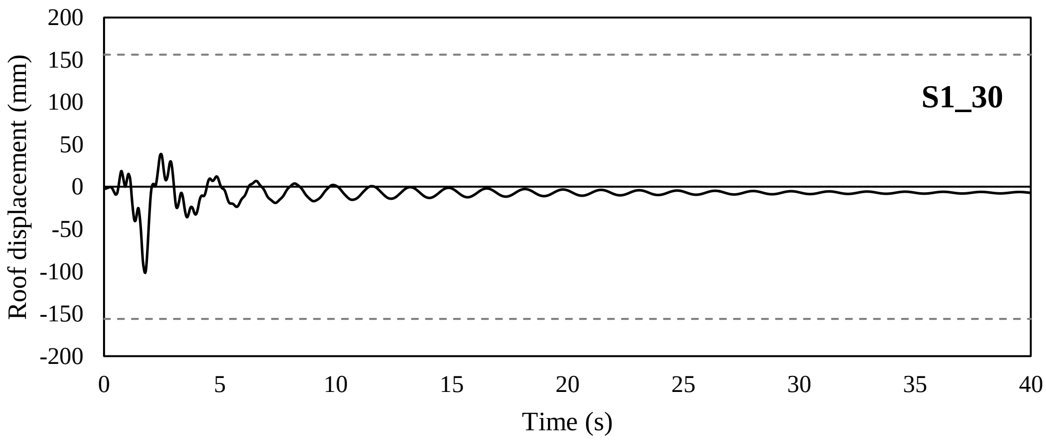
S1_30
Roof displacement (mm)
200
150
100
50
0
-50
-100
-150
-200
0
5
10
15
20
25
30
35
40
Time (s)

Scenario 2

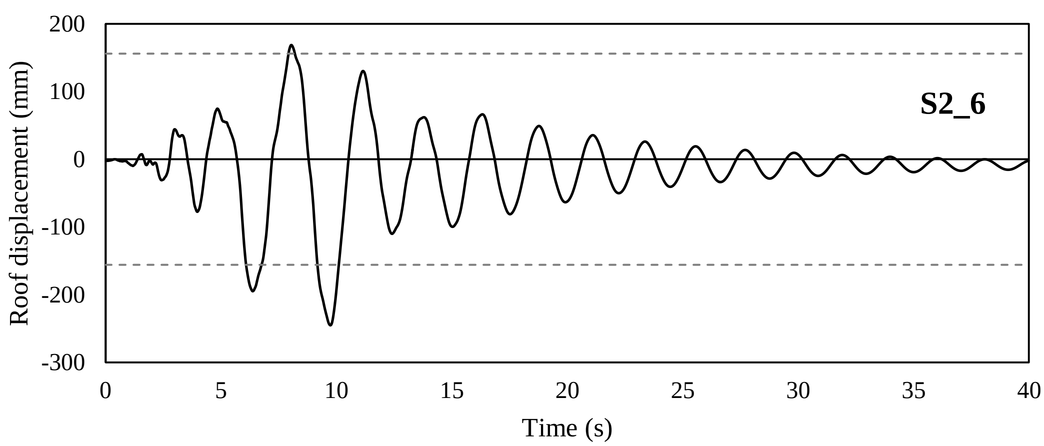
S2_6
Roof displacement (mm)
200
100
0
-100
-200
-300
0
5
10
15
20
25
30
35
40
Time (s)

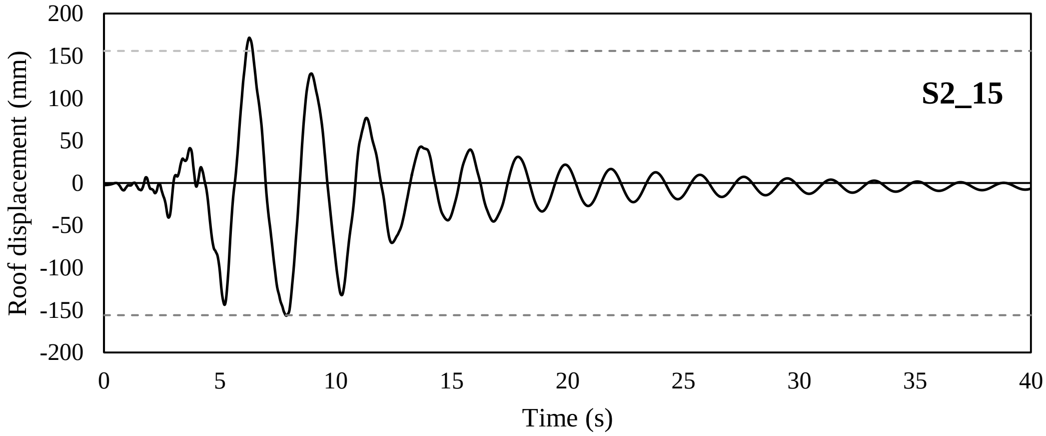
S2_15
Roof displacement (mm)
Time (s)
200
150
100
50
0
-50
-100
-150
-200
0
5
10
15
20
25
30
35
40

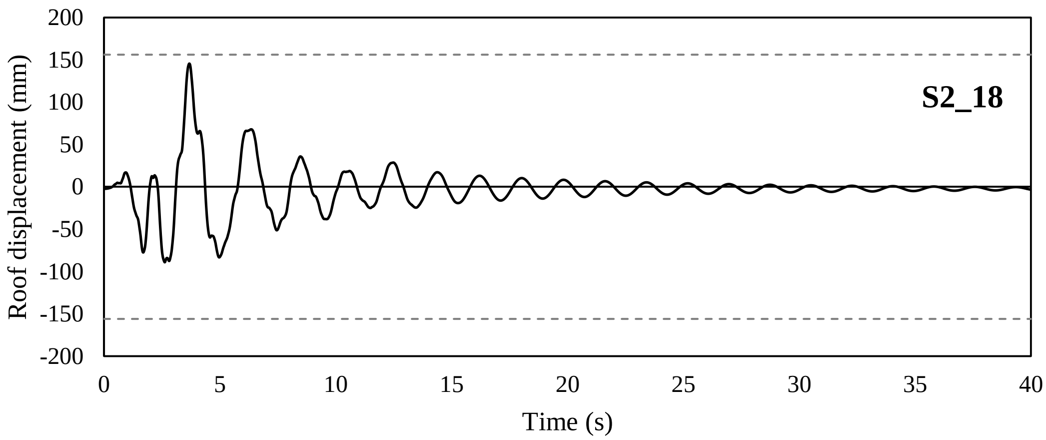
S2_18
Roof displacement (mm)
Time (s)
200
150
100
50
0
-50
-100
-150
-200
0
5
10
15
20
25
30
35
40

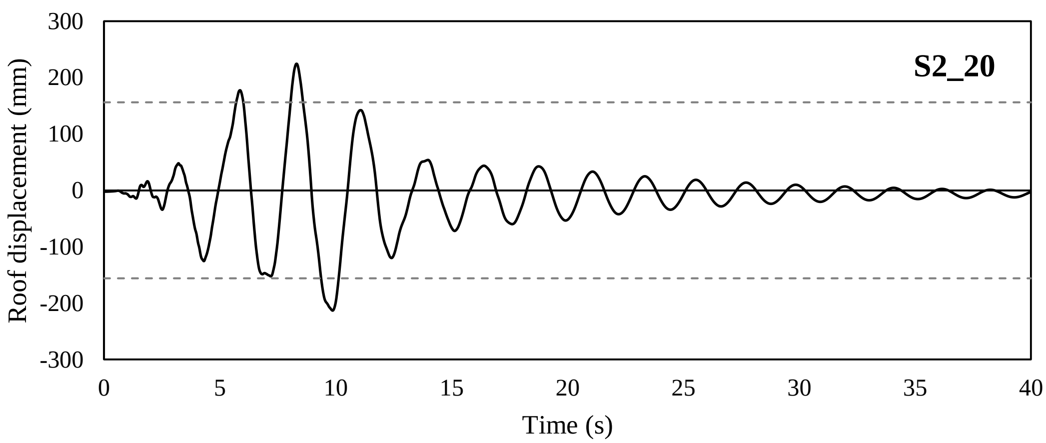
S2_20
Roof displacement (mm)
Time (s)
300
200
100
0
-100
-200
-300
0
5
10
15
20
25
30
35
40

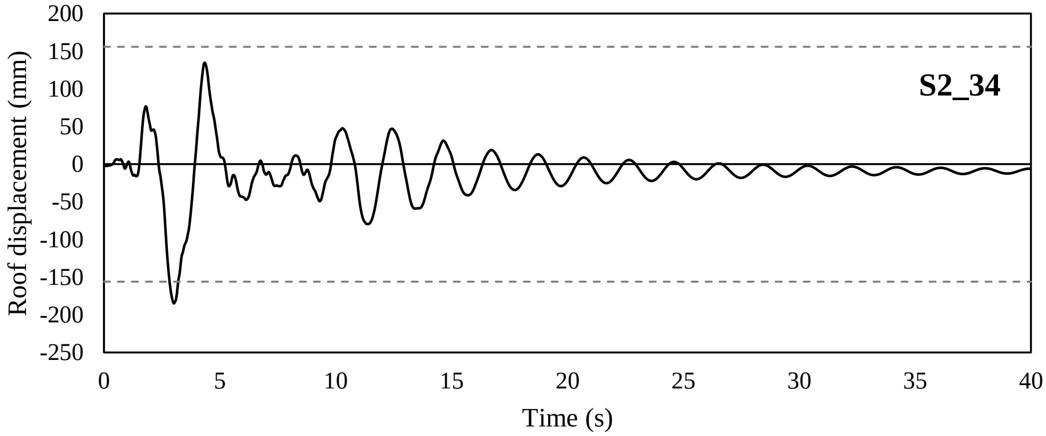
S2_34
Roof displacement (mm)
200
150
100
50
0
-50
-100
-150
-200
-250
0
5
10
15
20
25
30
35
40
Time (s)

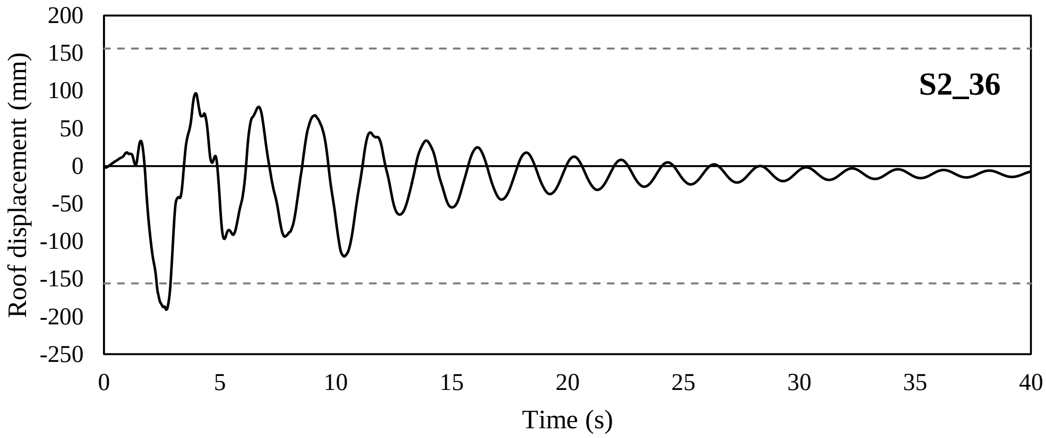
S2_36
Roof displacement (mm)
200
150
100
50
0
-50
-100
-150
-200
-250
0
5
10
15
20
25
30
35
40
Time (s)

Table C-4 - Roof displacement time histories of Wall MDHW

Scenario 1

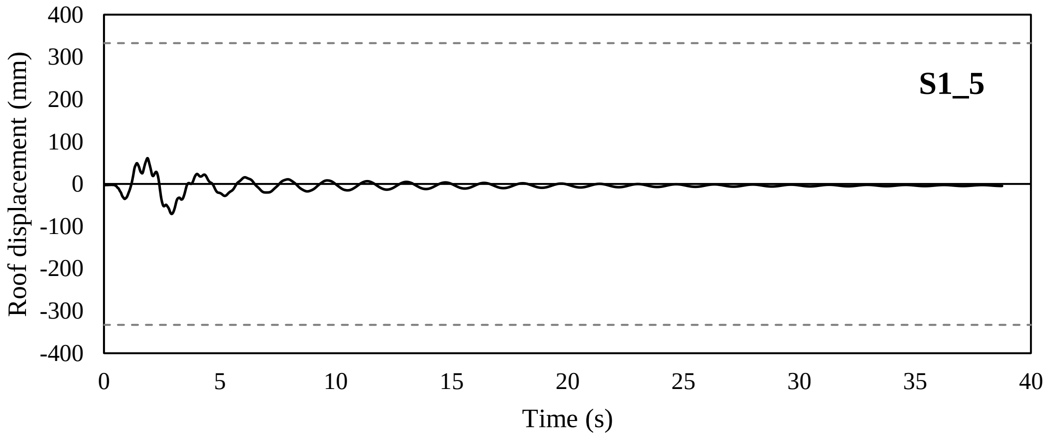

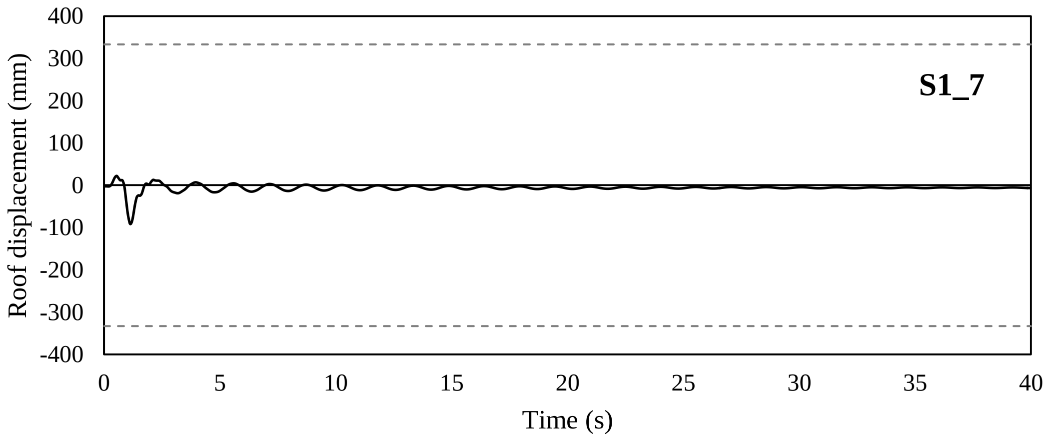

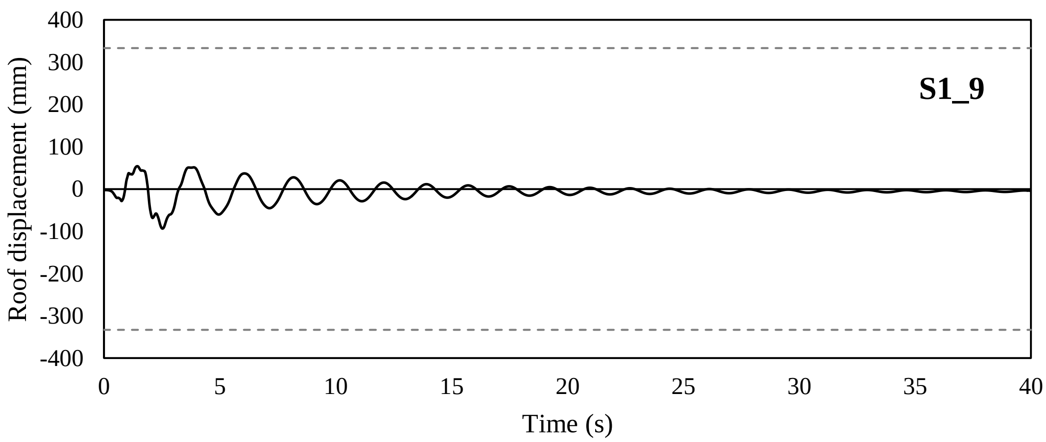

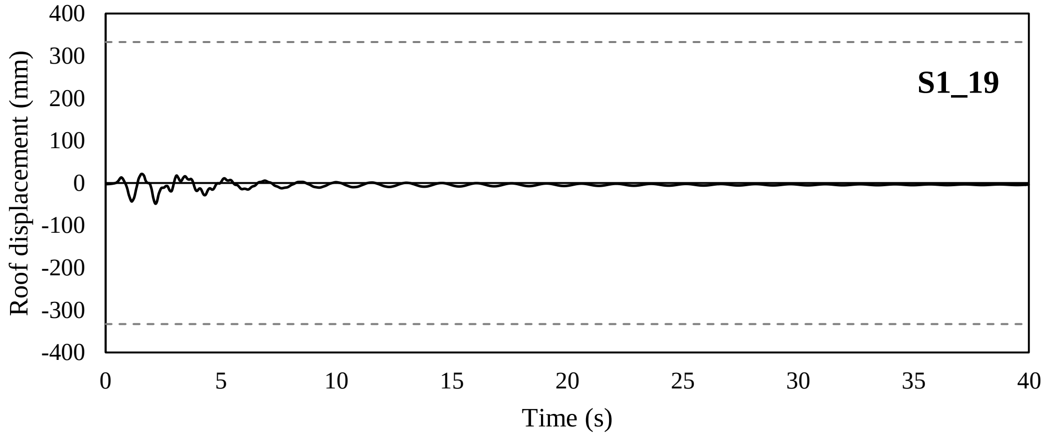
400
300
200
100
0
-100
-200
-300
-400
Roof displacement (mm)
S1_19
0
5
10
15
20
25
30
35
40
Time (s)

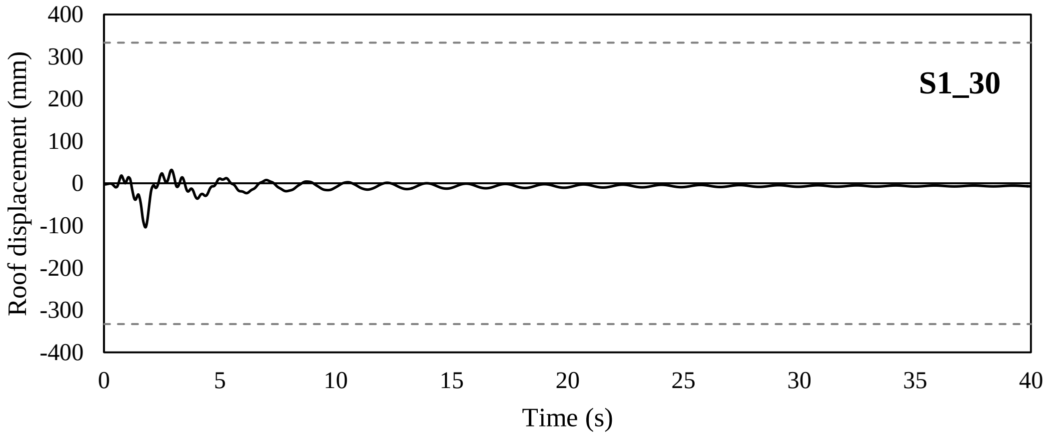
400
300
200
100
0
-100
-200
-300
-400
Roof displacement (mm)
S1_30
0
5
10
15
20
25
30
35
40
Time (s)

Scenario 2

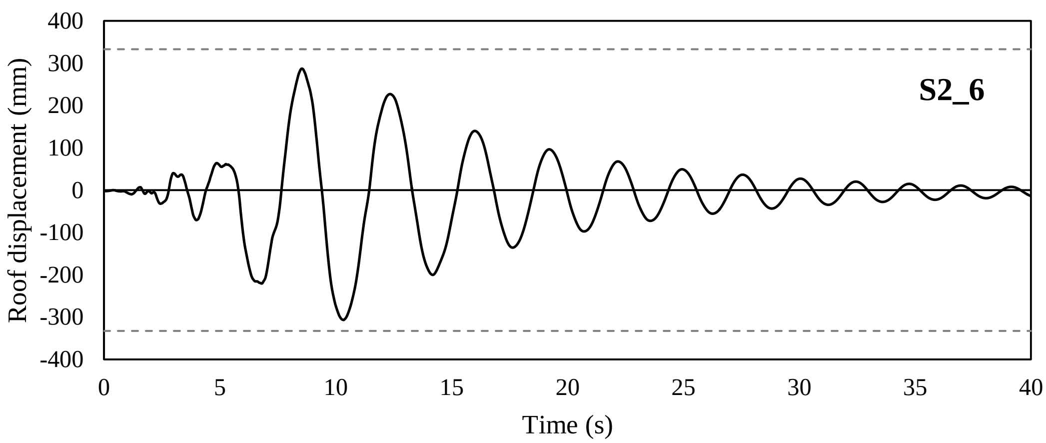
400
300
200
100
0
-100
-200
-300
-400
Roof displacement (mm)
S2_6
0
5
10
15
20
25
30
35
40
Time (s)

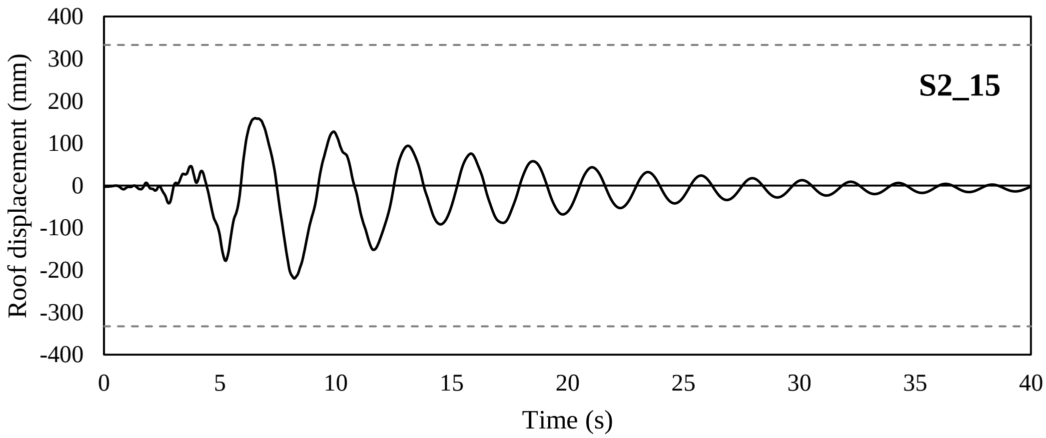
S2_15
Roof displacement (mm)
Time (s)
400
300
200
100
0
-100
-200
-300
-400
0
5
10
15
20
25
30
35
40

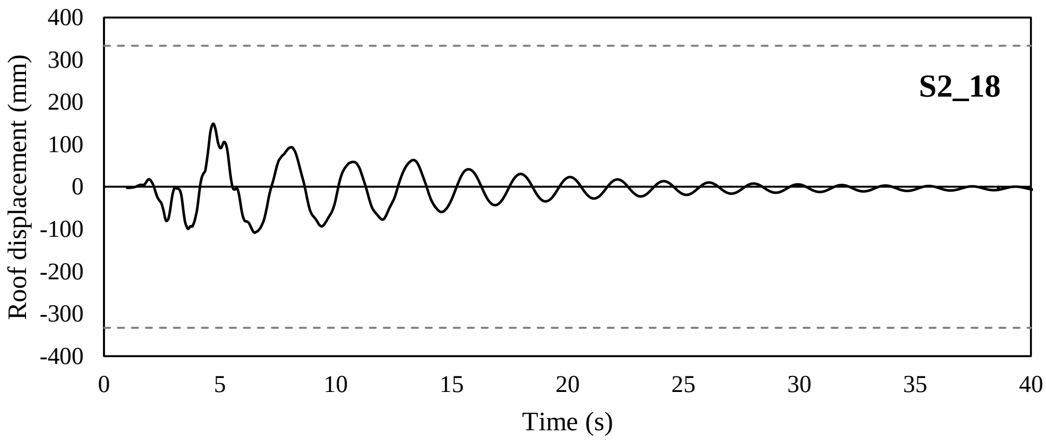
S2_18
Roof displacement (mm)
Time (s)
400
300
200
100
0
-100
-200
-300
-400
0
5
10
15
20
25
30
35
40

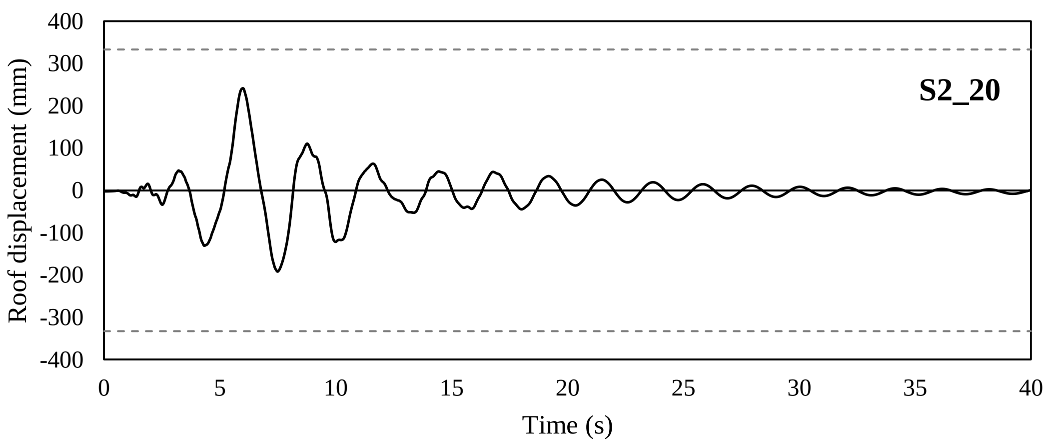
S2_20
Roof displacement (mm)
Time (s)
400
300
200
100
0
-100
-200
-300
-400
0
5
10
15
20
25
30
35
40

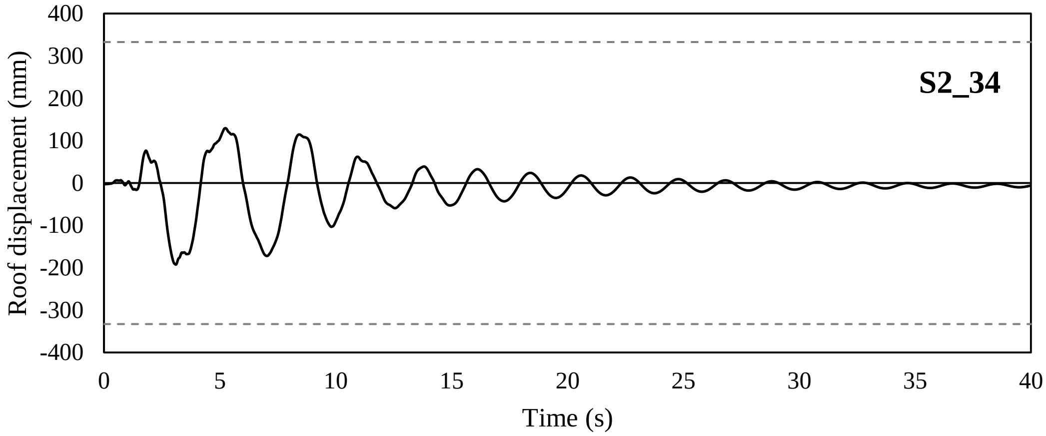
S2_34
Roof displacement (mm)
400
300
200
100
0
-100
-200
-300
-400
0
5
10
15
20
25
30
35
40
Time (s)

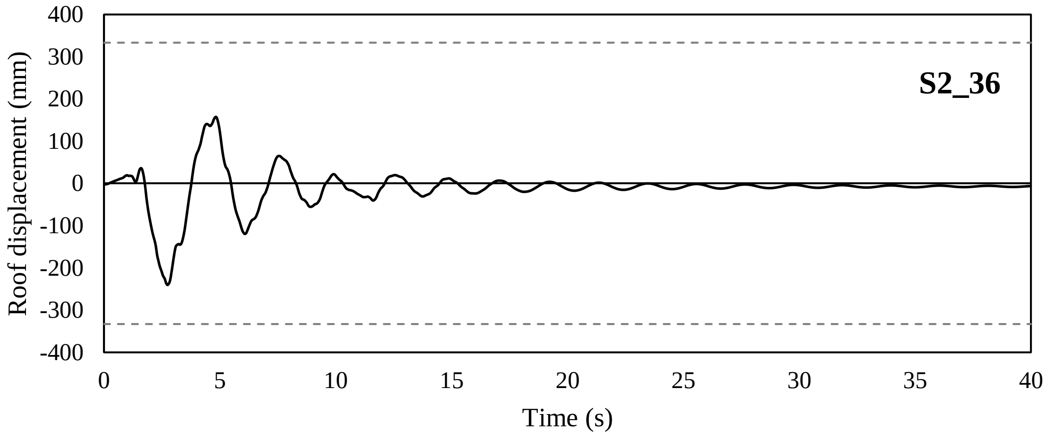
S2_36
Roof displacement (mm)
400
300
200
100
0
-100
-200
-300
-400
0
5
10
15
20
25
30
35
40
Time (s)